

## 2025 Design, Build, Fly Competition Summary



COLLINS AEROSPACE | PRATT & WHITNEY | RAYTHEON



The 2024-25 AIAA/Textron Aviation/RTX Design, Build, Fly Competition Flyoff was held at the Tucson International Modelplex Park Association in Tucson, AZ on the weekend of April 10-13, 2025. This was the 29<sup>th</sup> year of the competition. Of the 159 proposals submitted and judged, 112 teams were invited to submit a design report for the next phase of the competition. 111 teams submitted design reports and 96 teams attended the flyoff (22 international teams). Over 1200 students, faculty, and guests were present. This was a record year for the number of teams and students attending the fly-off. Of the 96 teams in attendance, 92 successfully completed tech inspection. The weather was hot and dusty but flying conditions were generally good, which allowed for non-stop flying. Of the 267 official flight attempts, 164 resulted in a successful score with 78 teams achieving at least one successful flight score and 24 teams successfully completing all missions (one ground and three flight missions). The quality of the teams, their readiness to compete, and the execution of the flights was exceptional.

The contest theme this year was an X-1 Supersonic Flight Test Program. The first mission was a Delivery Flight requiring the aircraft to complete three laps within five minutes. The second mission was a Captive Carry Flight including fuel tanks and an X-1 Flight Test vehicle, with score based on weight of the fuel tanks and time to fly three laps. The final mission included in-flight Launch of the X-1 Flight Test vehicle, with score based on number of laps flown prior to launch of the X-1 and the ability of the X-1 to release from the airplane and fly autonomously to a target area, with a bonus score base on the X-1 vehicle's weight and its landing position within the target area. Teams were also required to complete a ground mission demonstrating the efficiency of converting a production bomber airplane into a flight test platform. The team's final score is the product of the sum of the flight and ground mission scores and total report score plus participation score. More details on the mission requirements and scoring breakdown may be found at the competition website: <http://www.aiaa.org/dbf>.

First Place went to FH Joanneum, Second Place went to Royal Melbourne Institute of Technology, and Third Place went to Santa Clara University. A full listing of the results is included below. The Best Paper Award, sponsored by the Design Engineering TC for the highest design report score, went to the University of New South Wales with a score of 97.58.

For the fourth year, the Stan Powell Memorial Award recognized a team that exhibited the Most Meaningful Lessons Learned during the competition. This year, it was awarded to Virginia Polytechnic Institute and State University. Working through multiple issues that resulted in two failed flight missions, they rallied Sunday to post a very successful score for Mission 3.

We owe our thanks for the success of the DBF competition to the efforts of many volunteers from Textron Aviation, RTX, and the AIAA sponsoring technical committees: Applied Aerodynamics, Aircraft Design, Flight Test, and Design Engineering. These volunteers collectively set the rules, judge the proposals and reports, and execute the flyoff. Thanks also to the Premier Sponsors: Textron Aviation and RTX, and to the AIAA Foundation for their financial support as well as to our Gold sponsors this year – General Atomics, Mathworks, Stoke Space and The University of Arizona Aerospace and Mechanical Engineering. Special thanks go to RTX for hosting the flyoff this year.

Finally, this event would not be nearly as successful without the hard work and enthusiasm from all the students and advisors. If it weren't for you, we wouldn't keep doing it!!

DBF Organizing Committee

# 2025 Design, Build, Fly Competition Summary



Beechcraft

BY TEXTRON AVIATION



COLLINS AEROSPACE | PRATT & WHITNEY | RAYTHEON



## 2025 Design/Build/Fly Competition Final Results

Rank	Team	Part	Mission Scores					Report			2025 DBF Score
			P	GM	M1	M2	M3	Total	Prop	Design	
1	FH JOANNEUM	3	0.92	1.00	1.69	2.73	6.34	81	81.28	81.29	518.23
2	Royal Melbourne Institute of Technology	3	1.00	1.00	1.60	2.36	5.96	89	79.83	81.16	486.36
3	Santa Clara University	3	0.85	1.00	1.36	2.26	5.47	74	89.57	87.20	479.90
4	The University of Akron	3	0.42	1.00	1.97	2.51	5.89	64	83.50	80.55	477.78
5	Rensselaer Polytechnic Institute	3	0.08	1.00	1.93	3.00	6.01	87	75.07	76.80	464.60
6	The University of Texas at Austin	3	0.65	1.00	1.88	2.11	5.64	76	82.65	81.58	463.44
7	Virginia Polytechnic Institute and State University	3	0.63	1.00	1.42	2.35	5.40	70	87.80	85.19	463.16
8	University of Ljubljana	3	0.59	1.00	1.69	2.04	5.32	76	88.17	86.35	461.96
9	The University of Sydney	3	0.46	1.00	1.58	2.28	5.32	88	86.00	86.32	461.94
10	University of California, Los Angeles	3	0.17	1.00	1.42	2.22	4.82	84	92.43	91.13	441.97
11	University of Southern California	3	0.35	1.00	1.28	2.11	4.75	84	89.36	88.50	423.14
12	University at Buffalo	3	0.28	1.00	2.00	2.26	5.54	79	74.05	74.73	416.95
13	The University of Kansas	3	0.21	1.00	1.55	2.22	4.99	70	85.07	82.76	416.03
14	The Pennsylvania State University	3	0.08	1.00	1.55	2.15	4.78	79	85.07	84.16	405.19
15	Embry-Riddle Aeronautical University - Prescott	3	0.06	1.00	1.66	2.22	4.95	73	82.52	81.04	403.99
16	Columbia University	3	0.96	1.00	1.15	2.04	5.15	82	77.02	77.76	403.78
17	University of Illinois Urbana-Champaign	3	0.21	1.00	1.32	2.61	5.14	82	76.67	77.50	401.20
18	University of Maribor	3	0.22	1.00	1.48	2.57	5.27	68	75.87	74.65	396.62
19	The Hong Kong Polytechnic University	3	0.44	1.00	1.29	2.11	4.83	79	80.70	80.38	391.58
20	Universidad Pontificia Bolivariana	3	0.51	1.00	1.20	2.07	4.79	83	80.25	80.66	389.11
21	The University of Texas at Dallas	3	0.09	1.00	1.37	2.04	4.49	77	85.67	84.34	382.10
22	University of Oklahoma	3	0.20	1.00	1.34	2.22	4.76	74	80.47	79.49	381.73
23	Texas A&M University	3	0.24	1.00	1.21	2.11	4.56	66	71.30	70.50	324.53
24	University of Kentucky - Paducah	3	0.11	1.00	1.18	2.11	4.40	68	65.57	66.00	293.16
25	University of Michigan - Ann Arbor	3	0.88	1.00	1.23	0.00	3.11	77	90.42	88.44	278.48
26	University of Massachusetts Amherst	3	0.75	1.00	1.37	0.00	3.12	75	84.67	83.26	262.73
27	Georgia Institute of Technology	3	0.00	1.00	1.74	0.00	2.74	77	86.62	85.17	236.26
28	Universidade da Beira Interior Faculdade de Engenharia	3	0.22	1.00	1.36	0.00	2.58	66	86.02	82.98	217.18
29	Colorado State University	3	0.05	1.00	1.44	0.00	2.49	76	87.50	85.83	216.72
30	North Carolina State University	3	0.12	1.00	1.38	0.00	2.51	89	82.53	83.49	212.48
31	The Hong Kong University of Science and Technology	3	0.21	1.00	1.42	0.00	2.63	81	76.60	77.20	205.71
32	San Diego State University	3	0.22	1.00	1.71	0.00	2.93	71	67.98	68.49	203.73
33	University of Florida	3	0.16	1.00	1.22	0.00	2.38	84	81.72	82.08	198.59
34	San Jose State University	3	0.10	1.00	1.37	0.00	2.48	80	78.50	78.78	198.04
35	Washington University in St. Louis	3	0.13	1.00	1.11	0.00	2.24	83	83.17	83.09	188.75
36	Aviation and Aerospace University, Bangladesh	3	0.12	1.00	1.06	0.00	2.18	70	86.57	84.10	186.45
37	Khalifa University of Science and Technology	3	0.25	1.00	1.13	0.00	2.38	75	72.70	73.09	177.32
38	University of Notre Dame	3	0.17	1.00	1.09	0.00	2.27	78	74.50	74.98	172.88
39	Military Institute of Science and Technology	3	0.22	1.00	1.07	0.00	2.29	65	75.50	73.96	172.20
40	The University of Hong Kong	3	0.11	1.00	1.22	0.00	2.33	72	70.92	71.03	168.31
41	The Ohio State University	3	0.06	1.00	1.30	0.00	2.35	72	69.77	70.06	167.84
42	Utah State University	3	0.15	1.00	1.08	0.00	2.23	68	74.10	73.16	166.31
43	Trine University	3	0.06	1.00	1.16	0.00	2.23	63	75.05	73.25	166.24
44	Purdue University (Main Campus)	3	0.05	1.00	1.04	0.00	2.08	78	73.00	73.77	156.71
45	Missouri University of Science and Technology	3	0.00	1.00	1.30	0.00	2.30	73	65.17	66.29	155.32
46	Rowan University	3	0.12	1.00	1.12	0.00	2.24	72	66.33	67.21	153.25
47	University of Colorado Boulder	3	0.13	1.00	1.14	0.00	2.27	77	63.58	65.53	151.44
48	Clarkson University	3	0.77	1.00	0.00	0.00	1.77	77	79.13	78.87	142.50
49	Johns Hopkins University	3	0.07	1.00	1.01	0.00	2.08	78	58.03	60.98	129.83
50	California State University, Long Beach	3	0.04	1.00	1.00	0.00	2.05	68	60.03	61.27	128.47
51	University of Washington-Seattle	3	0.34	1.00	0.00	0.00	1.34	85	89.50	88.83	122.25
52	University of New South Wales	3	0.13	1.00	0.00	0.00	1.13	86	97.58	95.83	110.95
53	The University of Alabama	3	0.28	1.00	0.00	0.00	1.28	74	85.30	83.67	110.01
54	University of Maryland, College Park (UMCP)	3	0.38	1.00	0.00	0.00	1.38	88	73.92	76.09	107.65
55	Rutgers University - New Brunswick	3	0.24	1.00	0.00	0.00	1.24	76	85.87	84.34	107.61
56	Alexandria University	3	0.27	1.00	0.00	0.00	1.27	73	81.75	80.45	105.01

# 2025 Design, Build, Fly Competition Summary



Beechcraft

BY TEXTRON AVIATION



COLLINS AEROSPACE | PRATT & WHITNEY | RAYTHEON



## 2025 Design/Build Fly Competition Final Results (cont)

Rank	Team	Part	Mission Scores					Report			2025 DBF Score
			P	GM	M1	M2	M3	Total	Prop	Design	
57	Embry-Riddle Aeronautical University, Daytona Beach	3	0.14	1.00	0.00	0.00	1.14	74	90.70	88.22	103.42
58	Universidad de Antioquia	3	0.13	1.00	0.00	0.00	1.13	73	88.73	86.31	100.15
59	University of California, Irvine	3	0.22	1.00	0.00	0.00	1.22	62	82.10	79.10	99.46
60	Auburn University at Auburn	3	0.10	1.00	0.00	0.00	1.10	81	83.90	83.50	94.91
61	University of Maine	3	0.21	1.00	0.00	0.00	1.21	64	74.37	72.80	90.82
62	National University of Science and Technology POLITEHNICA Bucharest	3	0.06	1.00	0.00	0.00	1.06	67	81.60	79.37	86.90
63	DAYANANDA SAGAR COLLEGE OF ENGINEERING	3	0.00	1.00	0.00	0.00	1.00	78	84.50	83.53	86.53
64	George Washington University	3	0.07	1.00	0.00	0.00	1.07	63	77.92	75.61	84.10
65	VEERMATA JIJABAI TECHNOLOGICAL INSTITUTE	3	0.10	1.00	0.00	0.00	1.10	73	73.12	73.05	83.61
66	West Virginia University	3	0.03	1.00	0.00	0.00	1.03	71	78.75	77.66	83.11
67	Stanford University	3	0.00	1.00	0.00	0.00	1.00	66	81.73	79.32	82.32
68	Case Western Reserve University	3	0.09	1.00	0.00	0.00	1.09	64	68.17	67.50	76.85
69	John Brown University	3	0.04	1.00	0.00	0.00	1.04	66	70.37	69.64	75.35
70	North Dakota State University	3	0.00	1.00	0.00	0.00	1.00	72	67.30	68.01	71.01
71	The City College of New York	3	0.23	1.00	0.00	0.00	1.23	65	50.92	53.07	68.27
72	Saint Louis University	3	0.08	1.00	0.00	0.00	1.08	66	59.57	60.50	68.05
73	University of Arkansas	2	0.76	0.00	0.00	0.00	0.76	84	84.03	84.06	66.28
74	Massachusetts Institute of Technology	3	0.16	1.00	0.00	0.00	1.16	76	43.67	48.52	59.32
75	University of California, San Diego	3	0.06	1.00	0.00	0.00	1.06	61	47.23	49.29	55.16
76	University of Nebraska Lincoln	3	0.05	1.00	0.00	0.00	1.05	61	45.08	47.41	52.84
77	University of Georgia	3	0.00	1.00	0.00	0.00	1.00	62	47.47	49.64	52.64
78	Texas Tech University	3	0.00	1.00	0.00	0.00	1.00	64	44.68	47.56	50.56
79	University of Tennessee Knoxville	3	0.13	1.00	0.00	0.00	1.13	65	28.33	33.84	41.13
80	National University of Singapore	3	0.44	0.00	0.00	0.00	0.44	72	87.90	85.58	40.58
81	Seoul National University	3	0.17	0.00	0.00	0.00	0.17	75	84.95	83.46	17.47
82	Cornell University	3	0.16	0.00	0.00	0.00	0.16	84	77.58	78.47	15.20
83	Rochester Institute of Technology	3	0.08	0.00	0.00	0.00	0.08	81	75.83	76.62	9.09
84	University of North Carolina at Charlotte	3	0.06	0.00	0.00	0.00	0.06	74	79.63	78.79	7.66
85	University of Missouri - Columbia	2	0.06	0.00	0.00	0.00	0.06	72	69.92	70.28	5.91
86	University of California Merced	2	0.05	0.00	0.00	0.00	0.05	68	36.90	41.52	3.98
87	Birla Institute of Technology and Science , Pilani, KK Birla Goa Campus	3	0.00	0.00	0.00	0.00	0.00	77	75.57	75.78	3.00
88	University of South Alabama	3	0.00	0.00	0.00	0.00	0.00	68	55.15	57.00	3.00
89	University of Hartford	3	0.00	0.00	0.00	0.00	0.00	69	51.45	54.04	3.00
90	California State Polytechnic University Pomona	2	0.00	0.00	0.00	0.00	0.00	67	63.33	63.85	2.00
91	University of Vermont	2	0.00	0.00	0.00	0.00	0.00	70	25.18	31.89	2.00
92	Vaughn College of Aeronautics and Technology	2	0.00	0.00	0.00	0.00	0.00	62	22.73	28.62	2.00
93	Boston University	1	0.00	0.00	0.00	0.00	0.00	79	59.00	62.06	1.00
94	University of South Carolina	1	0.00	0.00	0.00	0.00	0.00	70	59.37	60.95	1.00
95	University of Missouri - Kansas City	1	0.00	0.00	0.00	0.00	0.00	67	53.07	55.10	1.00
96	University of Idaho	1	0.00	0.00	0.00	0.00	0.00	62	45.00	47.55	1.00
97	University of Arizona	0	0.00	0.00	0.00	0.00	0.00	67	32.03	37.30	0.00
98	Yildiz Teknik Universitesi	0	0.00	0.00	0.00	0.00	0.00	66	78.33	76.49	0.00
99	Iowa State University	0	0.00	0.00	0.00	0.00	0.00	69	74.33	73.52	0.00
100	Mukesh Patel School Of Technology Management and Engineering (Mumbai)	0	0.00	0.00	0.00	0.00	0.00	78	67.10	68.80	0.00
101	Ghulam Ishaq Khan Institute of Engineering Sciences and Technology	0	0.00	0.00	0.00	0.00	0.00	64	68.83	68.12	0.00
102	Cairo University	0	0.00	0.00	0.00	0.00	0.00	82	60.87	63.99	0.00
103	University of California, Davis	0	0.00	0.00	0.00	0.00	0.00	74	59.58	61.68	0.00
104	Gonzaga University	0	0.00	0.00	0.00	0.00	0.00	67	60.22	61.25	0.00
105	Colorado School of Mines	0	0.00	0.00	0.00	0.00	0.00	68	56.58	58.29	0.00
106	The University of Tennessee Chattanooga	0	0.00	0.00	0.00	0.00	0.00	68	53.97	56.12	0.00
107	Western Michigan University	0	0.00	0.00	0.00	0.00	0.00	61	46.33	48.53	0.00
108	Tribhuvan University	0	0.00	0.00	0.00	0.00	0.00	75	43.83	48.44	0.00
109	Clemson University	0	0.00	0.00	0.00	0.00	0.00	75	39.25	44.62	0.00
110	National Autonomous University of Mexico	0	0.00	0.00	0.00	0.00	0.00	61	34.13	38.11	0.00
111	University of Pennsylvania	0	0.00	0.00	0.00	0.00	0.00	65	22.33	28.74	0.00
112	James Madison University	0	0.00	0.00	0.00	0.00	0.00	61	0.00	9.17	0.00



PRESENTING

**BRICK**  
AND BRICK JR.

**AIAA DBF 24–25 DESIGN REPORT**

UNIVERSITY OF NEW SOUTH WALES



## Table of Contents

<b>Abbreviations, Acronyms and Symbols.....</b>	<b>3</b>
<b>1. Executive Summary.....</b>	<b>4</b>
<b>2. Management Summary.....</b>	<b>5</b>
2.1. Team Organisation and Roles .....	5
2.2. Schedule and Major Milestones .....	6
<b>3. Conceptual Design .....</b>	<b>7</b>
3.1. Problem Statement .....	7
3.2. System Design Requirements.....	8
3.3. Sensitivity Analysis.....	9
3.4. Aircraft Configurations Decision Matrix .....	10
<b>4. Preliminary Design .....</b>	<b>17</b>
4.1. Design Methodology .....	17
4.2. Mission Model .....	18
4.3. Aerodynamic Design Analysis.....	19
4.4. Mission Payloads .....	25
4.5. Propulsion Analysis .....	27
4.6. Stability Analysis .....	29
4.7. CFD Analysis.....	30
4.8. Preliminary Performance Prediction.....	32
<b>5. Detailed Design.....</b>	<b>32</b>
5.1. Dimensional Design Parameters.....	32
5.2. Structural Analysis.....	33
5.3. X-1 Glider .....	39
5.4. Avionics and Wiring.....	42
5.5. Weight and Balance .....	43
5.6. Flight Performance and Mission Specific Performance .....	44
5.7. Drawing Package .....	44
<b>6. Manufacturing Plan.....</b>	<b>49</b>
6.1. Investigated Manufacturing Processes .....	49
6.2. Material Selection.....	50
6.3. Manufacturing Timeline .....	52
<b>7. Testing Plan.....</b>	<b>52</b>
7.1. Testing Schedule.....	52
7.2. Testing Objectives .....	53
7.3. Sub-system Testing .....	54
7.4. Flight Tests .....	57
7.5. Flight Checklist.....	57
<b>8. Performance Results .....</b>	<b>58</b>
8.1. Subsystem Performance .....	58
8.2. Completed Aircraft Performance .....	59
<b>9. Bibliography.....</b>	<b>60</b>



## Abbreviations, Acronyms and Symbols

$\alpha$	Angle of Attack	<b>LG</b>	Landing Gear
$\beta$	Sideslip Angle	<b>M#</b>	Mission Number
$\delta$	Control Surface Deflection	<b>MAC</b>	Mean Aerodynamic Chord
$\delta_e$	Elevator Deflection	<b>MTOW</b>	Maximum Take-off Weight
$\zeta$	Damping Ratio	<b>n</b>	Load Factor
$\eta$	Propulsion Efficiency Factor	<b>NP</b>	Neutral Point
$\mu$	Ground Roll Friction Coefficient	<b>P</b>	Power
$\rho$	Density	<b>PLA</b>	Polylactic Acid
$\sigma$	Stress	<b>q</b>	Dynamic Pressure
$\tau$	Time Constant	<b>RC</b>	Remote-Controlled
$\phi$	Lumens	<b>RFP</b>	Request for Proposal
$\omega_n$	Natural Frequency	<b>T</b>	Thrust Force
<b>AC</b>	Aerodynamic Centre	<b>TE</b>	Trailing Edge
<b>AGL</b>	Above Ground Level	<b>S</b>	Planform Area
<b>AIAA</b>	American Institute of Aeronautics and Astronautics	$S_g$	Take-off Ground Roll
<b>AMSL</b>	Above Mean Sea Level	<b>SFD</b>	Shear Force Diagram
<b>AVL</b>	Athena Vortex Lattice	<b>SM</b>	Static Margin
<b>BMD</b>	Bending Moment Diagram	<b>UNSW</b>	University of New South Wales
$C_D$	Coefficient of Drag	<b>UAV</b>	Unmanned Aerial Vehicles
$C_{D_{min}}$	Minimum Coefficient of Drag	$v$	Voltage
$C_{D_{TO}}$	Take-off Coefficient of Drag	$V_Y$	Best Rate of Climb Airspeed
$\Delta C_{D_{tank}}$	Tank Drag Coefficient	$V_{TO}$	Take-off Velocity
$\Delta C_{D_s}$	Empirical Drag Coefficient	$V_{Cruise}$	Cruise Velocity
$C_L$	Coefficient of Lift	<b>VT</b>	Vertical Tail
$C_{L_{max}}$	Maximum Clean Coefficient of Lift	<b>W</b>	Weight Force
$C_{L_{TO}}$	Take-off Coefficient of Lift	$W_0$	Maximum Take-off Weight
<b>CAD</b>	Computer-Aided Design	$W_e$	Empty Weight of Aircraft
<b>CFD</b>	Computational Fluid Dynamics	$W_{PL}$	Payload Weight
<b>CF</b>	Carbon Fiber	$W_{ps}$	Propulsive System Weight
<b>CFRP</b>	Carbon Fiber Reinforced Polymer		
<b>CG</b>	Centre of Gravity		
<b>COTS</b>	Commercial Off the Shelf		
<b>DBF</b>	Design Build Fly		
<b>D</b>	Drag Force		
<b>E</b>	Energy		
<b>FEA</b>	Finite Element Analysis		
<b>FoS</b>	Factor of Safety		
<b>g</b>	Acceleration due to Gravity		
<b>GM</b>	Ground Mission		
<b>GPS</b>	Global Positioning System		
<b>HT</b>	Horizontal Tail		
$i$	Current		
<b>I</b>	Candela		
<b>IMU</b>	Inertial Measuring Unit		
<b>k</b>	Lift Induced Drag Factor		
<b>L</b>	Lift Force		
<b>LE</b>	Leading Edge		



## 1. Executive Summary

This design report details the University of New South Wales (UNSW) preliminary aerodynamic and structural design, part fabrication and testing of a RC aircraft. Submitted for the 2024-2025 request for proposal (RFP) from the American Institute of Aeronautics and Astronautics (AIAA), Design Build Fly (DBF) competition. The team designed around the AIAA's RFP of the X-1 supersonic flight program, an acknowledgment to the early prototype designed by the Bell Aircraft Company and NACA to investigate the challenges faced during supersonic flight. This RFP involved four main missions, a time trial for the GM, proof of flight for M1, maximising payload weight and speed for M2 and maximising number of laps and deploying the X-1 glider into the designated box in a timed trial for M3. The team constructed mission sensitivity studies and identified aircraft speed, payload weight for M2, and assembling time for GM as the three main contributors to score. Hence, the aircraft was constructed for an MTOW of 48.5lbs and was named the *BRICK*.

The BRICK is a dual motor tractor with a tricycle landing gear formation, with a high rectangular wing and conventional tail connected via a boom. The dual motor tractor was selected due to the high static thrust required at take-off and during flight at the selected MTOW, while a single motor would require components not readily available due to geographical constraints. The tricycle landing gear was opted for given the expected long ground roll distance aiding the pilot with increased manoeuvrability. The high wing was selected due to the propeller and pylons clearance required. The tail boom was selected to minimise the empty weight of the *BRICK* to maximise allowable payload, while the conventional tail was selected due to superior stability characteristics and structural simplicity. Further, the team selected two external fuel tanks weighing 6.61lbs each and an internal fuel tank weighing a maximum of 26.34lbs filled with steel pellets for maximum density. The BRICK was constructed out of plywood, balsa, and woven carbon fibre plates and rods, while the external aircraft was covered in Monokote film. The X-1 was constructed out of XPS foam to minimise the structural weight to maximise the M3 score, while the design consisted of a flying body, delta wing with elevons and H-tail configuration. The flying body was selected due to ease of manufacturing, while the delta wing allowed for sufficient lift and stability. The elevons were selected to limit number of servos to minimise weight, while providing adequate pitch and roll stability. The H-tail was selected to ensure adequate yaw stability without interfering with the main aircraft compared to winglets. The BRICK had an overall length of 78.9 in, a span of 72.0 in and a maximum height of 27.9 in. The X-1 had a length of 7.85 in, span of 5.98 in, and a height of 2.76 in. Overall performance for the BRICK is shown in Table 1.1.

**Table 1.1. Predicted Performance of the BRICK**

Properties	M1	M2	M3	GM
<b>Payload (lbs)</b>	N/A	35.3	2.2	N/A
<b>X-1 Weight (lbs)</b>	N/A	0.22	0.22	N/A
<b>Take-off Weight (lbs)</b>	13.2	48.5	15.4	N/A
<b>TOFL (ft)</b>	32.8	202.1	40.0	N/A
<b>Cruise Speed (ft/s)</b>	90.0	118.1	85.0	N/A
<b>Number of Laps</b>	3	3	9 (before X-1 Launch)	N/A
<b>Mission Time (sec)</b>	80	126	300	35

## 2. Management Summary

The UNSW DBF team is an entirely student managed team from UNSW consisting of 23 members, 4 of whom are seniors and the rest underclassman. The team is financially supported by the UNSW Engineering faculty and by various grants and sponsorships. Likewise, the team is technically advised by alumni and academics at periodical design reviews.

### 2.1. Team Organisation and Roles

The UNSW DBF technical team is divided into 3 main teams, following the functional organisation structure, paired with a student run Society Executive Board as seen in Figure 2.1.

The Society Executive Board are external to the technical team and govern societal functions like finances, member intake, events and direct communication with the Engineering Faculty.

On the technical side, each sub-team has a team lead, which is overseen by the chief engineer who manages the overall project. The chief engineer is responsible for maintaining and tracking the project timeline and communicates directly with the team leads setting up key milestones, meetings and deliverables. They also communicate directly with the executive team for logistics, events and funding issues, and organise design reviews with the academic supervisor.

Project deliverables are set out by the chief engineer and delegated amongst the members of each team by the sub-team leads, based on individual skills and interests. Members work closely with their team leads who report back to the chief engineer on deliverable updates. Any complications that arise or major design decisions that cause roadblocks result in a full team lead meeting to analyse the advantages and disadvantages and the subsequent steps forward in the design. Table 2.1 outlines the roles and responsibilities of each team.

**Table 2.1 Team Roles and Individual Skillsets**

Team	Tasks	Skills
<b>Structures</b>	Design and manufacture wing, tail and fuselage structure. Perform structural analysis and testing. Choose and analyse materials.	Knowledge in Solid Mechanics, Statics & Dynamics, CAD (Fusion [1]), FEA and various manufacturing techniques.
<b>Flight Dynamics</b>	Analyse and determine aerodynamic sizing of wings, tail, and aircraft configuration. Determine ideal propulsion package (motors, propeller, battery, esc).	Knowledge in aircraft performance and stability theory, computational assessment tools (MATLAB, XFLR5, CFD), propeller propulsion theory, eCalc, MotoCalc.
<b>Missions Systems</b>	Design and manufacture mission payloads (Fuel tanks + X-1). Conduct Ground Mission testing. Design avionics configuration (servos, Rx) and Data Acquisition System (DAQ)	Knowledge in avionics, electrical circuitry/PCB design, and flight control systems (ArduPilot, iNav, Betaflight).

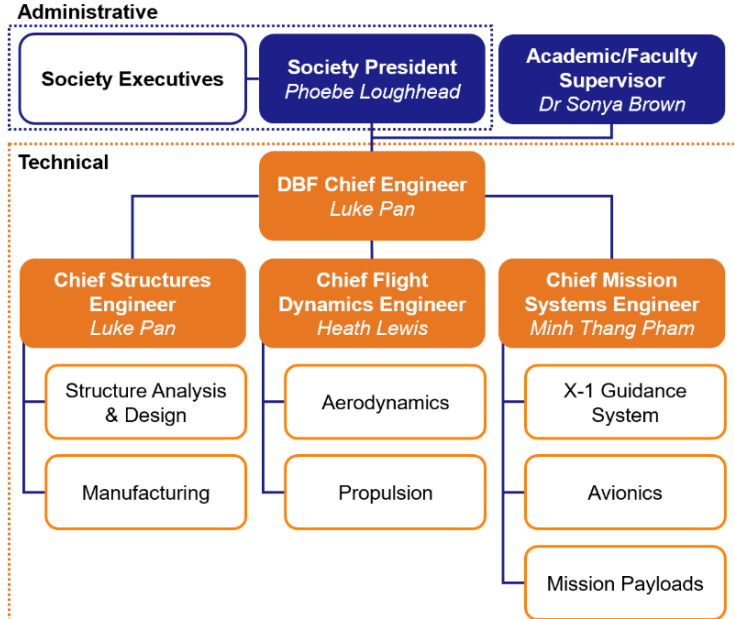


**Figure 2.1 UNSW DBF 2024-25 Organisational Structure**

## 2.2. Schedule and Major Milestones

The Gantt Chart in Figure 2.2 is utilised by the Chief Engineer to plan and oversee the progression of the team and the timeline for objectives and milestones related to the development of the DBF competition plane. The team refers to the Gantt Chart to track and monitor progress in the weekly full team workshops, where any tasks which are blockers or falling behind are identified and managed according to the schedule. As such, the schedule is constantly updated with the actual progress to track deliverables shown in Figure 2.2. Key milestones such as prototype fly days, competition due dates, and design reviews, have a specific due date. The Gantt Chart allows for the manufacturing of three main aircraft in which V1 involves testing the aerodynamics of the aircraft at empty and MTOW ensuring the take-off requirement is met, V2 includes pylon and X-1 design and implementation ensuring the X-1 is stable in flight and descends in the allocated time. V3 aims to increase aerodynamic performance of the aircraft by refining the manufacturing. Whilst progress this season has been good; it should be noted that a combination of bad weather, a longer university shutdown period, and university workshop closure at the end of the year delayed progression of the V2 and V3 prototypes and subsequent testing. As such, the team focused on the Design Report, which was completed ahead of schedule.

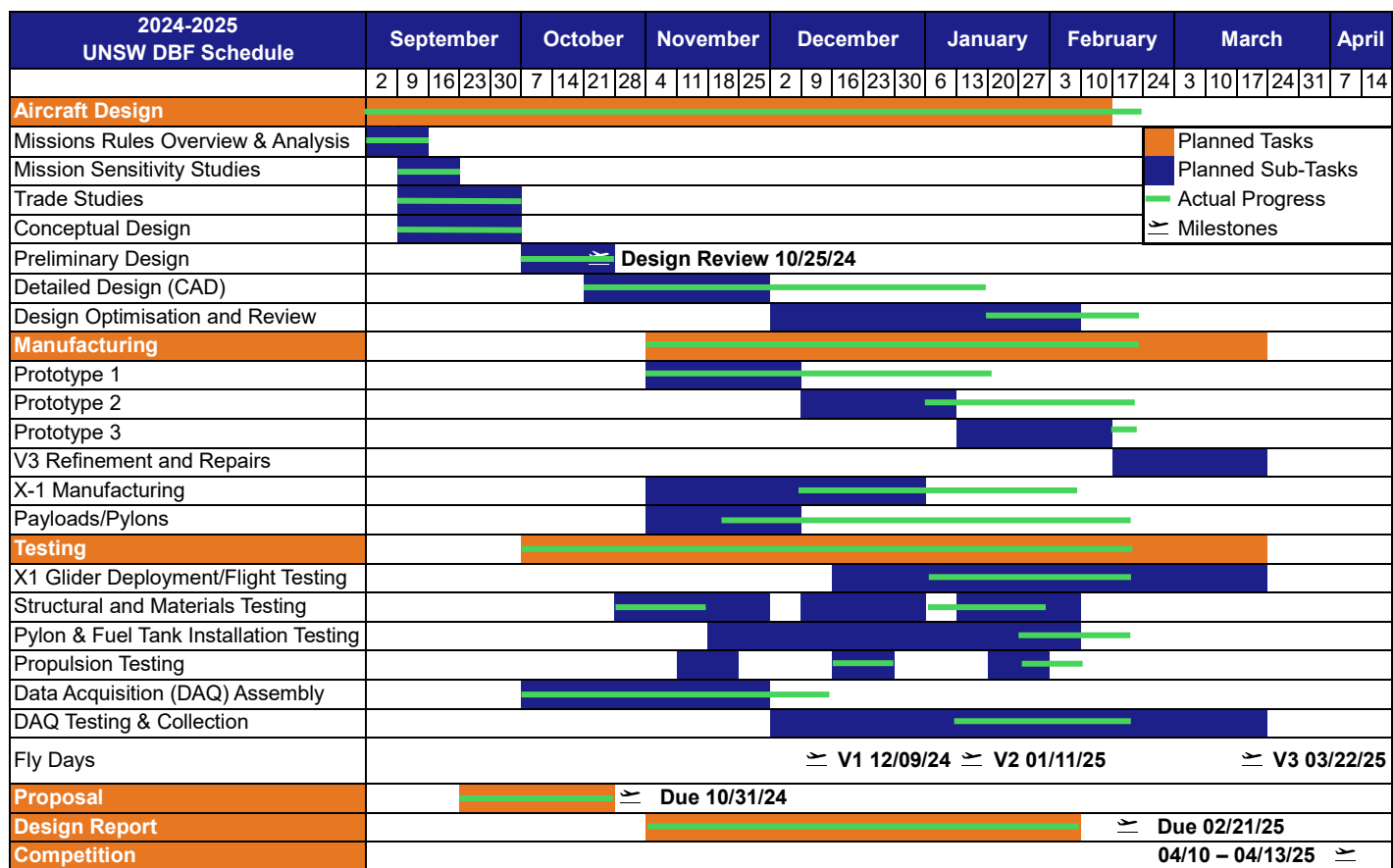


Figure 2.2 UNSW DBF 2024-25 Gantt Chart



### 3. Conceptual Design

#### 3.1. Problem Statement

The 2024-2025 AIAA DBF competition requires teams to develop a solution to four missions inspired by the X-1 supersonic flight program. The GM requires rapid assembly of the aircraft into flight configuration including pylons, fuel tanks and the X-1. For the flight missions, M1 is a proof of flight, M2 consists of flying with loaded fuel tanks and the X-1, while M3 requires deployment of the X-1 into stable autonomous flight.

##### 3.1.1. Mission Scoring

The competition has two main scoring avenues, the report and the missions. Each mission score is summed together to result in a total mission score, which is then multiplied by the report score. The report score is a function of the proposal score and the design report score. Further, a participation score of 1 is added for attending the competition, 2 for the aircraft passing the tech inspection and 3 for attempting M1. Each scoring mechanism is shown below in Eq's 1-3.

$$\text{Total Mission Score} = \text{GM} + \text{M1} + \text{M2} + \text{M3} \quad (1)$$

$$\text{Report Score} = 0.85 \times \text{Design Report Score} + 0.15 \times \text{Proposal Score} \quad (2)$$

$$\text{Overall Competition Score} = \text{Total Mission Score} \times \text{Report Score} + \text{Participation Score} \quad (3)$$

Before any mission can be attempted the aircraft must pass tech inspection to prove airworthiness and rules compliance. Once passed, the aircraft will be brought to the staging box with all propulsion battery packs and payloads removed from the aircraft. The ground crew member is then given 5 minutes to assemble the aircraft for each specific mission. Each flight mission consists of two 1,000ft straight segments, followed by two 180 degrees banked turns and a 360-degree loop,

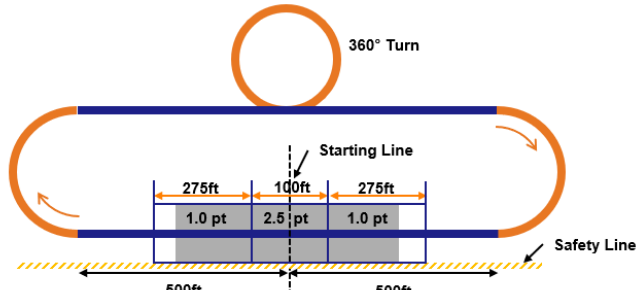


Figure 3.1 Flight Path

shown in Figure 3.1. To successfully complete a lap the aircraft must cross the finish line. While the landing is not counted in the time, a successful landing is required to complete the specified flight mission.

##### 3.1.2. Ground Mission – X-1 Flight Test Program Demonstration

The GM is a timed demonstration of the team's ability to equip the plane for the X-1 flight test program mission. The mission begins by entering the staging configuration without external fuel tank pylons, fuel tanks, and the X-1 test vehicle installed. The aircraft must be placed upright resting on the landing gear while blocks can be used to raise the aircraft. Once the stopwatch is started, the external pylons are installed, then the time is stopped. Once the number of external pylons is verified time will begin again, at which the ground crew member will install the declared fuel tanks and the X-1 test vehicle, securing all access hatches if used, then the time will be stopped. Once the number of fuel tanks installed and the X-1 test vehicle with all accompanying hatches is verified the pilot will verify all flight controls are working. The pilot will then release the X-1 test vehicle and ensure the lights are functioning after release. The GM time will then be noted down and the score is normalised by the lowest time recorded by a team shown by Eq. 4.



$$GM = \frac{\text{Time}_{\min}}{\text{Time}_{\text{UNSW}}} \quad (4)$$

### 3.1.3. Mission 1 – Delivery Flight

M1 involves the aircraft successfully completing 3 laps within the allotted 5-minute flight window. Upon successful completion one point is awarded to the team.

$$M1 = 1.0 \quad (5)$$

### 3.1.4. Mission 2 – Captive Carry Flight

M2 involves the aircraft flying three laps in the allotted 5-minute flight window with the X-1 vehicle and fuel tanks installed. The score is a function of the total fuel tank weight and time to complete three laps shown as Eq. 6.

$$M2 = 1 + \frac{\left( \frac{\text{Fuel Weight}}{\text{Time}} \right)_{\text{UNSW}}}{\left( \frac{\text{Fuel Weight}}{\text{Time}} \right)_{\max}} \quad (6)$$

### 3.1.5. Mission 3 – Launch Flight

M3 involves the aircraft flying as many laps as possible in the 5-minute allotted time with a minimum of two external fuel tanks mounted empty and the X-1 test vehicle installed. The aircraft must fly to a minimum height of 200ft AGL and launch the X-1 after a minimum of one lap and after crossing the finish line but prior to executing the upwind turn. The X-1 must transition to stable flight and have external lights turn on after being released. The aircraft must then complete a final lap, and the X-1 must land before the 5-minute allotted time ends. Additionally, the X-1 must not cross the safety line shown in Figure 3.1. The score is a function of laps completed before launch of the X-1, bonus points received from X-1 landing location shown in Figure 3.1 and X-1 test vehicle weight as seen in Eq. 7.

$$M3 = 2 + \frac{\left( \sum (\text{Laps Completed Before Launch}) + \frac{\text{Bonus Box}}{X - 1 \text{ Weight}} \right)_{\text{UNSW}}}{\left( \sum (\text{Laps Completed Before Launch}) + \frac{\text{Bonus Box}}{X - 1 \text{ Weight}} \right)_{\max}} \quad (7)$$

## 3.2. System Design Requirements

From the mission objectives stated in Section 3.1, the sub-system requirements were derived, shown in Table 3.1. These were further classified into must have requirements, and preferred desirable characteristics, denoted by ‘-R’ and ‘-D’ in the requirement number respectively. These constraints will help set the boundaries for the preliminary design analysis and on the final design of the BRICK.

**Table 3.1. Mission Sub-System Requirements**

Category	Subcategory	Requirement	Req. No.
Main Aircraft	Structures	Aircraft must be strong enough to handle payload weight at maximum G-force predicted.	§AR-ST-01
		Main plane weight should be minimised.	§AD-ST-02
	Aerodynamics	Aircraft must be capable of stable level flight in all mission configurations.	§AR-AD-01
		Aircraft should maximise L/D for missions to maximise efficiency.	§AD-AD-02
		Aircraft Wingspan must be a maximum of 6ft.	§AR-AD-03



	Propulsion	Aircraft must be able to climb to and fly at an altitude of 200ft AGL.	\$AR-AD-04
		Propulsion should operate at efficient ranges to maximise limited 100Wh battery capacity.	\$AD-PP-01
	Performance	Propulsion should enable plane to achieve a high velocity to minimise M2 time.	\$AD-PP-02
		Aircraft must have sufficient T/W and W/S to take-off within the runway length of approximately 300ft.	\$AR-PF-01
General	Payload	Pylons, hatches, and fuel tanks must be quick to install, strong enough to handle payload weight, and secure.	\$GR-PL-01
		Pylons and fuel tanks should be of minimal size possible to minimise overall drag.	\$GD-PL-02
		Fuel tank weight should be maximised.	\$GD-PL-03
X-1	Structures	X-1 attachment mechanism must be quick to install, but still secure.	\$XR-ST-01
		X-1 must be strong enough to handle aerodynamic forces in cruise for all missions.	\$XR-ST-02
		X-1 must have a maximum allowable weight of 0.55lbs.	\$XR-ST-03
		X-1 must have a minimum gap of 0.25in between any part of the main aircraft fuselage, wings or outer surface and must be between the two external fuel tanks.	\$XR-ST-04
		X-1 weight should be minimised.	\$XD-ST-05
	Performance	X-1 launch must be repeatable, adaptable to various heights and drop locations, and predictable.	\$XR-PF-01
		X-1 must transition into stable flight, conducting a 180 degree turn and fly a descending spiral pattern in the 2.5-point target box with a diameter of 150ft.	\$XR-PF-02
		X-1 flashing lights must be visible from at least 400ft away in daylight.	\$XR-PF-03
		X-1 should have a 20 second descent time from deployment.	\$XD-PF-04
	Avionics	X-1 must be autonomously controlled with no radio-controlled receivers integrated.	\$XR-AV-01
		X-1 must be able to detect its own deployment to transition into flight.	\$XR-AV-02

### 3.3. Sensitivity Analysis

A sensitivity analysis was conducted to evaluate the impact of key design parameters on overall mission performance, excluding M1 however, due to its binary nature and non-variable scoring. By systematically varying parameters from GM, M2 and M3 through MATLAB [2], a clear visualisation of what to maximise, minimise are acquired for a competitive performance. Figure 3.2 highlights payload weight, lap times, and X-1 weight as the most significant influence on the total score. The maximum scoring aircraft used was based on performance data from previous competitions. This result aligned with the team's initial discussions and further supported by the mathematical relationship as seen within the scoring equations. Notably, M2's lap time possesses an inverse relationship, which results in a nonlinear impact on scoring, whereas payload weight follows a linear relationship. Similarly, in M3, the X-1 weight, though capped by the bonus box score, still demonstrates a greater impact on scoring than that of M3's lap counts due to its inverse nonlinear proportionality. Thus, in terms of aerodynamic



performance, Figure 3.2 suggests that minimising M2 lap time, followed by maximising M2 payload weight, presents the greatest opportunity for achieving the highest score.

From this, the team focused the design of the BRICK on maximising the M2 mission score. This made sense due to the split nature of the M3 mission, where so long as the bonus points were achieved, increasing the number of M3 laps would not result in a significant increase to the overall mission score. From the results of Figure 3.2, energy consumption was investigated to narrow the scope of optimisation. Figure 3.2 reveals that the relationship between velocity and power consumption follows a cubic trend, whereas the relationship between payload weight and power is predominantly quadratic. Whilst decreasing M2 time results in the greatest score increase, the cubic increase in power consumptions at higher velocities make this less attractive due to power requirement §AD-PP-01.

These factors led the team to adopt a balanced approach. Specifically, the focus will be on achieving a moderate cruise velocity to optimise energy efficiency, whilst maximising payload capacity for M2. Additionally, the team will aim to secure maximum bonus points for the X-1 in M3 and minimise GM time in payload design.

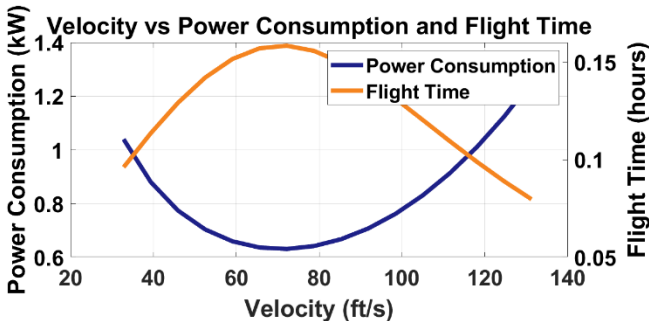


**Figure 3.3. Power Consumption Relationships**

#### 3.4. Aircraft Configurations Decision Matrix

Different configuration options were analysed using decision matrices, formulated as described in Table 3.2.

**Table 3.2 Configuration Selection Process**

No.	Step	Description
1	Identify Characteristics	The most desirable characteristics of the configuration option are identified.
2	Weighting	The characteristics are given a weighting out of 5 (most important) based on their importance to mission performance.
3	Identify Options	Potentially suitable configuration options are identified at a high level based on research and team experience.
4	Scoring	The potential options are scored out of 5 (best performance) based on how well they perform in relation to each characteristic.

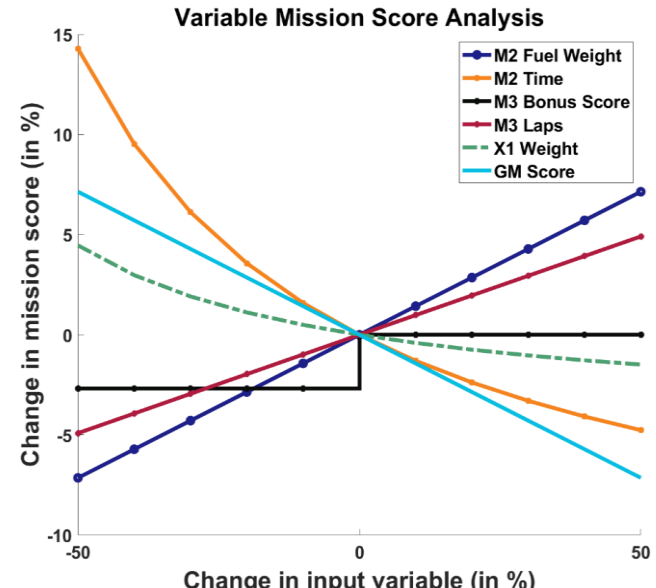


**Figure 3.2. Score Sensitivity**



5	<b>Total Score</b>	The total score for each option is calculated as the sum of the scores for the characteristics multiplied by their respective weights, with the option achieving the highest total score being selected. The total score formula is shown below: $\text{Total Score} = (\text{Weight 1}) \cdot (\text{Score 1}) + (\text{Weight 2}) \cdot (\text{Score 2}) + \dots$
---	--------------------	--

The characteristics that were identified as most mission-critical and the reasoning for choosing them are tabulated below in Table 3.3. Note that the weight given to each characteristic is not included due to it varying between components, since the importance of some characteristics will vary depending on the purpose of the component.

**Table 3.3 Chosen Characteristics for Decision Matrices**

<b>Characteristic</b>	<b>Reasoning</b>
<b>Stability</b>	Allows pilot greater focus on completing laps faster improving mission score and is especially important given the significant payload weight variation between missions, in addition to meet sub-system requirement §AR-AD-01.
<b>Weight</b>	Lower component weight allows for greater payload weight to meet §GD-PL-03 and generally improves aircraft performance.
<b>Manufacturability</b>	Components being easy to manufacture allows them to be built faster increasing the number of aircraft iterations and improves the aircraft's performance through testing.
<b>Transportability</b>	Critical for our team, being an international team having to transport the aircraft by air.
<b>Pylon/Propeller Clearance</b>	Ensures that the bottles chosen as external fuel tanks will clear the ground so that the bottles best suited to meeting requirements §GR-PL-01, §GD-PL-02 and §GD-PL-03 can be used. Further, ensuring adequate propeller clearance.
<b>Pitch/Yaw Stability</b>	Particularly important since trim adjustments are used to account for the large difference in payload weight between missions and ensures §AR-AD-01 is met.
<b>Control Complexity</b>	Important for completing mission manoeuvres and climbing quickly so that the course can be started sooner and complete laps faster as part of meeting §AD-PP-02.
<b>Maximum Thrust</b>	Greater thrust allows the plane to fly faster meaning more laps can be completed, meeting requirement §AD-PP-02, and to achieve desired take-off and cruise velocity.
<b>Energy Efficiency</b>	Greater energy efficiency ensures that the aircraft will be able to complete more laps by with equivalent battery capacity, meeting §AD-PP-02 and §AD-PP-01.
<b>Load Support</b>	The landing gear should support a heavy payload so requirement §GD-PL-03 is met.
<b>Payload Access</b>	Easy payload access speeds up the GM time and meets requirement §GR-PL-01.
<b>Drag</b>	Minimising drag is important in ensuring sub-system requirement §AD-AD-02 is achieved, which in turn allows faster lap speeds to meet §AD-PP-02.
<b>Ground Handling</b>	Good ground handling during take-off and landing lowers the risk of a crash during these manoeuvres which is a risk given the long ground roll prescribed in §AR-PF-01. While also preserving energy.
<b>Installation Time</b>	Installation time for the pylons and X-1 should be minimised to decrease GM time which also meets the requirement §GR-PL-01.
<b>Weight of X-1</b>	The weight of the X-1 should be minimised, meeting §XD-ST-03, because this increases M3 score and allows a greater payload weight in M2 to meet requirement §GD-PL-03.
<b>Operability</b>	Consistent and reliable operability of the X-1 release mechanism and descent to ensure that the X-1 will release when commanded during M3 and that it meets requirement §XR-PF-01 and §XR-PF-02.
<b>Structural Simplicity</b>	Reduces the weight of components which allows for a greater payload weight for M2, following requirement §GD-PL-03.
<b>Structural Integrity</b>	Ensure the mechanism can support high load factor manoeuvres.
<b>Cost/Accessibility</b>	Reduce cost to ensure all components can be purchased. Geographical constraints are considered with accessibility.



<b>L/D Ratio</b>	The L/D ratio for the X-1 should be optimised to meet §XR-PF-02 and §XD-PF-04.
<b>Location</b>	Ensure the X-1 lands in the correct 200ft box location to meet §XR-PF-02.
<b>Mountability</b>	Mountability concerning the tail of the X-1 is an important consideration since it needs to be easy to manufacture and attach but also needs to be effective to meet §XR-ST-02.

### 3.4.1. Main Aircraft Wing Configuration

The configurations considered for the wing placement were high wing, mid wing and low wing, as seen in Table 3.4. The mid wing and low wing configurations have a lower static stability than the high wing, and while the mid wing configuration has greater pylon clearance than the low wing, manufacturability is lower. The high wing configuration was selected due to its high stability which is a key concern with a heavy payload and large payload variation, but also due to providing the greatest pylon clearance which allows for the heavy payload and while being the same manufacturing simplicity as the low wing.

**Table 3.4 Wing Configuration Decision Matrix**

				
<b>Characteristics</b>	<b>Weight</b>	<b>High Wing</b>	<b>Mid Wing</b>	<b>Low Wing</b>
<b>Pylon and Propeller Clearance</b>	5	5	3	1
<b>Stability</b>	4	5	4	3
<b>Manufacturability</b>	3	4	2	4
<b>Total</b>	<b>57</b>		41	29

### 3.4.2. Tail Attachment Configuration

Three tail attachment configurations were considered in Table 3.5: conventional, tail boom and twin boom. The conventional and twin boom configurations were less desirable due to their heavier weight and poorer manufacturability and transportability. The tail boom was ultimately selected because it was lighter and is excellent in terms of manufacturability, drag reduction and transportability, being easy to assemble and disassemble to take overseas.

**Table 3.5 Aircraft Configuration Decision Matrix**

				
<b>Characteristics</b>	<b>Weight</b>	<b>Conventional</b>	<b>Tail Boom</b>	<b>Twin Boom</b>
<b>Weight</b>	4	3	4	3
<b>Manufacturability</b>	4	4	5	3
<b>Drag</b>	4	4	3	2
<b>Transportability</b>	3	3	5	5
<b>Total</b>	<b>53</b>		<b>63</b>	<b>47</b>

### 3.4.3. Main Aircraft Tail Configuration

Four different options were considered for the tail of the main aircraft: conventional, cruciform, V-tail and T-tail, shown in Table 3.6. Seven characteristics were chosen as most critical to mission performance, being pitch and yaw stability, drag, weight and structural simplicity of the tail, control complexity and manufacturability. The cruciform and T-tail required a heavier structure, while the V-tail had worse pitch and yaw stability. The conventional



tail configuration was chosen because of the high pitch and yaw stability provided while also being light, aerodynamic, rigid and easy to manufacture.

**Table 3.6 Tail Configuration Decision Matrix**

Characteristics		Weight	Conventional	Cruciform	V-Tail	T-Tail
Pitch Stability	5	4	3	3	2	
Yaw Stability	5	5	4	2	3	
Weight	5	3	2	4	1	
Drag	5	1	2	5	3	
Manufacturability	4	5	1	3	2	
Structural Simplicity	3	4	2	3	1	
Control Complexity	2	4	4	3	4	
Total		105	73	97	64	

#### 3.4.4. Main Propulsion Configuration

Tractor, dual tractor and dual pusher configurations were considered for propulsion and assessed based on their maximum thrust, energy efficiency, ground clearance and cost/accessibility. The single pusher was omitted due to the tail boom configuration picked in Section 3.4.2. The dual pusher configuration was rejected due to reduced efficiency from having the propeller sit behind the wing and thus not meeting §AD-PP-01. This also worsened the configurations propeller/pylon clearance due to having the propeller further aft. Whilst the single tractor configuration was attractive due to the higher efficiency and reduced weight, the cost of sourcing a higher voltage battery and required propeller to run the single engine configuration adequate for the required MTOW made it significantly less attractive, and thus the dual tractor configuration was chosen.

**Table 3.7 Propulsion Configuration Decision Matrix**

Characteristics		Weight	Tractor	Dual Tractor	Dual Pusher
Maximum Thrust	5	4	5	5	
Energy Efficiency	4	5	4	3	
Pylon/Propeller Clearance	2	2	3	3	
Cost/Accessibility	3	2	5	5	
Weight	4	5	3	3	
Total		70	74	71	

#### 3.4.5. Main Landing Gear Configuration

Three landing gear configurations were investigated including the tricycle, quadricycle and taildragger. These configurations were assessed for their load support, payload access, weight, manufacturability, drag and ground handling. The quadricycle configuration is great for load support and payload access but adds slightly more weight and manufacturing complexity which ultimately hindered the selection score. Taildragger is lighter than a quadricycle and easier to manufacture but suffers from poor payload clearance which would potentially limit X-1



mounting locations, whilst also having poor ground handling. The tricycle configuration was chosen because it performs well in all characteristics and it provides good payload clearance while being easier to build, in addition to having reduced drag and improved ground handling for easier take-off and landing in meeting §AR-PF-01.

**Table 3.8 Landing Gear Configuration Decision Matrix**

				
Characteristics	Weight	Tricycle	Quadricycle	Taildragger
<b>Load Support</b>	4	4	5	3
<b>Pylon/Propeller Clearance</b>	5	5	5	3
<b>Weight</b>	3	4	3	5
<b>Manufacturability</b>	3	4	3	5
<b>Drag</b>	4	4	3	5
<b>Ground Handling</b>	3	5	4	3
<b>Total</b>		<b>96</b>	87	86

### 3.4.6. Main Pylon Configuration and Location

Two major options were considered initially for the external pylon design. These included using an adapter around the bottle to act as a permanent clamp, versus a removable clamping solution as shown Table 3.9. These methods of securing the external fuel tanks were assessed for their installation time, drag and weight in each mission. The adapter would likely have a faster installation time than the clamp, owing to the ability to utilise a rail or quick insert mechanism to secure the adapter to the pylon, vs manual clamps. The adapter was also slightly preferred from a drag perspective, due to the reduced number of protrusions as opposed to the clamp design. However, whilst additional weight from the adapter is desired in M2, it is undesirable in M3 when the fuel tanks are empty. Nevertheless, the adapter was chosen due to its lower drag and installation time, meeting §GR-PL-01 and §GD-PL-03 to maximise GM and M2 score.

**Table 3.9. Payload Configuration Decision Matrix**

			
Characteristics	Weight	Adapter for Bottle	Clamps on Pylon
<b>Installation Time</b>	5	5	4
<b>Drag</b>	2	4	3
<b>M2 Weight</b>	2	5	3
<b>M3 Weight</b>	2	3	4
<b>Total</b>		<b>49</b>	40

The pylon location was also analysed shown in Table 3.10 with respect to the lift-to-drag ratio, structural rigidity and installation time. The lift-to-drag ratio is significantly impacted if installed on the upper surface since the majority of lift is generated above the wing. This would also cause significant flutter at higher speeds, however, installation of the pylons on the upper surface was considered to be easier. The fuselage option was better in lift-to-drag, but worse structurally due to the introduction of bending stress to the structure. The lower surface pylon design was thus chosen due to the balance between structural rigidity, lift-to-drag ratio and also ease of installation.



**Table 3.10. Payload Location Decision Matrix**

Characteristics	Weight	Lower Surface	Upper Surface	Fuselage Side
L/D Ratio	5	4	2	5
Ease of Installation	5	2	4	2
Structural Rigidity	4	3	2	2
<b>Total</b>	<b>42</b>		38	40

#### 3.4.7. X-1 Mounting Configuration

The X-1 mounting mechanism configurations consisted of inside the fuselage and below the fuselage. These were considered based on the mechanism weight, drag, and their operability. While storing the X-1 inside the fuselage would reduce drag, the added complexity and weight was found to outweigh the drag reduction benefits and as such below the fuselage was chosen.

**Table 3.11. X-1 Mounting Mechanism Matrix**

Characteristics	Weight	Inside Fuse	Below Fuse
Weight	5	2	5
Operability	4	2	4
Drag	3	5	1
<b>Total</b>		37	<b>44</b>

#### 3.4.8. X-1 Release System

The X-1 release system must adhere to the following sub-system requirements, including §XR-ST-04, §XR-AV-01 and §XR-AV-02, while also minimising the time required to attach the X-1 to the main aircraft for the GM. The complexity of the Single Slot and Cargo Hook was given a low score due to the increased likelihood of mechanical part failure, increasing the risk of a failed release while adding additional empty weight. Following on, the structural integrity of the connection was considered, as an unstable mount such as the Cargo Hook results in increased drag and potential premature detachment. The final criterion that was considered, was how quickly the X-1 can be mounted to the main plane, as this directly affects Ground Mission score. With all criteria considered, Pin Release was the top performing in all categories and as such ultimately chosen.

**Table 3.12. X-1 Release Mechanism Decision Matrix**

Characteristics	Weighting	Single Slot	Pin Release	Cargo Hook
Structural Simplicity	5	4	5	3
Structural Integrity	4	4	4	2
Installation Time	3	4	5	3
<b>Total</b>		48	<b>56</b>	32



### 3.4.9. X-1 Aircraft Configuration

Three X-1 configurations were considered including a conventional layout, tail boom, and lifting body shown in Table 3.13. The characteristics of structural simplicity, stability, and manufacturability were selected. While the conventional and tail boom provided the greatest stability, both were rejected due to structural simplicity and manufacturability. The lifting body was ultimately chosen due to its structural simplicity and rigidity, adequate stability, and its superior manufacturability.

Table 3.13. X-1 Configuration Decision Matrix

Characteristics	Weight	Conventional	Tail Boom	Lifting body
Structural Simplicity	5	3	4	5
Stability	4	4	3	2
Manufacturability	3	2	2	3
Total		37	38	42

### 3.4.10. X-1 Wing Configuration

The team considered different wing configurations for X-1's lifting body, a double delta, pure delta, and blended wing body shown in Table 3.14. The double delta had the best performance and stability, but was more difficult to manufacture, while a pure delta sacrifices some performance for manufacturability. The blended fuselage and wing design sacrificed performance for ease of manufacturing. Thus, the pure delta wing configuration was selected.

Table 3.14. X-1 Wing Configuration Decision Matrix

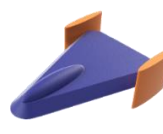
Characteristics	Weight	Pure delta	Double delta	Blended Wing
Stability	5	4	4	3
L/D ratio	4	2	3	1
Manufacturability	3	3	1	2
Total		37	35	25

### 3.4.11. X-1 Tail Configuration

A single tail, winglets, and H-tail were all considered for the X-1. The vertical stabiliser, while laterally stable would interfere with the clearance restriction and larger wing area was required to maintain adequate pitch stability. With winglets, pitch stability was increased, however at the detriment to structural reliability due to the outboard position and narrow surface. The H-tail was chosen as it was a blend between the winglet design and vertical stabiliser providing adequate pitch and yaw stability while also limiting the height and increasing structural reliability.



**Table 3.15. X-1 Tail Configuration Decision Matrix**

				
Characteristics	Weight	Winglets	Vertical Stabiliser	H-tail
<b>Stability</b>	5	2	5	4
<b>Mountability</b>	5	3	2	4
<b>Structural Integrity</b>	3	2	3	4
<b>Total</b>		31	44	<b>52</b>

### 3.4.12. X-1 Descent Pattern

Three descent patterns were assessed including the spiral, figure-eight and straight-down. Each option was assessed on controllability, stability and ensuring the X-1 stayed inside the 200ft box location, the matrix is shown in Table 3.16. Where straight down posed the greatest risk to the X-1 moving out of the required 200ft box and due to reaching terminal velocity, the controllability and stability would be negatively impacted. Figure eight and spiral equally scored in location and stability, however the figure eight would require sharper banked turns at the corners to ensure it stayed inside the 200ft box, hence the spiral was chosen.

**Table 3.16. X-1 Descent Pattern Decision Matrix**

Characteristics	Weight	Straight Down	Figure Eight	Spiral
<b>Location</b>	5	2	4	4
<b>Stability</b>	4	1	3	3
<b>Operability</b>	3	1	2	4
<b>Total</b>		12	38	<b>44</b>

## 4. Preliminary Design

The preliminary design was an iterative process used to converge on an optimised design for the main aircraft and X-1 test vehicle. A combination of simulations, sensitivity analysis, and trade studies were used to arrive at a final preliminary design. The specific methods used are outlined in the following section.

### 4.1. Design Methodology

The team's design methodology built on previous UNSW DBF techniques but also incorporated new techniques learned from coursework, off-season research, and industry experience. As seen in Table 3.1, systems engineering was used to breakdown the DBF2025 rules into system requirements, ensuring at each step of the preliminary design phase the design either met or exceeded the requirements stated. Building from the sensitivity analysis in Section 3.3, it was determined that M2 had the highest score variation, specifically through maximising the weight of the payload carried. From this, estimates for the initial empty weight of the BRICK were found based on previous similar competition aircraft. A constraint diagram was then constructed based on these requirements to further narrow the design choices into power and wing loading. Aerodynamic analysis started with airfoil selection and geometric parameters of the wing, tail and fuselage, simulated in XFLR5 [3] and then AVL [4]. Stability was then obtained from AVL and compared to the MIL-F-B785C standard. Likewise, given the constraint diagrams derived from mission requirements, various propulsion systems were analysed through eCalc [5] and MotoCalc [6] and tested to identify the most suitable configuration. These configurations were then simulated in a MATLAB based

mission model, simulating the flight path and predicted aircraft performance. Trade studies were conducted to optimise for the configuration that produced the best score under the stated requirements. If the preliminary design met all stated requirements in Section 3.2, the best scoring design was taken. A CAD model was then produced to meet the requirements for the payload and loads anticipated, which were then manufactured through laser-cutting and 3D printing. After manufacturing was complete, flight tests were conducted, and test data was obtained to validate the performance criteria, optimise designs, and adjust the mission model data. This iterative methodology is summarised in Figure 4.1 below.

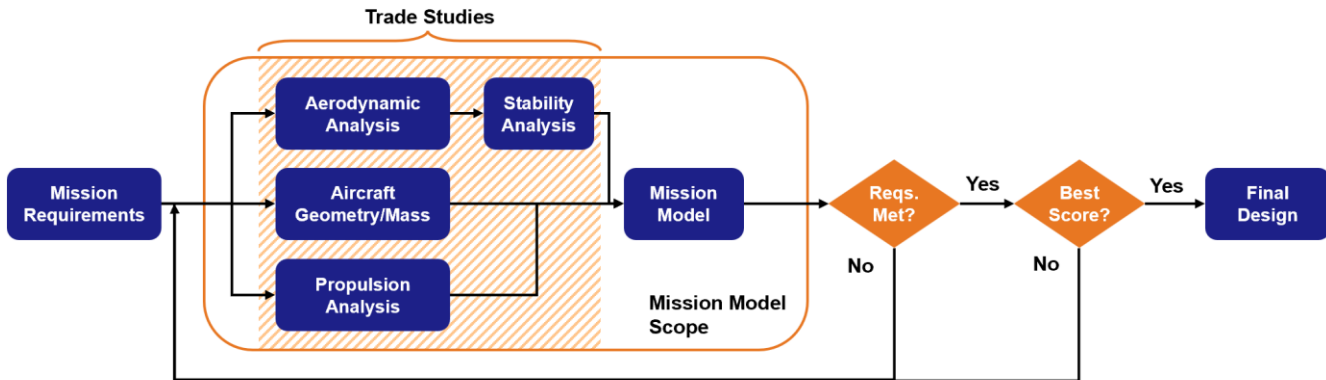


**Figure 4.1 Preliminary Design Methodology**

## 4.2. Mission Model

To obtain the predicted performance of the preliminary design and to help conduct various trade studies, a mission model was created on MATLAB to simulate the performance of the plane, based on aerodynamic data of the chosen geometric configuration and airfoil from XFLR5, as well as propulsion data from both eCalc and MotoCalc. As outlined in Figure 4.1, the outputs of the mission model were then checked against a series of requirements. The details behind each stage of the mission model, and the relevant requirements, are outlined in Table 4.1 corresponding to the mission lap shown in Figure 4.2.

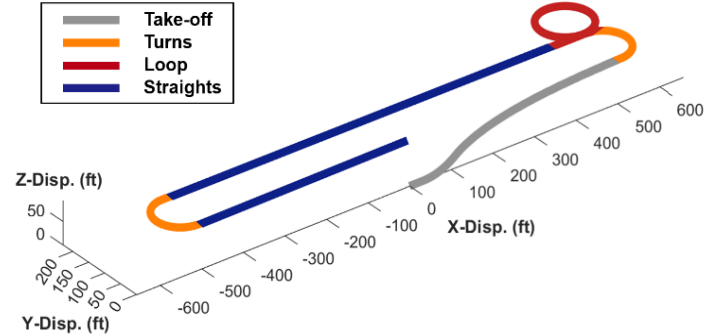


**Figure 4.2 Mission Model Lap Breakdown**

**Table 4.1 Mission Model Stages Breakdown**

Stage of Flight	Description
Take-off/Climb	Throttle is set to 100% for take-off roll and climb out. Ground roll friction coefficient of 0.04 for concrete runways was utilised [7]. The aircraft then accelerates to $v_{TO}$ , where it then pitches up increasing $\alpha$ until enough lift is produced to accelerate into the air. The aircraft then maintains full throttle and the required $\alpha$ until the target altitude is reached which marks the end of the climb. For M1/2 this altitude is 50 ft, for M3 it is 200ft as outlined in §AR-AD-04. The take-off length is recorded as the point where the aircraft's altitude is above 0ft and is required to be less than the runway length to count as a viable configuration. Failure to hit the desired altitude or take-off invalidates the configuration.



Straights	The throttle is adjusted dynamically to achieve a user set target airspeed which attempts to maximise battery usage whilst remaining under the recommended 85% usage for LiPo batteries and to give room for landing. $\alpha$ is adjusted to achieve level flight. If more than 85% battery is used, the configuration is invalidated.
Turns/Loop	The throttle is adjusted dynamically to achieve a user set target airspeed for the turns. $\alpha$ is increased until the target load factor or maximum permissible $\alpha$ is achieved, whilst still ensuring the bank angle produces sufficient upwards lift to balance the weight of the plane.

Whilst comprehensive, limitations of the approach include a simulation that is only based in 2D to simplify calculations. This was acceptable due to the level flight condition for turns and cruise, however this neglects, for example, the impact of AoA on the direction of the forces. As a result, losses to thrust in the forward direction due to AoA may produce optimistic results. To compensate, a safety factor was applied to lift and thrust values input into the model to account for idealisations.

### 4.3. Aerodynamic Design Analysis

#### 4.3.1. Weight Estimation for the BRICK

The power of propeller driven aircraft in steady and level flight can be calculated using Eq. 8 and 9.

$$D = \left( \frac{1}{2} \rho S C_{D_0} \right) V^2 + \left( \frac{2kW^2}{\rho S} \right) V^{-2} \quad (8)$$

$$P = \frac{DV}{\eta} \quad (9)$$

From Section 3.3 it was known the MTOW would be initially maximised to 55 lbs. The expected payload weight was found using Eq. 8 by using previous similar aircraft weight fractions shown in Table 4.2 [8]. The team took weight fractions from the DBF2021 competition due to the long runway distance and similar mission objectives. As such the preliminary payload weight was found to be 27.5 lbs, with an initial MTOW of 55lbs. The exact MTOW however is to be finalised with additional trade studies in Section 4.3.8, where propulsion considerations can be accounted for.

**Table 4.2. Comparable Aircraft Weight Fractions [11]**

	DSCE2021	UCF2021	ERAU2021	Average
$W_{ps}/W_0$	0.22	0.13	0.17	0.17
$W_e/W_0$	0.26	0.36	0.36	0.33

#### 4.3.2. Constraint Diagram for the BRICK

Trade studies were conducted to identify the available design space for the BRICK. The team's design philosophy was based on Section 3.2 and 3.3, where §AD-ST-02, §AR-AD-03, §AR-PF-01 and §GD-PL-03 set the boundaries to maximise score through maximising payload weight. To accomplish this, the aircraft was initially designed around an MTOW of 55 lbs for M2 and then designed to fly M1 and M3 at a slower speed. Hence, the constraint diagram was used to compare thrust-to-weight and wing loading for the aircraft, using Eq. 11-16 [7].



$$(T/W)_{TO} = \frac{1.21}{g\rho C_{L_{max}} S_g} (W/S) + \frac{0.605}{C_{L_{max}}} (C_{D_{TO}} - \mu C_{L_{TO}}) + \mu \quad (11) \quad (T/W)_{cruise} = q C_{D_{min}} \left( \frac{1}{W/S} \right) + k(1/q)(W/S) \quad (12)$$

$$(T/W)_{Constant\ velocity\ turn} = q \left[ \frac{C_{D_{min}}}{W/S} + k(n/q)^2(W/S) \right] \quad (13) \quad (W/S)_{stall} = \frac{1}{2} \rho V_{stall}^2 C_{L_{max}} \quad (14)$$

$$(T/W)_{Desired\ service\ ceiling} = \frac{1.667}{V_Y} + \frac{q}{W/S} C_{D_{min}} + \frac{k}{q}(W/S) \quad (15) \quad \left( \frac{T}{W} \right)_{cruise\ L/D} = \frac{1}{L/D} \quad (16)$$

The team then sourced similar aircraft from previous years, trying to match design constraints to the 2025 competition rules including wingspan, take-off and battery restrictions. However, it was also found that building an aircraft to sustain two distinctly different payload missions, that being 55 lbs and 27.5 lbs, was significantly different to previous competitions with an MTOW achieved of 28.18 lbs. Nevertheless, three main teams were identified, ERAU2023, WU2023 and DSCE2021, compared below in Table 4.3.

**Table 4.3. Similar Aircraft at MTOW from Previous DBF Competitions [9], [10], [11]**

	ERAU2023	USC2020	DSCE2021
<b>Cruise Speed (ft/s)</b>	83	90	58
<b>MTOW (lbs)</b>	28.18	24	18.20
<b>W/S (lb/ft<sup>2</sup>)</b>	4.65	4.03	3.45
<b>T/W</b>	1.08	0.76	0.11
<b>Stall Speed (ft/s)</b>	47	46	36
<b>Take-off Distance Requirement (ft)</b>	60	None for M2	100

Given the increase in MTOW and the short wingspan, the team had to increase the stall speed compared to previous teams. Hence the stall speed was estimated at 65 ft/s. Furthermore, the take-off distance, which was a main constraint in the 2023 competition, was now taken away as such lowering the significance in the constraint diagram. However, the team still realised this would take away time from the missions and so the team identified the runway length of 300 ft and applied a FoS by dividing the length required by 1.2, arriving at a maximum take-off length of 250 ft. The air density used was taken from TIMPA Field, Tucson, AZ with an elevation of 2,218ft AMSL.

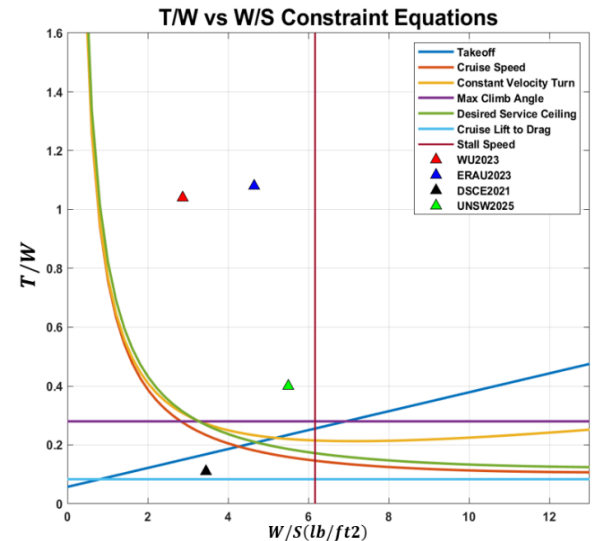


**Figure 4.3. Constraint Diagram for the BRICK**

The density used for take-off was the base elevation, whilst the density used for cruise and stall was at an elevation of 375ft, calculated from the cruise altitude for M3 of 250ft with a FoS of 1.5. Furthermore, the drag at take-off was estimated from Gudmundsson to be 0.04 [7], whilst the lift at take-off was estimated to be equal to the maximum lift achievable by the aircraft. This was assumed to be 1.4 based on previous aircraft the team had manufactured. The constraint diagram shown in Figure 4.3, identifies the design space available using Eq. 11-16. To lower the weight of the aircraft, the motor was a key component. Thus, the team picked a T/W close to the take-off equation design space to minimise the overall static thrust and lower component weight.

The team identified drag as a main aerodynamic driver due to the fixed wingspan. Various chord lengths, accounting for the changes in structural weight, were simulated in the mission model to identify the optimal wing dimensions to maximise M2 and M3. Varying chord length had negligible impact on M3 score due to the X-1 bonus points, however for M2 it had significant impact as the required AoA for turns was lower yielding less induced drag compared to the increased skin friction drag. Hence, the team picked the maximum point in Figure 4.4 and then verified this chord length gave a valid wing loading design point in the constraint diagram, overall the preliminary wing geometry is shown in Table 4.4.

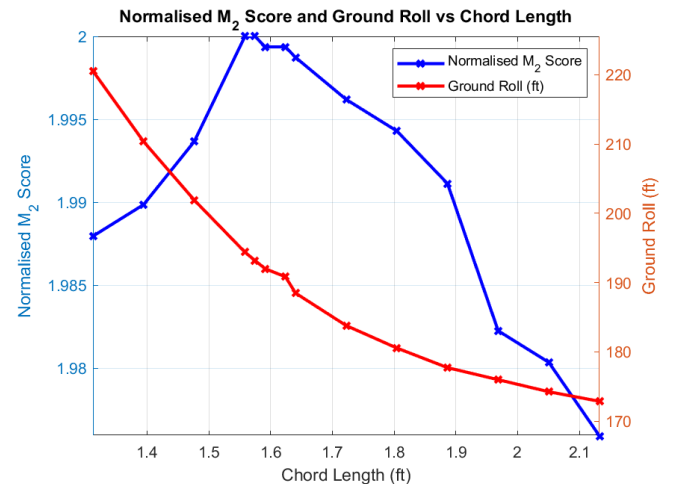


**Figure 4.4. Chord Sensitivity Study**

**Table 4.4 Wing Geometry Dimensions**

Wing Area	Span	Chord	Wing Loading	Aspect Ratio
9.43 ft <sup>2</sup>	6 ft	1.57 ft	5.83 lb/ft <sup>2</sup>	3.82

#### 4.3.3. Aerofoil Selection

Reynolds numbers ranging from 100,000 and 2 million were simulated for each aerofoil in XFLR5, with the results exported into an excel which was weighted based on the main requirements set out in the constraint diagram. This consisted of the maximum lift coefficient, lift to drag in cruise/turn and the pitching moment. Around 20 different aerofoils were simulated, from these the top five best performing aerofoils were taken into 3D space, with data exported and simulated using the mission model, which calculated the score on M2 and M3. This process resulted in two top performing aerofoils namely the MH84 and NACA5512 shown in Table 4.5, the team then investigated blending aerofoils using XFLR5's interpolate tool using 70% of the MH84 and 30% NACA5512, this allowed for the team to have the high lift-to-drag from the NACA5512 while also allowing for a high lift coefficient from the MH84 for sharper banked turns. The hybrid aerofoil is then plotted against the top five aerofoils in Figure 4.5 for the two main criteria being lift coefficient against angle of attack and coefficient of drag against lift coefficient.

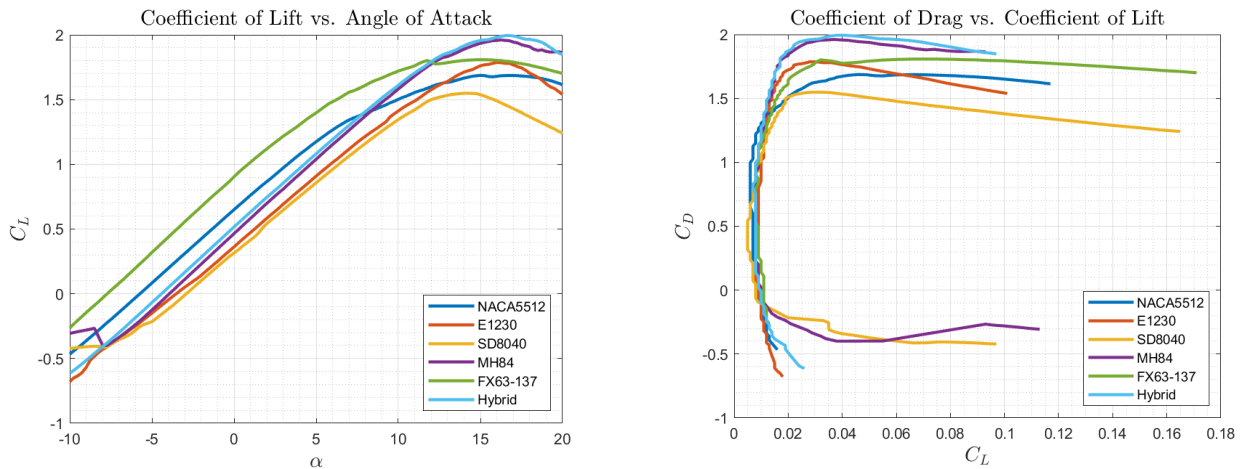


**Figure 4.5. a) Coefficient of Lift vs. Angle of Attack and b) Coefficient of Drag vs. Coefficient of Lift at Cruise Reynolds of 1.1million**



**Table 4.5. Top 5 Performing Airfoils**

Characteristics	Weight	E1230	MH 84	5512	SD8040	FX63-137
L/D for Turn	5	4	5	3	2	2
L/D for Cruise	3	1	2	3	2	3
Maximum Lift Coefficient	5	4	5	3	2	4
Manufacturability	4	2	2	3	4	1
Total	51	64	51	42	43	

#### 4.3.4. Wing Taper

The team investigated the use of taper to increase the performance of the aircraft without impacting the wing loading. Taper ratios from 1 to 0.6 were simulated in XFLR5 with only a 0.3% improvement shown in Figure 4.6. Hence, the team opted for a taper ratio of 1 on the wing to limit structural complexity for the main spar, while preventing tip stall.

#### 4.3.5. Drag Analysis

To size the propulsion system, the drag in cruise was required. Further, the team identified drag as a crucial factor for this competition due to the battery limit set out in §AD-PP-01 and the pylons. From this the team conducted a preliminary drag analysis on all components using the analysis method from Gudmundsson [7]. This analysis involved calculating the skin friction drag of all wing-like elements and applying a CRUD factor of 1.25 and then accounting for miscellaneous drag including the landing gear, followed by a 3D geometrical shape analysis of the bottle assuming the object was a cone using Eq. 17.

$$\Delta C_{D_{tank}} = 2 \times \Delta C_{D_s} \left( \frac{S_{tank}}{S} \right) \quad (17)$$

$\Delta C_{D_s}$  is an empirical relationship based on the tank attachment mechanism where the team used 0.50 to be conservative. The overall drag of the BRICK for each mission is shown as a pie chart in Figure 4.7.

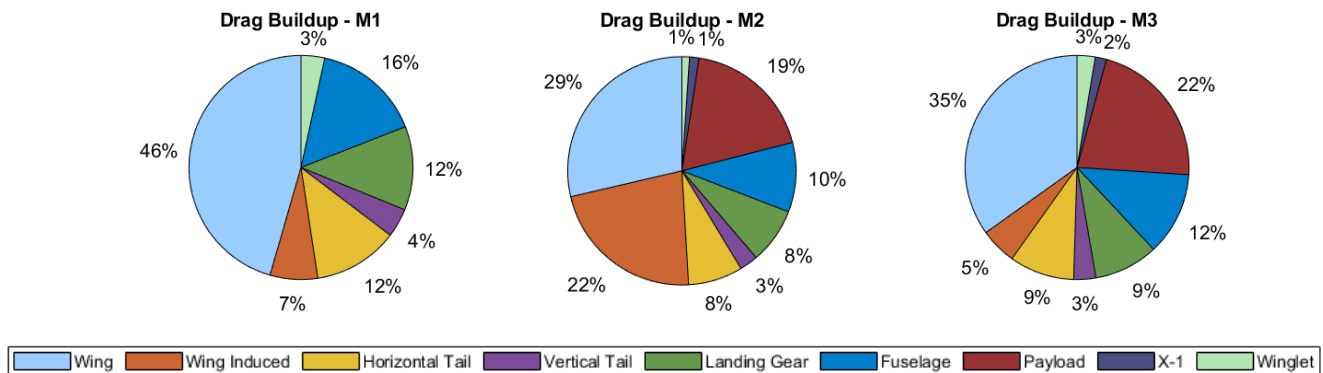


**Figure 4.7. Drag Build-up for Each Mission**

#### 4.3.6. Tail Sizing

Given the preliminary wing sizing, the preliminary tail geometry could be calculated. For the competition the team decided on using an internal fuel tank to minimise the lateral weight on the aircraft, while also minimising drag. The tail moment arm was estimated using the Eq. 18 [7].



$$L_t = \sqrt{\frac{2S_w(c_{HT}\bar{c}_w + c_{VT}b_w)}{\pi(R_1 + R_2)}} \quad (18)$$

Volume coefficients chosen were based on Raymer, Gudmundsson and previous dual motor aircraft from UNSW and other teams these values were initially estimated as 0.7 and 0.06 for the horizontal and vertical tail respectively [8] [7]. Preliminary design of the bottle indicated that fuselage radius would be 4.72 in and the tail boom radius would be 1.18 in. This resulted in a tail moment arm of 4.42 ft. Using the Eq. 19 and 20 from Raymer [8], the tail surface area could be found, assuming that the tail moment arms for horizontal and vertical tail were similar.

$$S_{HT} = \frac{c_{HT}\bar{c}_w S_w}{L_t} \quad (19)$$

$$S_{VT} = \frac{c_{VT}b_w S_w}{L_t} \quad (20)$$

This resulted in Table 4.6, given an aspect ratio of 2.5 and 1.5 for the horizontal and vertical tail respectively chosen from literature [7]. The NACA0012 was chosen for the HT and NACA0010 for the VT based on previous dual motor competition aircraft servo space requirements. Furthermore, the vertical positioning of the tail was found to be acceptable when in line with the wing using Raymer figure 4.33 [8]. Furthermore, taper was applied to the vertical tail to reduce skin friction drag while ensuring adequate yaw control, it was found that a taper ratio of 0.8 was acceptable.

#### 4.3.7. Control Surface Sizing

Control surfaces were sized using three stages, Raymer figure 6.3 and table 6.5 for preliminary sizing, AVL for trim and turn deflection and then a pilot test. The team used historical values from DBF2024 to guide initial sizing with the values shown in Table 4.7. This was then tested in AVL shown in Section 4.6 showing reasonable deflection. The team also investigated the use of flaps to decrease the ground roll, however opted against this due to increased drag.

#### 4.3.8. X-1 Preliminary Design

For the X-1 glider, the team used the derived sub-system requirements as a foundation for building constraint equations to identify a design space. Performance requirements which drove the decisions were §XR-PF-02 and §XR-PF-04, the 20 second descent requirement from 250 ft required the X-1 to have a decent rate of 12.5 ft/s. Eq. 21 calculates the vertical velocity for a glider, and comprises of three distinct variables that can be altered, including planform area, weight and endurance lift-to-drag. Further, Eq. 22 relates the range required from the X-1 to similar variables however includes the bank turn angle which was set at 30-degrees for a low load factor. While the range required was found to be 500 ft in total when dropped straight after the finish line according to Section 5.3.5, from

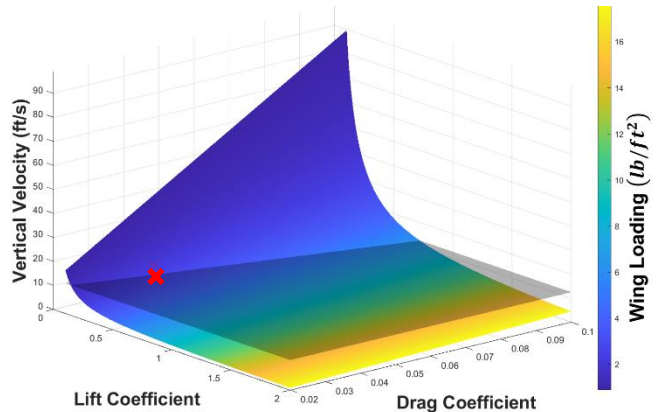


**Figure 4.8. X-1 Constraint Diagram**

these two equations a design space was created shown in Figure 4.8. The team picked a wing loading of  $1\text{lb}/\text{ft}^2$ , a  $C_L$  of 0.25 and a  $C_D$  of 0.04 represented as the red cross in Figure 4.8 as the design point.

$$V_v = \sqrt{\left(\frac{W}{S}\right) \frac{2}{\rho(C_L^3/C_D^2)}} \quad (21)$$

$$R = \frac{2W}{\rho S C_L g \sin(\phi)} \quad (22)$$

Furthermore, the team realised that the airspeed would change throughout the mission profile for the X-1 flight, with a maximum during launch and slowly plateauing to a minimum velocity when in stable flight. For this the team expected a drop velocity of 99ft/s from the main aircraft and a minimum stable velocity of 32ft/s. The team then used Eq. 23 to derive Eq. 24 to represent the relationship between aircraft airspeed and vertical velocity. From this the minimum and maximum lift-to-drag and glide angles could be found to sustain the descent speed of 12.5ft/s shown in Figure 4.8. The team also identified the stall speed to ensure the aircraft at each flight segment would be above the stall speed as this would ensure the aircraft met the stability requirement in §XR-PF-02, this resulted in a stall velocity of 30ft/s.

$$\frac{1}{\tan(\gamma)} = \frac{L}{D} \quad (23)$$

$$V_{airspeed} = V_v \frac{L}{D} \quad (24)$$

Given the wing loading requirement, the team identified the initial target weight for the X-1 to be 0.22lbs from the components list which is discussed in greater detail in Section 5.3.4. Further, the team identified the expected AR of a delta wing to be between 1.5-2, the team selected 1.5, thus the span and chord could be calculated shown in Table 4.9. Further, the team found the tail moment arm required using volume coefficients for delta wing aircraft using Eq. 18, from this the required elevon and VT surface area was found using Eq. 19 and 20 which resulted in span and chord dimensions for the tail using the specified AR's shown in Table 4.10 [7]. It was decided that the elevon would be sufficient for pitch and roll stability, while the VT would be sufficient without the use of a rudder due to the small nature of the X-1.

**Table 4.9. X-1 Preliminary Geometry Values**

Wing Area	Span	MAC	Wing Loading	Aspect Ratio
$0.22\text{ft}^2$	$0.57\text{ft}$	$0.38\text{ ft}$	$1\text{ lb}/\text{ft}^2$	1.5

**Table 4.10. X-1 Preliminary Tail Dimensions**

	$L_t(\text{ft})$	Volume Coefficient	$S(\text{ft}^2)$	$b(\text{ft})$	$\bar{c}(\text{ft})$	AR
Elevon	0.16	0.4	0.21	0.57	0.38	1.5
VT (Each)	0.16	0.07	0.055	0.166	0.166	1

The team also investigated a plethora of different airfoils of which were narrowed down to five at the average expected flight speed Reynolds number of 150,000 shown in Figure 4.9, of which the MH60 was chosen due to its near zero moment coefficient for expected angle of attack and suitable lift-to-drag during flight.

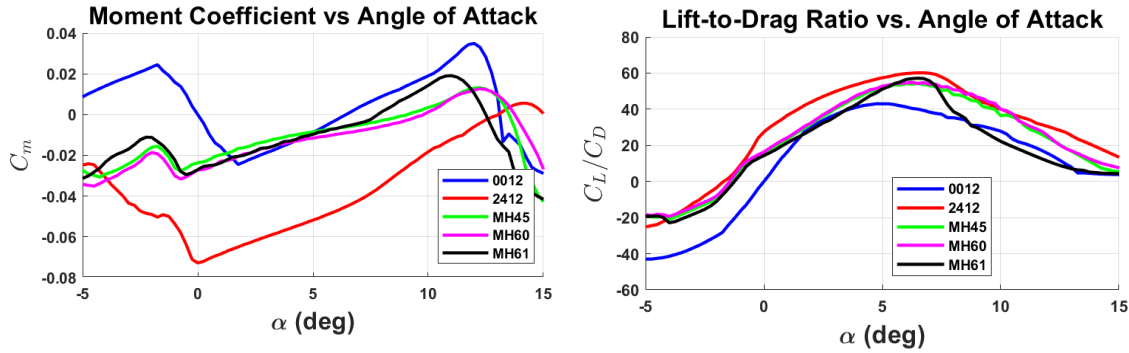


Figure 4.9. X-1 Airfoil Selection at  $Re = 150,000$

#### 4.4. Mission Payloads

##### 4.4.1. M2 Fuel Tank Weight and Allocation

Following determination of the initial sizing and aerodynamics, the mission model was utilised to determine the optimal combination of fuel weight and cruise velocity which achieved the best M2 score for the given configuration. The model simulated various combinations of cruise velocities and MTOW (payload weight plus empty plane weight) using the aerodynamic data chosen in previous sections for the M2 mission, producing the surface plot shown in Figure 4.10. From this plot, it is possible to see that higher average velocity and payload weight led to a higher M2 score, but only up to a limit. The cutoff on the right side of the surface represents the minimum velocity before stall, whilst the cutoff on the top represents mission combinations that would likely use too much energy and thus not meet requirement §AD-PP-01. This energy was approximated roughly as shown in Eq. 3 and 25, with an efficiency factor of 0.7 typical for propellers, as a propulsion system had not been finalised yet. From this, the optimal aircraft MTOW was 48.5lbs, with the average velocity target of 118 ft/s. This was slightly lower than the initial design target of 55lbs but was still considered acceptable for the design. Thus, using the weight fraction as determined in Section 4.3.1, the payload weight target for M2 was chosen to be 33lbs.

$$E = Pt \quad (25)$$

Thus, the choice of configuration to carry the target payload was determined. Three options were identified and evaluated using a FoM shown in Table 4.11. These were two large external tanks, multiple smaller external tanks, or two small external tanks and a large internal tank. Both weight capacity and Ground Mission were prioritised as these had direct impacts on the mission score, whereas drag and airplane dynamics had secondary impacts.

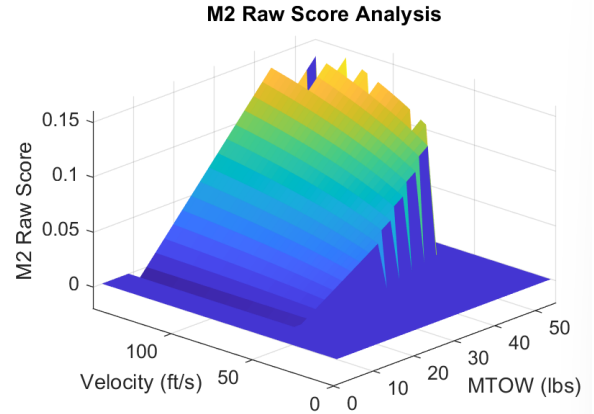


Figure 4.10 M2 Score Velocity vs MTOW



**Table 4.11 Aircraft Configuration Decision Matrix**

Characteristics	Weight	Two Large External Tanks	Multiple Smaller External Tanks	Two Small External Tanks + Internal Tank
<b>Weight Capacity</b>	5	4	5	5
<b>Ground Mission</b>	5	5	3	4
<b>Drag</b>	4	3	2	4
<b>Roll Stability</b>	3	3	2	4
	<b>Total</b>	66	54	73

From Table 4.11, having multiple smaller fuel tanks was disadvantageous as it not only increased drag but would also lengthen the GM time. Whilst having two large external fuel tanks would result in the lowest GM time, the drag and dynamic stability penalty was deemed too great, and so the internal fuel tank with two smaller tanks was the best configuration. The GM penalty from having the internal fuel tank was planned to be mitigated through the hatch and restraint design, with a goal of limiting that section of the GM to 5 secs. Whilst options sand and water were considered, steel shot/pellets were chosen as the weight due to their high experimentally determined fill density of 0.180 lbs/in<sup>3</sup>. This minimised volume and thus drag. The required volume for the bottles was then determined to be approximately 0.8 gal from the target payload weight of 33 lbs. Based on the commercial availability of bottles, a 0.52 gal (2L) bottle size was chosen for the internal fuel tank, whilst 20 oz (600mL) bottles were chosen for the external tanks to meet the minimum rule requirement. The specific brands chosen were finalised in Section 5.2.2 and 5.2.4.

#### 4.4.2. M3 Target Laps and X-1 Weight

The target number of laps for M3 was also evaluated through the mission model as discussed in Section 4.4.2. Using the estimated glide time for the X-1 as seen in Section Figure 4.8 and specified by §XD-PF-04 of 20 seconds, variations in the velocity for the M3 mission were simulated and plotted on Figure 4.10. Here, the cutoff on the surface is mainly due to energy limitations (exceeding the 85% discharge limit), and the team identified that the score/no. of laps is maximised at a velocity of roughly 85 ft/s completing 9 laps before X-1 deployment. Note here the score assumes a successful X-1 glider deployment achieving the bonus points, but this does not affect the results of the analysis.

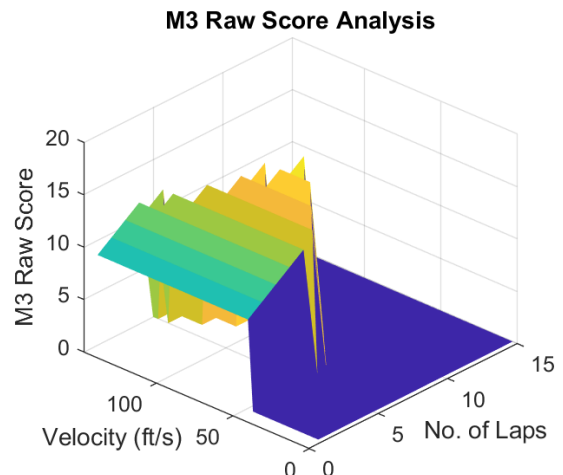


**Figure 4.11 M3 Score Velocity vs No. Laps**

The X-1 Weight was a critical component of the X-1 design due to its large weighting on the M3 bonus points. As such, the goal was to minimise this weight by only including the necessary components needed to complete the mission. The team concluded that package weighing around 0.22lbs was required, as this would equate to an equivalent lap score of 11 if all bonus points are secured, reducing the impact of teams who score many laps.



## 4.5. Propulsion Analysis

The aim of the propulsion analysis was to determine the ideal system which would achieve the desired static thrust requirements for take-off and climb, whilst also maintaining sufficient dynamic thrust to enable a high cruise velocity for M2 and high efficiency for M3 as required by §AD-PP-01, §AD-PP-02 and §AR-PF-01. The mission model was used extensively in this section to compare various propulsion systems and their impacts on mission scoring.

### 4.5.1. Rate of Climb Performance

The team identified the best rate of climb for the BRICK in each mission using the Eq. 26, this resulted in velocity for M1, M2 and M3 of 36ft/s, 64ft/s and 36ft/s respectively, all of which are above each missions' stall velocity.

$$V_{RoC} = \sqrt{\frac{2}{\rho} \left( \frac{W}{S} \right) \sqrt{\frac{k}{3C_{D_{min}}}}} \quad (26)$$

To determine the climb thrust required by the BRICK the climb angle of attack is found using Eq. 27 which was found to be 14 degrees using the M2 best rate of climb velocity. This is then used in combination with the Eq. 3 which required a T/W of 0.40 equating to 27.4lbs of thrust.

$$\gamma = \sin^{-1} \left\{ \left( \frac{\eta_p P_{br}}{W} \right) V^{-1} - \left( \frac{\rho S C_{D_0}}{2W} \right) V^2 - \left( \frac{2kW}{\rho S} \right) V^{-2} \right\} \quad (27)$$

### 4.5.2. Constant Velocity Turn Sensitivity Study

The team then identified the turn radius as a flight segment which could significantly increase the mission score for M2 and M3, as such the team varied the banked turn angle and speed resulting in Figure 4.12. Hence, the team found that given the maximum power of 4kW, the maximum banked turn angle was 65 degrees at 105ft/s, while the maximum banked turn at 118ft/s was 60 degrees. The team then used Eq. 28, which resulted in a 36.2% decrease in the turn radius when having a banked turn angle of 65 degrees.

$$R = \frac{V^2}{g \tan(\theta)} \quad (28)$$

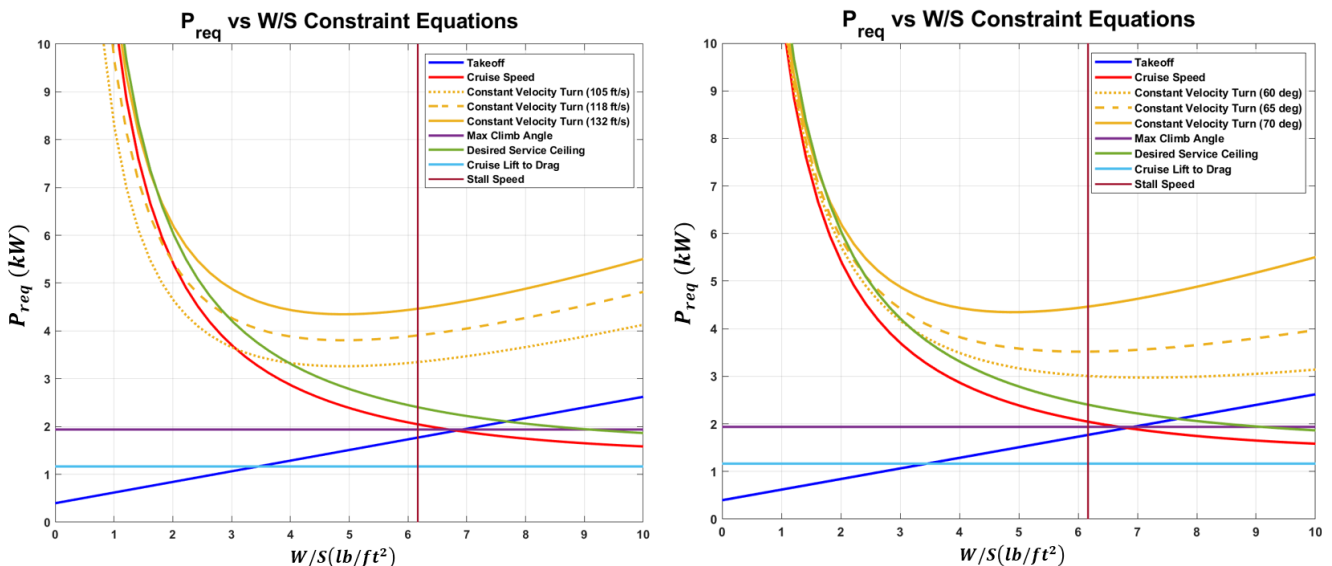


Figure 4.12. Constant Velocity Power Sensitivity Study



#### 4.5.3. Battery Selection

Based on the 4kW maximum power target from the sensitivity studies conducted in Section 4.5.2, and the choice of a dual motor configuration as outlined in Section 3.4.4, the power requirement for each propulsion system was roughly 2 kW. Using the power equation shown in Eq. 29, and the maximum current limit of 100 A outlined in the rules, the required voltage from the battery pack was to be at least 20.0 V. Thus, two six-cell (22.2 V) Dualsky 2200 mAh 50C LiPo batteries were selected to maximise total battery capacity at 97.7 Wh, with each battery pack running one motor and propeller. At 50C, the packs would have an allowable maximum discharge of 110A, which was above the maximum current limit of 100 A and thus deemed adequate.

$$P = VI \quad (29)$$

#### 4.5.4. Motor & Propeller Selection

With the voltage of the propulsion system finalised, a suitable motor and propeller combination could now be found based on the static thrust requirement of 22 lbs outlined in section 4.3.2 and the 4 kW total maximum power target from the sensitivity studies conducted in 4.5.2. The team then evaluated several configurations through eCalc and MotoCalc that met these initial requirements. These requirements are outlined in Table 4.12.

**Table 4.12 Propulsion Selection Requirements**

Parameter	Requirement
<b>Static Thrust</b>	Satisfy the minimum lower bound static thrust limit of 22 lbs
<b>Power</b>	Be capable of outputting 4kW of mechanical power
<b>M2</b>	Pick combinations of motors and propellers that achieve high dynamic thrust through increased propeller pitch or motor RPM, cruise speed of 118 ft/s
<b>M3</b>	Pick combination of motors and propellers that operate most efficiently at the throttle setting which gives a flight time of 5 minutes (at 85% discharge), cruise speed of 85 ft/s
<b>Product Availability</b>	Prioritise configurations where a pusher propeller is available for counter rotating propellers on each motor

The results of these analysis were then input into the mission model to determine the impact on the total mission score. From evaluating several configurations, the top 5 propulsion configurations are summarised in Figure 4.13. These configurations were also influenced by available stock in Australia, which is limited compared to the US.

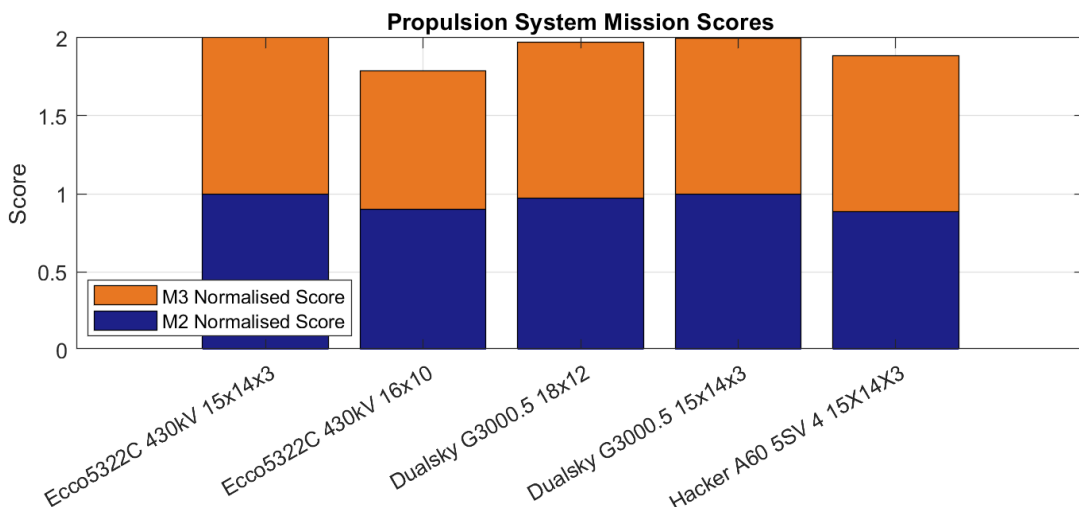


**Figure 4.13 Propeller/Motor Combinations vs M2/M3 Scores**



From Figure 4.13, it was identified that the Dualsky Ecco5322C 430kV motor with a 15x14x3 Master Airscrew propeller resulted in the highest total mission score and individual M2 and M3 scores compared to the other combinations tested. Due to the discrete scoring of the M3 mission, scores in the M3 did not vary much assuming the X-1 performance remained identical, since a large jump in performance was needed to gain an additional lap. For M2 however, the propulsion performance had a direct impact on the mission score and was the more influential mission. The properties of the propulsion system are shown in Table 4.13. All requirements were met besides M2 cruise speed which was 8ft/s slower than required.

**Table 4.13 Propulsion Performance Properties**

Property	Value
M2 $V_{cruise}$ (ft/s)	118
M3 $V_{cruise}$ (ft/s)	85
Static Thrust (lbs)	25.97
Max. Total Power (W)	4044

#### 4.5.5. Electronic Speed Controller and Fuse

Based on the analysis carried out on eCalc and MotoCalc, the maximum current draw predicted by the motor and propeller combination was a maximum of 100.7A peak during take-offs, with a cruise current draw of 88.7A. As such, the Hobbywing Skywalker 100A ESC was deemed suitable with a nominal current rating of 100A and a peak rating of 120A for 10s which would be sufficient for take-off. A 100A blade fuse was also deemed adequate for the peak and nominal currents expected, whilst still adhering to the rules.

#### 4.5.6. Finalised Propulsion System

**Table 4.14 Finalised Propulsion System**

Mission	Motor	Propeller	ESC	Battery	Fuse
1, 2, 3	2 x Dualsky ECCO5322C 430kV	Master Airscrew 15x14x3N + 15x14x3P	Hobbywing Skywalker 100A	2 x 2200mAh 6S Dualsky 50C LiPo	100A Blade Fuse

## 4.6. Stability Analysis

The preliminary design was constructed then in XFLR5 to ascertain if it was statically and dynamically stable. Each mission was tested, however results showed similarities due to the team designing the payload weights to act at the quarter chord of the aircraft which was the designated CG location. As expected, the only substantial change was the frequency, as the heavier M2 payload resulted in higher natural frequency.

#### 4.6.1. Static Stability

The required trim angle and elevator deflection was obtained from AVL. To ensure a positive trim angle for M2 the incidence angle on the horizontal tail was set at -2 degrees. Table 4.15 shows the trim angle and subsequent elevator deflection for the BRICK and X-1, while the SM

**Table 4.15. Static Stability**

Trim Angle (°)	BRICK			X-1
	M1	M2	M3	
$\delta_e$ (°)	-2.22	2.18	-2.22	2.35
$C_{L,cruise}$	3.34	0.83	3.34	-0.42
SM (%)	0.165	0.359	0.165	0.25
	17.4	22.4	17.0	12.9

was found using Eq. 30, where the NP is found from AVL. Small elevator deflection was required for each mission, validating the control surface selection.

$$SM = \frac{(X_{NP} - X_{CG})}{MAC} \quad (30)$$



The overall static stability derivatives for M1/3 and M2 were also computed using AVL and shown in Table 4.16 and compared to similar aircraft [12].

**Table 4.16. Static Stability Derivatives**

	Longitudinal [ $\text{rad}^{-1}$ ]			Lateral [ $\text{rad}^{-1}$ ]		
	$C_{m_a}$	$C_{m_q}$	$C_{m_r}$	$C_{l_\beta}$	$C_{n_\beta}$	$C_{n_r}$
<b>Requirements</b>	<0	<-3.6	-0.02 to 0.02	<0	>0	<-0.125
<b>M1 and M3</b>	-0.93	-11.0	0	-0.044	0.148	-0.223
<b>M2</b>	-0.98	-11.1	0	-0.089	0.154	-0.233
<b>X-1</b>	-0.24	-4.37	0	-0.165	0.426	-0.824

#### 4.6.2. Dynamic Stability

Longitudinal and lateral dynamic stability is crucial to having a stable and well optimised plane, the preliminary aircraft design was modelled in XFLR5 and found to be stable however could be fine-tuned in the preliminary design phase to limit drag and increase dynamic stability. This resulted in changing the tail moment arm to be slightly smaller, resulting in 41.34 in, the horizontal tail was lowered down vertically by 1.18 in while the vertical tail was level with the wing. With these changes the stability for all missions achieved level 1 flying qualities as assessed by MIL-F-B785C except for the spiral mode highlighted in orange which were level 2. Level 1,2 and 3 flying qualities are shown in Table 4.17, while M1/3, M2 and X-1 stability frequencies, damping ratios and time constants are shown in Table [13]. The M1 and M3 qualities were similar and as such only M1 was shown. Note, green represents Level 1, orange Level 2, and red Level 3 in the following tables.

**Table 4.17. MIL-F-B785C Class II Category B, Level 1/2/3 Flight Requirements**

Mode	$\xi[-]$	$\omega_n[\text{rad/s}]$	$\xi\omega_n[\text{rad/s}]$	Time to Double (s)	$\tau$
<b>Short Period</b>	$0.3 \leq \xi \leq 1.3$	-	-	-	-
<b>Phugoid</b>	$\xi \geq 0.04/0$	-	-	-	-
<b>Roll</b>	-	-	-	-	$\tau < 1.4/3/10$
<b>Dutch Roll</b>	$\xi \geq 0.08$	$\omega_n \geq 0.4$	$\xi\omega_n \geq 0.35$	-	-
<b>Spiral</b>	-	-	-	$t_2 \geq 20/8/4$	-

**Table 4.18. Dynamic Stability Values for M(1 and 3)/M2/X-1**

Mode	$\xi[-]$	$\omega_n[\text{rad/s}]$	$\xi\omega_n [\text{rad/s}]$	Time to Double (s)	$\tau$
<b>Short Period</b>	0.78/0.76/0.41	13.5/20.7/101	8.42/13.5/95.6	-	-
<b>Phugoid</b>	0.043/0.040/0.42	0.50/0.32/0.26	0.50/0.32/0.24	-	-
<b>Roll</b>	-	-	-	-	0.080/0.063/0.035
<b>Dutch Roll</b>	0.23/0.20/0.42	7.3/12.5/105	7.1/12.2/102	-	-
<b>Spiral</b>	-	-	-	6.11/11.1/9.5	-

Based on prior experience with our pilot, the DBF2024 plane also had similar level 2 flying qualities for the spiral mode, and the pilot was easily able to correct for the spiral mode.

## 4.7. CFD Analysis

### 4.7.1. Fuselage and Motor Mount

CFD was completed on V1 and V2 using ANSYS CFX [14] with the residual target set at 1e-4 and the k-epsilon method used. The results

**Table 4.19. Fuselage and Motor Mount CFD Study**

Mission	BRICK	$C_D$ (Preliminary)	$C_D$ (CFD)	Error (%)
<b>M1/3</b>	V1	0.0514	0.0453	9.11
	V2	0.0468	0.0412	11.40
<b>M2</b>	V1	0.0499	0.0460	7.82
	V2	0.0466	0.0402	13.73



are shown in Table 4.19. A mesh convergence study was conducted to validate the simulation on the initial V1 aircraft, in which five element sizes were chosen ranging from 100,000 to 2.5 million refining the inflation layer and increasing the element size. The simulation converged at 2 million elements; hence each simulation afterwards was simulated using the same mesh sizes totalling 2 million elements. The CFD drag aligned with the preliminary drag calculated in Section 4.3.4 resulting in a 5-15% error attributed to the CRUD factor. Further, there was a large negative pressure region acting on the motor mount which drove the team's decision to refine this area to minimise the skin friction drag of the aircraft between V1 and V2. Additionally, the fuselage design and width were driven by drag minimisation. Thus, the team identified the thinnest commercial bottle for the inside fuel tank to minimise the cross-sectional area of the fuselage. The simulation drag was also used to refine the MATLAB mission model.

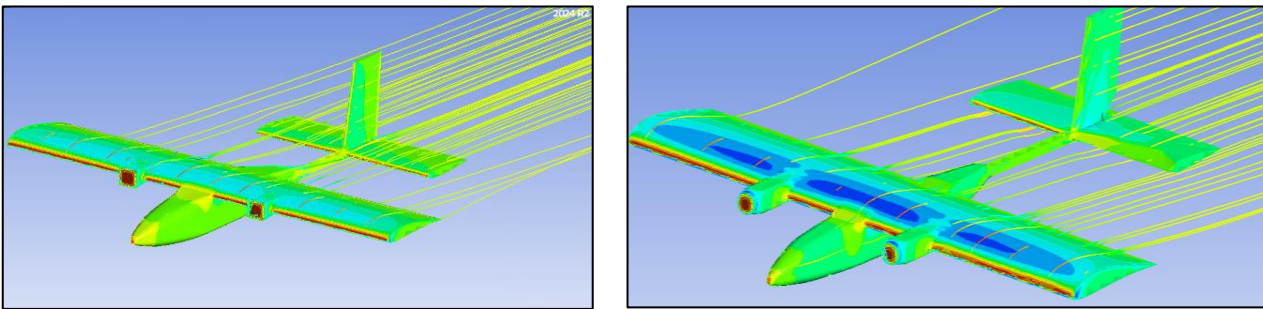


**Figure 4.14. CFD Aircraft Study Pressure Contour. V1 (Left). V2 (Right)**

#### 4.7.2. Winglet Design

From the requirement §AR-AD-03, the maximum wingspan was 6ft, the MTOW drove the planform requirement leading to a low AR, increasing induced drag, to maximise the performance of the aircraft the team investigated the use of winglets. This was based on a sensitivity study on the increase in skin friction drag compared to reduction in induced drag. While winglets provided the greatest benefit in drag reduction the team identified the difficulties involved in manufacturing, related to mould preparation and laying up. Instead, the team opted to use endplates. XFLR5 was used to simulate various endplate heights while keeping the chord constant. The team also calculated the induced and skin friction drag during flight, which was then plotted against the winglet length; the optimisation point was identified as a height of 1.4ft. CFD was conducted on two winglet designs and without a winglet shown in Figure 4.16 at an

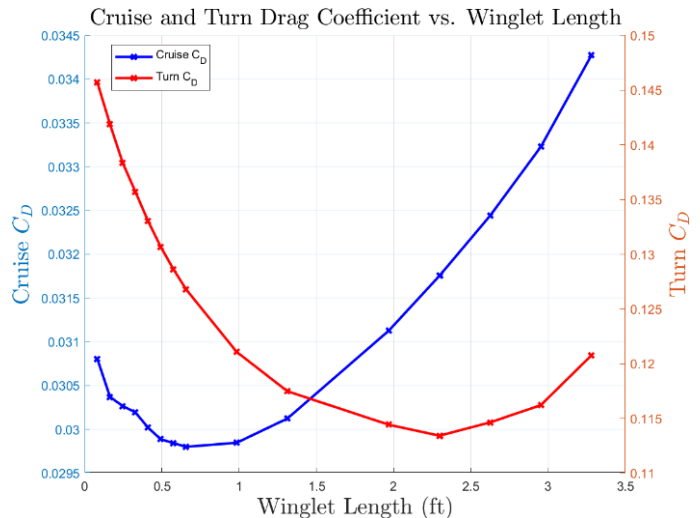


**Figure 4.15. Drag Coefficient vs. Winglet Length**

**Table 4.20. Lift-to-Drag Ratios for Winglet Geometry**

Option	L/D at -2.25°	L/D at 2.25°	L/D at 13°
No Winglets	8.51	14.37	8.50
Option 1	8.81	15.84	9.59
Option 2	8.80	15.33	9.17

AoA of 2.25. Various angles representing M1/3 cruise, M2 cruise and expected turning AoA was then compared to a simulation done without winglets with the L/D shown in Table 4.20, hence option 1 was chosen.

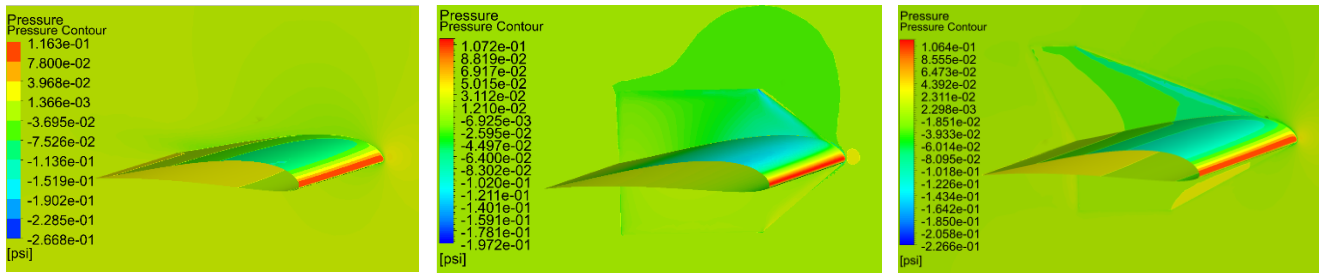


Figure 4.16. CFD Winglet Study Pressure Contour at AoA of 2.25 Degrees

## 4.8. Preliminary Performance Prediction

### 4.8.1. Preliminary Performance

From the results of the mission model and the preliminary analysis, the following performance predictions were obtained shown in Table 4.21.

Table 4.21 Preliminary Performance Prediction

Properties	M1	M2	M3
<b>Payload/Pylon (lbs)</b>	N/A	35.3	2.2
<b>X-1 Weight (lbs)</b>	N/A	0.22	0.22
<b>Take-off Weight (lbs)</b>	13.2	48.5	15.4
<b>TOFL (ft)</b>	32.8	202.1	40.0
<b>Average Throttle (%)</b>	60	90	60
<b>Cruise Speed (ft/s)</b>	90.0	110.0	85.0
<b>Battery Usage (%)</b>	40.0	85.0	85.0
<b>Number of Laps</b>	3	3	9 (before X-1 Launch)
<b>Mission Time (sec)</b>	80	126	300

### 4.8.2. Uncertainties

With all preliminary analysis techniques uncertainties are bound to occur, while the team aimed to estimate the most conservative values and frequently update the constraint diagrams and mission model drag, both analysis techniques could include substantial sources of error. To combat this the team applied a CRUD factor of 1.25 on the drag analysis to account not only for additional drag from miscellaneous objects but also from surface imperfections during manufacturing. Furthermore, the team applied safety margins on all constraint diagrams, AVL and XFLR5 data to account for any discrepancies between the simulation and built aircraft, dominated mostly by the inclusion of a fuselage which AVL and XFLR5 is unable to simulate accurately. Additionally, testing data was conducted in Sydney, Australia around sea level elevation resulting in a noticeable deviation from TIMPA, Tucson.

## 5. Detailed Design

Utilising the results from the preliminary design, the detailed design sought to optimise the structure and payloads of the aircraft to achieve the desired requirements, with emphasis on reducing weight and reducing GM times.

### 5.1. Dimensional Design Parameters

Table 5.1 shown below lists the final dimensional design parameters for BRICK.



Table 5.1. Final Dimensional Design Parameters

Wing		Horizontal Tail	
Airfoil	MH84/NACA5512 Hybrid	Airfoil	NACA0012
Span (ft)	6.00	Span (ft)	2.54
MAC (ft)	1.57	Chord (ft)	1.02
Planform Area (ft <sup>2</sup> )	9.45	AR	2.50
Aspect Ratio	3.81	Planform Area (ft <sup>2</sup> )	2.59
Incidence Angle (°)	1.00	Taper Ratio	1
Static Margin (%) [M1/M2/M3]	[17.4, 22.4, 17.0]	Incidence Angle (°)	-2.00
Fuselage		Tail Arm (ft)	
Length (ft)	6.56	Vertical Tail	
Width (ft)	0.39	Airfoil	NACA0010
Height (ft)	0.59	Span (ft)	1.14
Motor		Chord (ft)	0.77
Receiver	Futaba R30008SB	AR	1.5
Servos	Aileron – 2 x CRHV 7225-MG Elevator – 1 x CRHV 7225-MG Rudder – 1 x HITEC 7087MH Nose Steer. – 1 x SAVOX SV0220 X-1 Release – 1 x HITEC 7087MH	Planform Area (ft <sup>2</sup> )	0.75
Propulsion Bat.	Dualsky 2200mAh 6S 50C	Taper Ratio	0.8
Avionics Bat.	Dualsky 1000mAh 2S 25C	Incidence Angle (°)	0
ESC	100A Hobbywing Skywalker	Tail Arm (ft)	3.94
Propeller		Endplate	
M1/2/3	15x14x3 & 15x14x3P	Chord (ft)	1.57
X-1 Glider Wing		Height (ft)	1.00
Airfoil	MH60	Width (in)	1.18
Length (in)	7.85	Motor (x2)	
MAC (in)	5.50	Model	Dualsky ECCO5322C
Span (in)	5.89	kV	430
Planform Area (in <sup>2</sup> )	32.89	Max. Power (W)	2200
X-1 Glider Elevon		X-1 Glider VT	
Airfoil	MH60	Airfoil	MH60
Elevon MAC (in)	1.34	VT Span (in)	2.76
Elevon Span (in)	5.98	VT MAC (in)	3.15

## 5.2. Structural Analysis

The aerostructures team began by taking the expected flight conditions from the aerodynamics team in the preliminary design, as well as the load-factor results from the Mission Model. From this, a V-n diagram for the entire aircraft was constructed, shown in Figure 5.1. This allowed each component to be designed around a global constraint. Due to resource constraints and faculty restrictions, composite manufacturing was not viable, and so a balsa and plywood construction with prefabricated composite parts was pursued instead.

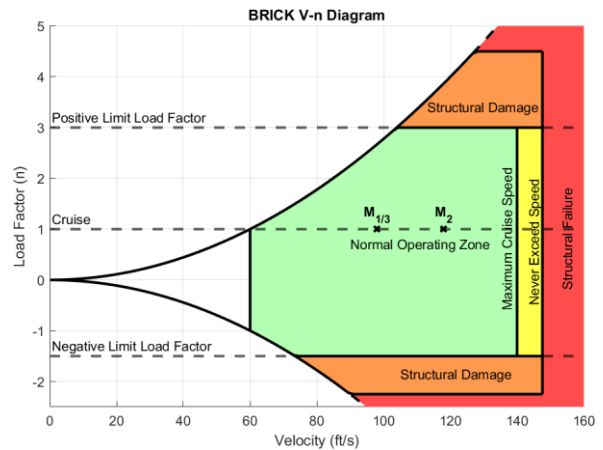
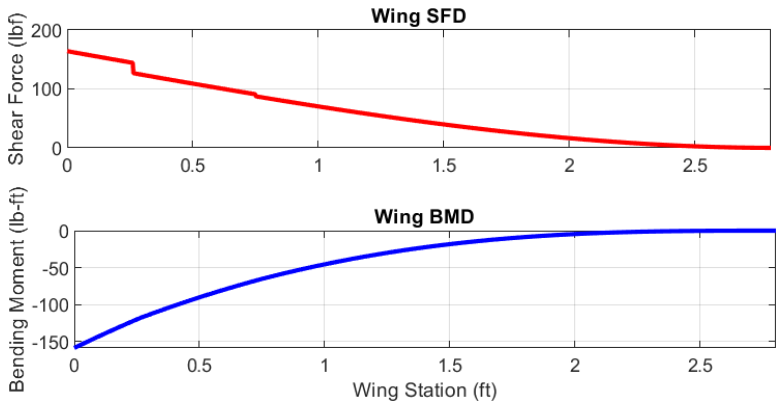


Figure 5.1. BRICK V-n Diagram

### 5.2.1. Wing Structure and Motor Mounts

Based on the V-n diagram, a SFD and BMD for the wing structure was constructed shown as Figure 5.2, using the Schrenk distribution model [15], with the maximum load factor experienced by the aircraft from the V-n diagram of 2.5 at 48.5lbs. From this the maximum bending moment and shear force was found to be -157.2lb-ft and 163.4lbf respectively. Applying a FoS of 1.5 times on the expected loads, the sizing for the main spar could be found using the Eq. 31, where the maximum bending stress was located at the root, and the maximum allowable bending stress was 87000 psi [16] for CFRP.



**Figure 5.2. SFD and BMD For Semi-Span Wing**

$$\sigma = \frac{My}{I} \quad (31)$$

The main spar was a CFRP woven rod sized to an outer diameter of 1.18 in, with a wall thickness of roughly 1/32 in and a length of 35.64 in per half span of the wing. This was then telescoped into a larger 1.26 in carbon fibre rod with the same wall thickness extending 4.72 in to span the width of the fuselage. A secondary spar of outer diameter 0.55 in was also used and telescoped into the fuselage wing mount. The wing is then locked into place with two M3 bolts and wingnuts that prevent the wing from slipping out. This is visually shown in Figure 5.3.

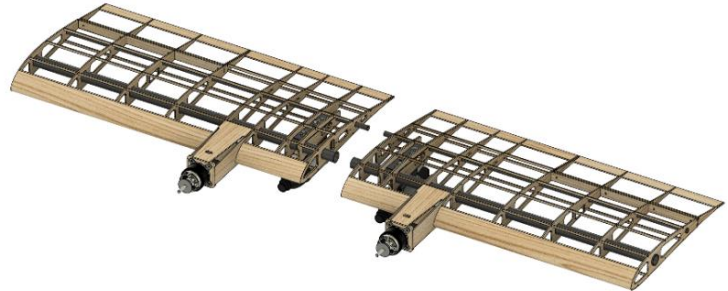


**Figure 5.3. Wing Structure**

The BRICK's overall wing structure had a semi-span of 33.6 in from wingtip to root, and a chord of 18.9 in with an aspect ratio of 3.81. The aerofoil cross-section is maintained with 1/8 in thick plywood ribs and stringers, with the leading edge moulded with 1/32 in balsa sheeting to maintain a smoother leading-edge curve shown in Figure 5.3. The outer surface was then covered in a Monokote film. The motor mounts were extended from the wing ribs and extended 4.14 in out from the leading edge of the wing for better CG placement. The motor mount firewall was made from 1/4 in plywood to withstand torsional, and shear loads from the propulsion system.

To validate the hand calculations, FEA was conducted on the wing in Figure 5.4 to ensure the deflection experienced by the wing would not cause plastic deformation. The FEA is shown below at maximum load conditions with a load factor of 2.5g, from this the maximum deflection was found to be 0.32 in and the maximum stress was 28000 psi, which gave a FoS of 3.1 for CFRP. This was deemed adequate.

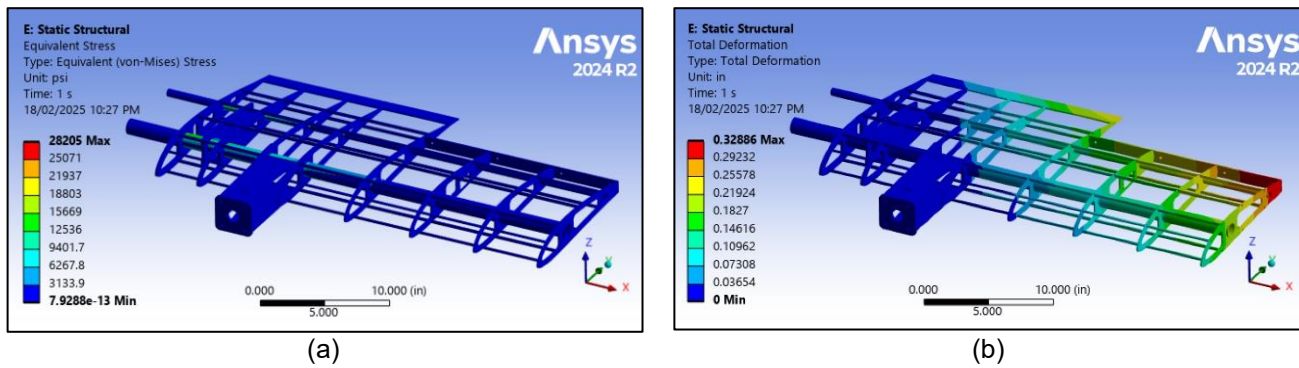


**Figure 5.4 FEA of Wing Under 2.5g MTOW Load**

### 5.2.2. Fuselage Structure

The fuselage structure was designed to carry through loads from the wing, empennage, landing gear, and payloads within the limits as outlined in the V-n diagram in Figure 5.1. The sizing was constrained by the size of the internal fuel tank, where two main options were considered seen in Figure 5.5. A nominal 0.5 gal capacity was required in order to meet the required payload mass of 35.3 lbs, as discussed in 4.4.1.



(a) Oi Ocha Green Tea Bottle (0.5 gal) (11x8x12 in)



(b) Pepsi Bottle (0.5 gal) (12.4x4.33x4.33 in)

**Figure 5.5 Dimensional Comparison of Internal Fuel Tank**

Based on the CFD analysis in Section 4.7, it was determined that a longer, but narrower, fuselage shape helped to reduce drag, and thus the Oi Ocha Bottle was selected due to its slenderer profile. From this, the width of the fuselage was sized at 4.72 in, with a height of 7.09 in to accommodate the bottle, battery, X-1 release mechanism and tail boom mount as shown in Figure 5.6.

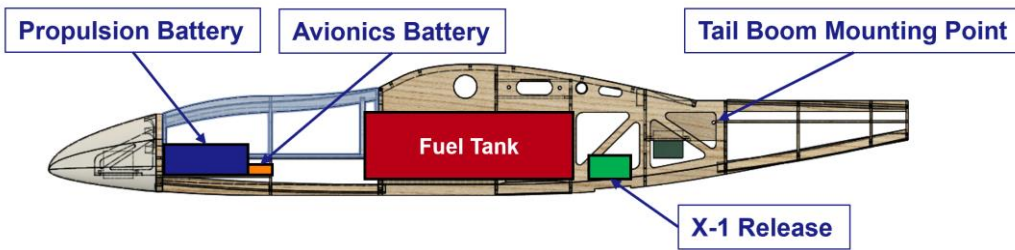


**Figure 5.6 Component Allocation within Fuselage**

To handle the landing, wing mount, and tail boom forces, the fuselage was constructed a plywood and balsa skin construction. To handle the landing case, longerons on the bottom edge of the fuselage were reinforced to deal with the forces of landing at MTOW, using 15/64 in plywood and an 0.31 in CFRP rod along the length of the fuselage in between the nose gear and main gear. Past the main landing gear mount, the forces were reduced, and so these sections used 1/8 in plywood to minimise weight. To handle the large shear forces near the wing-hard points, 15/64 in plywood was used at the interface of the main spar. A frame construction was utilised to provide a strong base to hold the main and auxiliary spars together and house the large internal fuel tank. Thus,



the ribs were also reinforced with 15/64 in plywood to handle the large shear forces at this point. A balsa skin with Monokote film was also used to provide additional shear strength and to enable smooth curved surfaces.

To accommodate for the internal fuel tank used in M2 and M3 and support Ground Mission loading, the fuselage features a detachable nose cover assembly highlighted in blue in Figure 5.7. The cover is secured onto the main body with spring latches which lock into holes on the main fuselage. The canopy also has a 15/64 in plywood to stop the internal fuel tank from sliding forward into the electronics. This is supported by the addition of small pieces of XPS foam secured onto the ribs to dampen shock impacts caused by landing.

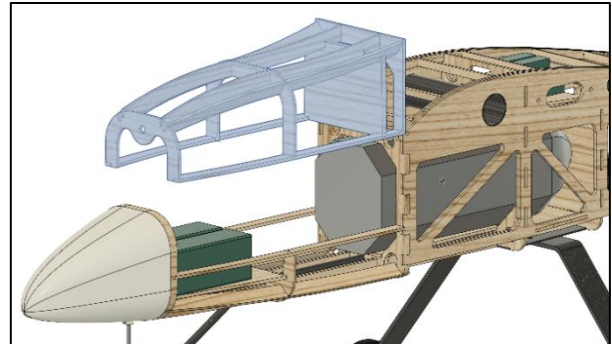


**Figure 5.7. Internal Fuel Tank Holder and Removable Canopy**

To validate the ability for the fuselage to effectively distribute the forces from the wing and tail an FEA was conducted to determine the strength of the design depicted in Figure 5.8. The fuselage was loaded for a 2.5g case at max-payload determined at the maximum limit load anticipated by the aircraft from the V-n diagram shown in Figure 5.1. The FEA showed a maximum stress of 4051.8 psi at the auxiliary wing mount, with a maximum deformation of 0.033 in. The ultimate strength of plywood is approximately 7000 psi [17], giving a resulting FoS of 1.75 which was considered ample.

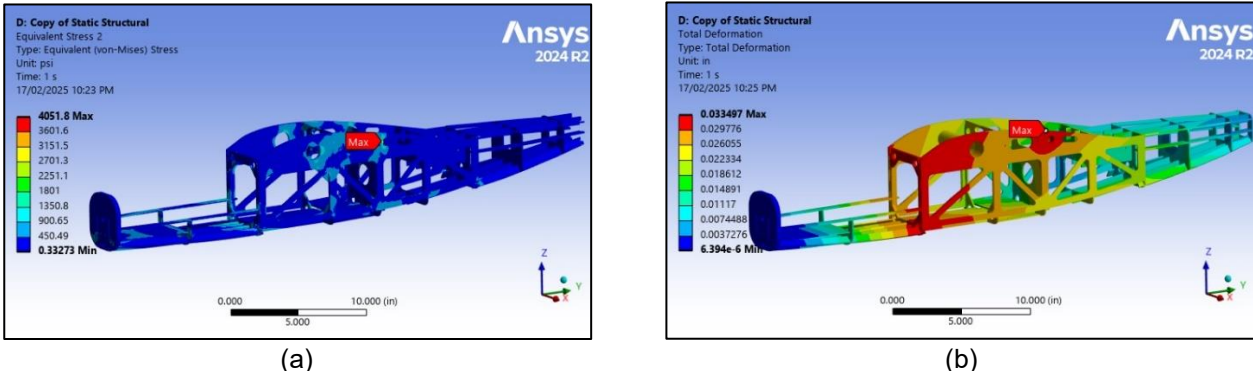


**Figure 5.8 FEA of Fuselage Under 2.5g MTOW Load**

### 5.2.3. Tail Structure

Much like the main wings, the horizontal and vertical tail spars were sized against the maximum foreseeable loads expected during full elevator and rudder movements. Using Eq. 31, carbon rods with outer diameters of 0.55 in for the HT and 0.31in for the VT, with a thickness of 1/32 in were chosen to minimise the overall deflection of the surfaces to no more than 0.2 in to minimise aerodynamic impacts. The HT spar was passed through the fuselage CFRP tail boom with an overall length of 30.5 in. Likewise, the VT spar also passed through both sides of the tail boom as shown in Figure 5.9. Both surfaces were secured with an M3 anti-rotation bolt that based through tail boom, as shown in Figure 5.9.

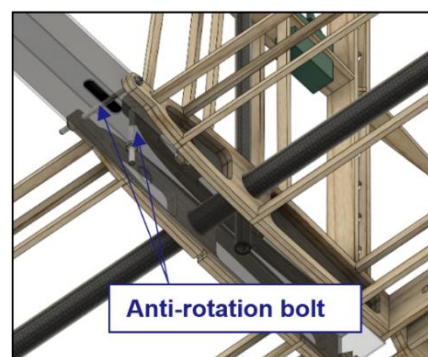


**Figure 5.9. Tail Mount Mechanism**



Additional 1/8 in plywood stringers and ribs were used to then support the aerofoil shape and carry the loads into the spar, with similar construction used on the control surfaces. For the VT the servo was mounted in the middle rib, however due to CG limitations, the HT elevator servo is positioned in the fuselage, and drives the elevators through a linkage within the tail boom to the centre of the elevator surface, seen in Section 5.7. 1/8 in plywood was also used on the rear auxiliary spar to support the hinges for the control surface, whilst improving torsional rigidity. A balsa leading edge was used for both the HT and VT, with Monokote film over the top.

#### 5.2.4. Pylon Structure and Mechanism

Based on the target weights in Table 4.21 of 6.61 lbs for each pylon, the pylon structure was required to both withstand this load at the maximum load factor of 3g, outlined in Figure 5.1, whilst also aiming to reduce GM assembly times. Much like the internal tank, several bottle options were considered as shown in Figure 5.10, with the final choice being the 600mL (20oz) Pepsi bottle. This was due to the uniform and relatively aerodynamic nose shape compared to the Coke bottle and Spring Water bottle, which had undesirable ridges and bumps.



Figure 5.10 Comparison of External Fuel Tank

##### 5.2.4.1. Fuel Tank Pylon Structure

The pylon structure consists of two distinct components, the adapter on the bottle, and the pylon itself. The team made use of a permanent adapter folded from 3/64 in aluminium sheet metal as shown in Figure 5.11 to clamp the bottle around the narrower section of the body and handle flight loads. M4 bolts and nuts were used to tighten the clamp, whilst also acting as a guide to insert into a rail. These were designed to remain within the 0.5 in dimensional limitations for the adapter. The pylon then had a corresponding rail made from tough PLA to handle flight loads and was constrained in the rear. The front was locked using a hinged section of the pylon, using an R-clip to lock in place. This single R-Clip attachment point would help reduce GM times by eliminating the need to align multiple holes or affix multiple attachment points. Foam was used to shape the pylon into a NACA0012 aerofoil shape to help reduce drag and interface flush with the wing's surface.

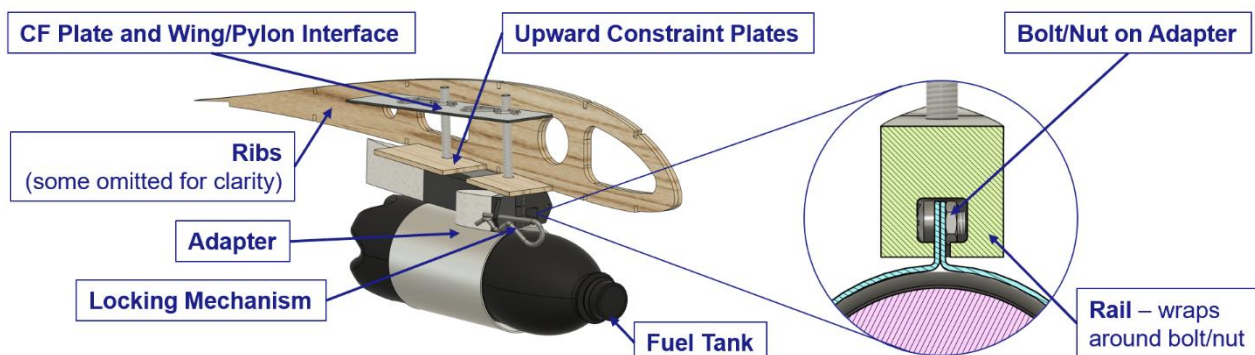


Figure 5.11 Pylon Structure

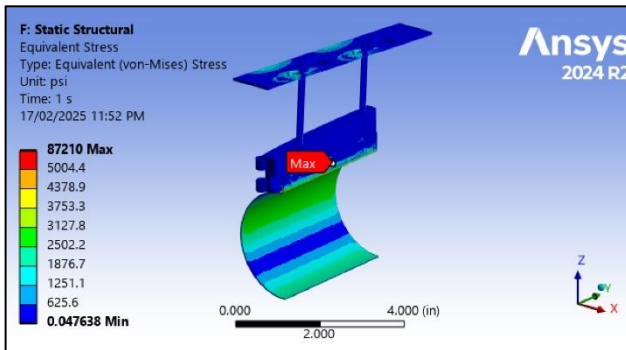


#### 5.2.4.2. Pylon to Wing Interface

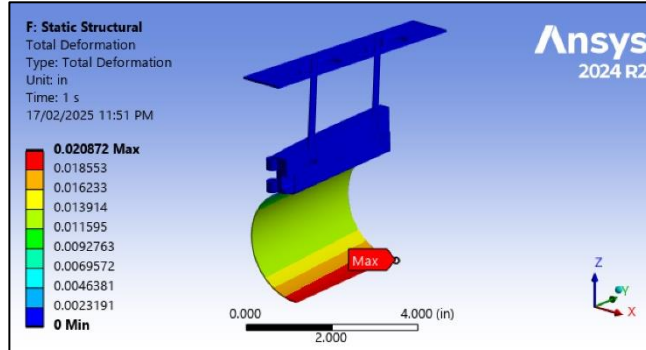
The pylon to wing interface consisted of two M6 bolts installed on the underside of the rail and feeding through into the wing, to comply with the 0.25 in max uncovered hole dimensions. The bolts then pass through a CF plate which acts as the main support. This CF plate was installed between the main and auxiliary spars and nested between the ribs to handle the large downforce at high load factors. The M6 bolts were then secured to the main plate through the 1/8 in upward plywood constraint plates, and an R-Clip on top the CF plate, as shown in Figure 5.11, which would firmly fix the pylon to the wing in compliance with the permanent fastener requirements. An access hatch on top of the wing would be used to access the R-clips for installation, sealed with tape to maintain a smooth wing surface.

#### 5.2.4.3. Pylon Structural Analysis

An FEA of the pylon assembly was also conducted to ensure adequate strength at the maximum load factor. A 6.61 lbs mass was applied to the adapter and subject to a load factor of 3g. The maximum stress was located on the contact point between the bolt and rail, with a peak stress of 87210 psi, which was under the ultimate strength for hardened steel [18] of 90000-10000. However, this result was likely a singularity due to the contact surface, and the stress of the PLA rail was manually checked and below the yield strength for tough PLA [19] at 6889.3 psi, with a maximum stress no higher than 3000 psi. The total deformation was only 0.02 in, which was still sufficient for the adapter to maintain contact and clamp the bottle.



(a) Stress on Pylon Assembly



(b) Deformation on Pylon Assembly

Figure 5.12 FEA of Pylon Assembly (Half Section)

#### 5.2.5. Landing Gear Structure

The landing gear structure was designed to handle the forces experienced upon landing at the maximum payload weight of 48.5lbs, assuming a maximum load factor of 2.5 on landing. The nose landing gear was constructed from 5/32in steel wire with a 5/16in CF tube acting as a cross brace to reduce bending loads. Wheelbase and tube adapters were 3D printed from tough PLA. The nose gear was also designed to steer allowing the pilot to have better ground roll control. This was driven by the long take off distance as estimated in Section 4.8 and reduced airflow over the VT from the wing-mounted motors at low speed.

An FEA study, shown in Figure 5.13, was conducted using a simulated load factor of 2.5 at MTOW for the entire fuselage, mimicking the deceleration the aircraft would experience upon landing. Displacement constraints were imposed on the  $x$  and  $z$  displacements for the nose gear, and  $y$  and  $z$  displacements on the main gear. The



maximum stress experienced on nose gear assembly was approximately 65199 psi on the steel wire member, which with a 1.5 FoS, is below the ultimate tensile strength for hardened steel which lies around 90000-100000 psi [18]. The maximum principal stress, a more appropriate measure for brittle materials like CF, was lower at 54217 psi on the main LG, which was under the ultimate strength for CFRP at 87000 psi [16]. Thus, the landing gear design was considered sufficient.

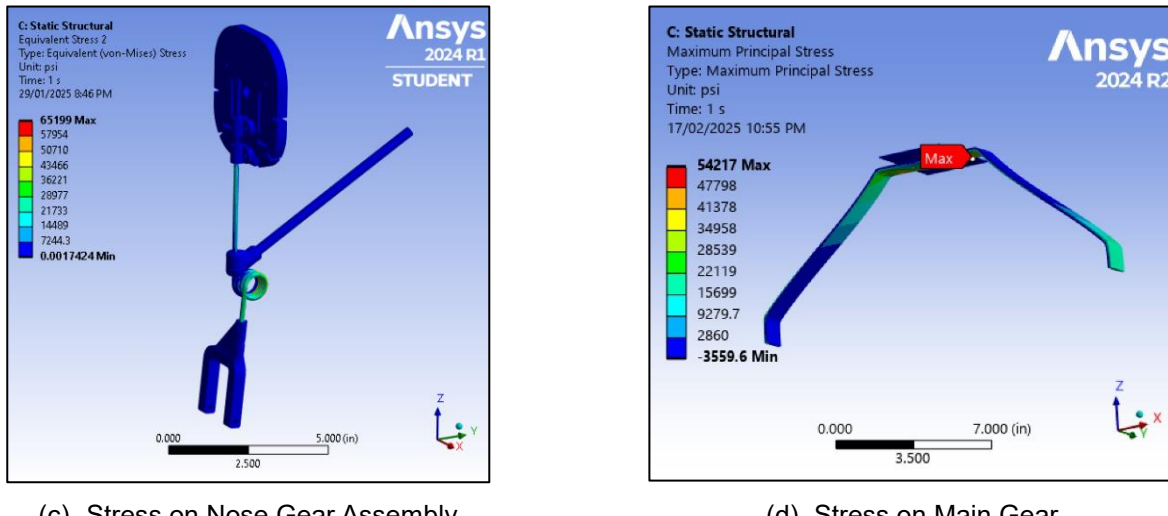


**Figure 5.13 FEA of Landing Gear Assembly**

### 5.3. X-1 Glider

#### 5.3.1. Dimensional Design Parameters

The X-1 was designed to be compact and lightweight ensuring adequate size to facilitate the electronics and ensuring ample moment arms for both static and dynamic stability requirements. Finalised design parameters after testing were shown in Table 5.2 and component placed is visualised in Figure 5.14.

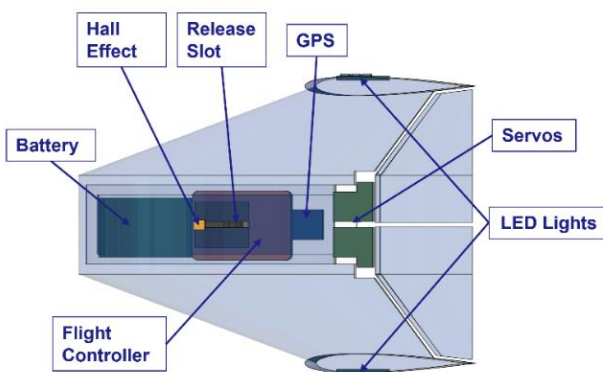


**Table 5.2. Final Design Parameters**

Wing		Vertical Stabiliser
Aerofoil	MH 60	NACA 0012
Span (in)	5.511	2.362
Base Chord (in)	7.874	3.150
Tip chord (in)	3.150	3.150

**Figure 5.14. X-1 Assembly**

#### 5.3.2. Structure

The X-1 structure was made to sustain high impact velocity on the underside of the glider. From Figure 4.8, the expected maximum landing velocity was found to be 99 ft/s, giving a stopping time of one second the expected force exerted on the X-1 when landing was found to be 0.84 lbf using Eq.32. Further, the team found the expected

bending moment experienced on the X-1 due to expected gentle banked turns of 30 degrees, resulting in a bending stress of 2.15 psi, far lower than the yield strength of XPS foam at 14.5 psi [20].

$$F = \frac{mv}{t} \quad (32)$$

To accommodate for the release mechanism interfacing with the X-1 from the main plane, a slot with a pinhole for the pin release mechanism was attached, with the corresponding hall sensor located nearby. A channel was cut out of the lifting body to accommodate the necessary electronics, whilst the LED strips were located on the wingtips for best visibility. These were covered in a hard plastic to prevent damage during landings. The control surfaces rely on direct actuation from the servos, eliminating the need for linkages and hinges.

### 5.3.3. Release Mechanism

The team aimed for a simple and reliable release mechanism which resulted in using the Pin Release method. This mechanism consists of a single servo and linkage. This structure was 3D printed with PLA and can be seen in Figure 5.15. The linkage attached to the servo arm passes through 2 concentric holes bridging a gap between the two. In the open position, the linkage slides backwards, allowing for the X-1 to be attached in between the gap. In the closed position, the linkage will pass through the X-1 attachment point and through the outer hole, thus holding the X-1. When the X-1 is ready to be released, the linkage is pulled from the hole, releasing the X-1. To avoid interference with the landing gear, the mechanism was located at the rear of the fuselage. In accordance with the rules, the mechanism is accessed via a bomb bay door, covering the opening seen in Figure 5.16.

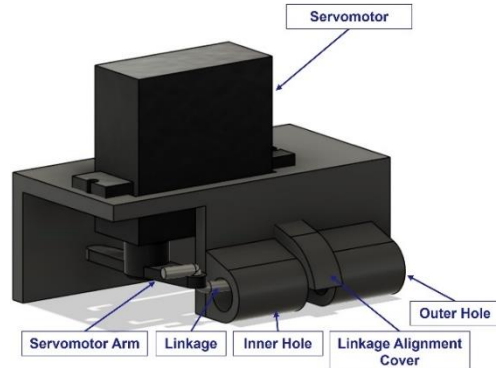


**Figure 5.15. Pin Release Mechanism**



**Figure 5.16. Bomb Bay Hatch (Closed vs Open)**

### 5.3.4. Components, Weights, and Control Mechanism

As the bonus score depends on the mass of the X-1, components and control devices have been stripped down to the bare minimum. Basing the design off modern UAVs, the X-1 incorporates a GPS, IMU (Accelerometer & Gyroscope), compass and servos in-order to achieve controllability during flight. The approach to the control can be described as the Inner and Outer control loops. The Inner (High Frequency Loop) is responsible for the stability and responsiveness to dynamics, working in conjunction with the Outer Loop (Low Frequency Loop) focusing on the mission objectives and waypoint navigation. The table listing each functions and parts required for the X-1 can be seen in Table 5.3 and wiring diagram can be seen in Figure 5.17.

**Table 5.3. X-1 Components**

Outer Loop		Inner Loop	
Components	Role	Components	Role
<b>GPS (M8Q-5883)</b>	Provides real time positional data (Latitude, Longitude, Altitude)	<b>Gyroscope (MPU6000/ ICM20602)</b>	Determine rate of roll, pitch, yaw Monitor X-1 attitude
<b>Barometer (BMP280)</b>	Provides atmospheric pressure 2 <sup>nd</sup> point of estimation for Altitude	<b>Accelerometer (MPU6000/ ICM20602)</b>	Determines acceleration and load factors in 3 main axes
<b>Magnetometer (M8Q-5883)</b>	Determines heading, direction and orientation relative to the Earth's magnetic field	<b>Servos(FS403)</b>	Actuate elevons movements based on status and orientations
<b>Hall Effect Sensor (UGN3503UA)</b>	Detects changing voltage in magnetic fields, works in tandem with a magnet to act as an indicator for Mission Start.		
<b>LEDs (T10 W5W 4041)</b>	Ensure visibility at 400 ft throughout flight.		

The weights of these components are summarised in Table 5.4. We can see that the total weight of all components is approximately 0.212 lbs, which is less than the required weight per Table 4.21.

**Table 5.4. X-1 Mass Table**

Components	Mass (lb)
<b>Controller</b>	0.0463
<b>GPS &amp; Compass</b>	0.0154
<b>IMU</b>	0.0110
<b>Servo (x2)</b>	0.0397
<b>Hall Sensor</b>	0.0044
<b>Barometer</b>	0.0088
<b>LED (x2)</b>	0.0309
<b>Structure</b>	0.0553
<b>TOTAL</b>	<b>0.212</b>

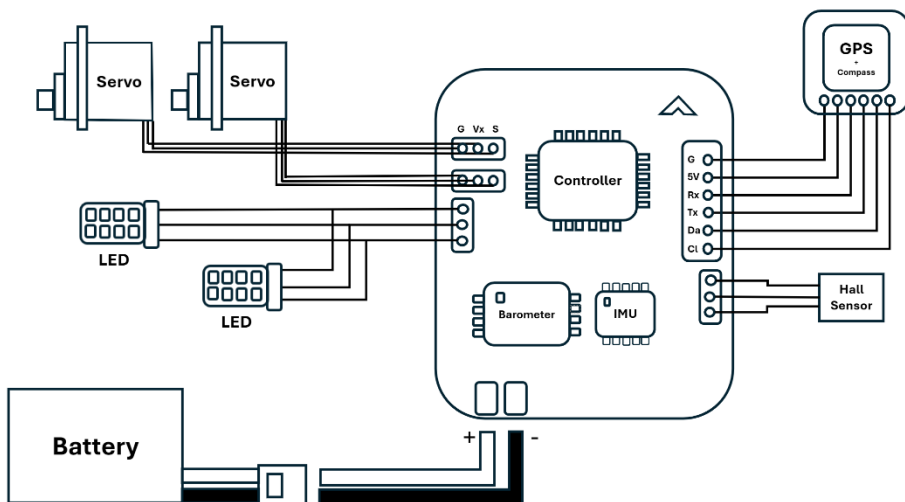


**Figure 5.17. X-1 Controller Diagram**

### 5.3.5. Autonomous Flight

The implementation of autonomous flight on the X-1 utilises ArduPilot to allow for precise control and navigation in an unmanned state. This system utilises a custom-built version of the ArduPilot firmware, enabling LUA scripting for landing trajectories, fly-by-wire capabilities and miscellaneous controls whilst removing unnecessary bloatware such as camera options, proximity checks, telemetry capabilities and RC control. Using a Matek F765, a geofence was erected around the perimeter of the competition's flight path, ensuring no possibility of straying away from M3's bonus

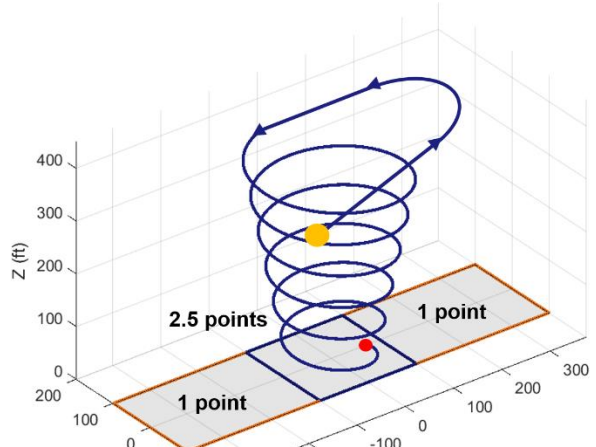


**Figure 5.18 X-1 Planned Descent Path**



box area. A home waypoint is set at the desired Latitude, Longitude and Altitude. The logic is as follows, using the current latitude, longitude and heading which can be determined with respect to true North, a target heading is generated with regards to the target waypoint's position, of which the fly-by-wire system will be responsible for following the new waypoint. This then loops until the altitude reaches 0 ft or the target waypoint has been achieved. This is shown diagrammatically in Figure 5.18. The ideal drop location was determined to be as soon as the main plane passes over the finish line to minimise the necessary distance travelled and minimise X-1 gliding time.

### 5.3.6. LED Selection

To determine the desired power for the LEDs such that it would be visible from 400ft, Eq. 33 was used. For a minimum contrast in visibility, often a lux value of 0.25 is required, resulting in 3716 cd.

$$E = \frac{I}{d^2} \quad (33)$$

$$I = \frac{\Phi}{2\pi \left(1 - \cos\left(\frac{\theta}{2}\right)\right)} \quad (34)$$

Then using Eq. 34 to convert candela to lumens, this gives a desired lumens value of 795.6 lumens when using a commercial narrow beam LED with an angle of 30 degrees. T10 4041 W5W LEDs were chosen for their low wattage of 5W and a lumens output of 800 lumens. For maximum visibility, 2 LEDs will be positioned on the wingtips of the X-1. For the average commercial aircraft, anti-collision strobe lights are often around the range of 40-100 cycles every minute or a range of 0.66-1.66Hz. For enhanced visibility, a strobe rate of 1.5Hz has been used, as this has been proven to be the most effective at capturing attention after various testings.

## 5.4. Avionics and Wiring

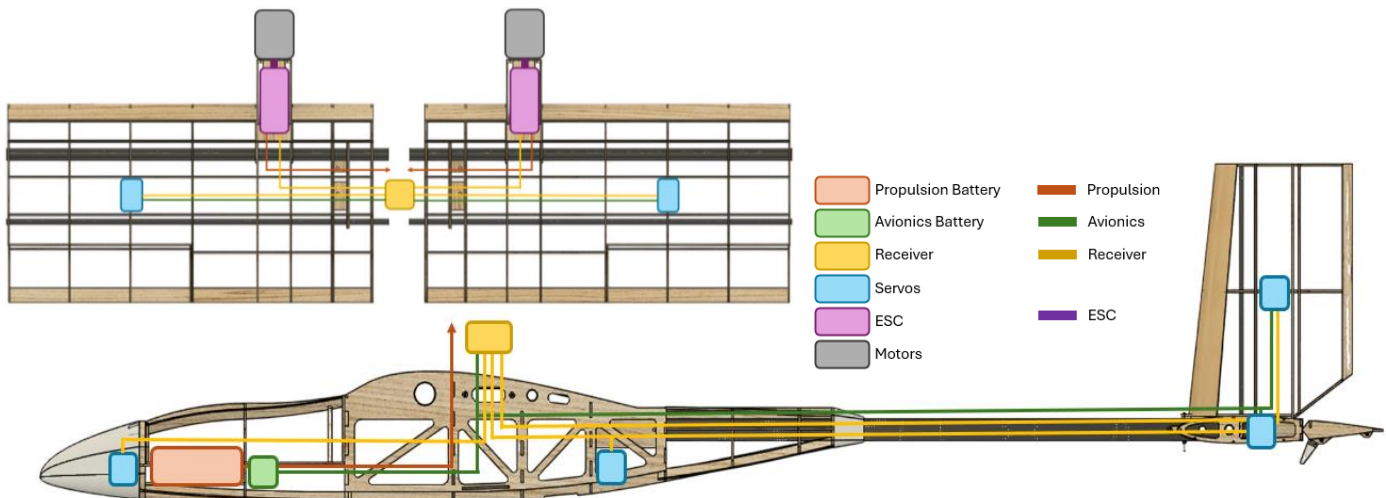


**Figure 5.19. BRICK Wiring Diagram**

Figure 5.19 illustrates the wiring setup for the BRICK's onboard avionics and motors. The UNSW team focused on streamlining the wiring to reduce both weight and complexity, which ultimately enhances repairability. As a result, all components and wiring are kept to the essentials. The system operates with a twin puller configuration, where each Dualsky ECCO5322 motor is connected to a Hobbywing Skywalker 100A ESC, a 100A fuse, and the propulsion battery. A separate 2S Dualsky 1000mAh LiPo Battery powers the avionics, which includes six servos

as referred to in Table 5.1, a Futaba R30008SB receiver, and each motor's ESCs. An inline switch has been integrated to disconnect the receiver from the battery when needed.

Servos were selected based on the necessary torque at the estimated maximum airspeed of 118ft/s across all the missions and required surface area as determined in Section 4.3.7 and Eq. 35 [21]. An empirical formula was used to derive the required torque in oz-in, note all dimensions are for each individual control surface.

$$\text{Torque}_{\text{Req}} = 4.22 \times 10^{-5} \left[ \frac{(MAC)^2 V^2 b \sin(\delta) \tan(\delta)}{\tan(\theta_{\text{Servo}})} \right] \quad (35)$$

**Table 5.5 Servo Torque Requirements**

Control Surface	Servo Model	Required Torque (oz-in)	Servo Torque (oz-in)
Aileron	CRHV-7225-MG	238.2	347.18
Rudder	HITEC 5087MH	45.3	59.71
Elevator	CRHV-7225-MG	267.2	347.18

## 5.5. Weight and Balance

The mass for each of the components listed in Table 5.6 was measured using scales, with certain components being grouped together such as the avionics, tail boom and landing gear being grouped in with the fuselage and the wings being grouped with their mounted motors and control surfaces. The servo motors were also included

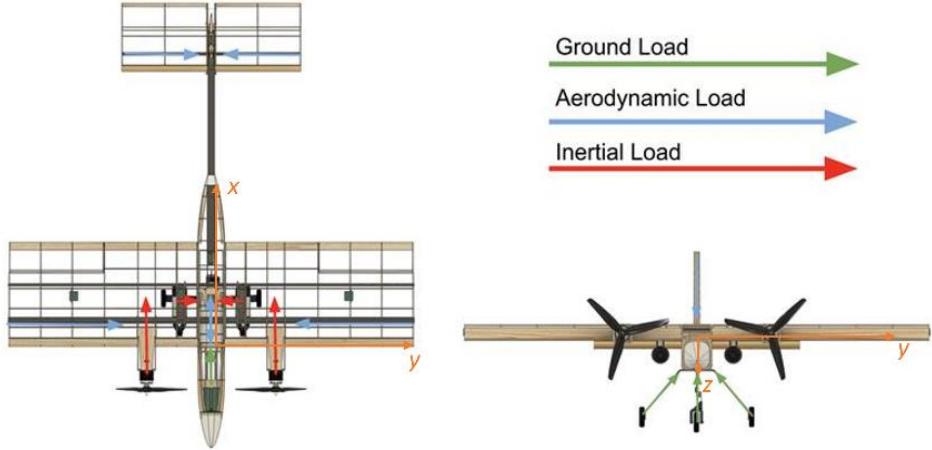


**Figure 5.20 Load Path and Axes Diagram**

with the control surfaces. These components were then balanced to find the CG whose position was then measured relative to the leading edge of the wing according to the axes shown in Figure 5.20 and tabulated in Table 5.6. This was then separated into the following configurations: Empty, Mission 1, Mission 2 and Mission 3, with the total mass for each configuration summed and each CG position calculated as the sum of moments about the leading edge divided by the total weight.

**Table 5.6 Weight and Balance Table**

Component	Mass (lb)	x-position (in)	y-position (in)	z-position (in)
Fuselage	2.31	6.89	0.00	3.74
HT Left	0.44	47.52	8.07	5.59
HT Right	0.44	47.52	-8.07	5.59
Left Prop	0.19	-5.71	9.17	0.00
Right Prop	0.19	-5.71	-9.17	0.00
VT	0.28	47.36	0.00	-7.09
Right Wing (inc. motor)	2.86	1.97	-10.83	-0.20
Left Wing (inc. motor)	2.86	1.97	10.83	-0.20
Right Winglet	0.45	7.20	-32.95	0.00



Left Winglet	0.45	7.20	32.95	0.00
<b>Empty (CG)</b>	<b>10.47</b>	<b>8.28</b>	<b>0.00</b>	<b>1.00</b>
Propulsion Batteries	2.11	-8.07	0.00	4.43
<b>Mission 1 (CG)</b>	<b>12.58</b>	<b>5.53</b>	<b>0.00</b>	<b>1.57</b>
Propulsion Batteries	2.11	-8.07	0.00	4.43
Right External Tank (full)	6.61	3.48	-6.50	4.51
Left External Tank (full)	6.61	3.48	6.50	4.51
X-1	0.12	15.55	0.00	6.71
Internal Fuel Tank	22.96	4.65	0.00	2.80
<b>Mission 2 (CG)</b>	<b>48.89</b>	<b>4.59</b>	<b>0.00</b>	<b>2.95</b>
Propulsion Batteries	2.11	-8.07	0.00	4.43
Right External Tank (Empty)	0.05	3.48	-6.50	4.51
Left External Tank (Empty)	0.05	3.48	6.50	4.51
X-1	0.12	15.55	0.00	6.71
<b>Mission 3 (CG)</b>	<b>12.81</b>	<b>5.61</b>	<b>0.00</b>	<b>1.65</b>

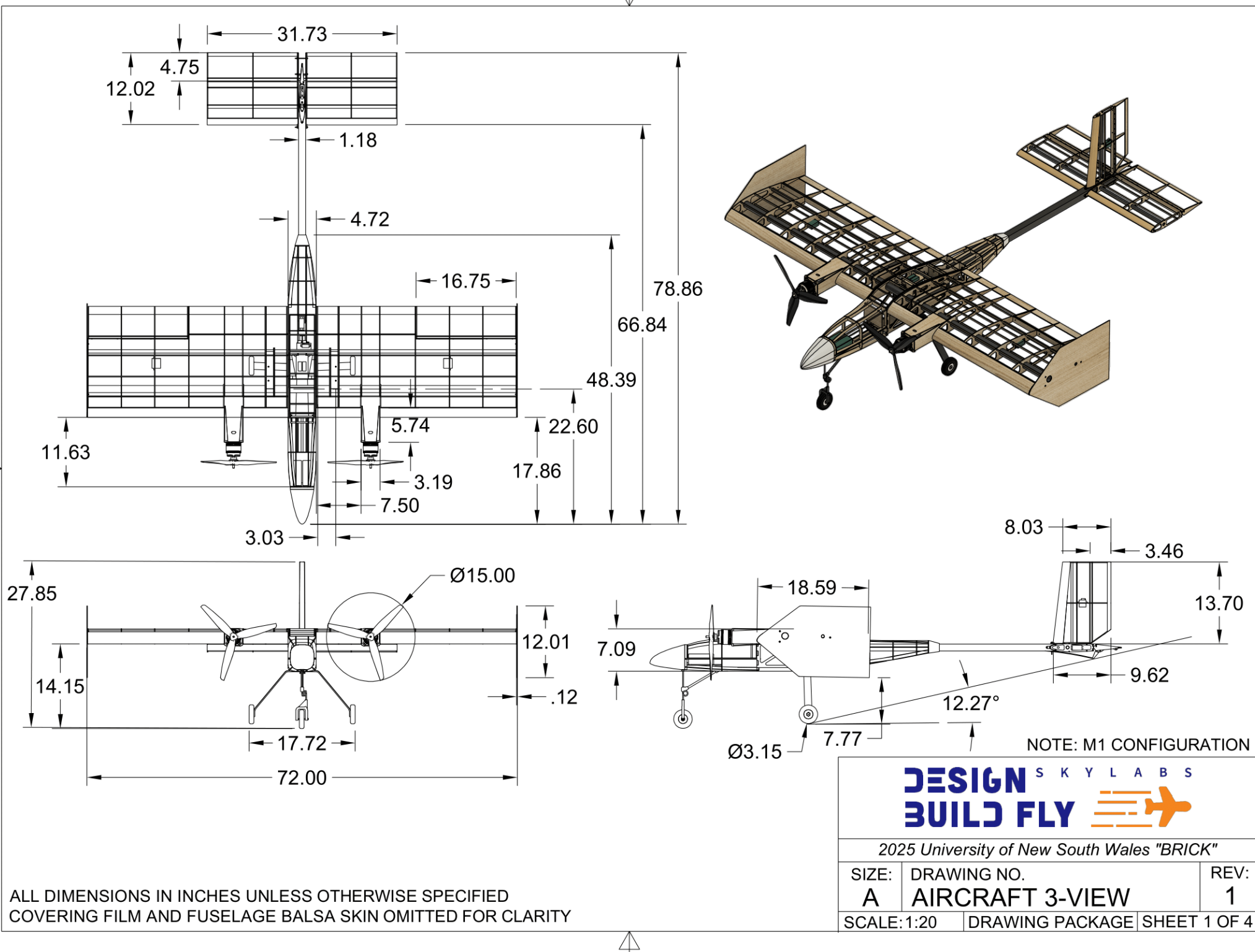
## 5.6. Flight Performance and Mission Specific Performance

Flight performance was determined using the finalised design parameters in Table 5.1 in conjunction with the Mission Model, MotorCalc, eCalc, XFLR5 and AVL. From this the expected aircraft weight, speed and lap time was computed shown in Table 5.7

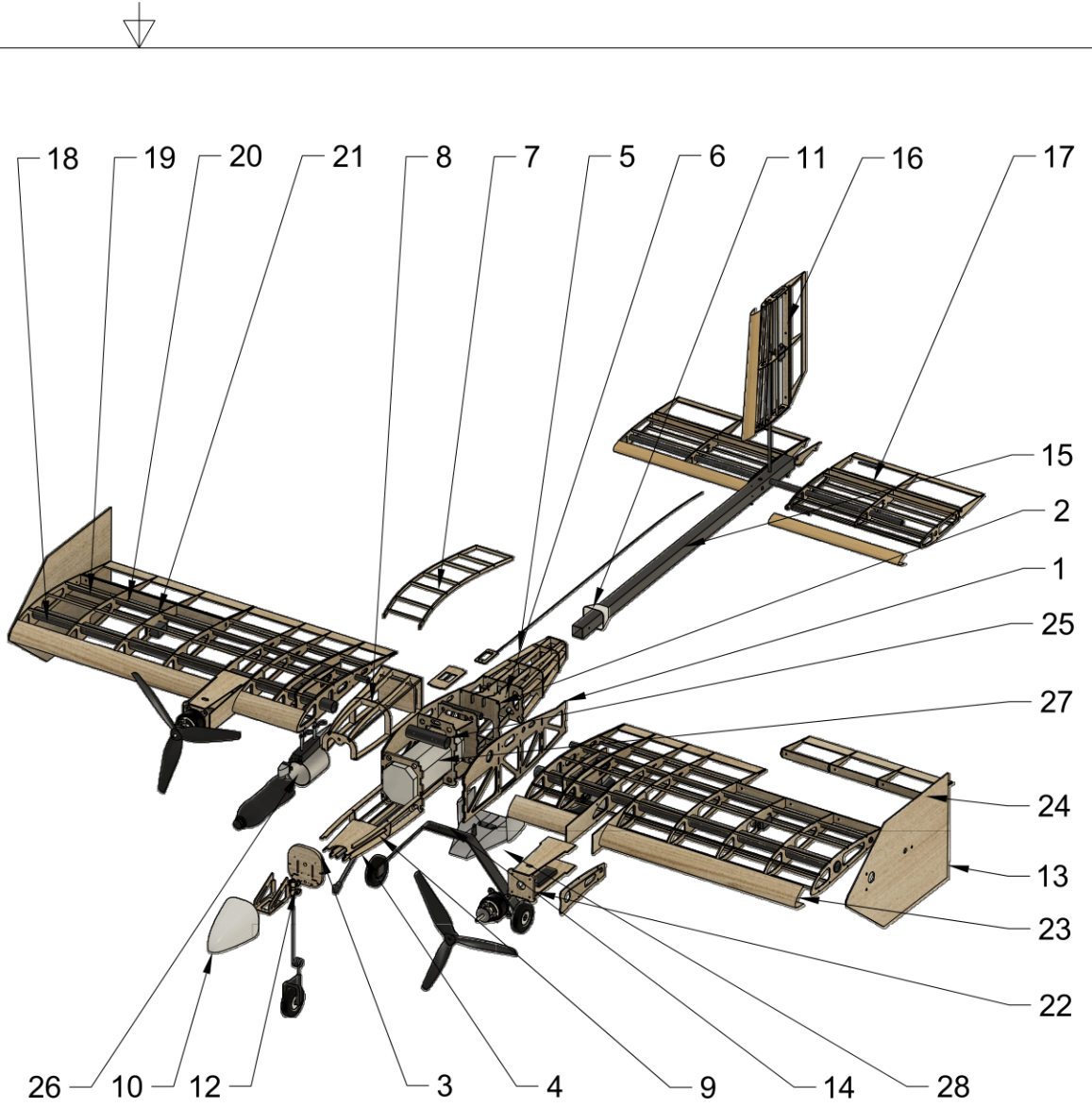
Table 5.7. The BRICKS Finalised Flight Performance

Properties	M1	M2	M3
<b>Payload (lbs)</b>	N/A	35.3	2.2
<b>TOW (lbs)</b>	13.2	48.5	15.4
<b>TOFL (ft)</b>	32.8	202.1	40.0
<b>Average Throttle (%)</b>	60	90	60
<b>Cruise Speed (ft/s)</b>	90.0	101.0	85.0
<b>Maximum Speed (ft/s)</b>	102.9	118.1	94.5
<b>Banked Turn Speed (ft/s)</b>	88.0	92.7	75.5
<b>Battery Usage (%)</b>	40.0	85.0	85.0
<b>Number of Laps</b>	3	3	9 (before X-1 Launch)
<b>Mission Time (sec)</b>	80	118	300

## 5.7. Drawing Package



ITEM NO.	PART NUMBER	DESCRIPTION	QTY
1	Fuselage Wing Box Side Panel	Plywood	2
2	Fuselage Ribs	Plywood	9
3	Fuselage Nose Gear Bulkhead	Plywood	1
4	Fuselage Forward Longerons	Plywood	6
5	Fuselage Rear Longerons	Plywood	10
6	Fuselage Tail Connection	Plywood	1
7	Fuselage Top Hatch	Plywood + Balsa	1
8	Fuselage Front Hatch	Plywood + Balsa	1
9	Fuselage Floor	Plywood	2
10	Nose Cone	PLA	1
11	Tail Cone	PLA	1
12	Nose Gear Assembly	Steel, Rubber, PLA, CF, Plywood	1
13	Winglets	Plywood	2
14	Main Landing Gear Assembly	Plywood, Rubber, CF	1
15	Tail Boom	CF	1
16	Vertical Tail	Balsa, Plywood, CF	1
17	Horizontal Tail	Balsa, Plywood, CF	1
18	Main Wing Spar	CF	2
19	Auxillary Wing Spar	CF	2
20	Wing Stringers	Plywood	20
21	Wing Ribs	Plywood	16
22	Wing Motor Mount	Plywood	2
23	Wing Leading Edge	Balsa	2
24	Wing Aileron	Plywood + Balsa	2
25	Wing Mount Interface/Bolts	CF, Steel	1
26	External Wing Pylon Assembly	Aluminium, PLA, Foam, Steel	2
27	Internal Fuel Tank	Steel Pellets	2
28	X-1	XPA Foam	1

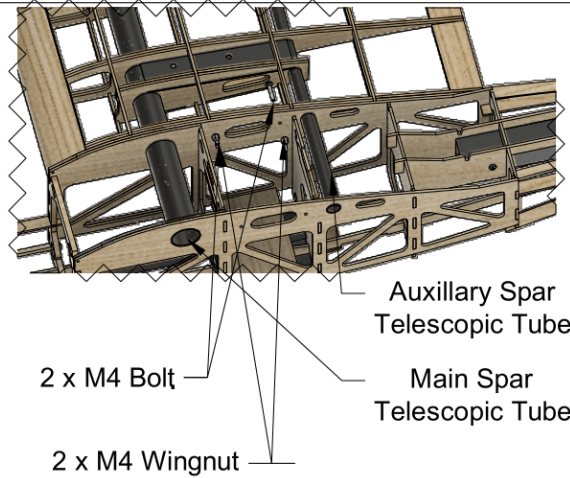


NOTE: M2 CONFIGURATION

**DESIGN SKY LABS**  
**BUILD FLY** 

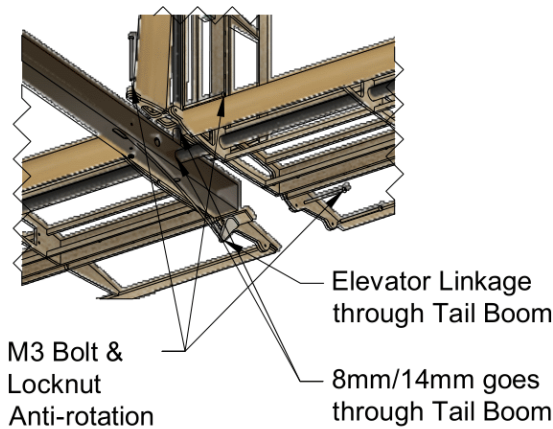
2025 University of New South Wales "BRICK"

SIZE: A	DRAWING NO. STRUCTURAL LAYOUT	REV: 1
SCALE: 1:18		DRAWING PACKAGE
SHEET 2 OF 4		

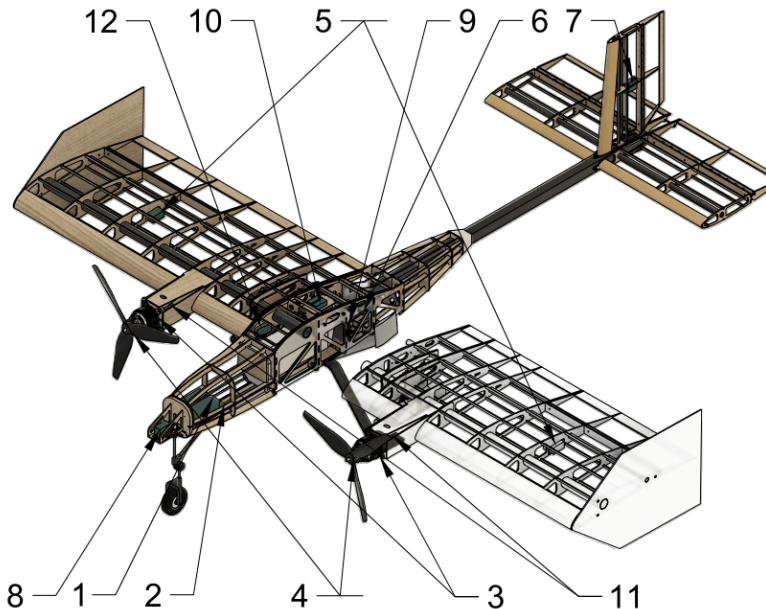
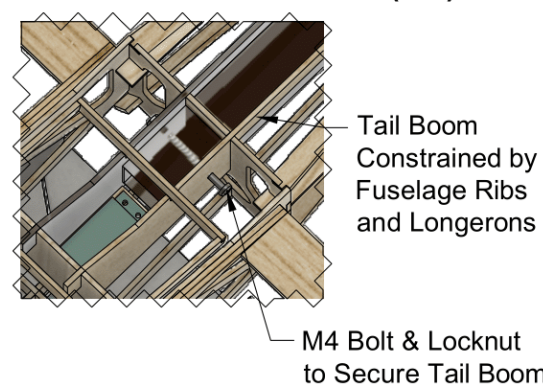


#### WING MOUNT MECHANISM (1:8)

#### TAIL MOUNT MECHANISM (1:8)



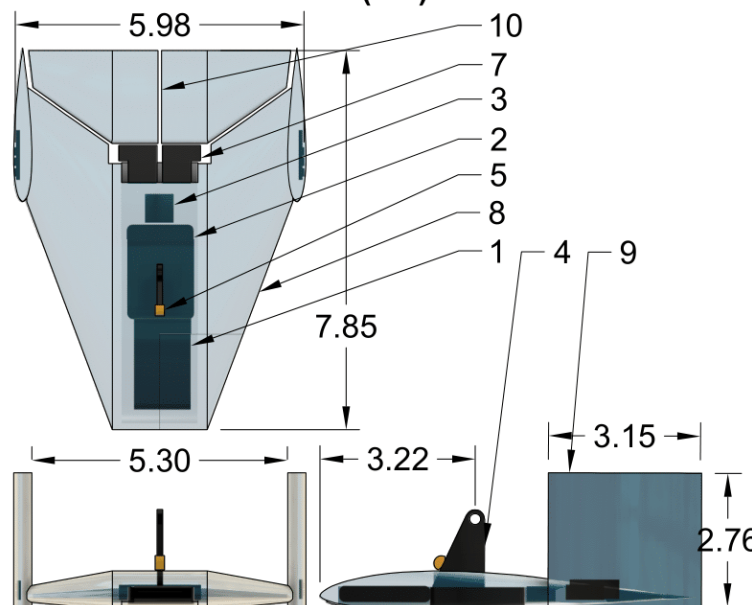
#### TAIL BOOM MOUNTING (1:4)



ITEM NO.	PART NUMBER	DESCRIPTION	QTY
1	Propulsion Battery	Dualsky 2200mAh 50C 6S	2
2	Avionics Battery	Dualsky 1000mAh 25C 2S	1
3	Motor	Dualsky ECCO5322C 430kV	2
4	Propeller	15x14x3 (N/P)	2
5	Aileron Servos	CRHV-7225-MG	2
6	Elevator Servos & Linkage	CRHV-7225-MG	1
7	Rudder Servo	HITEC 5087MH	1
8	Nose Steering Servo	SAVOX S0220MG	1
9	X-1 Release Mechanism	HITEC 5087MH	1
10	Blade Fuse	100A	2
11	ESC	100A Hobbywing Skywalker	2
12	Radio Receiver	R3007SB	1

#### ELECTRONICS & AVIONICS SYSTEMS

#### X-1 CONFIGURATION (1:4)



ALL DIMENSIONS IN INCHES UNLESS OTHERWISE SPECIFIED

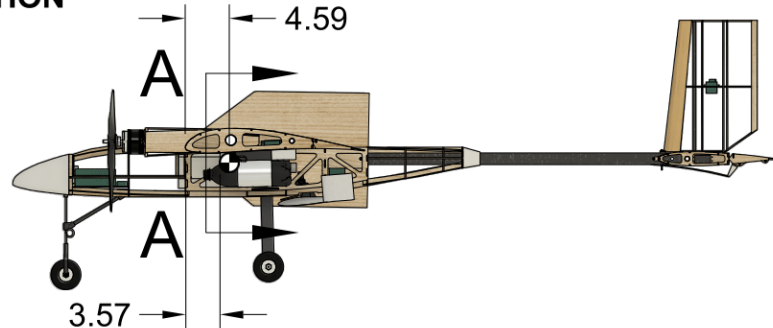
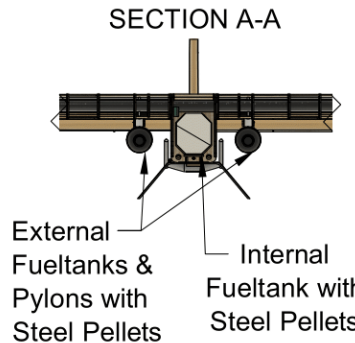
ITEM NO.	PART NUMBER	DESCRIPTION	QTY
1	Battery	Dualsky 400mAh 25C 2S	1
2	Flight Controller	Mateksys F405-Wing	1
3	GPS	Mateksys M8Q-5883	1
4	Release Hook	PLA	1
5	Hall Effect Sensor	-	1
6	LED	T10 4041 W5W	2
7	Elevon Servos	PES GH-37D	2
8	Lifting Body	XPA Foam	1
9	Vertical Stabilisers	XPA Foam	2
10	Elevons	XPA Foam	2

**DESIGN SKY LABS**  
**BUILD FLY**

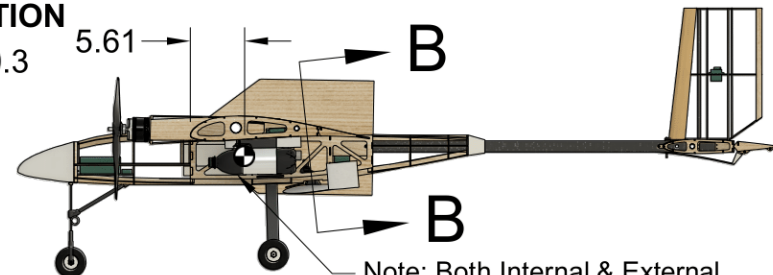
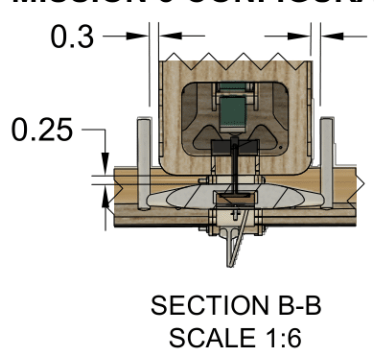
2025 University of New South Wales "BRICK"

SIZE: A	DRAWING NO. SYSTEMS LAYOUT	REV: 1
SCALE: 1:20		DRAWING PACKAGE SHEET 3 OF 4

## MISSION 2 CONFIGURATION

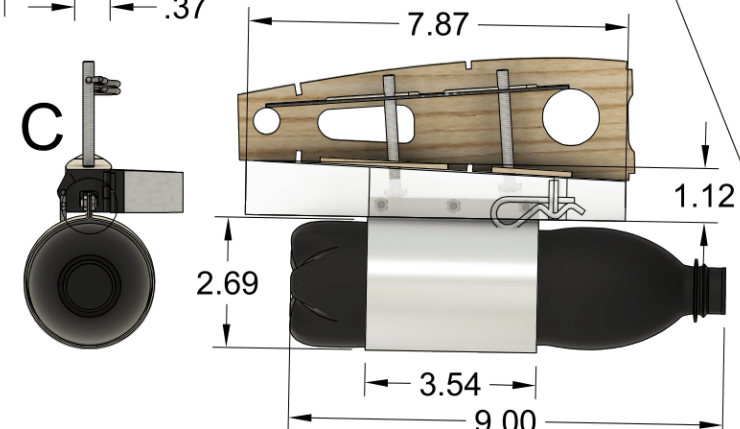
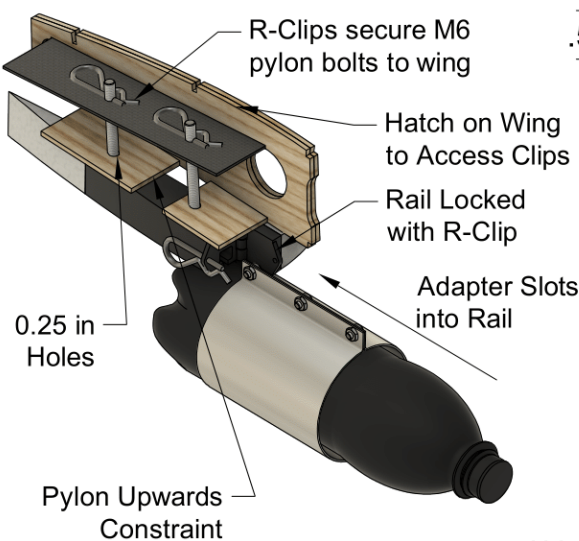


## MISSION 3 CONFIGURATION



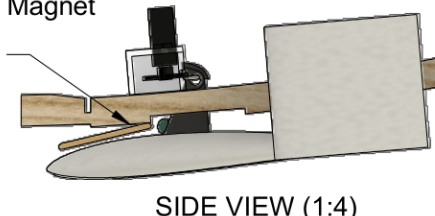
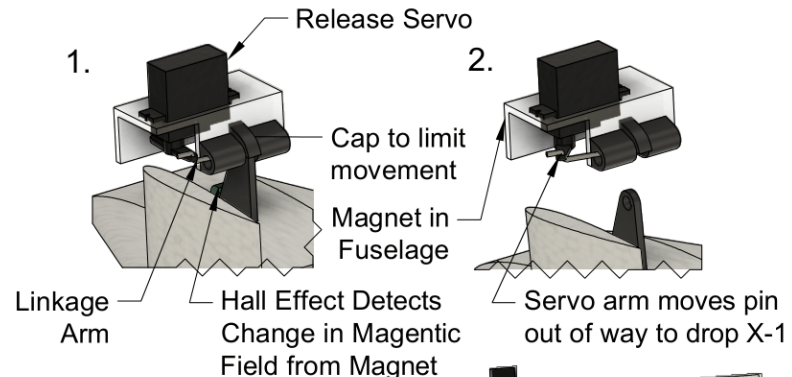
SECTION B-B  
SCALE 1:6

## PYLON MECHANISM (1:4)

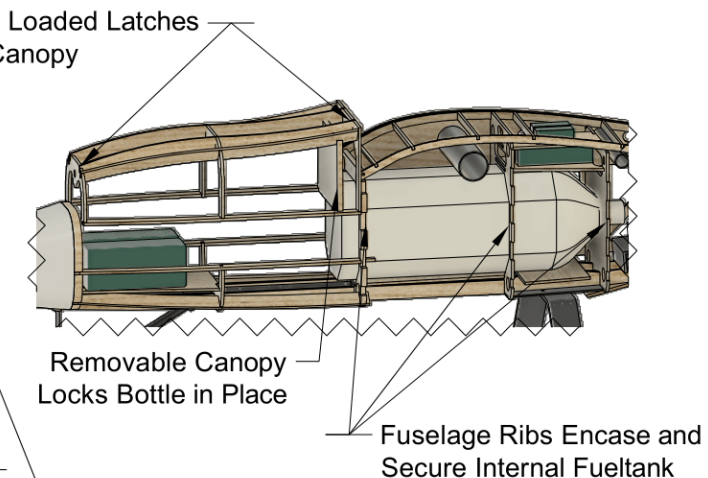


ALL DIMENSIONS IN INCHES UNLESS OTHERWISE SPECIFIED

## X-1 RELEASE MECHANISM (1:3)



## INTERNAL FUEL TANK MECHANISM (1:8)



**DESIGN SKY LABS  
BUILD FLY**

2025 University of New South Wales "BRICK"

SIZE: A	DRAWING NO.	REV: 1
MISSIONS LAYOUT		

SCALE: 1:20 DRAWING PACKAGE SHEET 4 OF 4



## 6. Manufacturing Plan

### 6.1. Investigated Manufacturing Processes

The team first identified various materials and manufacturing techniques to then evaluate the effectiveness and complexity for the skillset the UNSW DBF 2024-2025 team had.

#### 6.1.1. *Laser Cutting*

Laser cutting is a process used commonly on wood and acrylic, involving a laser that heats up the material leaving a through cut. Laser cutting is limited to 3D thin objects however handles complex jobs with high accuracy. Furthermore, laser cutting utilises vector ordering to decrease the time required and thus allowing for a quicker manufacturing time ideal for quick turnaround times on a design. However, warping can occur due to the heat the material experiences.

#### 6.1.2. *Additive Manufacturing*

Additive manufacturing builds from the ground up generally using plastic. With careful consideration of the pattern, additive manufacturing can have substantial strength, with a plethora of design decisions available to the manufacturer to optimise for strength and weight. However, additive manufacturing is a long process dependant on the size and required strength of the part being manufactured.

#### 6.1.3. *Composite Manufacturing*

Composites are used extensively in engineering applications due to their high strength-to-weight ratio. The process of constructing a composite piece can involve moulds and subsequent wet-layups, infusion or pre-impregnated composite fibres that are laid over the mould with a vacuum bag, then heated in an autoclave for maximum strength. This procedure takes considerable time and facilities, limiting the amount of aircraft iterations.

#### 6.1.4. *Heated Monokote Cover Film*

Monokote cover film is a clear and flexible plastic film when heated the material shrinks allowing for ease of moulding to complex objects. Used to wrap around aircraft parts to provide a smooth layer to limit flow separation. However, due to the materials thin nature it is prone to punctures, additionally due to the material shrinking it can cause buckling of other thin lightweight materials.

#### 6.1.5. *CNC Milling*

CNC Milling is a subtractive manufacturing technique, involving the use of a programmable high-powered machine to drill away at a bulk of material. CNC Milling can be up to 6 degrees of freedom and results in accurate 3D shaped geometry down to the smallest drill bit used. However, due to the use of a drill bit, sharp corners are not achievable, and due to subtractive manufacturing, the parts have a long lead time.

#### 6.1.6. *XPS Foam Wire Cutting*

Wire cutting XPS foam is a subtractive manufacturing technique which involves using hot wire cutters to carve out an object from a foam block. XPS foam is useful for constructing moulds of complex geometry and is an efficient manufacturing technique however has subpar geometric precision.



### 6.1.7. *Balsa Skinning*

Balsa skinning involves dampening the thin balsa wood and moulding it to the desired geometry, upon drying the wood the balsa becomes rigid in place and maintains the moulded geometry. Balsa skinning allows for curved geometry to be covered increasing shear strength and aerodynamic efficiency of the aircraft, however complex corners are difficult to skin and result in segmenting often causing additional drag and long lead times.

## 6.2. Material Selection

The selection process for materials and manufacturing techniques are based on weighted analysis. Each part was assessed to find the ideal material and manufacturing process to maximise the following criteria shown in Table 6.1 and Table 6.2.

**Table 6.1. Manufacturing Selection Process**

Characteristics	Weight	Materials						
		Laser Cut	3D Print	Composites	Monokote Skin	CNC	Foam	Balsa
Weight	5	3	3	3	5	3	4	4
Durability	5	3	4	5	2	4	2	3
Time	4	5	3	2	4	2	4	4
Simplicity	3	4	3	2	5	3	5	3
Experience	3	5	4	1	4	2	3	4
Cost	2	4	3	1	3	2	5	5
Total		85	74	59	84	62	80	82

Weight is deemed most important, followed by durability. Manufacturing turnaround time was next, followed by ease of manufacturing, the team's familiarity with the manufacturing method and finally cost.

**Table 6.2. Manufacturing Processes Selected for Various Parts**

Component	Material	Technique
Fuselage		
Wing	Plywood	Laser Cutting
Empennage		
Spars & Tail Boom	Carbon Fibre	Purchased (COTS)
Skin	Balsa, Monokote Film	Hot Iron, Balsa Moulding
Landing Gear	Carbon Fibre	Purchased (COTS)
Pylons	Tough PLA	3D Printing
X-1	XPS Foam	Foam Cutting

### 6.2.1. *Fuselage, Landing Gear and X-1 Launch Mechanism*

The fuselage was constructed using a combination of plywood, epoxy and balsa skinning. The longerons and frames were constructed using 1/8" plywood, laser cut into the required geometry, the critical location for shear stress on the fuselage being the side panel connecting the wing was double stacked resulting in 1/4 in plywood with epoxy used as a sandwich for double shear. Each longeron and frame was initially super glued to hold shape and then epoxy was used to bond the pieces together. Balsa skin used over the longerons to build the cylindrical shape for ease of applying the heated Monokote film for a streamlined finish. Further, the main landing gear was a CF COTS, attached to the fuselage



**Figure 6.1. Fuselage Manufacturing**



via a carbon fibre woven 1/16 in plate to sustain the landing impact at 48.5 lbs. While the front landing gear was also COTS made from steel with a CF rod acting as a strut, allowing for another connection point to the fuselage to distribute the load.

### 6.2.2. Wing



**Figure 6.2. Wing Ribs and Spars Attachment**

The wing was constructed from plywood, epoxy, balsa and COTS CF woven rods. Ribs and stringers were laser cut out of 1/8 in plywood, epoxy was used to bond the ribs and stringers together. Three different spars were used, the main spar was located at the quarter chord, to support the lift force, an aft spar, and a back spar. The main and aft spars were made from carbon fibre woven rods with 19/16 in and 35/64 in diameter respectively, used to resist the bending load. Further, a TE plywood spar was used to prevent local buckling induced by the heated Monokote film applied around the upper and lower surface of the wing. Balsa skinning was applied at the LE of the wing to maintain the aerodynamic profile and prevent the LE caving as compared to just Monokote film. The aileron ribs and stringers were constructed from plywood, while the LE was made from sanded down balsa blocks for a smooth profile when applying the heated Monokote film.

### 6.2.3. Tail

The vertical and horizontal tail were constructed using plywood, epoxy, COTS CF woven rods and heated Monokote film. The ribs and stringers were constructed using laser cut 1/8 in plywood and bonded together using epoxy, while the main spar was made from 35/64" CF rod for the horizontal tail and 20/64 in for the vertical tail. Both tails were covered in heated Monokote film to maintain an aerodynamic surface finish. The control surfaces were made using 1/8 in laser cut plywood and epoxy and then heated Monokote solar film was applied on the upper and lower surface.



**Figure 6.3. Completed HT and VT with Monokote Film**

### **6.2.4. X-1**

XPS foam was used for the X-1 as minimising weight was the main priority. Laser cut stencils of the body and wingtip rudders were placed onto XPS foam where hot wire cutters moulded the foam into the required geometry as seen in Figure 6.4. This allowed for rapid manufacturing and quick turnaround. Epoxy was used to attach the elevons as well as H-tail to the wing.



## Figure 6.4. X-1 Stencils

### **6.3. Manufacturing Timeline**

The manufacturing timeline for the competition is shown in Figure 6.5. Previous prototypes were constructed with a planned timeline of roughly 5 weeks, however unforeseen delays discussed in Section 2.2 delayed the V1 prototype timeline. Whilst the final competition aircraft had been given an extended period of 10 weeks with 5 weeks to repair and improve the design, this has been shortened to 6 weeks. This, however, should still give ample time to manufacture the final plane whilst ensuring all components are made to outstanding quality.

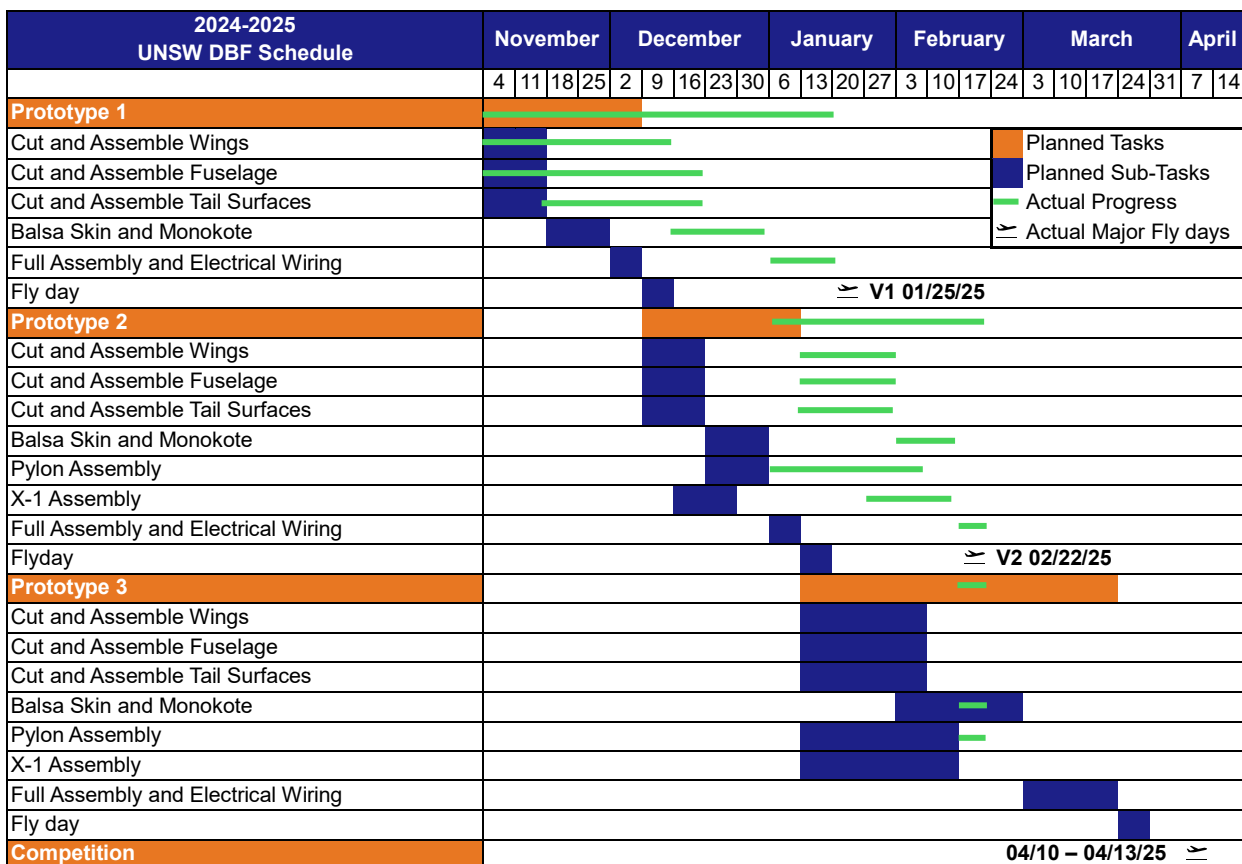


## Figure 6.5 Manufacturing Schedule

## 7. Testing Plan

### **7.1. Testing Schedule**

The schedule for testing the various sub-system components and aerodynamic performance of the aircraft is outlined in Figure 7.1. The objectives and results of this testing are outlined in Section 7.2 and Section 8.

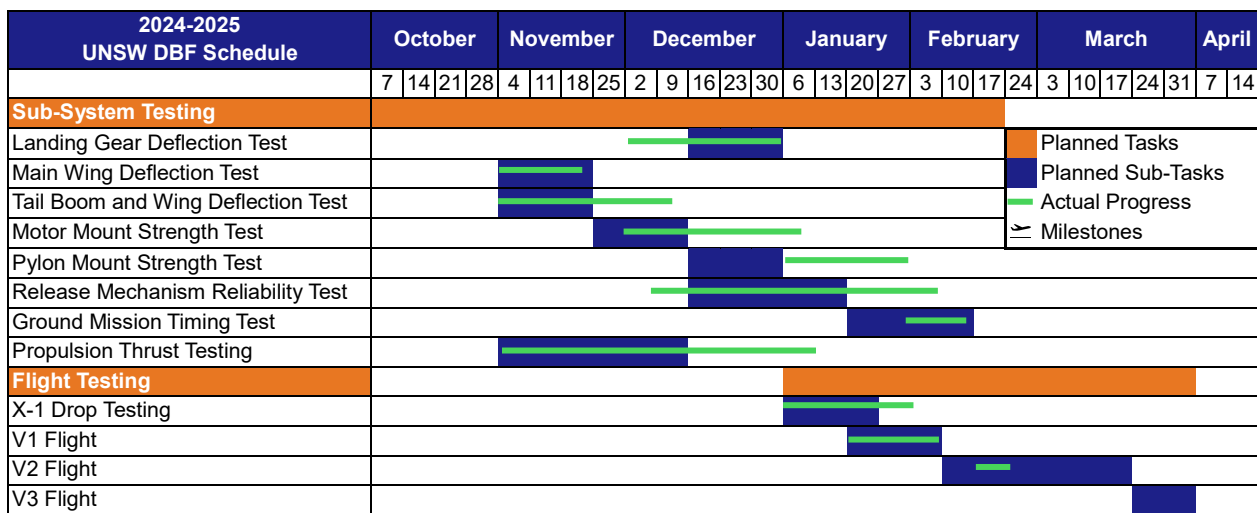


Figure 7.1 Testing Schedule

## 7.2. Testing Objectives

The objectives for each test are outlined in Table 7.1.

Table 7.1 Testing Objectives

Testing Category	Objectives
<b>Aerodynamics</b>	
Flight Test	Confirm XFLR5 and AVL predictions for lift, drag and stability characteristics
	Receive pilot feedback on performance and manoeuvrability characteristics
<b>Propulsion</b>	
Battery Testing	Determine battery aging, charging capabilities and discharge characteristics
Thrust Test	Compare theoretical thrust, torque and propeller wash against real world performance
<b>Performance</b>	
Flight Test	Validate calculated performance parameters such as ground roll, cruise speed, average lap times, and endurance
<b>Structures</b>	
Bending Test	Determine if spars and tail booms are of sufficient stiffness and strength to sustain desired load
Thrust Test	Determine if motor mounts are of sufficient strength to endure thrust, torque and shear force applied at full throttle.
Drop Test	Confirm that fuselage is capable of withstanding energy transferred from landing gears on worse case scenarios while at MTOW.
<b>Payload &amp; X-1</b>	
Pylons Test	Determine if pylons are capable of withstanding 2.5 times the maximum load factor.
Release Test	Confirm if mechanism performs reliably and is capable of withstanding 1.2 times expected flight speeds.
Ground Mission Test	To refine Ground Mission routine and minimise Ground Mission runtime.
<b>Landing Gear</b>	
Drop Test	Determine if landing gears are capable of elastically withstanding MTOW landing loads.
Taxi Test	Confirm that the front landing is of sufficient stiffness and strength to withstand maximum MTOW taxiing conditions.



## 7.3. Sub-system Testing

### 7.3.1. Landing Gear and Bulkhead

The team identified the landing gear a crucial point of failure due to the significant MTOW of the BRICK. To ensure the front landing gear was able to sustain the bending load while taxing the team designed the BRICK V1 and taxied it around the UNSW campus with string attached to the aircraft to push it through terrain including grass and road potholes with MTOW of 48.5lbs installed. The team assessed the deflection afterwards and found plastic deformation



**Figure 7.2. Front Landing Gear V1**

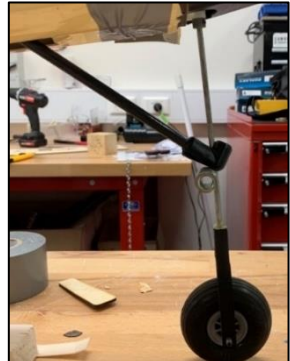


**Figure 7.3. Front Landing Gear V2**

present in the steel front landing gear shown in Figure 7.2. Hence, to prevent excessive deformation from bending the team constructed a strut connecting the front landing gear to the fuselage via a 3D print shown in Figure 7.3 again this was tested and prevented plastic deformation and substantially reduced the deformation while taxing.

### 7.3.2. Main Wing Spar Deflection and Tail Boom

The main wing spar was tested using a cantilever beam deflection equation derived from first principles based on a singular point load applied at the free end - the testing is depicted in Figure 7.4. - this resulted in the max deflection at the free end of the beam given by Eq. 35.

$$\delta_{max} = \frac{PL^3}{3EI} \quad (36)$$

The team found the elastic modulus by applying a point load equivalent to 44 lbs which resulted in a deflection measured to be 2.17 in, paired with calculating the length of the beam and the second moment of area. The elastic modulus was found to be 5,323 ksi. The team then used this value to further iterate on the design for V2, to find the maximum deflection which would be experienced by the aircraft during flight to ensure the main spar would not experience plastic deformation.



**Figure 7.4. Main Wing Carbon Fibre Spar Testing**

The team also identified the tail boom as a significant failure point both structurally and aerodynamically. Excessive deflection would cause the horizontal tail to have an unwanted positive incidence causing the aircraft to naturally pitch down during flight, with an MTOW of 48.5lbs this could cause significant stability problems. To mitigate this the team identified first the elastic modulus of the square CF rod which resulted in 13,256 ksi from the testing rig shown in Figure 7.4. Hence, the team identified a maximum



**Figure 7.5. Tail Boom Testing Rig**



acceptable deflection of 0.2 in which would require the rod to sustain 66,282 psi in the longitudinal direction, which was deemed far below the expected load from the HT and VT combined during flight.

### **7.3.3. Motor Mount**

The motor mount was tested to ensure the mount could sustain the torque, compression and shear force when at full throttle. The team built a test V1 prototype and fastened the motor on, the motor was then applied at full throttle for one minute, the team then turned off the motor and safely inspected the mount to ensure there was no immediate damage. Further, the team wanted to ensure the motor mount could sustain multiple test flights, so the team fatigue tested the motor by applying one-minute increments at full throttle fifteen times. The motor mount survived this static and dynamic testing and provided the team with confidence the motor mount would survive multiple test flights and competition flights in Tucson, AZ.

### **7.3.4. Fuselage Drop Impact**

The aircraft's landing speed was assumed to be the same as the take-off speed, due to the high stall speed in M2, the aircraft would need to land at a speed of roughly 72 ft/s. Due to the high landing speed, the aircraft would experience an abrupt landing applying a significant amount of compressive force onto the main and front landing gear. The team identified this in the detailed design when constructing the CAD. However, to ensure the structure was rigid enough, the team conducted stress tests by dropping the aircraft from 11.8 in with the expected loading. This simulated a 7.8 ft/s descent rate when landing which is considered a hard landing. The aircraft was then dropped and recorded to determine the deflection and is shown in Figure 7.6.. This deflection was found to be 2.47 in compared to the simulated 1.57 in. As such, a thicker landing gear frame was deemed necessary for V2/3.



**Figure 7.6. Fuselage Drop Test  
Loaded to MTOW weight**

### **7.3.5. Fuel Tank Pylon Mount**

Fuel tank mounts were paramount to the success of the BRICK for this competition, hence ensuring their durability was key. For this the team identified in Section 5.2.4, the maximum load factor experienced would be 2.5. Hence, the team applied 2.5 times the expected weight of 6.61 lbs to the fuel tank and ensured the pylon mount could sustain this load. This simulated the maximum loading scenario of the pylon mount ensuring it was rigid for competition. There were no signs of structural damage after this test, and thus the design was validated.

### **7.3.6. X-1 Release Mechanism, Stability, Landing Location and External Light**

X-1 testing had two stages, including ground and mid-flight. Once the ground test was passed with ample success the team then tested it during flight to simulate more accurate conditions. For the release mechanism and external lights, the off-air test consisted of repeated attachment and detachment, timing attachment and release time separately. This was repeated 30 times with a final success rate of 96.6%. After the off-air test was deemed a success, the mid-flight test can be conducted, testing at 118 ft/s (1.2 times Expected Drop Velocity) simulating



worst-case scenario. This highlights any instabilities or points of failures that could result in a premature detachment whilst attached and flying at top speed.

The X-1 stability was first tested from height with zero initial velocity, once after 10 attempts both criteria were met without failure the team deemed the system to be suitable. The team then conducted the mid-flight test in which the X-1 was dropped from 1.2 times the expected airspeed during the competition to ensure the aircraft was again stable and landed in the correct location. Once this test was completed successfully, 5 times in a row the team deemed this as a successful prototype.

### **7.3.7. *Ground Mission Timing Test***

The ground mission timing test consisted of testing and timing the loading and installation of each of the ground mission components to identify troublesome areas of the GM and optimise for future improvement. The V2 aircraft was used as the test bench, and each stage of the ground mission was timed and repeated several times to derive an average for each stage of the GM. These consist of the pylon installation stage, requiring the opening of the wing hatch, sliding of the pylon through the wing, and securement with the R-clips. Then for the next stage, all the fuel tanks were installed and secured, as well as the X-1. Additionally, the reliability of the X-1 drop was also examined under time pressure. Additionally, the need for the staging blocks was assessed in these tests. The results for this test are shown in Section 8.1.4.

### **7.3.8. *Propulsion Thrust Test***

Thrust tests were conducted to validate and confirm the thrust and power consumption of the propulsion systems.

Tests were conducted on the 15x14x3 Propeller from MasterAirscrew and the APC 16x10E Propeller, using the chosen Dualsky ECCO5322C 430kv motor, powered by a 2200mAh 6S battery. The thrust jig in Figure 7.7 Thrust Jig Setup was built using a 44.09 lb strain gauge loadcell and a HX711 Load-cell amplifier, connected to an Arduino Uno to record thrust values using the Arduino Serial Monitor. The Arduino was also used to control the motors speed, starting at 0%, increasing every 5 seconds in 25% intervals until 100% throttle is reached, reverting to 0% after another 5 seconds. A 5 second gap is provided to ensure the thrust stabilises at a constant value. The thrust jig is clamped to a desk to ensure accurate results, to prevent the thrust force being applied to the entire thrust jig instead of just the strain gauge, as is intended. The thrust jig was calibrated before collecting data, using a known weight. Additionally, the power usage was estimated by observing the rate of change of the battery capacity at various throttle settings.



**Figure 7.7 Thrust Jig Setup**

### **7.3.9. *Aerodynamic Testing***

Due to technical restrictions and administration, the team were not able to access the wind tunnel to conduct aerodynamic testing on various components. As a result, flight tests were the only reasonable method of collecting aerodynamic data, and the team put heavy emphasis on collecting as much data as possible from these tests to infer the aerodynamic properties of the plane.



## 7.4. Flight Tests

Several flight tests simulating various aspects of the missions were conducted to analyse and validate the actual performance of the BRICK. The telemetry package consisting of an IMU, GPS, Airspeed Sensor and Barometer was utilised to measure the performance during each flight. The scheduling and objectives for these tests are outlined in Table 7.2, and the results of these are noted in Section 8.1.1.

**Table 7.2 Flight Test Schedule and Objectives**

Date	Location	Aircraft	Objectives
December 23-28 <sup>th</sup> 2024	HMAS, Vineyard, NSW, Australia	V1	Test Stability and Propulsion Characteristics Test Aerodynamic Handling and Performance Test General Structural Performance Trim Aircraft
January 13-18 <sup>th</sup> 2024		V2	Test Mission Fuel Tank Payloads and Weight Test X-1 Deployment and Guidance Simulate and Validate Performance in M1, M2 and M3
February 15-22 <sup>th</sup> 2024		V3.1	Validate M1, M2 and M3 Performance in Final Configuration
March 22-29 <sup>th</sup> 2024		V3.2	Test Competition Performance of Plane

## 7.5. Flight Checklist

The UNSW team utilised the following checklists to ensure safety and correct documentation of flight data are met before all tests.

**Table 7.3. Flight Checklist**

Ground Inspection		Flight Inspection																											
Assembly		Pre-Flight																											
Visual Inspection	<input type="checkbox"/>	Date, Time, Location	<input type="checkbox"/>																										
Wing & Tail Connection	<input type="checkbox"/>	Wind Speed	<input type="checkbox"/>																										
Control Surfaces	<input type="checkbox"/>	DAQ System	<input type="checkbox"/>																										
3D Printed Cover	<input type="checkbox"/>	Wing Tip Test	<input type="checkbox"/>																										
Payload Attachment	<input type="checkbox"/>	Centre of Gravity	<input type="checkbox"/>																										
Avionics		Propeller Rotation																											
Linkages	<input type="checkbox"/>	Fuse In	<input type="checkbox"/>																										
ESCs	<input type="checkbox"/>	Propulsion & Avionics Battery	<input type="checkbox"/>																										
Receivers	<input type="checkbox"/>	Post-Flight																											
DAQ System	<input type="checkbox"/>	Avionics Battery	<input type="checkbox"/>	Fuse Out	<input type="checkbox"/>	Failsafe	<input type="checkbox"/>	Propulsion Battery Level	<input type="checkbox"/>	Propulsion		Avionics Battery Level	<input type="checkbox"/>	Motors	<input type="checkbox"/>	DAQ System	<input type="checkbox"/>	Propellers	<input type="checkbox"/>	Visual Inspection	<input type="checkbox"/>	Ground Clearance	<input type="checkbox"/>			Propulsion Battery	<input type="checkbox"/>		
Avionics Battery	<input type="checkbox"/>	Fuse Out	<input type="checkbox"/>																										
Failsafe	<input type="checkbox"/>	Propulsion Battery Level	<input type="checkbox"/>																										
Propulsion		Avionics Battery Level	<input type="checkbox"/>																										
Motors	<input type="checkbox"/>	DAQ System	<input type="checkbox"/>																										
Propellers	<input type="checkbox"/>	Visual Inspection	<input type="checkbox"/>																										
Ground Clearance	<input type="checkbox"/>																												
Propulsion Battery	<input type="checkbox"/>																												



## 8. Performance Results

### 8.1. Subsystem Performance

Each main subsystem performance required for the DBF 2025 competition was tested using various equipment to further iterate the design and is mentioned below.

#### 8.1.1. Main Aircraft Aerodynamics

For each flight iteration the team utilised an accelerometer to obtain flight data. Main interest was in the airspeed on the straight, 180 degrees turn and the 360-degree loop. Paired with this was the load factor experienced during the turn and loop to ascertain the turn radius of the aircraft. Furthermore, airspeed during take-off was measured also to calculate the time taken for the aircraft to reach required take-off velocity to then recalculate the take-off distance accounting for the transient phase of starting up the propellers. All data is then shown in Table 8.1 and Table 8.2 for each plane iteration and the different flight segments, further values highlighted in green meet the requirements set out in the preliminary design and red fail to meet the requirements. The team's expected cruise speed of 118 ft/s was achieved.

#### 8.1.2. Propulsion

The results of the propulsion thrust tests are shown in the Figure 8.1 and Figure 8.2. As can be seen in Figure 8.1, the 16x10E produced less maximum thrust than the eCalc prediction, maxing out at 6.0kg of thrust. The 15x14x3 Master Airscrew produced less static thrust at 5.7kg, but it should be noted that it was likely due to the propeller being stalled which was observed through the change in the audible pitch of the propeller. Whilst undesirable for take-off, theoretical predictions from eCalc predicted higher dynamic thrust with the 15x14x3 and given the close correlation in the static thrust tests, the 15x14x3 was validated as the ideal propeller of choice.

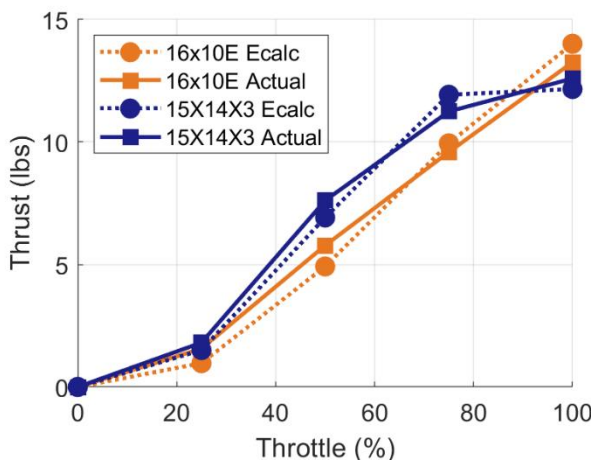
Power consumption shown in Figure 8.2 correlated well with eCalc estimations, only slightly above the predicted power consumption. However, the behaviour of the power consumption vs dynamic thrust was unable to be inferred directly, and so this particular aspect of the plane will be monitored in the flight tests. Following these test, refinements were made to the mission model to improve the accuracy of the simulations.

Table 8.1. BRICK Airspeed Data M1/2/3

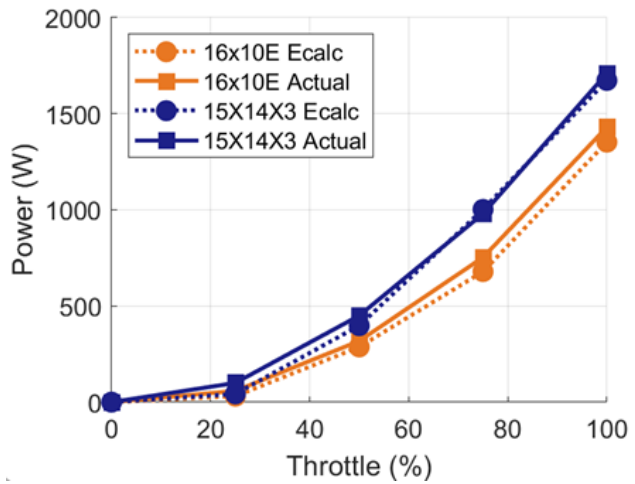
Flight Segment	Airspeed [M1/2/3] (ft/s)	
	BRICK V1	BRICK V2
Take-Off	75/83/76	75/83/76
Straight Cruise	91/112/91	98/119/98
180-Degree Turn	90/92/90	90/100/90
360-Degree Turn	88/92/89	88/101/89

Table 8.2. BRICK Bank Angle and Ground Roll Distance Data M1/2/3

Aircraft Iteration	BRICK V1	BRICK V2
Bank Angle for M2 (Deg)	59.1	61.3
Ground Roll Distance for M2 (ft)	213	205



**Figure 8.1 Static Thrust vs Throttle**



**Figure 8.2 Power vs Throttle**

### 8.1.3. X-1 Descent Time and Landing Location

X-1 descent time and landing location was critical for the M3 score and as such the team continuously iterated on the design by using data from each previous version. Given sub-system requirements §XR-PF-02 and §XR-PF-04, the X-1 testing involved gathering altitude data at a high sampling frequency to analyse how the glider was descending at each time interval. This allowed the team to further iterate on the glide angle to ensure the 20 second descent time was reached, a stable pattern was maintained and the X-1 landed in the 200ft box, this data for each iteration is shown in Table 8.3.

### 8.1.4. Ground Mission

The Ground Mission this year relied on speed, accuracy and ease of assembly. The Ground Mission team designed the fuel tank mounts to ensure they were rigid and quick to use paired with the X-1 release mechanism, the team then calculated the time taken for each segment of the GM and the average data is shown in Table 8.4 for each iteration. Additionally, it was found there was no significant change in the time when using the staging blocks. Thus, to help with transportation logistics, the team opted out of the staging blocks for the GM.

**Table 8.3. X-1 Descent Time Testing**

Aircraft Iteration	X-1 V1	X-1 V2
Stable Pattern	No	Yes
Landed in 200ft Box	No	Yes
Descent Time (s)	15	20

**Table 8.4. Ground Mission Testing Times**

GM Sub Interval	V2 Iteration Time (s)	Expected Top Team Time (s)	Difference (s)
External Pylons Installed	15	10	-5
Fuel Tanks and X-1 Installed	20	10 (No Internal Fuel Tank)	-10

## 8.2. Completed Aircraft Performance

The BRICK comprised of two distinct prototypes to arrive at the final refined version. Each prototype shared the same geometric features but varied parameters to ascertain the difference in competition score achieved. The first prototype, V1 comprised of a dual motor configuration with a conventional aircraft design, sized for an MTOW of 48.5lbs and was necessary to test the power consumption and structural rigidity for both M2 and M3 during the straights and turns. This prototype was used to validate the mission model shown in Section 4.2 and test the stall speed during M2 flight. From this it was found that a M2 complete lap took 42 seconds, while the aircraft was capable of 9 laps for M3 before the X-1 was launched. Using the data collected from V1, the next prototype V2



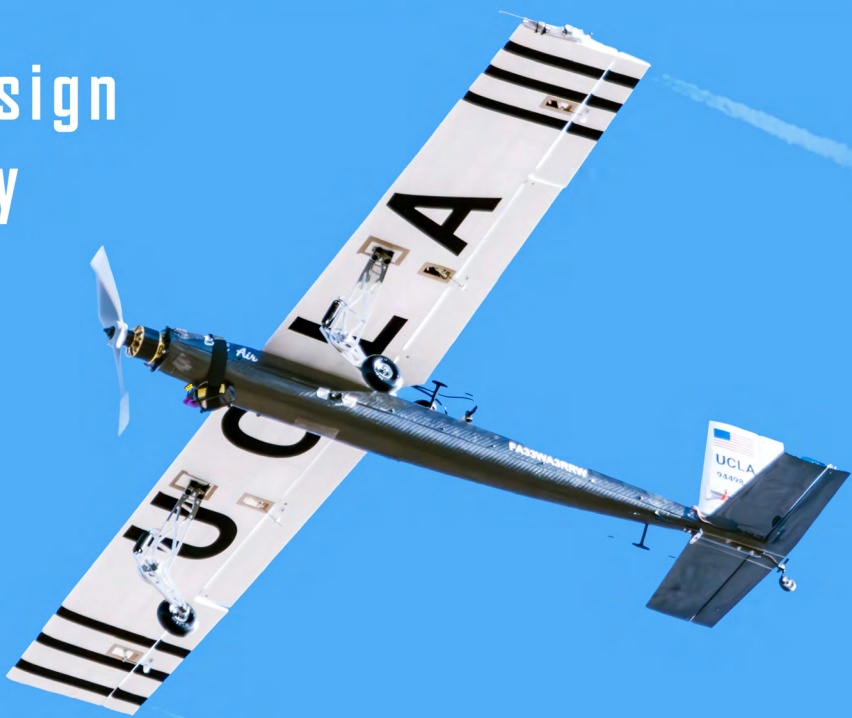
increased the chord, lowering the stall speed and allowed for higher lift to be generated during the turns. V2 also saw the refinement of the pylon design to lower overall skin friction drag of the aircraft. With this it was found that a complete lap for M2 took 39 seconds, paired with the aircraft still being capable of 9 now for M3. Further, the X-1 deployment mechanism was refined, and the X-1 design was tested with the V2 variant capable of a stable pattern and landing inside the 2.5-point box within 20 seconds. As of writing this report, the team is currently building the BRICK V3 the aircraft that will be used for competition, the pylon has been further refined to limit skin-friction drag to increase the aircrafts speed, while small changes to the overall fuselage and X-1 have been made to decrease power consumption and descent time respectively.

## 9. Bibliography

- [1] Autodesk, "Fusion," 2025, Accessed: 2025.
- [2] Mathworks, "MATLAB", 2024b, Accessed: 2025
- [3] Techwinder, "XFLR5," Nov 2023, Accessed: 2024.
- [4] Drela, M. and Youngren, H., "Athena Vortex Lattice," Apr 2022, Accessed: 2024.
- [5] Müller, M., "eCalc," 2024.
- [6] Capable Computing, Inc, "MotoCalc," 2021
- [7] Gudmundsson, S., General Aviation Aircraft Design - Applied Methods and Procedures, Elsevier, 6th ed., 2022.
- [8] Raymer, D. P., Aircraft Design: A Conceptual Approach, AIAA, California, 2018.
- [9] AIAA, Winning Reports 2020, AIAA, Reston, 2020.
- [10] AIAA, 2023 Design, Build, Fly Competition Summary, AIAA, Reston, 2023.
- [11] AIAA, AIAA Design Build Fly Competition Summary 2020-21, AIAA, Reston, 2021.
- [12] Robert, N. C., Flight Stability and Automatic Control, McGraw-Hill, 1998.
- [13] Moorhouse, D. J. and Woodcock, R. J., "BACKGROUND INFORMATION AND USER GUIDE FOR MIL-F-878SC, MILITARY SPECIFICATION FLYING QUALITIES OF PILOTED AIRPLANES," Tech. rep., DTIC, 1982.
- [14] ANSYS Inc, "ANSYS Workbench", 2024, Accessed: 2024.
- [15] Ardema, M. D., Chambers, M. C., Patron, A. P., Hahn, A. S., Miura, H., and Moore, M. D., "Analytical Fuselage and Wing Weight Estimation of Transport Aircraft," Tech. rep., NASA, California, 1996.
- [16] Composites, P., "Mechanical Properties of Carbon Fibre Composite Materials," 2025, Accessed: 2025-01-29.
- [17] Wang, T., Wang, Y., Crocetti, R., and Wälinder, M., "In-plane mechanical properties of birch plywood," Construction and Building Materials, Vol. 340, 2022.
- [18] United States Department of Defence, "Metallic Materials and Elements for Aerospace Vehicle Structures," 2003, Accessed: 2025-01-15.
- [19] Ultimaker, "Ultimaker Tough PLA Technical data sheet," 2022, Accessed: 2024-02-20.
- [20] MatWeb, "Overview of materials for Polystyrene, Extrusion Grade," 2025, Accessed: 2025-01-15.
- [21] Gadd, C., "Servo Torque Formula," 2024, Accessed: 2025.
- [22] Anderson, J. D., "Aircraft Performance & Design", McGraw-Hill Education, 1998

# UCLA

AIAA Design  
Build Fly  
2025



## Bell-Air

## Contents

<b>1.</b>	<b>Executive Summary .....</b>	<b>4</b>
<b>2.</b>	<b>Management Summary .....</b>	<b>5</b>
2.1.	Team Organization .....	5
2.2.	Design Schedule .....	5
<b>3.</b>	<b>Conceptual Design .....</b>	<b>6</b>
3.1.	Mission Requirements .....	7
3.2.	Design Requirements .....	8
3.3.	Translation of Design Requirements into Subsystem Design Goals .....	9
3.4.	Scoring Sensitivity Analysis .....	10
3.5.	Configuration Selection .....	11
3.6.	Final Conceptual Design .....	13
<b>4.</b>	<b>Preliminary Design .....</b>	<b>13</b>
4.1.	Design Methodology .....	13
4.2.	Design Trade Studies .....	14
4.3.	Aircraft Performance .....	20
4.4.	Aircraft Stability .....	25
4.5.	Predicted Mission Performance .....	26
4.6.	Uncertainties .....	27
<b>5.</b>	<b>Detail Design .....</b>	<b>27</b>
5.1.	Dimensional Parameters .....	27
5.2.	Structural Characteristics .....	28
5.3.	Subsystem Design .....	30
5.4.	Weight and Balance .....	38
5.5.	Flight Performance .....	39
5.6.	Mission Performance .....	39
5.7.	Drawing Package .....	40
<b>6.</b>	<b>Manufacturing Plan .....</b>	<b>44</b>
6.1.	Manufacturing Process Investigation .....	44
6.2.	Manufacturing Process Selection .....	45
6.3.	Manufacturing Schedule .....	47
<b>7.</b>	<b>Testing Plan .....</b>	<b>48</b>
7.1.	Test Objectives and Schedule .....	48
7.2.	Ground Testing .....	49
7.3.	Flight Testing .....	52
7.4.	Pre-Flight Checklist .....	54
<b>8.</b>	<b>Performance Results .....</b>	<b>55</b>
8.1.	Subsystem Performance .....	55
8.2.	Aircraft Flight Performance .....	59
<b>9.</b>	<b>Bibliography .....</b>	<b>60</b>

## Abbreviations, Acronyms, and Symbols

<b>A</b>	Amp	<b>N</b>	Newton
<i>AR</i>	Aspect Ratio	$N_{Laps, M3}$	Number of Laps Completed in Mission 3
<b>AIAA</b>	American Institute of Aeronautics and Astronautics	<b>oz</b>	Imperial Ounces
<i>b</i>	Wingspan	<i>P</i>	Power
<b>CAD</b>	Computer-Aided Design	$\bar{P}$	Averaged Power
$C_d$	2D Coefficient of Drag	$P_s$	Power in Straight
$C_D$	3D Coefficient of Drag	$P_T$	Power in Turn
$C_{D,0}$	3D Zero-Lift Drag Coefficient	<b>PCB</b>	Printed Circuit Board
<b>CE</b>	Component Engineer	<b>PID</b>	Proportional Integral Derivative
<b>CF</b>	Carbon Fiber	<b>psi</b>	Pounds per Square Inch
<b>CFD</b>	Computational Fluid Dynamics	<b>P0</b>	Prototype 0
<b>CG</b>	Center of Gravity	<b>P1</b>	Prototype 1
$C_{HT}$	Horizontal Tail Volume Coefficient	<i>R</i>	Turn Radius
$C_{VT}$	Vertical Tail Volume Coefficient	<b>R&amp;D</b>	Research & Development
$C_l$	2D Coefficient of Lift	<b>RC</b>	Radio-Controlled
$C_L$	3D Coefficient of Lift	<i>Re</i>	Reynolds Number
$C_{L,\alpha}$	3D Coefficient of Lift, Estimated at a Given Angle	<b>RX</b>	Receiver
$C_m$	Coefficient of Moment	<b>s</b>	Second
<b>CNC</b>	Computer Numerical Control	$S_{LO}$	Ground Roll Distance
<b>COTS</b>	Commercial Off-the-Shelf	<b>S</b>	Series
<i>d</i>	Lap Duration	$S_w$	Wing Area
<i>D</i>	Drag Force	$S_{HT}$	Horizontal Stabilizer Area
$\bar{D}$	Average Drag Force	$S_{VT}$	Vertical Stabilizer Area
<b>DBF</b>	Design/Build/Fly	$S_{Bonus\ Box}$	Score of Bonus Box
<b>e</b>	Propulsion System Efficiency	<i>T</i>	Thrust
<i>E</i>	Total Energy Consumption	$t_{GM}$	Time for Ground Mission
<b>ESC</b>	Electronic Speed Controller	$t_{M2}$	Time for Mission 2
<b>FC</b>	Flight Controller	<b>TX</b>	Transmitter
<b>FEA</b>	Finite Element Analysis	<b>UCLA</b>	University of California, Los Angeles
<b>fl oz</b>	Imperial Fluid Ounces	<b>V</b>	Volt
<b>FOM</b>	Figure of Merit	<i>V</i>	Airspeed
<b>ft</b>	Imperial Foot	$V_{LO}$	Airspeed at Liftoff
<b>g</b>	Gravitational Constant	$V_{Stall}$	Stall Speed
<b>GM</b>	Ground Mission	$V_s$	Airspeed in Straight
<b>GNC</b>	Guidance, Navigation, and Control	$V_T$	Airspeed in Turn
<b>GPS</b>	Global Positioning System	<i>W</i>	Weight
<b>h</b>	Hour	$W_f$	Weight of Fuel Tanks
<b>Hz</b>	Hertz	$W_{X-1}$	Weight of X-1 Test Vehicle
<b>in</b>	Imperial Inch	<b>Wh</b>	Watt-hour
<b>k</b>	Kilo (Thousand)	<b>X-1</b>	X-1 Test Vehicle
<i>K</i>	Lift-Induced Drag Factor	$\alpha / \text{AOA}$	Angle of Attack
<i>L</i>	Lift Force	$\epsilon$	Oswald's Efficiency Factor
$\bar{L}$	Average Lift Force	$\zeta$	Damping Ratio
$L_{HT}$	Horizontal Tail Lever Arm	$\theta$	Bank Angle
$L_{VT}$	Vertical Tail Lever Arm	$\lambda$	Glide Angle
<b>lb</b>	Imperial Pounds	$\mu$	Coefficient of Friction
<b>lbf</b>	Pounds-force	$\rho$	Air Density
<b>M1</b>	Mission 1	$\sigma$	Damping Factor
<b>M2</b>	Mission 2	$\phi$	Takeoff Angle
<b>M3</b>	Mission 3	$\omega$	Angular Velocity
<b>MAC</b>	Mean Aerodynamic Chord	$\omega_n$	Natural Frequency
<i>n</i>	Load Factor	$\Omega$	Ohm

## 1. Executive Summary

This design report outlines the general design, manufacturing, and testing for Bell-Air, a radio-controlled (RC) aircraft designed by the University of California, Los Angeles (UCLA) for the 2024-25 American Institute of Aeronautics and Astronautics (AIAA) Design/Build/Fly (DBF) Competition. Based on the X-1 Supersonic Flight Program, the 6-foot wingspan aircraft carries a payload consisting of fuel tanks and an X-1 test vehicle (X-1) to complete three flight missions and one ground mission. Mission 1 (M1) is a delivery flight that demonstrates the aircraft's flight capabilities without a payload. Mission 2 (M2) is a captive carry flight that includes the X-1 and fully loaded fuel tanks. Mission 3 (M3) is a launch flight that demonstrates the deployment of the X-1. Finally, the Ground Mission (GM) is a timed demonstration of aircraft assembly, payload installation, and flight controls checks.

### Aircraft Configuration

The design of the aircraft was split into three phases: conceptual, preliminary, and detailed design. During the conceptual design phase, the competition mission requirements were broken down into design requirements to determine the overall aircraft configuration. The preliminary design phase included trade studies focused on aircraft sizing, performance, and stability. The detailed design phase focused on the structural implementation of all aircraft components and the subsystem design for the aerodynamic surfaces, electronics system, and mission specific mechanisms. Based on the overall design process, a high-wing monoplane with a conventional tail and taildragger landing gear was selected as shown in Figure 1. A high-wing configuration was chosen for better stability and adequate fuel tank and pylon clearance. A taildragger landing gear configuration was selected to ensure sufficient propeller clearance for the required propulsion specifications and reduce the overall weight of the aircraft. To maximize the aircraft endurance and efficiency of the propulsion system, a single motor configuration was selected. The monoplane and conventional tail configurations were selected for their reduced weight, drag benefits, manufacturability, and standardized design.

### Mission Performance

A manufacturing timeline and testing schedule were outlined to ensure the completion of the final competition aircraft. Through flight testing, the predicted performance of the aircraft was determined as detailed in Table 1.

Table 1: Mission Performance

Performance Parameter	M1	M2	M3	GM
Gross Weight [lbs]	9.21	18.73	9.48	--
Payload Weight [lbs]	--	9.26 (Fuel Tanks Weight)	0.19 (X-1 Weight)	--
Completed Laps [#]	3	3	7	--
Mission Time [s]	95	110	275	63
Cruise Airspeed [ft/s]	112	127	112	--

Figure 1: Bell-Air



## 2. Management Summary

### 2.1 Team Organization

The 2024-25 DBF at UCLA team consists of 45 undergraduate students with 7 seniors and 38 underclassmen. The leadership team includes administrative leads, technical leads, and a faculty advisor who assists with design reviews and inspects the final competition aircraft. Overseeing the administrative branch, the Project Manager is responsible for planning meetings and ensuring the completion of competition objectives with support from the Vice Project Manager. The Internal Affairs Officer tracks finances while the External Affairs Officer handles outreach efforts. The Lab Manager enforces laboratory organization and safe practices. On the technical side, the Chief Engineer directs the design, building, testing, and analysis of the aircraft. General members contribute to one or more of seven subteams, each led by a technical lead. The Aerodynamics Subteam completes aircraft sizing and performance optimization analysis, while the Computer-Aided Design (CAD) Subteam creates detailed models of the aircraft's components. Fabrication and assembly of the aircraft is handled by the Manufacturing Subteam. The Propulsion Subteam selects and optimizes propulsion components and avionics setups. New technologies and design ideas are investigated by the Research & Development (R&D) Subteam. The structural integrity of aircraft components are verified by the Structures Subteam through computational studies and testing. The Pilot/Flight Test Lead trains members to fly RC aircraft through flight simulators and hands-on practice. Three Component Engineers (CE) are responsible for mechanisms and aspects of the design specific to the 2024-25 DBF Competition [1]. The Pylon Mechanism CE falls under the CAD Subteam; the Guidance, Navigation, and Control (GNC) CE falls under the Propulsion Subteam; and the Release Mechanism CE falls under the R&D Subteam. The team organization is shown in Figure 2.

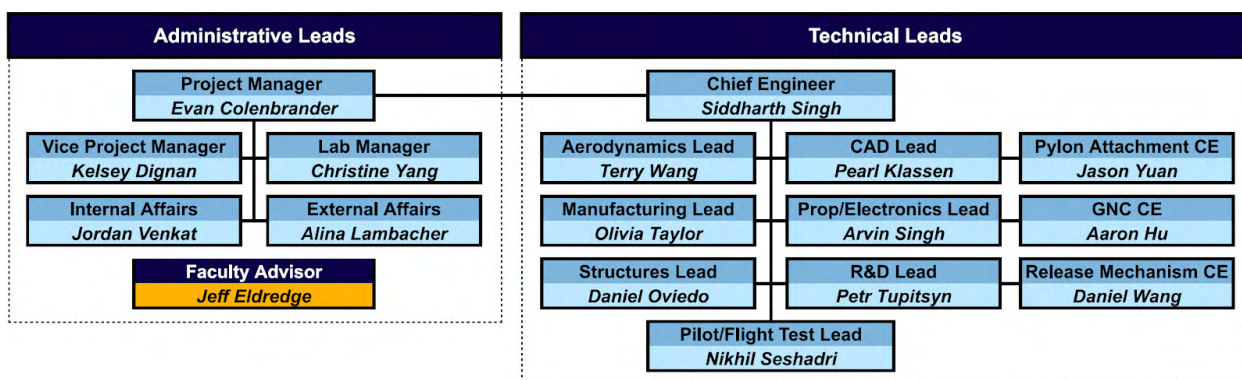


Figure 2: Team Organization

### 2.2 Design Schedule

A Gantt chart was created at the beginning of the year to mark the dates of key events and track progress. This timeline allocates time for two prototype aircraft to be produced and tested before the final competition aircraft. Each aircraft undergoes design, manufacturing, testing, and data analysis. The Gantt chart is shown in Figure 3.

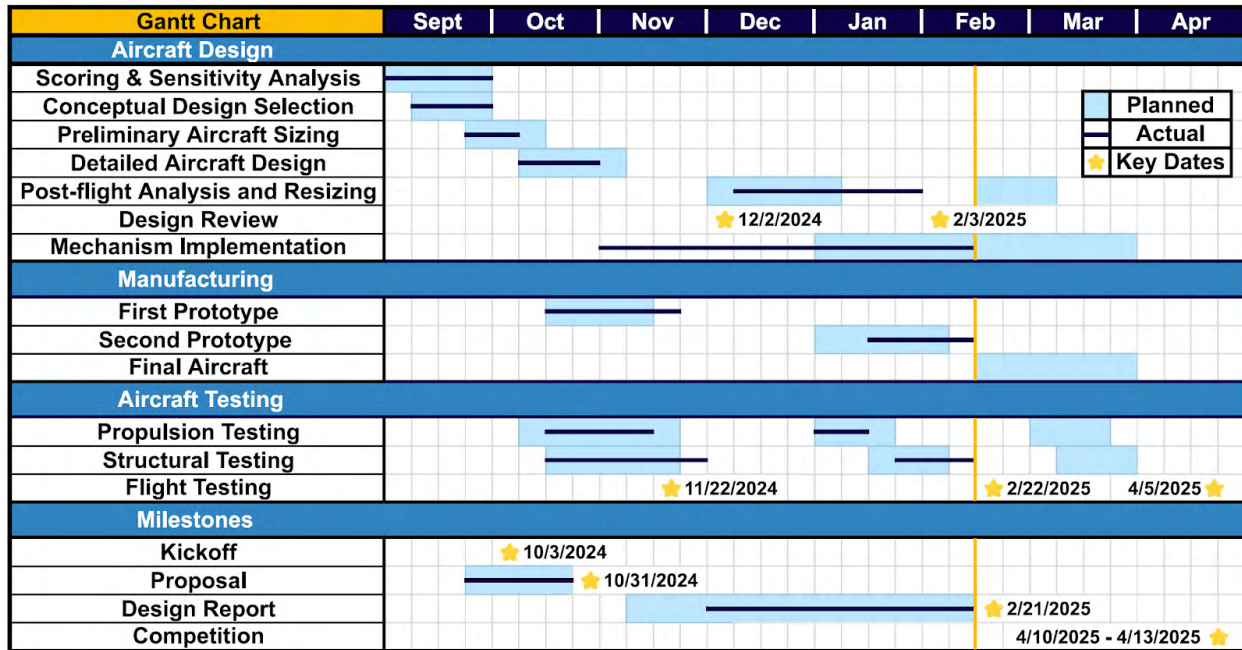


Figure 3: Team Gantt Chart

### 3. Conceptual Design

The conceptual design stage involves decomposing the competition rules [1] into design objectives and constraints to select an aircraft configuration. A sensitivity analysis of the mission scoring equations yielded information on which aspects of the competition have the greatest impact on the aircraft's final score. Ultimately, a high-wing, monoplane, taildragger with a conventional tail and single-tractor propulsion system was selected to maximize UCLA's total mission score.

#### 3.1 Mission Requirements

The 2024-25 AIAA DBF competition is inspired by the X-1 Supersonic Flight Program. As such, the competition missions involve payload objectives, the carry and release of an autonomous X-1, and a demonstration of the aircraft's ability to transition between configurations. The total mission score is defined in Equation 1 as the sum of the scores of three flight missions and one ground mission.

$$\text{Total Mission Score} = M1 + M2 + M3 + GM \quad (1)$$

The total report score, defined by Equation 2, is the sum of the proposal score and design report score, weighted by 15% and 85%, respectively. Both documents are scored on a 100-point rubric.

$$\text{Total Report Score} = 0.15 \times \text{Proposal Score} + 0.85 \times \text{Design Report Score} \quad (2)$$

The competition score defined by Equation 3, which determines the team's final ranking, is the product of the total report score and total mission score in addition to an extra participation score,  $P$ . The teams are

awarded a participation score of 1, 2, or 3 points, respectively, for attending the fly-off, completing tech inspection, and attempting a flight mission.

$$\text{Competition Score} = \text{Total Report Score} \times \text{Total Mission Score} + P \quad (3)$$

### 3.1.1 Staging & General Mission Requirements

Before each flight attempt, there is a 5-minute staging window to install all necessary components to the aircraft. For each mission, the flight window, limited to 5 minutes, begins when the aircraft throttle is advanced for the first take-off attempt. For any flight to count as completed, a successful landing must be demonstrated wherein the aircraft touches down on the runway without significant damage, as deemed by the flight-line judge.

A full competition lap consists of two 1000 ft straights connected by an upwind and downwind turn as outlined in Figure 4. The downwind straight additionally features a 360-degree turn. A lap is considered complete once the aircraft reaches the start/finish line after executing the downwind turn. For M3, bonus boxes allow teams to score additional points using their X-1, as detailed in Section

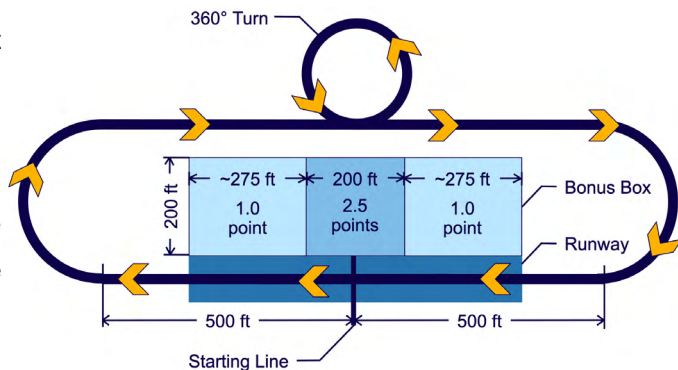


Figure 4: Competition Lap

3.1.4. The bonus boxes stretch the entire length of the runway, approximately 750 ft, and extend 200 ft away from the edge of the runway. The middle bonus box, which is 200 ft long and centered on the start/finish line, corresponds to a bonus box score of 2.5 points. The two bonus boxes flanking the middle box and extending to the ends of the runway correspond to a bonus box score of 1.0 points.

### 3.1.2 Mission 1

M1 is a delivery flight meant to demonstrate the aircraft's ability to fly. Three full competition laps must be flown within a 5-minute flight window with no payload to earn 1.0 points as shown by Equation 4.

$$M1 = 1.0 \quad (4)$$

### 3.1.3 Mission 2

M2 is a captive carry flight meant to demonstrate the aircraft's performance while carrying a payload consisting of the X-1 and fuel tanks. The subscore given to each team is a function of the total weight of the fuel tanks and the time taken to fly 3 laps. Upon completing the mission, the team is awarded 1.0 points plus the team's subscore divided by the maximum subscore of all teams, as defined by Equation 5. Accordingly, the maximum possible score for this mission is 2.0 points.

$$M2 = 1.0 + \frac{[W_f(t_{M2})^{-1}]|_{UCLA}}{[W_f(t_{M2})^{-1}]|_{Max}} \quad (5)$$

### 3.1.4 Mission 3

M3 is a launch flight in which teams carry unloaded fuel tanks and fly as many laps as possible within the 5-minute flight window, before releasing the X-1 on the final lap. The release must occur after the aircraft crosses the start/finish line but before making the upwind turn, at an altitude of 200-400 ft. The X-1 must then achieve stable flight, execute a 180-degree turn, and land in a bonus box.

Each team is given a subscore as the sum of the number of laps achieved by the aircraft before releasing the X-1 and the quotient of the awarded bonus box score, detailed in Section 3.1.1, divided by the X-1 weight. Each team that completes M3 is awarded 2.0 points plus the team's subscore divided by the maximum subscore of all teams, as defined by Equation 6. Accordingly, the maximum possible score for this mission is 3.0 points.

$$M3 = 2.0 + \frac{[N_{Laps,M3} + S_{BonusBox}(W_{X-1})^{-1}]|_{UCLA}}{[N_{Laps,M3} + S_{BonusBox}(W_{X-1})^{-1}]|_{Max}} \quad (6)$$

### 3.1.5 Ground Mission

GM is an X-1 flight test program demonstration. The aircraft enters a designated ground mission staging area with all payloads uninstalled. A ground crew member of the team will be timed to install the pylons, empty fuel tanks, and the X-1. The pilot will then demonstrate that the aircraft has functional flight controls and is able to release the X-1.

After completing GM, the team will be given a subscore equal to the total time taken to install all the payloads. The GM score is equal to the quotient of the minimum subscore out of all teams divided by the team's subscore, as defined by Equation 7. Accordingly, the maximum possible score for this mission is 1.0 points.

$$GM = \frac{(t_{GM})|_{Min}}{(t_{GM})|_{UCLA}} \quad (7)$$

## 3.2 Design Requirements

As outlined in the 2024-25 AIAA DBF Rules [1], the aircraft and payload must satisfy a particular set of requirements which serve as goals for the aircraft conceptual design.

### 3.2.1 Aircraft and Mission Requirements

The general aircraft requirements, such as dimensional limitations, are outlined and labeled in Table 2. Requirements that address aspects of the competition missions are detailed in Table 3.

**Table 2: Aircraft Requirements**

Label	Requirement
GR.1	The aircraft can be any design configuration except rotary wing or lighter-than-air
GR.2	The aircraft weight must not exceed 55 lbs
GR.3	The aircraft wingspan must not exceed 6 ft
GR.4	The aircraft assembly and payload installation must be completed within a 5-minute staging window
GR.5	The aircraft must successfully fly three missions, each requiring a specified payload
GR.6	The aircraft must be propeller-driven and powered by a single nickel-cadmium, nickel-metal hydride, or LiPo propulsion battery
GR.7	The aircraft must have a separate avionics battery for the RX/servos
GR.8	The battery packs must be COTS, must not exceed 100 Wh, and must be labeled with cell chemistry
GR.9	The aircraft propulsion system must have an arming fuse with a maximum current rating of 100 Amps
GR.10	The aircraft must have an externally accessible switch to turn on the RC system

**Table 3: Mission Requirements**

Mission	Label	Requirement
M1	M1.1	The aircraft must fly without a payload
	M1.2	The aircraft must fly 3 laps within a 5-minute flight window
M2	M2.1	The aircraft must carry a payload of the X-1 and loaded fuel tanks
	M2.2	The aircraft must fly 3 laps as fast as possible with as much weight as possible in the fuel tanks
M3	M3.1	The aircraft must carry a payload of the X-1 and unloaded fuel tanks
	M3.2	The aircraft must fly as many laps as possible within a 5-minute flight window before releasing the X-1
	M3.3	The X-1 should be as light as possible
GM	GM.1	Scored on total time to install pylons, fuel tanks, and the X-1

### 3.2.2 Payload Requirements

The payload includes a combination of fuel tanks, wing-mounted pylons, and the X-1. Requirements that address aspects of the payload are detailed in Table 4.

**Table 4: Payload Requirements**

Component	Label	Requirement
Fuel Tanks & Pylons	PR.1	The fuel tanks must be a commercially available beverage bottle of any size or shape with a screw-on cap
	PR.2	The external fuel tanks must have a minimum capacity of 16 fl oz
	PR.3	The fuel tanks must be filled with varying amounts of an inert material to achieve a desired weight
	PR.4	At minimum, two external fuel tanks must be carried
	PR.5	The pylons must be removable and not a permanent feature of the aircraft's design
	PR.6	The pylons must be able to securely attach to the bottle to sustain all flight forces
X-1 Test Vehicle & Release Mechanism	PR.7	The X-1 must be unpowered and autonomously-controlled
	PR.8	The X-1 must transition to stable flight after release, execute a 180-degree turn, and attempt to land
	PR.9	The X-1 must have strobe lights that come on after it is released from the aircraft
	PR.10	Once the X-1 comes to rest, the strobe lights must remain turned on and intact
	PR.11	The X-1 will be awarded points corresponding to the bonus box region in which it lands (Section 3.1.4)
	PR.12	The X-1 must be carried between the two external fuel tanks
	PR.13	There must be a minimum gap of 0.25 inches between the X-1 wings and any part of the aircraft's outer surface

### 3.3 Translation of Design Requirements into Subsystem Design Goals

From the previously stated design requirements, subsystem design goals were established for driving conceptual aircraft design. Such goals are broken down in Table 5.

**Table 5: Subsystem Design Goals**

Category	Parent Requirements	Subsystem Requirement
Aerodynamics	GR.1, GR.2, GR.3	Ensure compliance with competition configuration, weight, and wingspan limits
	GR.5, M1.1, M2.1, M3.1	Select an aircraft configuration that is suitable for all payloads
	M1.2, M2.2	Achieve a target time for 3 laps (determined in section 4.5)
	M3.2	Minimize drag to achieve a target cruise speed (determined in section 4.5)
	M2.1	Optimize lift generated to carry greater payload weights
	GR.1	Have adequate stability and control characteristics
Propulsion	M3.2	The propulsion system must be able to support flight for up to 5 minutes
	GR.8	The battery capacity must be optimized to maximize score
	GR.9, GR.10	Verify that the propulsion system can reliably be activated and disabled
	GR.6, GR.7, GR.8	All batteries must comply with safety regulations
Mechanisms	GR.4, PR.5, GM.1	Ensure all mechanisms are ergonomic for fast and reliable operation and installation
	PR.1, PR.2, PR.6	Select beverage bottles that have geometry suitable for pylon integration
	PR.3, PR.4	Optimize fuel tanks to a target weight (determined in section 4.5)
	M3.3	The X-1 must be under a target weight (determined in section 4.2.8)
	PR.7, PR.8	Automate the X-1 to land in the bonus box after release
	PR.9, PR.10, PR.11	Incorporate strobe lights that are lightweight and durable to remain on after landing
	PR.12, PR.13	The X-1 must be held by a release mechanism, at the CG for stability purposes

### 3.4 Scoring Sensitivity Analysis

A numerical analysis of the mission score variables was conducted to determine which would have the most impact on increasing overall score. The six variables analyzed were GM completion time, M2 payload weight, M2 flight time, M3 number of laps, X-1 weight, and M3 bonus box score. By varying each of these variables, except the bonus box score, the trend in their overall sensitivity was determined. The plots in Figure 5 show the impact of each possible bonus box score, which alters the sensitivity of the X-1 weight on the overall score. Assuming the maximum bonus box score is achieved, the three most influential design parameters for increasing score are reducing GM time, M2 time, and X-1 weight. The sensitivity trends of these design parameters are exponential, while the others are linear or stepwise.

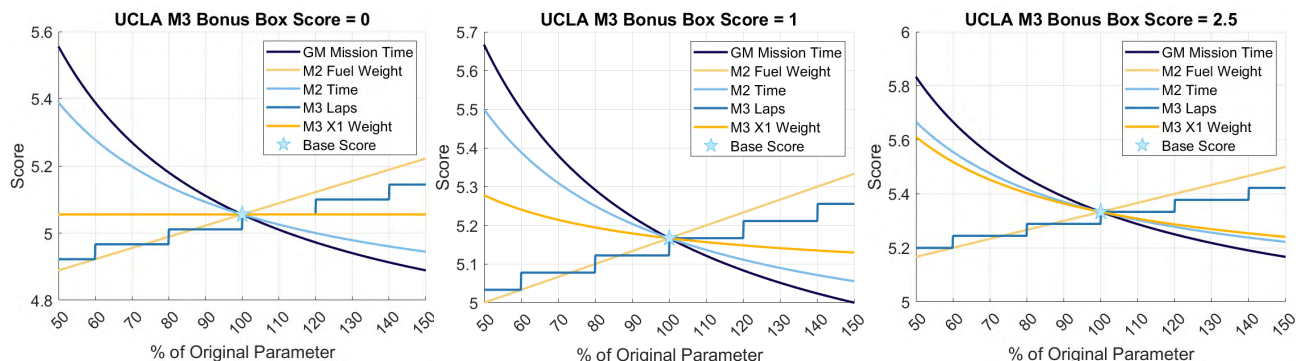


**Figure 5: Scoring Results with Varying Bonus Box Scores**

### 3.5 Configuration Selection

The selection of key elements of the aircraft configuration were determined using Figure of Merit (FOM) charts, where each element was assigned performance metrics weighted by relative importance. Configuration options for each metric were scored between -2 and 2 based on commonly accepted flight characteristics and the team's experience with past aircraft.

#### 3.5.1 Overall Configuration

Monoplane, biplane, flying wing, lifting body, and tandem wing configurations were considered for the aircraft's wing layout configuration. The quantitative analysis of these configurations is summarized in Table 6. Flying wing and lifting body configurations were deemed ill-suited for this year's mission requirements, which emphasize stability and control over internal volume. Although biplane and tandem wing configurations offer benefits in lifting capacity, the lack of a takeoff distance limit meant that a monoplane was deemed the optimal choice for this year's aircraft.

Table 6: Wing Layout FOM Chart

Performance Metric	Weight (%)	Monoplane	Biplane	Flying Wing	Lifting Body	Tandem Wing
Weight	20	0	-2	0	-1	-1
Stability & Control	25	0	0	-1	-2	0
Drag	10	0	-1	1	-2	0
Lift	15	0	2	-1	-2	1
Manufacturing	10	0	-1	0	-1	-1
Internal Volume	10	0	0	-1	2	0
Cargo Access	10	0	-1	0	1	-1
Total	100	0	-40	-40	-100	-25

#### 3.5.2 Wing Configuration

High, mid, and low-wing placements were weighed against each other based on their impact on aircraft controllability and ergonomics. The wing placement FOM chart is summarized in Table 7. A mid-wing configuration offered little benefit whilst being challenging to implement due to the main wing spar passing through the fuselage.

Table 7: Wing Placement FOM Chart

Performance Metric	Weight (%)	Low	High	Mid
Stability	25	0	2	1
Wing Installation	15	0	1	-2
Complexity	15	0	0	-2
Landing Gear Placement	15	0	1	1
Cargo Access	30	0	2	-2
Total	100	0	140	-80

Compared to a high-wing arrangement, a low-wing was on par or inferior in all figures of merits deemed relevant. Thus, a high-wing placement was chosen primarily due to its increased roll stability and superior ease of access to the external fuel tanks and pylons.

### 3.5.3 Propulsion Configuration

The propulsion configuration was selected from a list of tractor, pusher, double tractor, and push-pull motor configurations. This is shown in Table 8. Since there is no takeoff distance limit for this year's competition, less emphasis was placed on maximum available thrust. As a result, the double tractor and push-pull configurations did not offer enough benefits to outweigh their negative impacts on weight, efficiency, and installation interference. A pusher propulsion system did not offer any benefits over an equivalent tractor implementation, so a tractor configuration was chosen for the competition aircraft.

Table 8: Propulsion Layout FOM Chart

Performance Metric	Weight (%)	Tractor	Pusher	Double Tractor	Push-Pull
Weight	30	0	0	-1	-1
Max Thrust	10	0	-1	2	1
Efficiency	30	0	-1	-1	-1
Interference	20	0	-1	-1	-2
Handling	10	0	0	-1	0
Total	100	0	-60	-70	-90

### 3.5.4 Tail Configuration

In accordance with the selected conventional overall configuration, various tail types were analyzed to determine the optimal choice, as shown in Table 9. The T-tail, cruciform, and U-tail options all offered varying benefits in yaw and pitch stability, when compared to a conventional tail. However, these benefits came at the cost of manufacturability and weight for an equivalently structurally-sound tail installation. Although a V-tail offers a small decrease in drag and weight, the increased manufacturing difficulty and decreased stability resulted in the conventional tail being chosen.

Table 9: Tail Configuration FOM Chart

Performance Metric	Weight (%)	Conventional	T	Cruciform	V	U/H
Yaw Stability	10	0	2	1	-1	1
Pitch Stability	20	0	1	0	-1	1
Weight	25	0	-1	-1	1	-1
Drag	15	0	0	0	1	0
Manufacturing	30	0	-2	-2	-2	-2
Total	100	0	-45	-75	-50	-55

### 3.5.5 Landing Gear Configuration

Landing gear choices were limited to taildragger or tricycle configurations, as shown in Table 10. Although tricycle landing gear offered superior landing characteristics over a taildragger, the team had historically implemented taildragger landing gear on previous competition aircraft without issues. All other characteristics of a taildragger were determined to be advantageous; hence, it was the chosen configuration.

Table 10: Landing Gear FOM Chart

Performance Metric	Weight (%)	Taildragger	Tricycle
Weight	25	0	-1
Drag	25	0	-1
Landing Characteristics	20	0	1
Integration	25	0	-1
Prop Clearance	5	0	-1
Total	100	0	-60

### 3.5.6 X-1 Test Vehicle Configuration

Similar to the main aircraft, a general configuration needed to be chosen for the X-1. As seen in Table 11, choices were limited to a monoplane, flying wing, or lifting body. Both the lifting body and flying wing brought with them serious compromises in terms of stability and control. Due to the small size and lack of a power plant, this

Table 11: X-1 FOM Chart

Performance Metric	Weight (%)	Monoplane	Flying Wing	Lifting Body
Weight	25	0	0	-1
Stability & Control	25	0	-1	-2
Drag	20	0	1	-2
Lift	20	0	-1	-2
Manufacturing	10	0	1	1
Total	100	0	-15	-145

was judged to be detrimental to the performance of the X-1 in potentially windy conditions. Overall, the monoplane was chosen as it represented a good balance of all merits analyzed.

## 3.6 Final Conceptual Design

The final selected configuration consisted of a high-wing, taildragger monoplane with a conventional tail and a tractor propulsion system, as shown in Figure 6. The main aircraft was designed to carry the X-1 of conventional configuration, with a set of external fuel tanks slung underneath the wings.

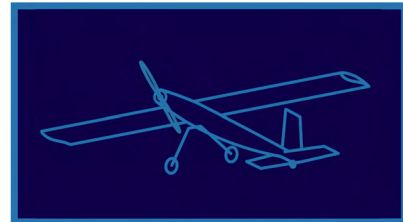


Figure 6: Final Conceptual Design

## 4. Preliminary Design

### 4.1 Design Methodology

A structured design and analysis methodology was adopted to develop the final aircraft, as shown in Figure 7. The process began with a conceptual design phase, where FOM charts were used to establish

an aircraft configuration. The preliminary design phase followed, where aerodynamic and propulsion optimization was used to determine the aircraft flight characteristics and weight distribution. During the detailed design phase, SolidWorks [2] was utilized to generate a CAD model of all the aircraft components. The manufacturing phase focused on prototyping and fabricating parts according to the manufacturing timeline in Section 6.3. The final design phase involved analyzing the results from ground and flight testing to ensure the aircraft met all initial design and performance requirements.

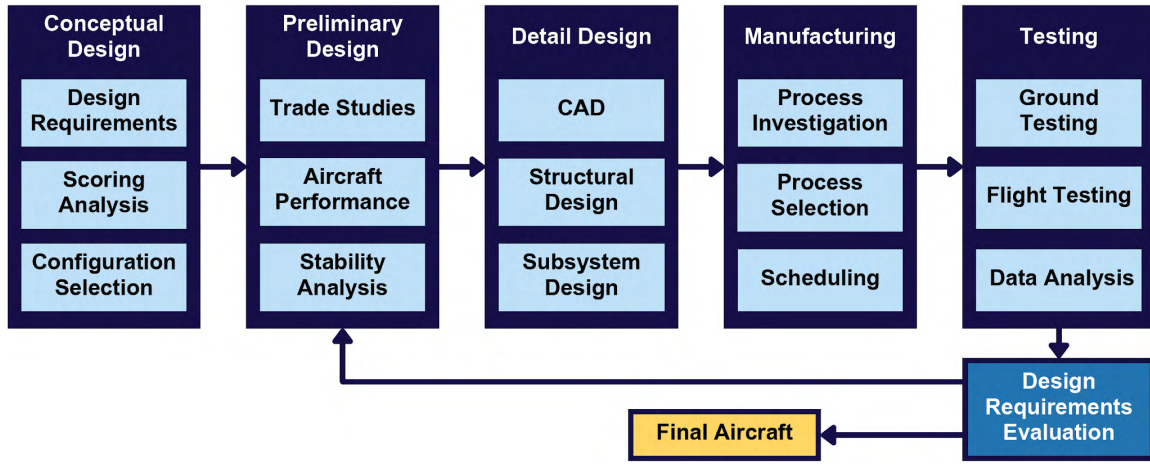


Figure 7: Design Methodology

## 4.2 Design Trade Studies

### 4.2.1 General Sizing

Aircraft performance was initially approximated as a function of empty weight, payload weight, wing area, wing aspect ratio (AR), and six more variables representing the target cruise and turn speeds during each of the three flight missions. The various constraints and bounds for these independent variables were drawn from the team's past aircraft (i.e. historical data) and the 2024-25 competition rules [1]. The resulting trend of aspect ratio and surface area vs. score is displayed in Figure 8.

Parameters such as the zero-lift drag coefficient ( $C_{D,0}$ ) and Oswald's efficiency factor ( $\epsilon$ ) were taken from historical data; these parameters vary minimally between previously designed aircraft of similar size and configuration. The exception to this is the coefficient of lift ( $C_L$ ) vs. angle of attack ( $\alpha$ ) slope, which was

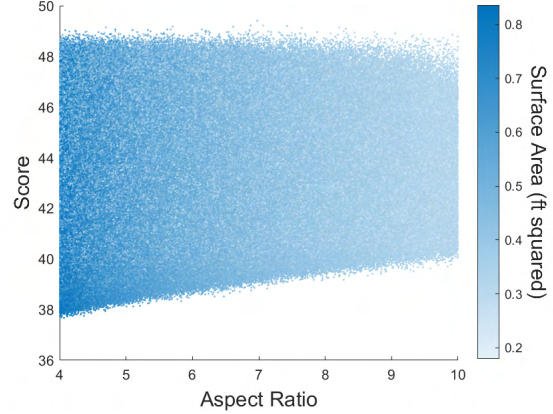


Figure 8: Score vs. Aspect Ratio and Wing Planform Area

chosen based on thin airfoil theory described in Anderson [3] with a correction factor derived from potential flow theory. This was helpful in filtering out inadmissible designs with low aspect ratios that would result in unstable and inefficient wings. The remaining parameters were taken from publicly available environmental data and reference values [3, Raymer 4].

The initial sizing script consisted of two components: a randomization script to provide a preliminary analysis of what competing designs might look like, and a gradient descent script to finalize an optimal design. In total, the randomization script considered around 40 million aircraft configurations. The gradient descent algorithm was taken from Boyd and Vandenberghe [5]. It was chosen since this year's rule set [1] could be represented by a differentiable score function. An additional feature implemented during this stage was a modified score function that included a diversity term. This term helped produce a list of distinctive designs, from which the final design was manually selected.

The final selected configuration possessed a wingspan of 6 feet (ft) and a mean chord of 10.59 inches (in). The empty weight was 11.41 pounds (lb) and the M2 payload weight was 9.26 lb. The target cruise speeds for M2 and M3 were determined to be 131 ft/s and 106 ft/s respectively. In addition, the target turn parameters were optimized to be 106 ft/s over a 128.4 ft turn radius and 85 ft/s over a 88.1 ft turn radius for M2 and M3 respectively.

#### 4.2.2 Propulsion Optimization

The propulsion system was designed around aircraft aerodynamic characteristics, the competition rules [1], and commercial off-the-shelf (COTS) components. Based on the scoring analysis results, cruise power efficiency was optimized to maximize endurance. For propeller-motor selection, a Python [6] script was created to sweep through over 300 propeller-motor-battery configurations in QPROP [7], a program used to aerodynamically model and analyze propellers coupled with motors. The script imposed the following constraints on the configurations: aircraft weight, aspect ratio, wing area, battery voltage, battery capacity, battery resistance, motor Kv, motor phase resistance, and desired endurance. For M2 and M3, the script was run based on the predicted aircraft weights. Propeller options were limited to the APC product catalog [8], the team's propeller sponsor. A list of motors was chosen based on the approximate thrust class of the aircraft and historical values from the team's past propulsion systems. Motor Kv, phase resistance, and recommended battery voltage were provided by the respective manufacturer. Lithium-ion polymer (LiPo) battery cell internal resistance was assumed to be approximately  $5 \text{ m}\Omega$ , determined by averaging the team's past system metrics. The usable battery capacity was set as 80% of 100 Watt-hours (Wh), the maximum rule-compliant capacity [1], to allow a 20% safety margin for preserving battery health. The top-performing propulsion system combinations for each mission are summarized in Table 12.

**Table 12: Propulsion Sizing Script Top 5 Results per Mission**

Battery Capacity (Wh)	Battery Resistance (mΩ)		Wing Area (ft^2)			Aspect Ratio	
80.00	0.005		5.30			6.80	
Motor Model	Propeller Pitch and Diameter	Motor Resistance (mΩ)	Battery Voltage (V)	Takeoff Thrust (lbf)	Takeoff Current (A)	Cruise Speed (ft/s)	Net Efficiency
<b>Mission 2 - 11.55 lbs - 3 Laps</b>							
Scorpion A-5025 310 Kv	18x14x2	8.65	29.6	17.47	102	140.2	81.61%
Scorpion A-5025 310 Kv	16x14x2	8.65	29.6	15.29	89	140.5	81.34%
Scorpion A-5025 415 Kv	17x13x2	5.45	22.2	17.31	126	138.4	79.99%
T-Motor AT7215 245 Kv	18x14x2	20.00	44.4	23.18	106	138.7	78.73%
T-Motor AT7215 220 Kv	18x14x2	24.00	44.4	20.09	84	139.2	78.33%
<b>Mission 3 - 20.82 lbs - 5 Minutes</b>							
Scorpion A-5025 310 Kv	18x14x2	8.65	29.6	17.47	102	112.7	79.57%
Scorpion A-5025 415 Kv	18x14x2	5.45	22.2	16.09	126	111.9	79.14%
Scorpion A-5025 310 Kv	16x14x2	8.65	29.6	15.29	89	112.9	78.35%
Scorpion A-5025 415 Kv	16x12x2	5.45	22.2	15.04	103	111.9	77.77%
T-Motor AT7215 245 Kv	18x14x2	20.00	44.4	23.18	106	111.0	75.76%

Based on the top results from the script, the Scorpion A-5025 310 Kv, 18x14x2 propeller, and 29.6 volt (V) LiPo battery were chosen. Figure 9 visualizes efficiency of the selected motor-propeller combination at various pilot throttle inputs and consequent aircraft speeds.

#### 4.2.3 Empennage Sizing

An aircraft with aggressive maneuverability and low drag was desired to minimize lap times and maximize endurance. Many COTS RC aircraft were experimented with to identify one with optimal maneuverability characteristics. From this, a correlation between tail volume coefficients and maneuverability was established, leading to a horizontal tail volume coefficient ( $C_{HT}$ ) of 0.46 and a vertical tail volume coefficient ( $C_{VT}$ ) of 0.033 for Prototype 1 (P1). Similarly, the P1 moment arm lengths ( $L_{HT}$  and  $L_{VT}$ ) were both determined to be 32.72 in. Given these quantities, the tail surface areas were calculated using

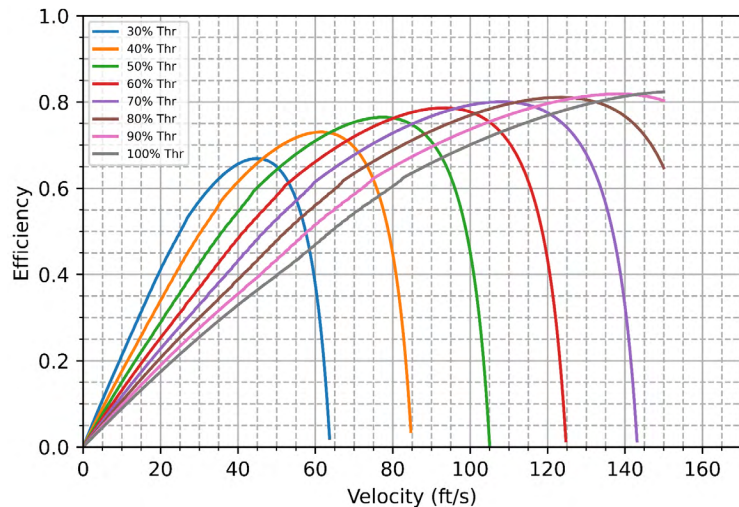


**Figure 9: Net Efficiency vs. Velocity with Scorpion A-5025 310 Kv and APC 18x14x2**

Equations 8 and 9 derived from Raymer [4], with mean aerodynamic chord (*MAC*) and wingspan (*b*) as inputs. Equation 8 determined the horizontal tail area while Equation 9 determined the vertical tail area.

$$S_{HT} = \frac{C_{HT}(MAC)S_w}{L_{HT}} \quad (8)$$

$$S_{VT} = \frac{C_{VT}bS_w}{L_{VT}} \quad (9)$$

Based on XFLR5 [9] induced drag analysis, a 0.75 taper ratio was deemed optimal for both the horizontal and vertical stabilizers. These parameters led to the finalized tail dimensions in Section 5.1.

#### 4.2.4 Airfoil Selection

An airfoil database scraped through multiple online databases, including Airfoil Tools [10] and the University of Illinois, Urbana-Champaign Airfoil Coordinates Database [11]. 2D vortex-panel methods were used from the XFOIL software [12] to evaluate the lift and drag characteristics of each airfoil. Airfoils were ranked by their coefficient of lift ( $C_l$ ) to coefficient of drag ( $C_d$ ) ratio ( $C_l/C_d$ ), at the target cruise  $C_l$  of 0.19. Any airfoils not fitting a set of imposed constraints, including a minimum thickness to avoid hindering wing spar selection, and a maximum  $C_l$  requirement to ensure proper takeoff time, were discarded. The top 20 airfoils were manually analyzed to filter out unreasonable or non-manufacturable designs and the top-ranked remaining airfoil, S3016, was selected.

S3016 was deemed to have favorable flight characteristics based on its gentle lift drop-off at higher  $\alpha$ 's, indicating predictable stall behavior and performance similar to airfoils in previous years. To further refine the design of the airfoil, a particle-swarm optimization algorithm, taken from the program XOptFoil2 [13], was employed to minimize the airfoil's drag in cruise whilst retaining acceptable flight characteristics. The particle-swarm algorithm relied on a population of 50 airfoils, each randomly traversing a solution space to search for an optimal combination of parameters. In this case, the surface of the airfoil was parameterized by a total of 14 Hicks-Henne bump functions, each of which contained 3 parameters that generate a perturbation on the surface [13]. In total, 42 individual variables were responsible for determining the surface of the airfoil.

To ensure the newly-optimized airfoil generally mimics the characteristics of S3016, the original airfoil's drag-to-lift relationship was used as a starting point to generate the objective function for the algorithm. A target  $C_d$  vs.  $C_l$  distribution for the new airfoil was created by examining the  $C_d$  vs.  $C_l$  distribution of S3016, and scaling the  $C_d$  down by a factor proportional to its proximity to the aircraft's cruise  $C_l$ . In other words, the most ambitious drag reduction, 10%, was centered on a  $C_l$  of 0.19, and every point along the curve thereafter was scaled by some factor less than a 10% reduction. Using the newly created curve, 19 points

were selected as targets for the optimization algorithm, with a higher density of points near the cruise  $C_l$  to further encourage the algorithm to prioritize this region.

After 1500 iterations, the particles converged on a new airfoil, dubbed 'UCLA\_1', outlined in Figure 10. The new airfoil appeared qualitatively similar, with meaningful differences including airfoil thickness changing from 9.50% to 8.87% and the aft section of the airfoil being slightly broadened.

UCLA\_1 was examined and compared to S3016 across every parameter relevant to airfoil performance including  $C_l$ ,  $C_d$ ,  $C_l/C_d$ , and coefficient of moment ( $C_m$ ). Furthermore, the new airfoil's performance was observed in a wide range of Reynolds Numbers ( $Re$ ) including 50k, 200k, 300k, 400k, 574k (the average predicted  $Re$  for M3), 712k (the average predicted  $Re$  for M2), and 1000k, to ensure that UCLA\_1 performed consistently for a range of conditions.

Figures 11 and 12 show a small sample of the polars generated in the analysis

phase, which are representative of trends seen almost universally across the  $Re$  listed above. As seen in Figure 11, UCLA\_1 successfully decreased drag in cruise conditions by 4.34% compared to its predecessor. Additionally, UCLA\_1 recorded a 6.08% and a 5.21% improvement in maximum  $C_l$  at the predicted M2 and M3 cruise  $Re$ , respectively. This progress, coupled with UCLA\_1 generally stalling at higher  $\alpha$  values than S3016, led the analysis to conclude that the optimized airfoil had improved stall and drag characteristics over its unoptimized counterpart. UCLA\_1 was selected over S3016 because the new airfoil achieved its goals: decreasing drag developed by the wing in flight, improving maximum  $C_l$ , and retaining overall consistent flight characteristics.

#### 4.2.5 Control Surface Sizing

Wing control surface sizing was done per a reference table provided by Raymer [4] for aircraft of similar size. This resulted in a span percentage of 65% for the flaps, 35% for the ailerons, and a chord percentage of 25% for both. The tail control surfaces were sized referencing a table from the same source. The elevator and rudder chord percentages were both chosen to be 35%, and had span

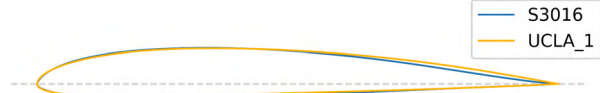


Figure 10: Overlay Comparison of S3016 and UCLA\_1

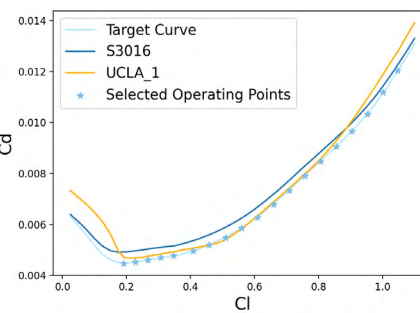


Figure 11:  $C_d$  vs.  $C_l$ , UCLA\_1 vs S3016 (Re 712021)

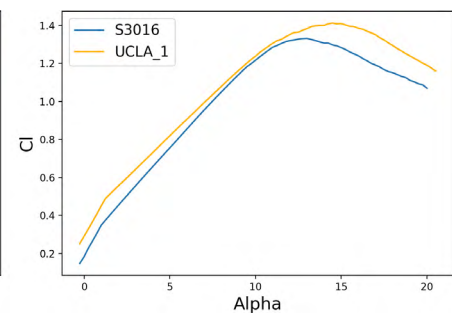


Figure 12:  $C_l$  vs.  $\alpha$ , UCLA\_1 vs S3016 (Re 712021)

percentages of 100%. For ease of manufacturing, the flaps and ailerons were designed to take up the entire span of the wing.

A range of flap deflections were surveyed to determine the optimal flap setting for the aircraft at takeoff as shown in Figures 13 and 14. At increments of 1 degree, flap deflections from 10 to 20 degrees were examined in an  $\alpha$  sweep of the main wing's airfoil for the predicted takeoff  $Re$  of around 270k. Predictably, higher flap deflections resulted in a higher maximum  $C_L$  value, but a regression in stall characteristics and an increase in drag. To balance takeoff speed with comfortable flight characteristics, a 15-degree deflection was selected for the flaps during takeoff.

#### 4.2.6 Landing Gear Sizing

Referencing requirements for propeller clearance and trade studies on flap deflection and wing incidence, an optimal takeoff angle of 13.5 degrees was chosen for the taildragger landing gear. This provided a balance of favorable lift characteristics and a comfortable margin for propeller clearance. The lengthwise angle formed between the gear strut and the center of gravity was sized to 20 degrees, and the spanwise angle between the strut and the fuselage was sized to 45 degrees [4].

#### 4.2.7 Fuel Tank Design

A preliminary study was conducted to determine an adequate combination of fuel density and number of bottles needed to achieve the payload weight of 9.26 lb discussed in Section 4.5. The study aimed to minimize the volume of the external fuel tanks and decrease cross-sectional area, mitigating drag losses. Given the competition's requirement that each fuel tank be at least 16 fluid ounces (fl oz) and that the aircraft have at least two external fuel tanks, the effective minimum volume of all the fuel was 32 fl oz.

A survey of available materials determined that using metal as the fuel would be sufficient to reach the target payload weight while retaining the absolute minimum volume of 32 fl oz. Subsequently, the most cost-effective metal was determined to be US pennies. A sample of 50 pennies showed the average weight and volume of a penny was 0.090 ounces (oz) and 0.012 fl oz respectively. Therefore, a total of 1640 pennies would meet the payload weight while only occupying 19.4 fl oz.

Given that the selected fuel could comfortably meet sizing requirements with 2 external fuel tanks, an internal fuel tank was deemed unnecessary and omitted to decrease the size and weight of the fuselage,

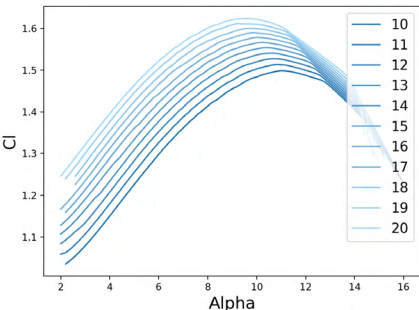


**Figure 13:  $C_L$  vs.  $\alpha$  Comparison Between Flap Deflections**

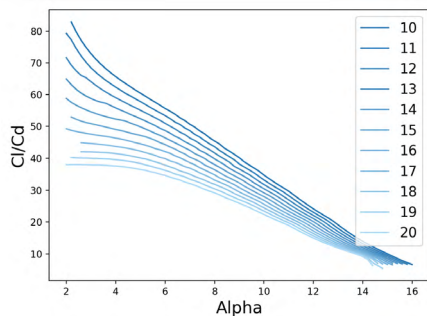


**Figure 14:  $C_L/C_d$  vs.  $\alpha$  Comparison Between Flap Deflections**

improve ergonomics, and shorten ground mission time. Accordingly, the external fuel tank options were limited to only survey bottles closest to the minimum volume of 16 fl oz, such as the more commonly available 16.9 fl oz bottles. Ultimately, a 16.9 fl oz Tejava Iced Tea bottle, shown in Figure 15, was selected as having the best ergonomics because of its wide opening for easy packing of fuel, and inset ridges allowing for easy integration with the pylon.



**Figure 15:**  
Fuel Tank

#### 4.2.8 X-1 Test Vehicle Sizing

The X-1 was sized with a separate script, where the main independent parameters were reduced to the wing dimensions. Sink rate and release speed were set to 10 ft/s and 70 ft/s respectively based on range requirements for the X-1 given a minimum release height of 200 ft. From these results, a target glide angle and a corresponding target  $C_L/C_D$  ratio was calculated as described in Section 4.3.3.

A diversity system was used to output unique combinations from which the final X-1 design was hand-picked. Due to the comparatively simpler geometry of the search space, each local maximum could be computed directly. Because of this, the final configuration was selected from a list of locally optimal configurations. The final predicted weight of the X-1 was 0.27 lb, with 0.20 lb worth of electronics and the rest allocated to the airframe. The X-1 dimensional parameters are summarized in Section 5.1.

### 4.3 Aircraft Performance

#### 4.3.1 Lift and Drag Analysis

Lift and drag build-ups for each prototype were updated several times as more aspects of the wing were finalized. During initial sizing, the target  $C_L$  was calculated via Equation 10 from the target mission speeds. Equations 11 and 12, which relate the overall drag coefficient to the parasitic drag coefficient, aspect ratio, lift coefficient, and Oswald's efficiency factor, were used to calculate  $C_D$ . The estimated  $\alpha$  required for the target  $C_L$  was calculated via Equation 13, where the  $\alpha$  was expressed in terms of degrees, and the  $C_L$ - $\alpha$  slope was determined with the correction factor discussed in Section 4.2.1. Equations 10 through 13 were taken from Jones [14].

$$C_L = \frac{2W}{\rho S_w V^2} \quad (10)$$

$$C_D = C_{D,0} + KC_L^2 \quad (11)$$

$$K = \frac{1}{\pi AR \epsilon} \quad (12)$$

$$C_{L,\alpha} = C_{L,0} + \frac{AR}{AR+2} \left( \frac{\pi^2}{90} \right) \alpha \quad (13)$$

The value of  $C_{L,0}$  was set to be the average of the two target mission  $C_L$  values because the aircraft would be flying at least one of the missions at a near zero  $\alpha$  ideally. Values of 0.70 and 0.04 were used for  $\epsilon$  and  $C_{D,0}$  respectively based on past designs. Summarized in Figure 16 are the lift and drag build ups for the final selected configuration.

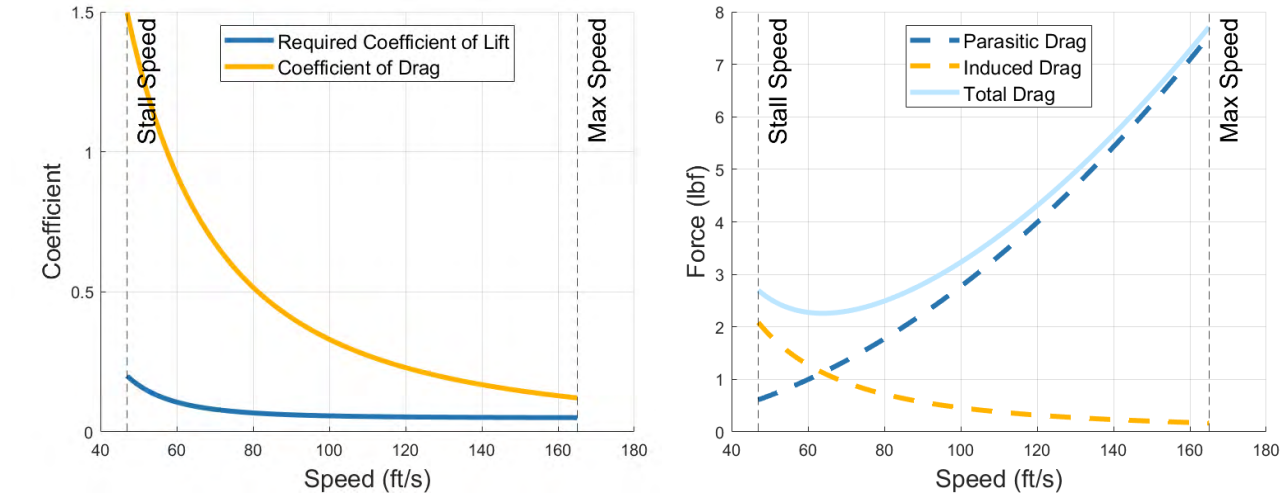


**Figure 16: Lift and Drag Coefficient (Left) and Force (right) Plots**

Incompressible CFD was run on past aircraft designs with the fuel tanks underneath the wing to determine a suitable adjustment factor for the drag when calculating mission performance in M2 and M3. It was determined that increasing the  $C_{D,0}$  to 0.044 would sufficiently model the increased drag. This was confirmed to be an accurate assumption based on a CFD model of the final aircraft in M2 and M3 configurations as shown in section 5.3.1.

**Table 13: Cl and Cd Values**

Parameter	M1	M2	M3
Lift coefficient	0.16	0.19	0.16
Drag coefficient	0.042	0.047	0.046

The final predicted values for the lift and drag coefficients for M2 and M3 are listed in Table 13, as determined from the target weight and mission cruise speeds as listed in section 4.2.1.

#### 4.3.2 Maneuverability

Three maneuvers were considered for sizing: a flat turn, pull up, and pull down. Only the first was deemed relevant to the mission score, while the other two were used to eliminate undesirable configurations. The analysis of these maneuvers relied on the load factor defined in Equation 14 [3].

$$n = \frac{L}{W} \quad (14)$$

For this analysis, propulsion system effects were not considered for the sake of simplicity and their limited impact on the predicted score. For the flat turn, the bank angle and turn speeds were initialized as independent variables to optimize. To facilitate calculations, it was advantageous to describe the bank angle via the load factor during a flat turn, defined by Equation 15 [3].

$$n = \frac{1}{\cos(\theta)} \quad (15)$$

Thus, the maximum load factor occurs when lift is maximized. From this, an upper bound for the bank angle was derived to calculate turn radius ( $R$ ) and angular velocity ( $\omega$ ) as outlined by Equations 16 and 17 [3].

$$R = \frac{V^2}{g \sin(\theta)} \quad (16)$$

$$\omega = \frac{g \sin(\theta)}{V} \quad (17)$$

For a flat turn, the bank angle and speed that produced the maximum  $\omega$  was not utilized, as despite M2 being a sprint mission, power consumption was capped to maintain power throughout the full mission. Similarly, M3 is an endurance mission with a time limit. A turn speed and bank angle that minimized a balance of power consumption and total time spent in turns was needed to optimize score. As such, directly optimizing for maximal  $\omega$  did not produce the highest score for a given aircraft configuration. This justified the decision to set turn speed and bank angle/load factor as separate independent variables.

Maximum pull up and pull down angular velocities and radii were calculated via Equations 18 - 21 [3] and compiled in Table 14.

$$\omega_{Max, Pull Up} = \frac{g(n-1)}{V} \quad (18)$$

$$R_{Min, Pull Up} = \frac{V^2}{g(n-1)} \quad (19)$$

$$\omega_{Max, Pull Down} = \frac{g(n+1)}{V} \quad (20)$$

$$R_{Min, Pull Down} = \frac{V^2}{g(n+1)} \quad (21)$$

The limiting values for each maneuver are shown in Table 14. Various maneuverability plots of the selected configurations are shown in Figure 17.

**Table 14: Maneuver Performance Limitations**

Maneuver	Minimum Radius (ft)	Airspeed for Minimum Radius (ft/s)	Maximum Angular Velocity (deg/s)	Airspeed for Maximum Angular Velocity (ft/s)
Flat Turn	68.86	165	137.29	165
Pull Up	74.70	165	126.57	165
Pull Down	34.32	47	148.92	165

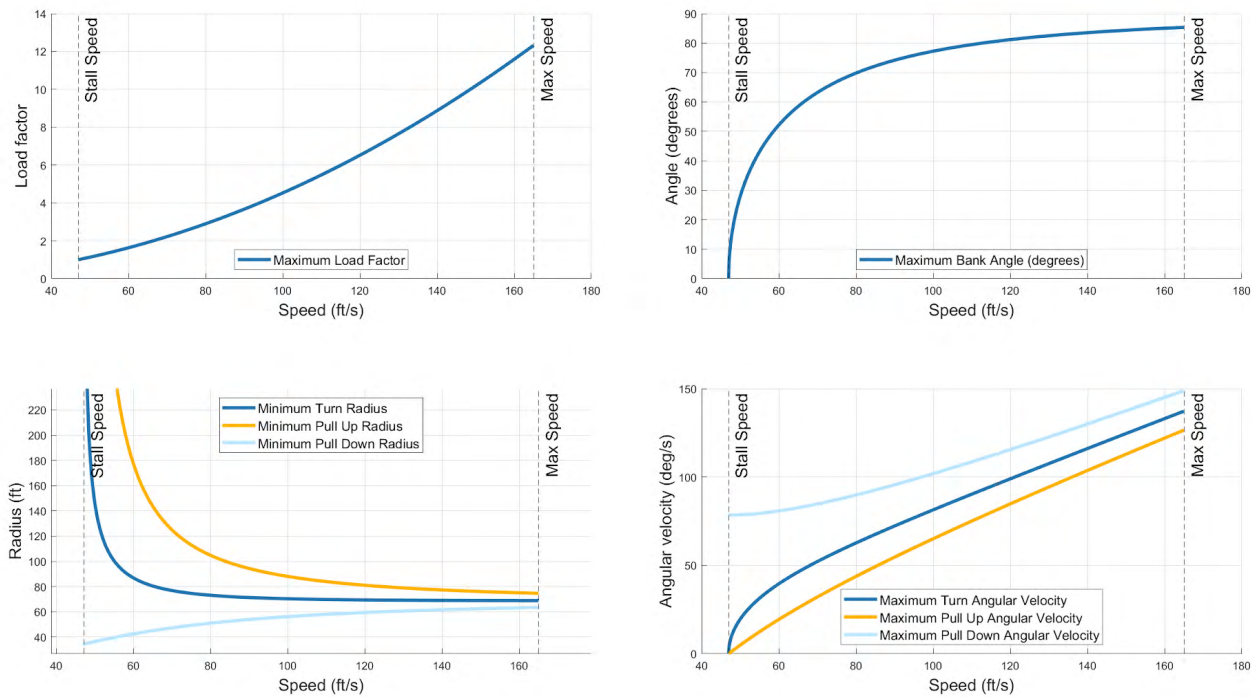


Figure 17: Maneuverability Plots

### 4.3.3 Glide Analysis

Minimum glide angle was defined as the minimum pitch angle maintainable in the absence of thrust. This is relevant for landings in the event of a propulsion system failure or complete loss of power, and was calculated via Equation 22 [4].

Glide angle was utilized to select reasonable aircraft configurations. Given that the parameter does not directly contribute to competition score, a suboptimal glide angle was tolerated for configurations with high scoring. The minimum glide angle for P1 without flaps was calculated to be around 6.6 degrees at 62 ft/s, shown in Figure 18.

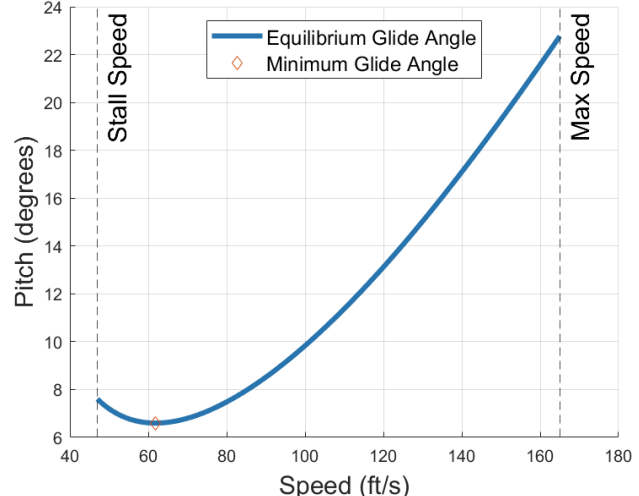


Figure 18: Equilibrium Glide Angle vs. Airspeed

$$\lambda = \min \left( \arctan \left( \frac{C_D}{C_L} \right) \right) \quad (22)$$

#### 4.3.4 Endurance

Power consumption during the straights and the turns were calculated using Equation 23 [3], which states that the product of thrust and velocity is equal to the product of efficiency and electrical power.

$$TV = eP \quad (23)$$

As stated in Table 12, the selected prop system has a net efficiency value of 81.61% at M2 speeds and 79.57% at M3 speeds. Thrust was assumed to be equal to drag at cruise velocity.  $C_D$  values, listed in Section 4.3.1 on a per mission basis, were used to evaluate drag for straights and turns.

A weighted average of power draw during straights and turns was calculated via Equation 24 to get the average power consumption across each lap.

$$\frac{1}{d} \left( \frac{2\pi R}{V_T} P_T + \frac{2000}{V_S} P_S \right) = \bar{P} \quad (24)$$

$$\frac{2\pi R}{V_T} + \frac{2000}{V_S} = d \quad (25)$$

Ultimately, Equation 23 yielded a time-averaged power draw prediction for M1, M2, and M3 of 587 W, 1759 W, and 788 W respectively. Considering the available battery energy of 80 Wh established in Section 4.2.2, the maximum possible sustained flight duration is 163 s for M2 and 356 s for M3 as calculated from Equation 25. With each M2 lap spanning 30.40 s and M3 requiring 300 s of flight, the aircraft has sufficient endurance to complete each mission.

#### 4.3.5 Takeoff Distance

Takeoff distance was not a primary concern given the lack of constraints on it in the rules. However, for the purposes of confirming that the final design would be feasible for propulsion reasons, a hard limit of 80 ft was set. For the calculation itself, the base formula from Anderson [3] was modified. The takeoff speed was approximated as 1.2 times the stall speed and calculated via Equation 26 [3].

$$V_{LO} = 1.2 V_{Stall} = 1.2 \sqrt{\frac{2W}{\rho S_w C_{L,max}}} \quad (26)$$

The  $C_{L,max}$  was taken to be 1.53 from the buildup in section 4.2.5. The average lift and drag could be approximated as the lift and drag at 70% of the takeoff speed from the formulae and buildup in Section 4.3.1, which was also used to calculate the takeoff angle. Due to the large takeoff angle, the thrust was decomposed into its normal and axial directions for a more accurate calculation. The final equations for takeoff distance are Equations 27 - 29 [3].

$$\bar{D} = D_{0.7V_{LO}} = 1.44 \frac{\rho}{2} S_w (C_{D,0} + K C_{L,max}) V_{LO}^2 \quad (27)$$

$$\bar{L} = L_{0.7V_{LO}} = 1.44 \frac{\rho}{2} S_w C_{L,max} V_{LO}^2 \quad (28)$$

$$S_{LO} = \frac{1.44W^2}{g\rho S_w C_{L,max} (T \cos(\phi) - \bar{D} + \mu(W - \bar{L} - T \sin(\phi)))} \quad (29)$$

A value of 0.040 was used for the ground friction coefficient ( $\mu$ ), and the standard value of 32.17 ft/s<sup>2</sup> was used for the gravitational acceleration constant (g). The air density ( $\rho$ ) was taken to be 0.068 lb/ft<sup>3</sup> from publicly available meteorological data of Tucson, Arizona found at Air Density Online [15]. The minimum thrust required to meet the 80 ft takeoff distance restriction was calculated to be 15.06 lbf.

## 4.4 Aircraft Stability

### 4.4.1 Static Stability

After sizing the tail using experimentally determined volume coefficients, as discussed in Section 4.2.3, the aircraft wing and tail dimensions were modeled in XFLR5 [9]. Then, a detailed center of gravity (CG) buildup was created utilizing 5 parameters. These include the expected weight of the payload, the weight of propulsion/electronics components, historical weight estimates for the wing and empennage, material densities of carbon fiber (CF), and an initial estimate of fuselage shape and length. The predicted fuselage weight was determined by measuring the density of sample 2-ply CF layups (0.038 lb/in<sup>3</sup>) and the dimensions based on a cylindrical shape (length of 43.5 in, thickness of 0.036 in, diameter of 3 in). These numbers are tabulated in Table 15. A 15% static margin was targeted based on pilot feedback after flying previous years' aircraft. XFLR5 [9]

was then used to sweep across  $\alpha$ s and determine the neutral point. The position of the battery and motor—thereby the nose position, and thus overall fuselage length—were iteratively adjusted until the optimal CG location of 3.24 in behind the wing leading edge was achieved.

**Table 15: Preliminary Component Weights and Placement for XFLR5 Weight Buildup**

Component(s)	Weight (lbf)	Position Behind Wing LE (in)
Fuselage (2-ply CF)	0.57	14.62 (center)
Wing	2.00	3.24 (1/4-chord)
Tail	0.50	35.96 (1/4-chord)
Motor + Propeller	1.50	-9.14
Battery + ESC	1.76	-2.39
Payload (M2 only)	9.26	1.57 (at CG)

Next, XFLR5 [9] was used to determine the optimal horizontal tail incidence (-0.90 degrees) for the aircraft to trim at the predicted M3 target cruise speed (106 ft/s). Since M3 is primarily an endurance mission, it was decided to trim for M3 flight conditions to minimize elevator trim drag, thus maximizing cruise efficiency for M3. The corresponding trim condition for M2 was verified and found to be within 4 ft/s of the predicted M2 target cruise speed (131 ft/s), so no further changes to the tail incidence were made.

#### 4.4.2 Dynamic Stability

The dynamic stability of the aircraft was evaluated using XFLR5 [9] for cruise conditions. A root-locus plot for the complex roots of the modes is shown in Figure 19. A mode is stable if the real part of the root is negative, and the frequency of the oscillation is proportional to the magnitude of the imaginary part.

The aircraft is stable in the roll, dutch roll, and short period pitch modes. It is slightly stable in the phugoid mode, and slightly unstable in the spiral mode. However, both of these modes have complex roots very close to zero, meaning their growth rates and oscillations are very slow. Hence, they are easily correctable by the pilot. Table 16 details the characteristic values of each complex mode.

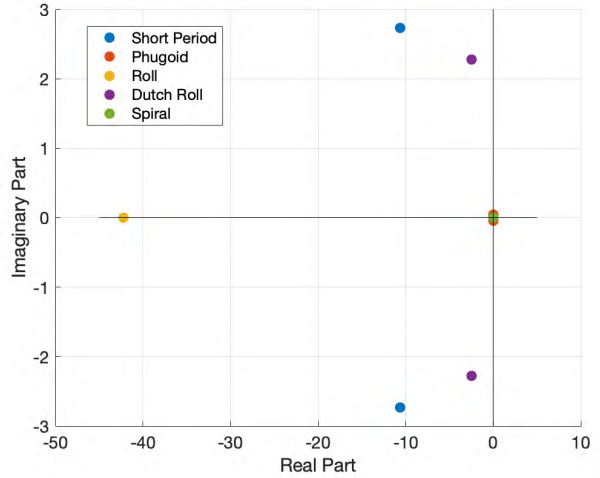


Figure 19: Complex Poles of Stability Modes

Table 16: Summary of Aircraft Stability Modes

Mode	$\zeta$	$\omega_n$ [rad/s]	$ \sigma $ [rad/s]	Time to Half Amplitude[s]
Short Period	0.53	20.20	10.71	0.07
Phugoid	0.03	0.30	0.01	67.51
Roll	N/A	N/A	42.22	0.02
Dutch Roll	0.17	2.31	0.39	1.77
Spiral	N/A	N/A	0.02	33.01

#### 4.5 Predicted Mission Performance

The raw predicted mission performance of the selected configuration was calculated using Equations 4 - 7. However, each raw mission score needed to be normalized by the maximum unscaled score of all possible configurations. To account for this, the sizing script was run twice: first solely optimizing for the M2 score, and then just the M3 score.

From this, it was determined that the maximal possible M2 subscore would be 0.37 points. Similarly, accounting for a contribution of 10 points from the X-1, the maximal possible M3 subscore was predicted to be 20 points.

For the main aircraft, the target lap time for M2 and M3 were determined to be 30.40 s and 31.90 s respectively. As such, it was predicted that the aircraft could complete M2 in a total of 91 s and fly 7 laps in M3 (accounting for takeoff and X-1 release). The final normalized scores for the two flight missions, M2 and M3, are 1.81 and 2.70 respectively. The M2 score is composed of 1.0 points for completion and 0.81

points from the normalized mission score, and the M3 score is composed of 2.0 points for completion and 0.70 points for the normalized mission score.

#### 4.6 Uncertainties and Assumptions

The initial sizing process was intentionally general, avoiding computationally intensive methods such as CFD. It assumed that the various subsystems of the aircraft were more or less independent of each other. This was an assumption requiring continuous verification in detailed sizing. For instance, it was necessary to confirm that the wake from the fuel tank bottles did not affect flow over the tail and thus the stability.

Other assumptions mainly concerned the historical values like maximum  $AR$  and  $\epsilon$  utilized during sizing, due to the number of additional external structures needed for this year's competition. Ultimately, it was assumed that the fuel tanks and X-1 would not affect most historically sourced constants, and the only change enacted was to switch the  $C_{D,0}$  from the previous 0.040 to 0.044 (see section 4.3.1). This assumption was based on CFD of the X-1 and bottle surface models attached to previous designs and is also later confirmed in CFD of the final design in section 5.3.1.

### 5. Detailed Design

#### 5.1 Dimensional Parameters

An overview of the final dimensions for both the aircraft and the X-1 are presented in Table 17.

**Table 17: Dimensional Parameters**

Bell - Air					
Wing		Horizontal Stabilizer		Vertical Stabilizer	
Airfoil	UCLA_1	Airfoil	NACA 0008	Airfoil	NACA 0008
Span	72.00 in	Span	18.82 in	Span	8.68 in
Root Chord	11.45 in	Root Chord	6.96 in	Root Chord	7.30 in
Tip Chord	9.73 in	Tip Chord	5.22 in	Tip Chord	5.47 in
Aspect Ratio	6.80	Aspect Ratio	3.09	Aspect Ratio	1.36
Reference Area	5.30 ft <sup>2</sup>	Reference Area	0.80 ft <sup>2</sup>	Reference Area	0.39 ft <sup>2</sup>
Control Surfaces			Fuselage		
	Span	Mean Chord	Max Deflection	Total Length	45.62 in
Ailerons	12.60 in	2.51 in	50 deg	Max Width	3.59 in
Flaps	23.40 in	2.72 in	30 deg	Max Height	3.93 in
Elevator	18.82 in	2.13 in	30 deg	Frontal Area	7.86 in <sup>2</sup>
Rudder	8.68 in	2.24 in	30 deg	Wetted Area	3.14 ft <sup>2</sup>
X-1					
Wing		Horizontal Stabilizer		Vertical Stabilizer	
Airfoil	AG12	Airfoil	NACA 0010	Airfoil	NACA 0010
Span	12.23 in	Span	4.56 in	Span	1.99 in
MAC	2.84 in	MAC	1.48 in	MAC	1.46 in

## 5.2 Structural Characteristics

### 5.2.1 Detailed Fuselage Design

The fuselage is one continuous piece from the nose to the empennage. The CAD model is shown in Figure 20. The fuselage is constructed from 2-ply CF stacked at alternating 45 degrees weave directions, improving structural integrity. The decision to utilize a 2-ply CF layup was made using preliminary finite element analysis (FEA) simulations with Ansys ACP [16], demonstrating that the fuselage could reliably withstand an extreme load case of 200 lbf (25g load) on the wing mount area, providing a significant margin of safety for the operational load case of 100 lbf (5g load). The FEA is shown in Figure 21.

In order to access the electronics in the nose cone, a hatch was made on the side of the fuselage. The structural integrity of the fuselage was once again verified using Ansys ACP [16]. A vertical force of 135 lbf was applied to the top of the fuselage. The resulting peak stress was 70,000 psi, safely below the CF's ultimate strength

of 300,000 psi, validating the hatch. The normal force analysis is shown in Figure 22. Additional analysis of a 250 lbf-in moment load applied to the top of the fuselage, shown in Figure 23, revealed that the structure would experience a maximum stress of 126,880 psi, still below the ultimate strength.

### 5.2.2 Detailed Wing Design

The internal wing structure consists of a wooden rib and stringer structure with a hexagonal CF spar. The wing is attached to the fuselage by a basswood wingbox to distribute the load generated by the wing. The airfoil ribs are constructed using basswood for its ideal max strength and strength to weight ratio. The wing assembly CAD model is shown in Figure 24. The

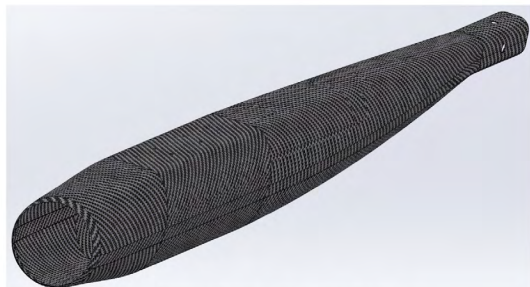


Figure 20: Fuselage CAD

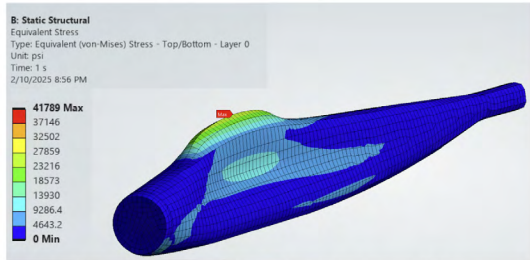


Figure 21: Fuselage Loads from Wing  
(Deformation is at 4.2x scale)

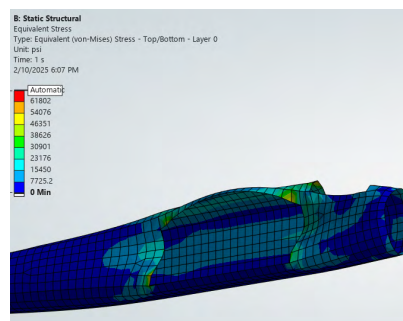


Figure 22: Normal Force Analysis on Fuselage

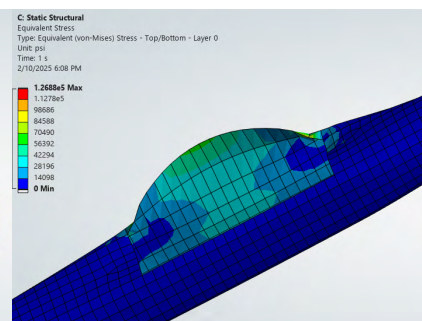


Figure 23: Moment Load Analysis on Fuselage

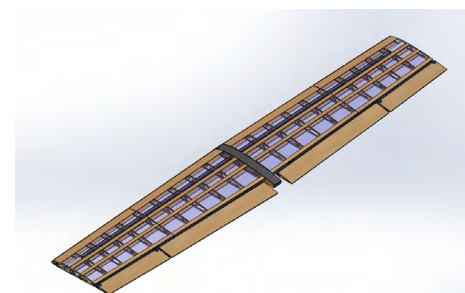


Figure 24: Wing Assembly

maximum predicted lift force is 180 lbf, calculated from Equation 30, given the maximum predicted airspeed and highest  $C_L$  possible.

$$L_{max} = \frac{1}{2} \rho S_w C_{L,max} V_{max}^2 \quad (30)$$

To select a wing spar, several COTS spar options were gathered and put into a MATLAB [17] script, which used conventional Euler-Bernoulli beam bending calculations to predict spar performance under the maximum lift load. The spars were sized to withstand the maximum predicted lift with a factor of safety of 2 to account for the load with pylons.

Further analysis in Ansys FEA [16] proved that the hexagonal spar would meet the loading requirements.

Additionally, in order to investigate other failure points, the entire wing structure was evaluated in FEA using the predicted maximum 270 lbf load with a 1.5 factor of safety as shown in Figure 25. The stress on the ribs was calculated to be below the yield strength of basswood, except near the wingbox where the stringers meet the ribs. To rectify this, the wingbox was reinforced with CF around areas of high stress.

### 5.2.3 Detailed Empennage Design

The empennage, modeled in Figure 26, is part of the monocoque CF fuselage. A basswood tailbox is bonded to the fuselage and interfaces with the horizontal and vertical stabilizers. To simplify computation, the tailbox, horizontal stabilizer, and vertical stabilizers were evaluated separately with load application to the proper sections of the models.

The horizontal stabilizer needed to handle the negative lift that stabilizes the rear of the aircraft, which was calculated to be around 10 lbf using Equation 30. The spar used was made of CF to ensure the stabilizer could handle this load. According to the FEA in Figure 27, the maximum stress on the horizontal stabilizer was well below the ultimate stress of the CF, so the stabilizer could handle the expected load and more.

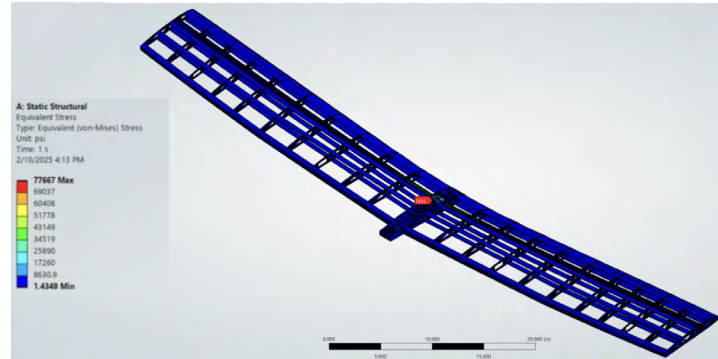


Figure 25: Full Wing FEA

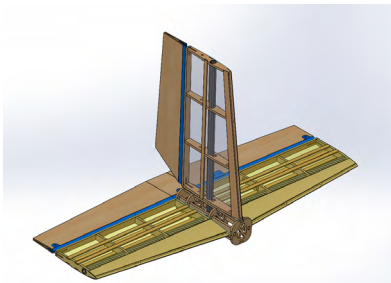


Figure 26: Empennage Assembly

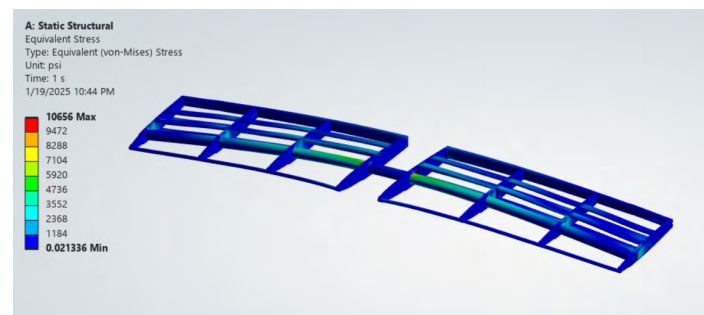


Figure 27: Horizontal Stabilizer FEA Results

The vertical stabilizer was similarly evaluated using FEA and the lateral load was calculated to be around 20 lbf via Equation 30.

The main consideration for the tailboxes' design was its ability to withstand the force exerted by the horizontal and vertical stabilizers. FEA indicated that the structure experienced failure when 50 lbf of downwards force was applied, and since 50 lbf was significantly higher than the maximum expected load, the structure was deemed sufficiently strong.

#### 5.2.4 Detailed Landing Gear Design

The landing gear was machined from 7075-T6 aluminum alloy and features several lightening holes to reduce weight. Since the landing gear was mounted directly to the wing spar, a spring suspension system was implemented to soften landing impacts. The CAD model is shown in Figure 28.

To ensure that the landing gear structure would withstand a hard landing, FEA was conducted under a vertical load of 120 lbf as shown in Figure 29 and a lateral load of 20 lbf. A worst case scenario was assumed where the spring does not function and the landing gear effectively becomes a single homogenous piece. With respect to the vertical load, the maximum stress on the structure was 22,885 psi. Under a lateral load, the maximum stress on the structure was 50,013 psi, with a majority of the stress concentrated in the upper half of the landing gear near the spar. In both cases, the maximum stresses were located in the vertice where the two pieces meet, which is typical of finite element methods. Both stress values were under the yield strength of 7075-T6 aluminum.

### 5.3 Subsystem Design

#### 5.3.1 Aerodynamic Subsystem Design

For final verification of flight characteristics, CFD simulations were conducted to assess the final lift and drag characteristics of P1. A total of three Reynolds numbers were considered for analysis, those being the Reynolds numbers that corresponded to stall speed, M2 target mission cruise speed, and M3 target mission cruise speed. An  $\alpha$  sweep of simulations from 0 degrees to +18 degrees in increments of 2 degrees were conducted for each of these conditions, with results shown in Figure 30. From these, accurate turn performance and energy consumption estimates could be calculated.

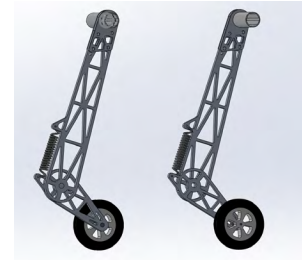


Figure 28: Landing Gear CAD

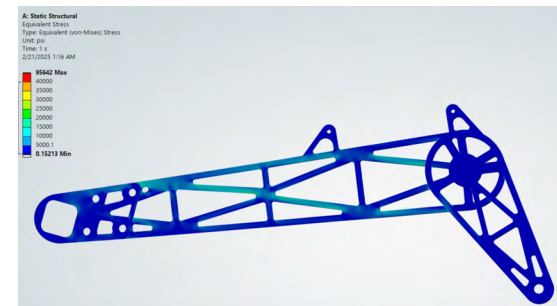
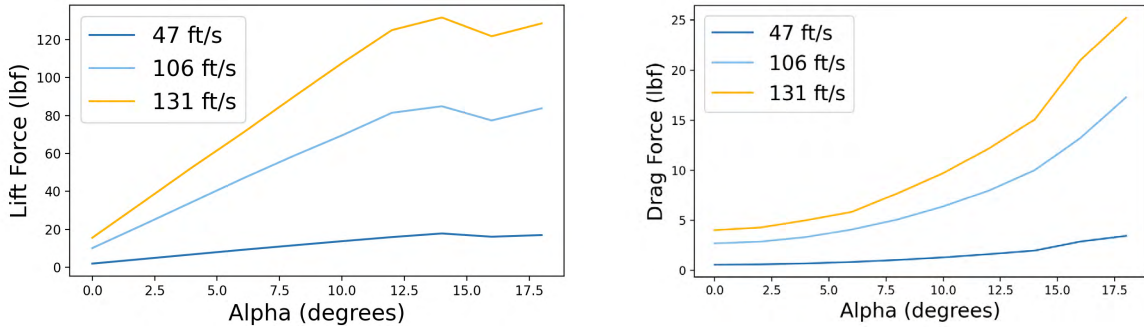


Figure 29: FEA Results for Vertical Force



**Figure 30: Lift (Left) and Drag (Right) vs.  $\alpha$  at Various Speeds**

### 5.3.1.1 Wing Taper and Washout Optimization

The wing geometry was designed to create an elliptical spanwise lift distribution that, according to lifting-line theory, maximizes the lift-to-induced-drag ratio of the wing. Elliptical wings were deemed too difficult to manufacture, so the wing was designed with a combination of wing taper and washout to mimic an elliptical lift distribution.

Taper ratios from 0.2 to 1 were evaluated using a MATLAB [17] script, in which the Prandtl lifting-line equation was used to compute theoretical lift, induced drag, and  $\epsilon$ , shown in Figure 31. A taper ratio of 0.4 yielded the best lift to drag results, but would severely limit the size of the wing spar in practice. Therefore, a compromise taper ratio of 0.85 was chosen in order to fit the appropriate wing spar while still maintaining a relatively high lift to induced drag ratio.

With the taper ratio of 0.85 and the rest of the wing's properties defined, the MATLAB [17] script computed the angle of attack required at each spanwise point to produce an elliptical lift distribution, from which the geometric twist was derived. The resulting twist distribution is plotted in Figure 32. Analysis in XFLR5 [9] confirmed the efficiency gain, with  $\epsilon$  for the wing calculated to be 0.901. This is substantially higher than the average historical  $\epsilon$  value of 0.7 and corresponds to a 22% reduction in induced drag.

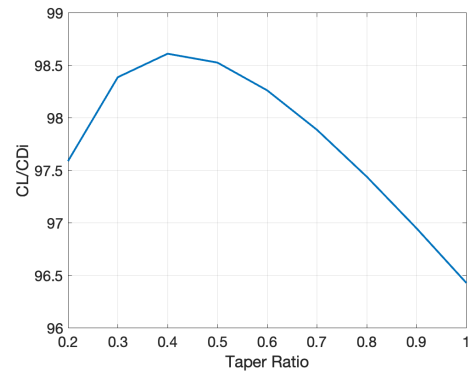


**Figure 31: CI to Induced Drag Ratio Evaluated for Different Taper Ratios**

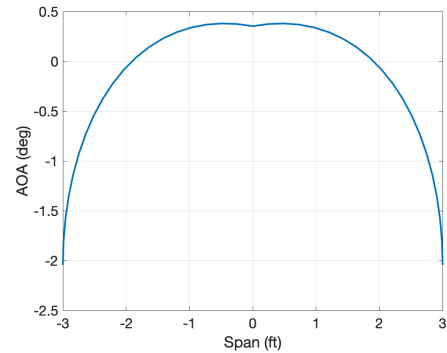


**Figure 32: Spanwise Angle of Attack Distribution**

### 5.3.1.2 Trade Studies

As part of the design process, various additional aerodynamic components were considered for improving performance.

To enhance aerodynamic efficiency around the landing gear, wheel fairing designs were developed using SolidWorks [2] surface modeling. CFD simulations at mission cruise speeds were conducted to evaluate the drag performance of each prototype, leading to the selection of a final fairing design that minimizes weight while maintaining an aerodynamic shape, as shown in Figure 33.

Comparison CFD simulations were performed at the predicted M3 target mission cruise speed (106 ft/s) on the landing gear with and without fairings. Figure 34 presents the streamlines around the wheel for both configurations. Quantitatively, adding the wheel fairings decreased the drag force from 0.95 lbf to 0.89 lbf, a 6.42% reduction. Without fairings, the wake is more turbulent, further supporting the observed drag reduction. To validate these predictions, the wheel fairing design was 3D printed and mounted to the landing gear for testing in UCLA's wind tunnel. Details of the testing methodology and analysis are discussed in Sections 7.2.3 and 8.1.2. With each fairing weighing 0.030 lb, the drag reduction achieved compensated for the slight increase in weight due to their addition.

To mitigate trailing edge vortex formation at the wingtips and reduce induced drag, endplates were investigated. Endplates with 1/4 inch thickness and 1 inch offset from the airfoil were attached to the existing CFD surface model, as displayed in Figure 35. Larger endplates were not considered as any manufacturable model would be too weight costly.

A CFD sweep at 106 ft/s (M3 cruise speed) between -1 and 2 degrees  $\alpha$  was conducted on the model. The results of the CFD are displayed in Figure 36 and

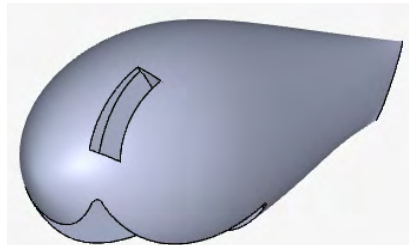


Figure 33: Wheel Pant CAD Model

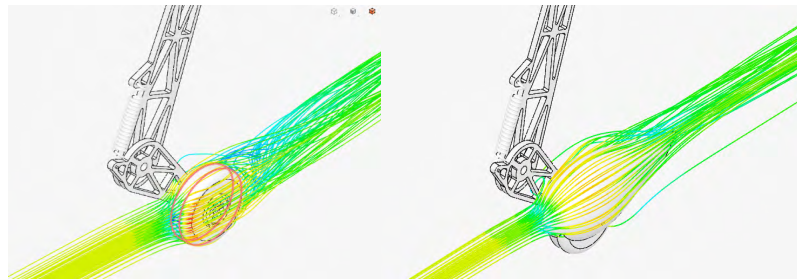


Figure 34: Flow Streamlines Without Pant (left)  
Flow Streamlines With Pant (right)



Figure 35: CFD Model of Endplates

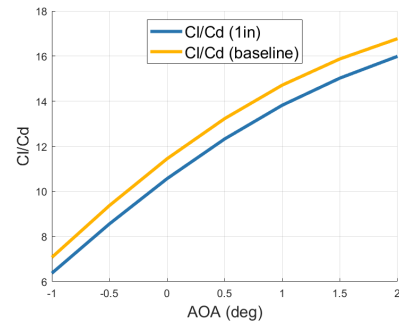


Figure 36: L/D Ratio Plot at Various  $\alpha$ s

show a negative change in the  $L/D$  ratio across the board. As such, this was ultimately not implemented in the final design.

### 5.3.2 Propulsion Specifications

The propulsion subsystem was preliminarily designed around the optimization of the motor-propeller combo, which yielded the same results for both missions. The final selected components, all of which are located in the nose of the aircraft, are listed in Table

Table 18: Propulsion Components Specifications

Item	Model	Mass (lbs)
Propeller	APC 18 x 14	0.35
Motor	Scorpion A-5025 310 Kv	1.15
ESC	Castle Phoenix Edge Lite HV 120 A	0.26
Fuse	100 A Maxi	0.20
Propulsion Battery	Gaoneng 8s 3300mAh LiPo	1.50
<b>Total</b>		3.46

18. The 29.6 V Gaoneng GNB 8S 3300 mAh LiPo battery was selected for its low internal resistance and higher C-rating compared to similar COTS options. The lightweight Phoenix Edge Lite HV 120 A electronic speed controller (ESC) was selected for its data logging capabilities and appropriate specification for the expected maximum current draw. Per competition rules [1], a 100 A fuse was placed between the ESC and battery for safety and as an arming plug.

### 5.3.3 Avionics Specifications

The Avionics PCB, a custom signal distribution PCB designed in Altium Designer [18], is located in the fuselage and is powered by a 2-cell 8.4 V 1000 mAh LiPo battery. The PCB is shown in Figures 37 and 38. The PCB contains a Hobby Eagle A3 V2 gyro and FrSky RB-10 Redundancy Bus, with ports to plug in external electronics such as servos and sensors. A gain-adjustment knob on the TX gives the pilot precise control of the aircraft gyro's sensitivity in flight.

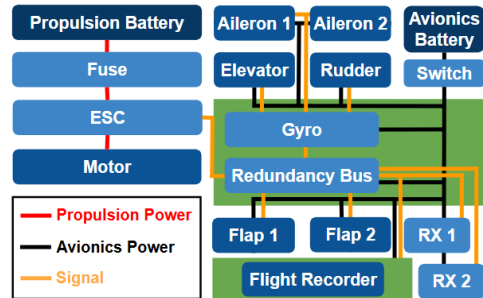


Figure 37: Avionics PCB Design

The TX16S transmitter was selected for its telemetry logging capability and highly customizable firmware. The RB-10 Redundancy Bus connects to two FrSky R9 Slim+ RXs and uses the RX with the best radio connection. The two 915 MHz RXs and a FrSky R9M TX module were used to maximize radio range and minimize interference compared to 2.4 GHz radio systems. The RX also supports telemetry, allowing Smart Port protocol sensors to send live data to the TX for the pilot to log and monitor. Each RX is located in the fuselage with antennas on the top and bottom of the aircraft to reduce radio blind spots induced by the conductive CF structure.

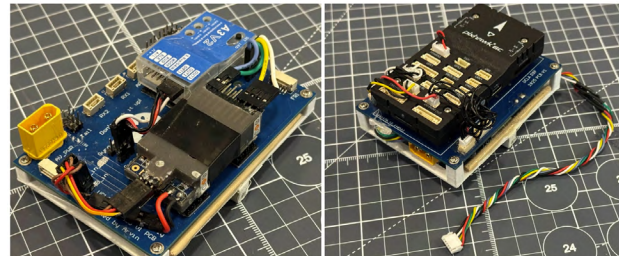


Figure 38: Avionics PCB Assembly (Left) and Flight Recorder PCB Assembly (Right)

The tail, wing, and release mechanism contains KST X10, DS113MG, and HB08B servos, respectively. The sensor suite consists of a custom g-sensor, a FrSky VARI ADV altimeter, a FrSky FAS100 propulsion current sensor, and a FrSky ASS100 ADV air speed sensor. All data from the sensors are telemetized to the live data screen on the pilot's transmitter using the FrSky Smart Port protocol, except for the MS4525DO airspeed sensor that uses the I2C protocol to log on-board data onto the Flight Recorder.

The Flight Recorder is a custom-made black box centered around a Pixhawk 6C Flight Controller (FC) that records flight data onto an SD card for the Aerodynamic Subteam to analyze and refine the performance of the aircraft. A removable HolyBro M9N GPS and HolyBro MS4525DO airspeed sensor can be mounted onto the aircraft to provide additional data for logging. The FC and GPS are not for use during the competition to comply with competition rules [1]. The Flight Recorder PCB and Avionics PCB communicate using a 6-pin port to allow the Pixhawk 6C to record all necessary data from the aircraft's sensors. Table 19 shows the specifications for all avionics used on the aircraft.

**Table 19: Aircraft Avionics Breakdown**

Location	Item	Model	Mass (lbs)
Nose	Current Sensor	FrSky FAS100	0.070
Wing	4 x Wing Servos	KST DS113MG	0.026
	Telemetry Airspeed Sensor	FrSky ASS100 ADV	0.035
	Flight Recorder Airspeed Sensor	HolyBro MS4525DO	0.035
Fuselage Center of Gravity	Altimeter	FrSky Vari ADV	0.010
	Release Mechanism Servo	KST HS08B	0.020
	Gyro	Hobby Eagle A3 Pro	0.025
	Redundancy Bus	FrSky RB-10	0.022
	Avionics Battery	Ovonic 2s 1000 mAh LiPo	0.130
	Primary RX	FrSky R9 Slim Plus	0.020
	Avionics Switch	Generic Toggle Switch	0.020
	Microcontroller for G-Sensor	Arduino Nano	0.015
	Accelerometer for G-Sensor	GY-521 MPU-6050	0.008
	GPS	HolyBro M9N	0.071
Flight Recorder (Fuselage)	Flight Controller	HolyBro Pixhawk 6C	0.185
	Battery	Spektrum 3s 300 mAh LiPo	0.055
Tail	Secondary RX	FrSky R9 Slim Plus	0.020
	2 x Tail Servos	KST X10	0.070
Total			0.837

### 5.3.4 Mission Subsystem Design

#### 5.3.4.1 Fuel Tanks & Pylons

For the fuel tank, plastic 16.9 fl. oz. Tejava bottles were chosen for their smooth outer shape and conveniently-placed divots. The divots provided a place for the pylon to grab onto and prevent the tank from slipping forward or backward. Major considerations for pylon design were weight, strength, and aerodynamic impact. Aluminum, CF, and 3D-printed plastics were considered for the pylon's construction. 3D-printed polyethylene terephthalate glycol (PETG) was chosen for its

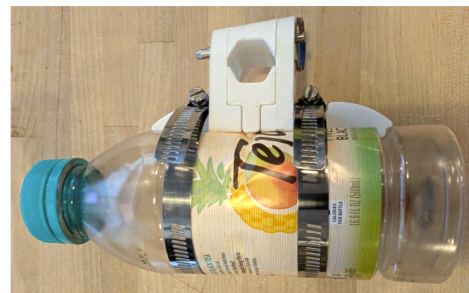


**Figure 39: Pylon Installed on Fuel Tank**

durability compared to polylactic acid (PLA), lower density compared to metal, and geometric flexibility.

The final pylon design has two main components and attaches to the wing spar, as shown in Figure 39. The lower piece slots up the bottom of the spar and the upper piece is placed by aligning the built-in grooves, as seen in Figure 40. There are small extrusions that extend from the bottom face and press into the fuel tank divots. The pylon maintains a low profile around the wing to minimize drag. Once the two halves are in position, a quick-release pin is pushed into the two pieces to securely attach the pylon to the spar. To attach the fuel tanks, hose clamps are slotted through the pylon and tightened with a drill around the fuel tank. To improve ergonomics, the pin hole was placed at an angle to the wing. During M1 and before GM, the holes for the pylons in the wing are covered with wood veneer and stuck with velcro for easy removal.



Figure 40: Pylon Components Before Assembly (Left), Assembled Pylon Pieces (Middle), and Full Pylon (Right)

#### 5.3.4.2 X-1 Airframe

The X-1 airframe was designed to be as light as possible while being strong enough to survive hard landings. The full CAD model is shown in Figure 41. The wing is composed of a foam body that is reinforced with a CF rod and laminated with packing tape. The fuselage is composed of CF rods and a central CF plate to mount to the wing and release fin. The CF release fin has chamfers to facilitate insertion into the release mechanism and is located atop the CG of the X-1 to avoid imbalances. The CF control surfaces are attached with packing tape hinges and actuated by steel push rods. A mechanism was created using two thin steel rods to actuate both surfaces simultaneously with one servo, as shown in Figure 42.

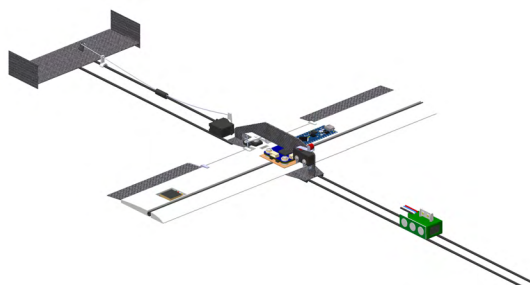


Figure 41: Full X-1 CAD Assembly with Electronics

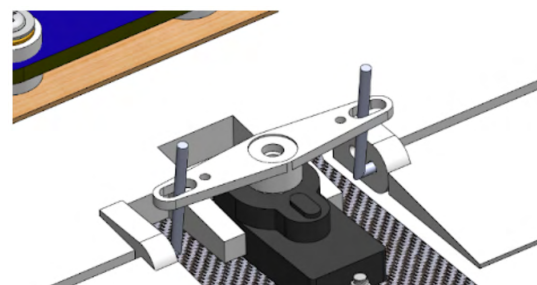


Figure 42: Aileron Mechanism

### 5.3.4.3 X-1 GNC & Avionics

The X-1 employs an on-board electronic GNC system to guide itself into the bonus box upon release from the aircraft. The GNC system runs on a Matek H743-MINI V3 FC running ArduPilot [19], a guidance firmware that allows for custom scripts configured using the Mission Planner [20] software. The X-1 is completely autonomous with no RX. A sequence of 3D waypoints based on GPS coordinates and altitudes are created in Mission Planner [20] and uploaded to the FC. Upon release from the aircraft, a limit switch is toggled and triggers a microcontroller on the X-1 to send a mission-start signal to the FC using the MAVlink [21] serial protocol, upon which the X-1 begins flying to the waypoints, initially headed towards Waypoint 2 in Figure 43. Waypoints are sequentially placed to allow the X-1 to fulfill the 180-degree turn requirement and land in the center of the competition bonus box. Upon initial testing, waypoint-based X-1 flight paths proved to be inconsistent and prone to falling outside of the bonus box in windy conditions. To improve landing location accuracy, a custom control law was developed to function within Ardupilot [19] using custom-coded Lua [22] scripts. The Lua [22] script dynamically determines its distance from the landing point and adjusts its trajectory accordingly. Wind is detected by comparing the zero-wind reference glideslope to the instantaneous glideslope the X-1 experiences, ranging from 10 to 20 degrees. The reference glideslope was measured in flight tests and set as a constant. A PID controller calculates elevator input based on the difference between measured and reference glideslope. The guidance law in the script



**Figure 43: Competition Mission with Waypoints at Local Airfield, Northbound Takeoff**

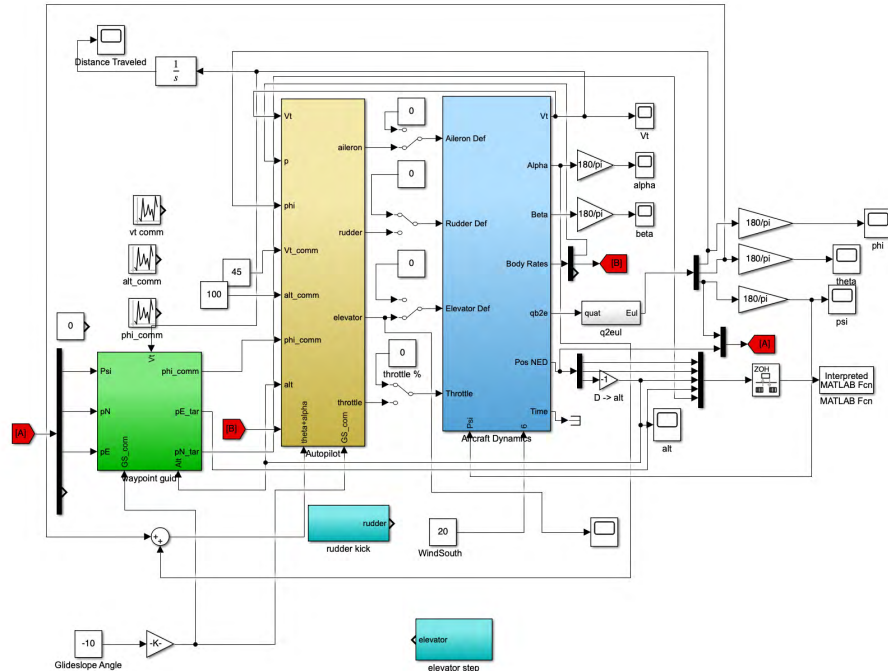


**Figure 44: Simulink Model Used to Develop Control Law**

predicts the remaining glide distance and uses this value to calculate when to execute the 180-degree turn and proceed towards the bonus box.

The custom control law was developed and simulated in Simulink [23], as shown in Figure 44. Aerodynamic characteristics of the X-1 were determined using in-flight measurements and wind tunnel testing. The simulation was run across various release velocities, altitudes, positions, and wind conditions. After refining the Simulink [23] control law, the program was converted to a Lua [22] script with ArduPilot [19] compatibility and uploaded to the FC.

The final avionics buildup for the X-1 is summarized in Table 20 and shown in Figure

45. The HGLRC M100-MINI GPS was selected for its short warm-up time and high accuracy. A STVL1530X LiDAR was implemented to account for low-altitude inaccuracies to avoid rough landings, while the Matek H743-MINI V3 FC's internal barometer and GPS are primarily used for altitude measurement. An ESP32 Arduino Nano was chosen for its MAVlink [21] compatibility to initiate the GNC program. FH-2502 micro servos were chosen for their light weight to actuate the elevator and ailerons of the X-1. The uniLIGHT 24 W DUAL Strobe light module was chosen for its small form factor and high luminosity to ensure it can be seen from long distances. The Palm Power 3s 100 mAh Gen2 LiPo battery was selected for its small size and 12 V compatibility with the strobe lights. The strobing of the LEDs are controlled by the YM E-Bright LED strobe controller.

#### 5.3.4.4 X-1 Release Mechanism

The X-1 release mechanism is located at the CG, internal to the fuselage of the main aircraft. The CAD model is shown in Figure 46. It consists of a 3D-printed case, KST HS08B servo, servo arm, and pushrod. To interface with the release

**Table 20: X-1 Avionics Breakdown**

Location	Item	Model	Mass (lbs)
Nose	Avionics Battery	Palm Power 3s 100 mAh Gen2 LiPo	0.027
	Strobe LED	uniLIGHT 24 W DUAL Strobe 12V/3S	0.009
	Strobe Controller	YM E-Bright LED strobe controller	0.008
Wing	Aielron Servo	Flash Hobby FH-2502	0.007
	GPS	HGLRC M100-MINI	0.006
	LiDAR	HolyBro ST VL53L1X	0.005
	Microcontroller for MAVlink	ESP32 Arduino Nano	0.016
	Limit Switch	Generic Limit Switch	0.005
	Flight Controller	Matek H743-MINI V3	0.017
Fuselage	Elevator Servo	Flash Hobby FH-2502	0.007
<b>Total</b>			<b>0.107</b>

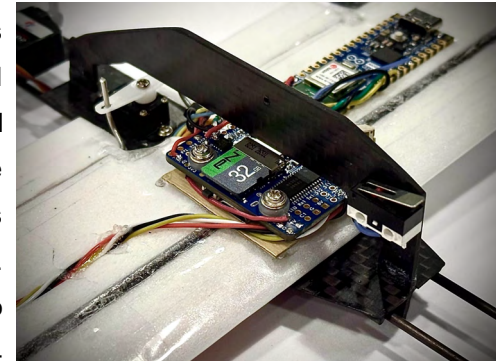


**Figure 45: Assembled X-1 Electronics Close-up**

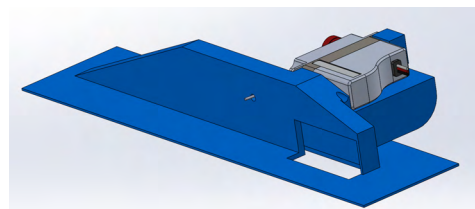


**Figure 46: X-1 Release Mechanism**

mechanism, a CF fin with a hole in the center is attached to the X-1. The chamfers allow drag on the X-1 to vector a downward force to aid in release.

The casing has a slot that matches the profile of the X-1's fin and constrains the fin in every direction while the X-1 is loaded. The servo inserts the pushrod through both a hole in the case and fin while the X-1 is fully loaded, vertically constraining the X-1. To release the X-1, the servo pulls the pushrod out to allow the fin, and consequently the X-1, to drop.

#### 5.4 Weight and Balance

Critical components of P1 are listed in Table 21 along with their weight and relative position behind the nose of the aircraft. Note that the pylons, bottle payload, X-1, and X-1 release mechanism were centered around the CG of the aircraft. The fuselage position is based on where its center of gravity is located. The motor + propeller position is negative due to being in front of the nose. The wires, additional electronics, fasteners, adhesives, and other miscellaneous items are distributed throughout the aircraft, and thus do not have a specified position.

**Table 21: P1 Component Weights and Positions**

Component	X location behind Nose (in)	Weight (lbf)		
		M1	M2	M3
Fuselage	25.07	0.65	0.65	0.65
Horizontal Stabilizer	42.26	0.25	0.25	0.25
Vertical Stabilizer	42.18	0.14	0.14	0.14
Wing	8.64	1.50	1.50	1.50
Landing Gear (both)	10.29	1.13	1.13	1.13
Pylons + Bottle Payload	11.29	0.00	9.33	0.07
X-1 + Release Mechanism	11.29	0.10	0.29	0.29
Motor + Propeller	-2.00	1.50	1.50	1.50
Battery	5.75	1.50	1.50	1.50
ESC	5.75	0.26	0.26	0.26
Avionics Battery	38.64	0.13	0.13	0.13
Wires + Additional Electronics	-	0.90	0.90	0.90
Fasteners, Adhesives, Miscellaneous	-	1.15	1.15	1.15
<b>Total Weight (lbf)</b>		9.21	18.73	9.48
<b>Neutral Point (in. behind nose)</b>		11.95	11.79	11.79
<b>CG Location</b>		10.36	10.20	10.20
<b>Static Margin (%)</b>		15.00	15.00	15.00

## 5.5 Flight Performance

The sizing script calculated lift and drag polars for the aircraft, as outlined in section 4.5. From these polars, various flight performance values could be calculated. Stall speed for a fully loaded flight was calculated via Equation 31 from [3].

$$V_{stall} = \sqrt{\frac{2W}{\rho S_w C_{L,max}}} \quad (31)$$

The other flight speeds considered were Carson's speed, maximum speed, maximum range speed, and

**Table 22: Summary of Important Flight Speeds**

Types of Velocities	Values (ft/s)
Stall Speed	47.28
Maximum Range Velocity	61.9
Carson's Speed	84.4
Maximum Speed	165

maximum endurance speed [3]. Although these are not the speeds at which M2 and M3 are flown, they were still useful for restricting infeasible configurations. Maximum speed was calculated using data from aerodynamic and propulsive analysis. Carson's speed was found by maximizing  $C_L^{3/2}/C_D$ , and maximum range speed was found by maximizing  $C_L/C_D$ . The results are summarized in Table 22.

## 5.6 Mission Performance

Table 23 summarizes flight mission performances and expected scores in comparison to hypothetical best-performing teams. UCLA's expected total score is 5.84, which is the best performing aircraft overall according to this year's sizing script.

**Table 23: Final Mission Performance Predictions and Comparisons**

Parameter	M1	M2	M3	GM
Gross Weight (lb)	11.41	20.81	11.55	-
Target Cruise Speed (ft/s)	105.96	131.23	105.96	-
Stall Speed (ft/s)	38.4	47.282	38.4	-
Lap Time (s)	-	30.44	31.94	-
Predicted Performance	Complete	0.30 lb/s	7 laps	75 s
Estimated Maximum Performance	N/A	0.37 lb/s	10 laps	25 s
Predicted Score	1	1.81	2.7	0.33
Total Score		5.84		

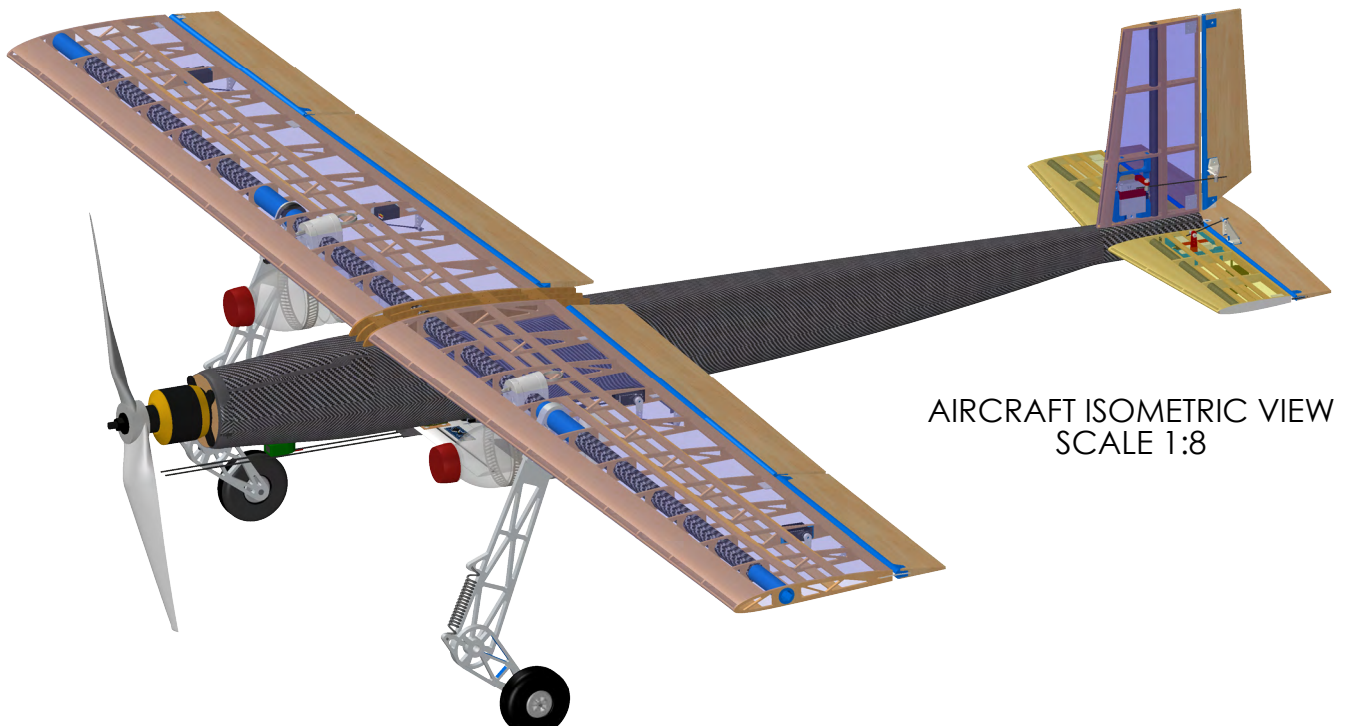
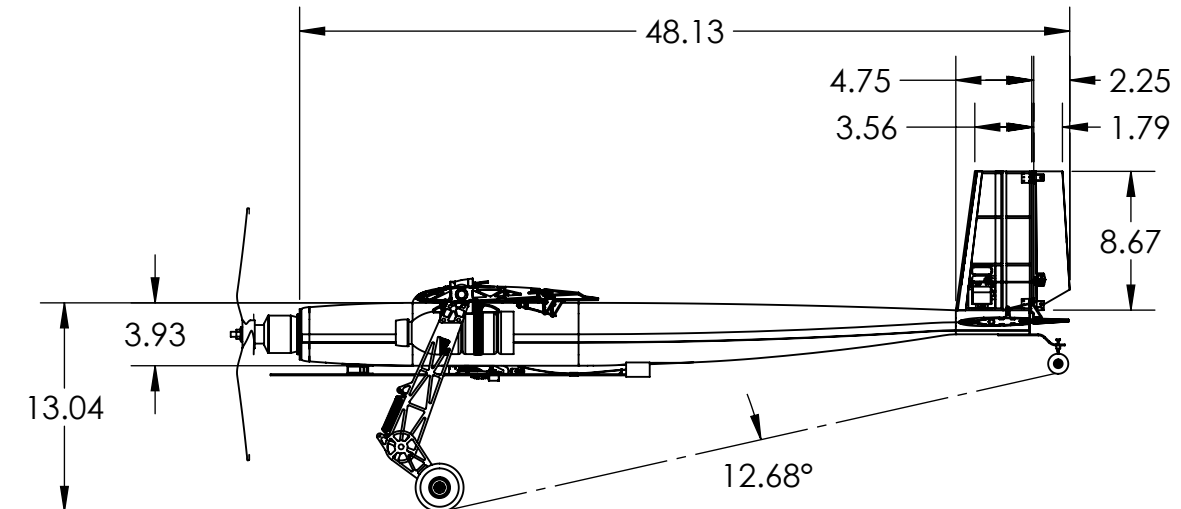
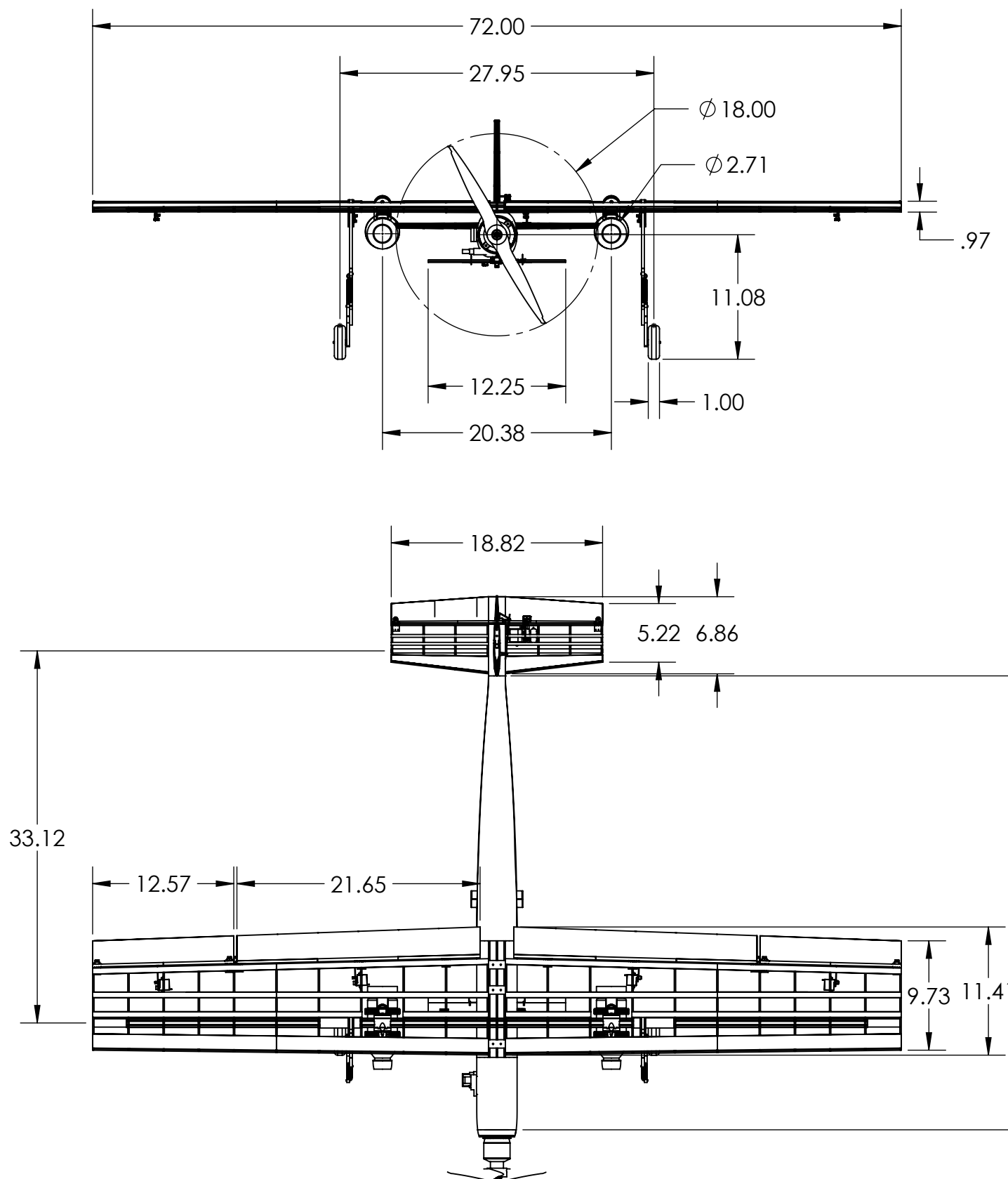
4

3

2

1

B



Bell-Air

DRAWN BY  
Grace Mullen

Aircraft Three-View

SCALE: 1:12

CHECKED BY  
Siddharth Singh

University of California, Los Angeles

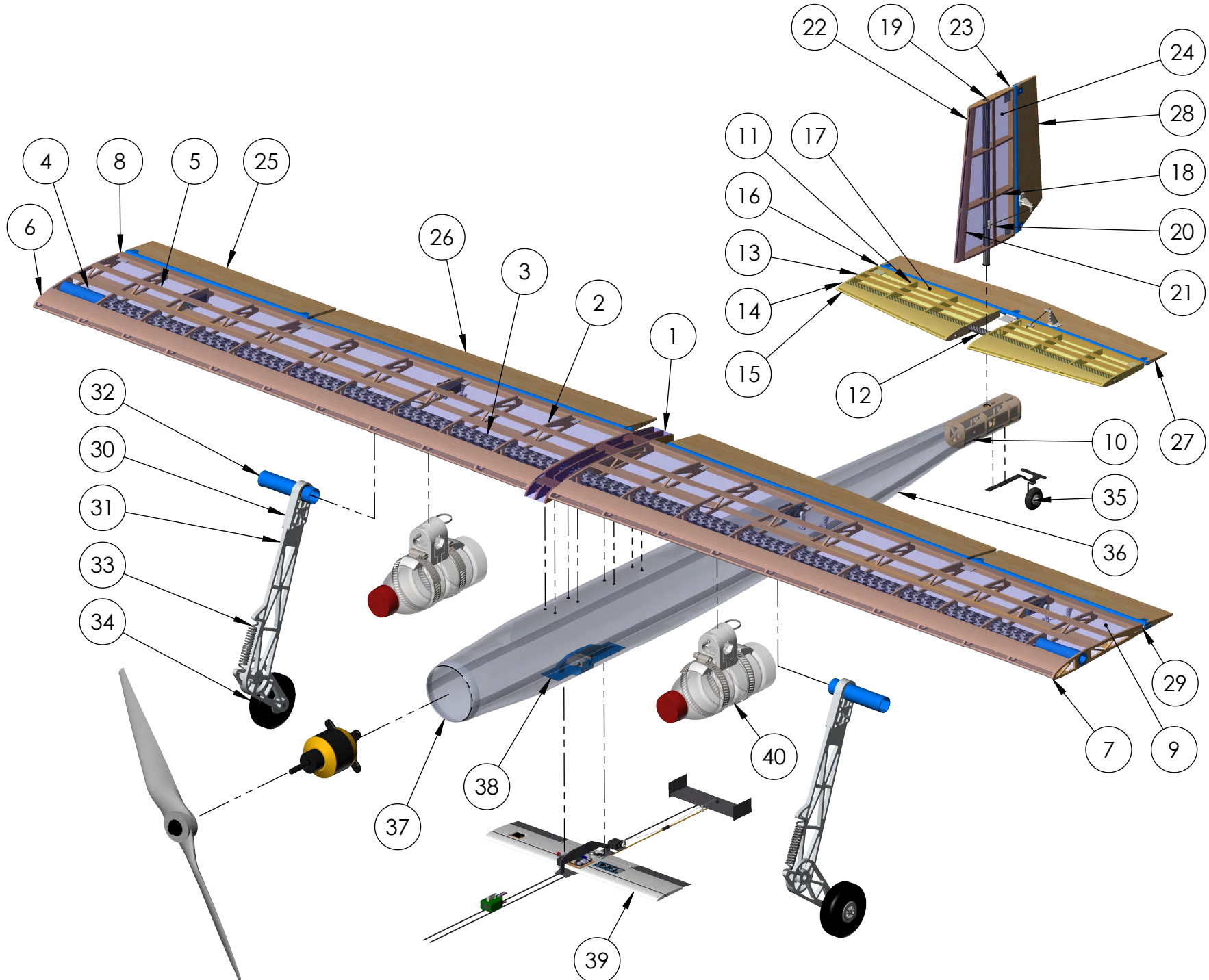
DATE  
02/21/2025

All dimensions are inches unless otherwise specified.

11x17

SHEET 1 OF 4

ITEM NO.	PART	MATERIAL	QTY.
1	Wing Box	Basswood	1
2	Wing Rib	Basswood & Balsa	22
3	Wing Spar	Carbon Fiber	1
4	Wing Spar Extender	PETG	2
5	Wing Stringer	Balsa	18
6	Wing Leading Edge Cover	Balsa	8
7	Wing Leading Edge Dowel	Birch	4
8	Wing Trailing Edge Web	Balsa	2
9	Wing MonoKote	MonoKote	2
10	Tail Box	Basswood	1
11	Horizontal Stabilizer Rib	Basswood	8
12	Horizontal Stabilizer Spar	Carbon Fiber	1
13	Horizontal Stabilizer Stringer	Balsa	8
14	Horizontal Stabilizer Leading Edge Cover	Balsa	4
15	Horizontal Stabilizer Leading Edge Dowel	Birch	2
16	Horizontal Stabilizer Trailing Edge Web	Balsa	2
17	Horizontal Stabilizer Monokote	MonoKote	2
18	Vertical Stabilizer Rib	Basswood	4
19	Vertical Stabilizer Spar	Carbon Fiber	1
20	Vertical Stabilizer Stringer	Balsa	2
21	Vertical Stabilizer Leading Edge Cover	Balsa	2
22	Vertical Stabilizer Leading Edge Dowel	Balsa	1
23	Vertical Stabilizer Trailing Edge Web	Balsa	1
24	Vertical Stabilizer Monokote	MonoKote	1
25	Aileron	Balsa/PETG	2
26	Flap	Balsa/PETG	2
27	Elevator	Balsa/PETG	1
28	Rudder	Balsa/PETG	1
29	Hinge	-	15
30	Front Landing Gear Mount	Al 7075-T6	2
31	Front Landing Gear	Al 7075-T6	2
32	Front Landing Gear Spacer	PETG	2
33	Front Landing Gear Suspension	Steel	2
34	Front Landing Gear Wheel	Rubber	2
35	Tail Gear	-	1
36	Fuselage	Carbon Fiber	1
37	Motor Mount	Carbon Fiber & Balsa	1
38	X-1 Release Mechanism	-	1
39	X-1 Glider	-	1
40	Pylon & Fuel Tank	-	1



Bell-Air		
DRAWN BY Pearl Klassen	Structural Arrangement	SCALE: 1:7
CHECKED BY Siddharth Singh	University of California, Los Angeles	DATE 02/21/2025
All dimensions are inches unless otherwise specified.	11x17	SHEET 2 OF 4

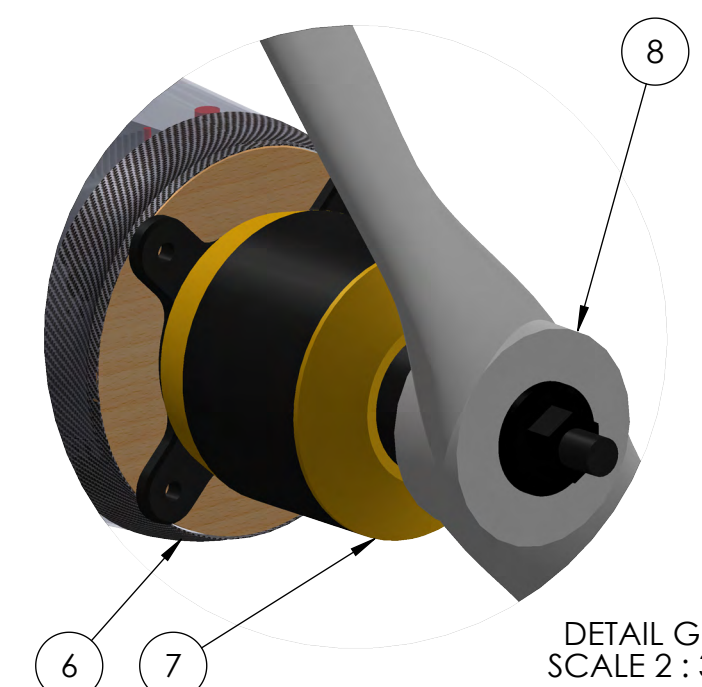
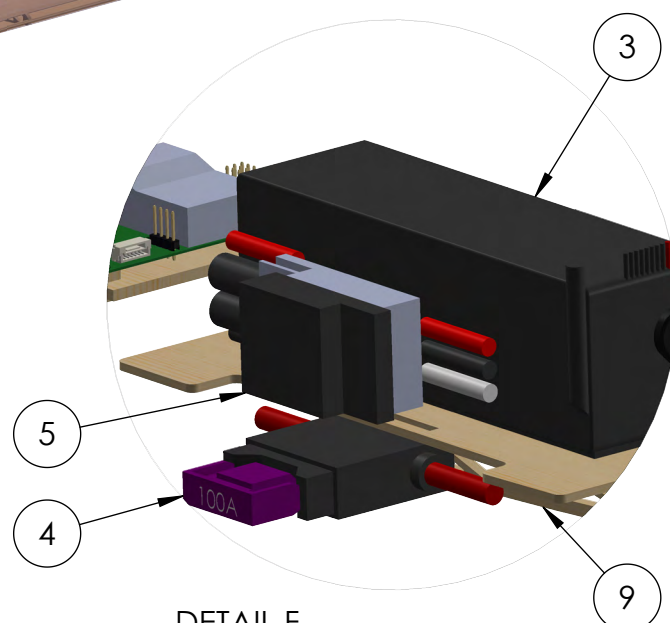
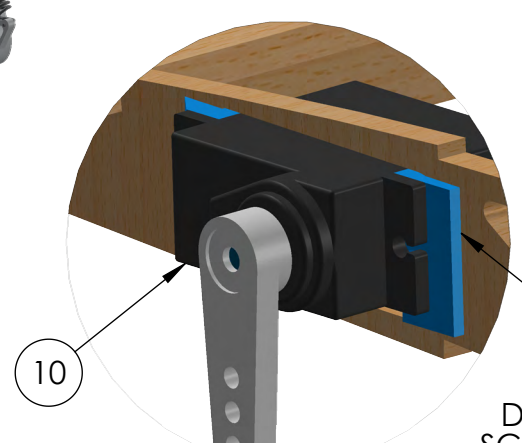
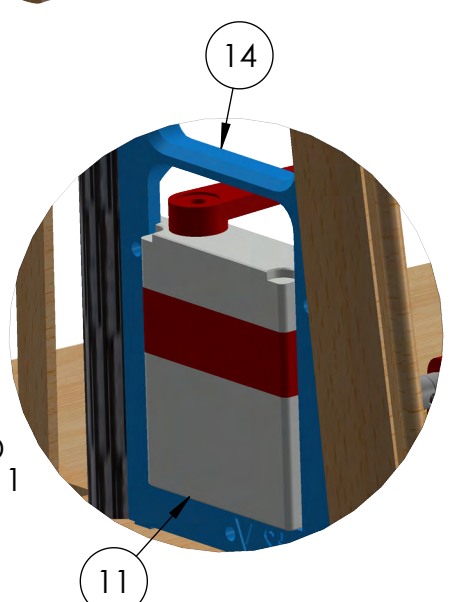
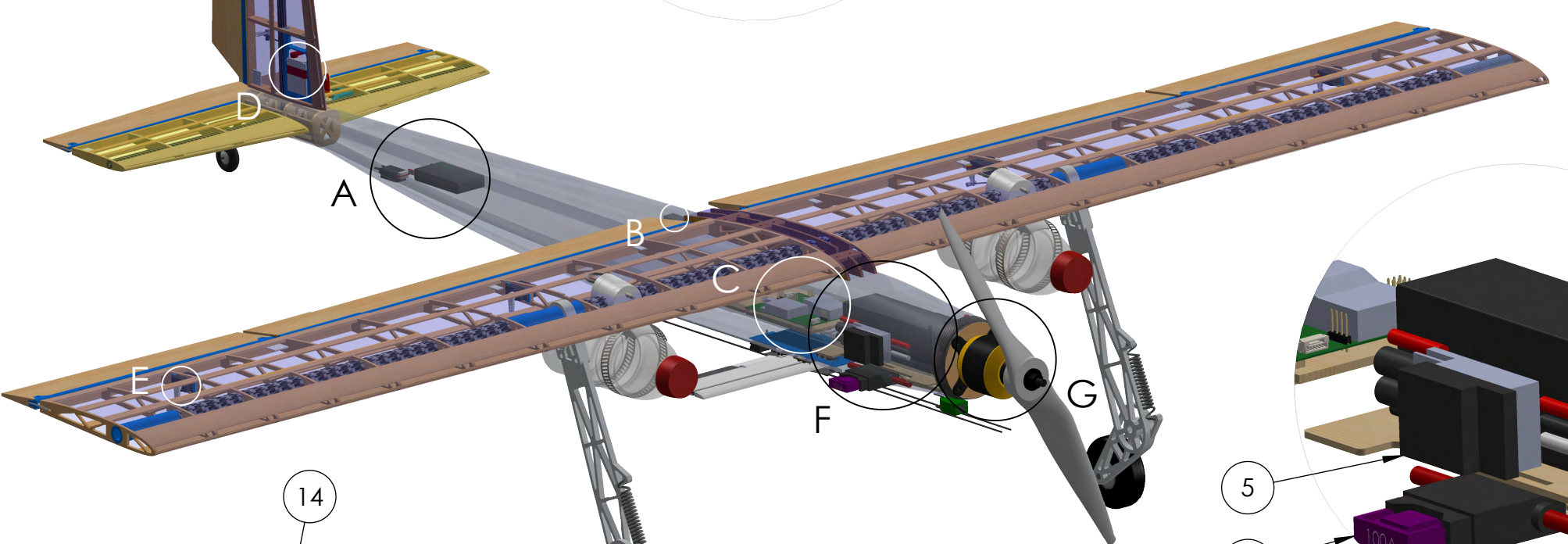
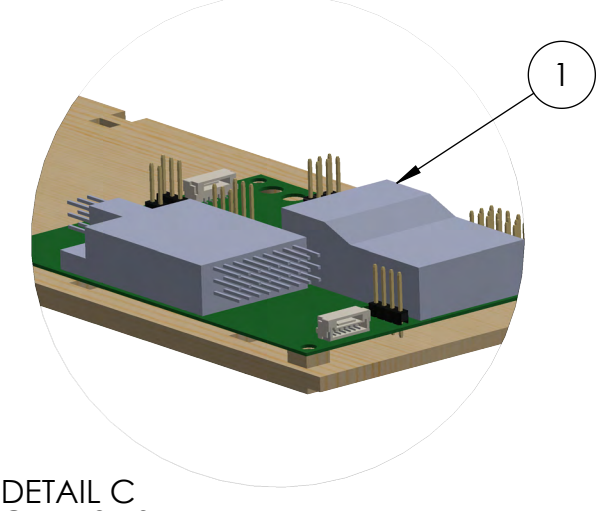
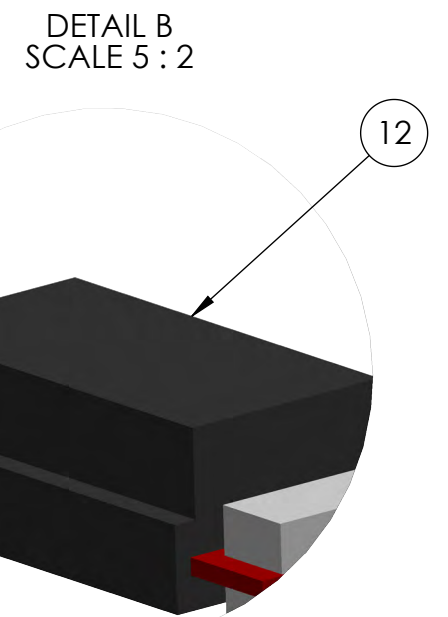
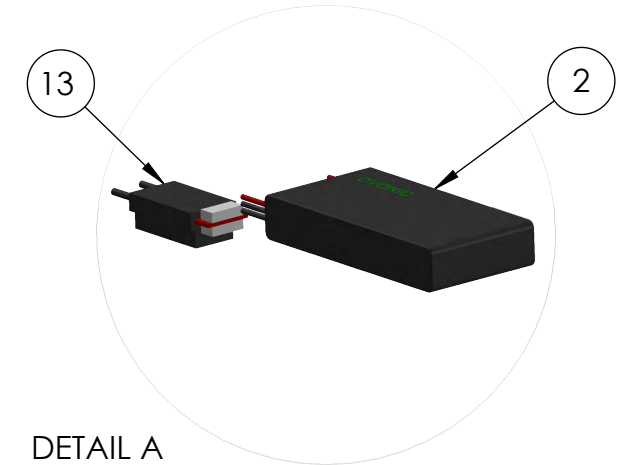
4

3

2

1

B



ITEM NO.	PART	MATERIAL	QTY.
1	Avionics PCB	-	1
2	Avionics Battery	-	1
3	Propulsion Battery	-	1
4	Fuse	-	1
5	ESC	-	1
6	Motor Mount	-	1
7	Motor	-	1
8	Propeller	-	1
9	Fuselage Floor	Basswood	1
10	Wing Servo	-	4
11	Tail Servo	-	2
12	Primary Receiver	-	1
13	Secondary Receiver	-	1
14	Tail Servo Mount	PETG	2
15	Wing Servo Mount	PETG	4

Bell-Air

Systems Layout

SCALE: 1:6

DRAWN BY  
Lauren HanCHECKED BY  
Siddharth Singh

University of California, Los Angeles

DATE  
02/21/2025

All dimensions are inches unless otherwise specified.

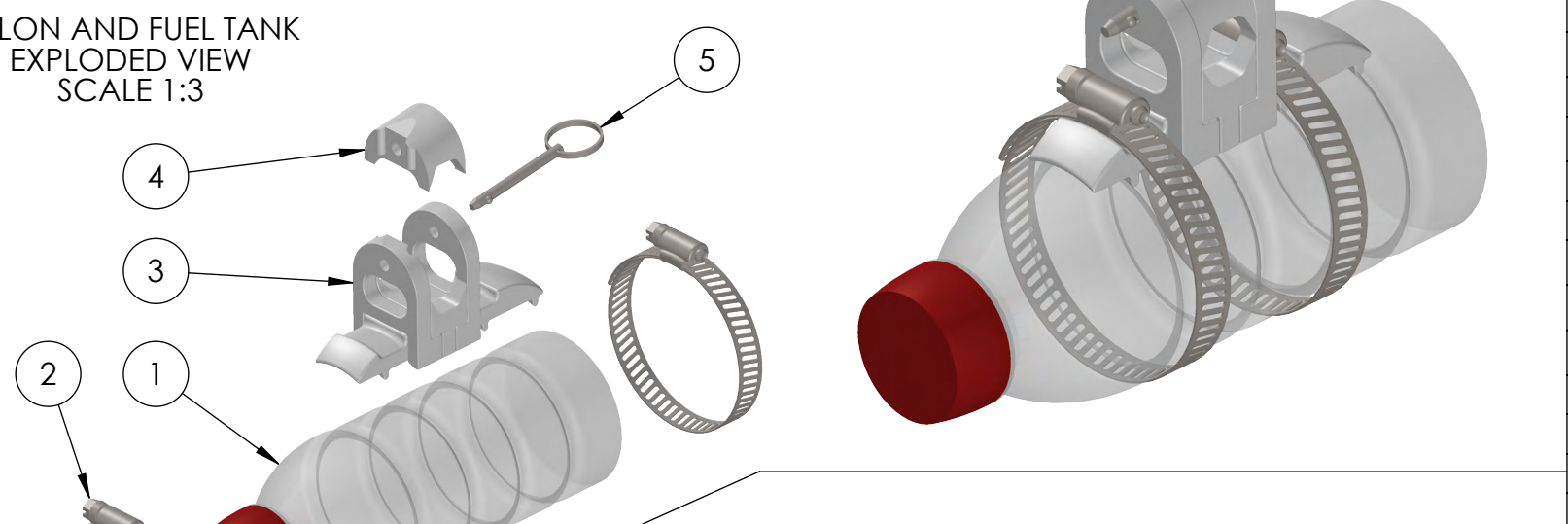
11x17

SHEET 3 OF 4

4

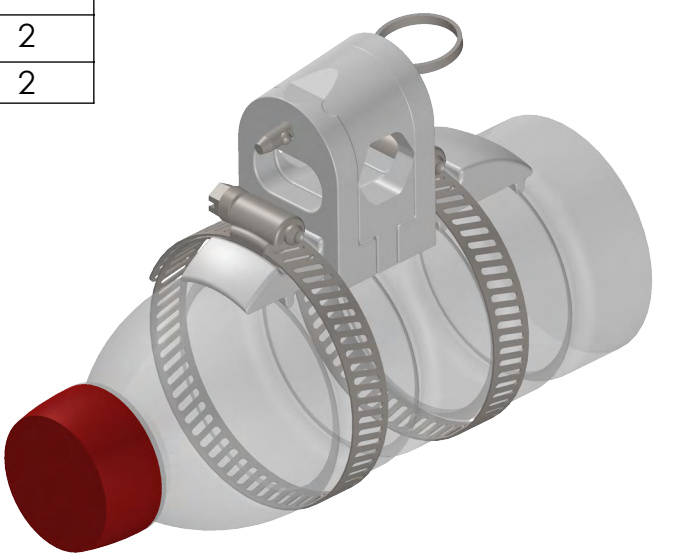
ITEM NO.	PART NUMBER	MATERIAL	QTY.
1	Fuel Tank	-	2
2	Hose Clamp	Steel	4
3	Pylon Base	PETG	2
4	Pylon Top	PETG	2
5	Quick-Release Pin	Steel	2

PYLON AND FUEL TANK  
EXPLODED VIEW  
SCALE 1:3



3

PYLON AND FUEL TANK  
ISOMETRIC VIEW  
SCALE 1:2



2

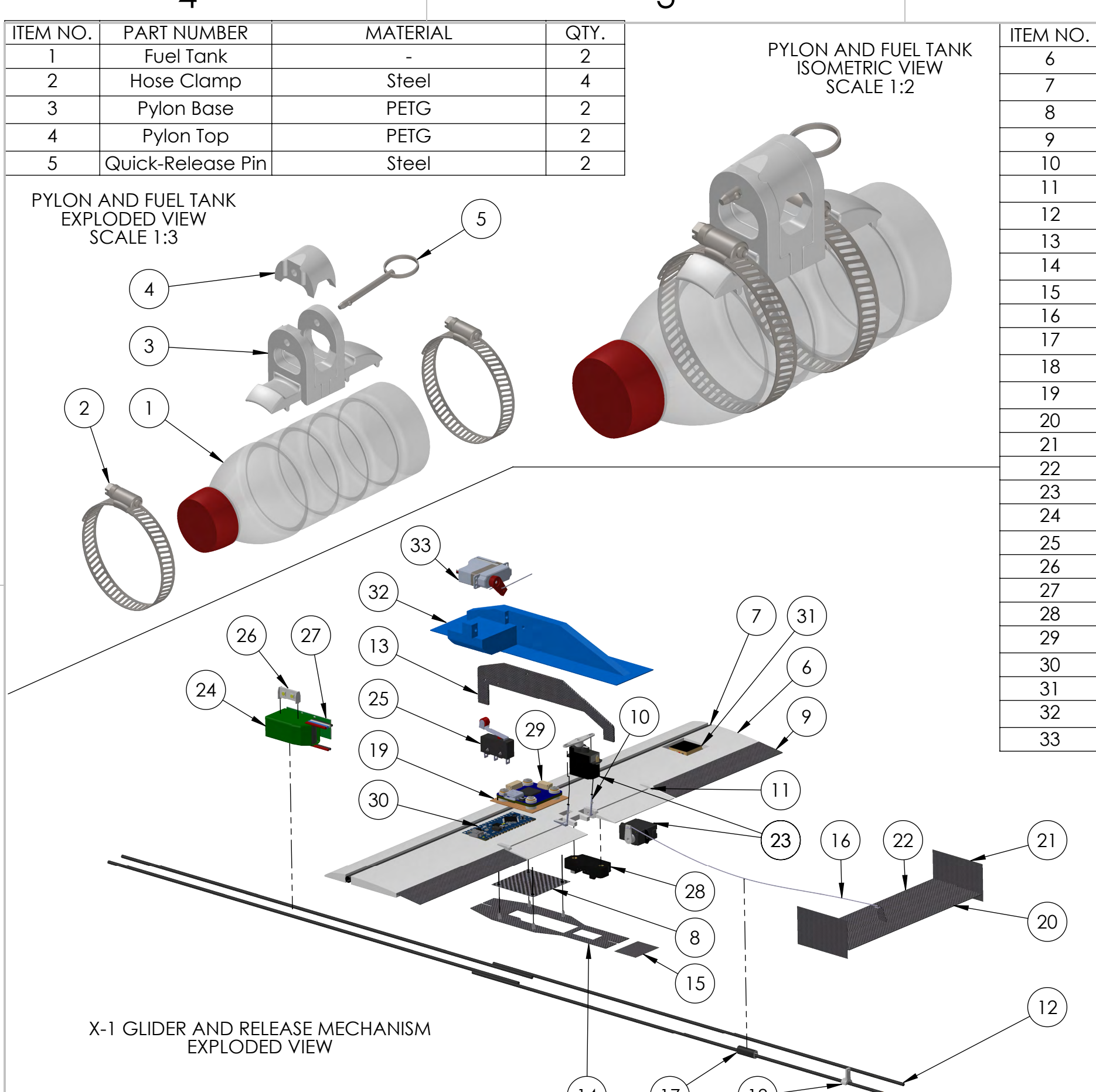
ITEM NO.	PART NUMBER	MATERIAL	QTY.
6	X-1 Wing Structure	Foam	1
7	X-1 Wing Spar	Carbon Fiber	1
8	X-1 Wing Mount	Carbon Fiber	1
9	X-1 Aileron	Carbon Fiber	2
10	X-1 Aileron Rod	Steel	2
11	X-1 Aileron Rod Guide	Nylon	4
12	X-1 Fuselage Spar	Carbon Fiber	4
13	X-1 Release Fin	Carbon Fiber	1
14	X-1 Fuselage Plate	Carbon Fiber	1
15	X-1 Elevator Servo Mount	Carbon Fiber	1
16	X-1 Elevator Rod	Steel	1
17	X-1 Front Elevator Rod Guide	Vinyl	1
18	X-1 Rear Elevator Rod Guide	Nylon	1
19	X-1 Flight Controller Mount	Wood Veneer	1
20	X-1 Elevator	Carbon Fiber	1
21	X-1 Vertical Stabilizer	Carbon Fiber	1
22	X-1 Horizontal Stabilizer	Carbon Fiber	1
23	X-1 Servo	-	2
24	LiPo Battery	-	1
25	Limit Switch	-	1
26	Strobe LED	-	1
27	Servo Controller	-	1
28	LIDAR Module	-	1
29	Flight Controller	-	1
30	Arduino	-	1
31	GPS Module	-	1
32	Release Mechanism Body	PETG	1
33	Release Mechanism Servo	-	1

B

B

A

X-1 GLIDER AND RELEASE MECHANISM  
EXPLODED VIEW

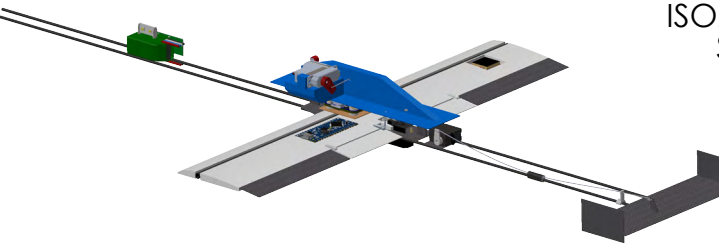


3

2

A

X-1 GLIDER AND RELEASE MECHANISM  
ISOMETRIC VIEW  
SCALE 1:5



1

1

## 6. Manufacturing Plan

### 6.1 Manufacturing Process Investigation

Out of the wide range of manufacturing techniques available to the team, those used are simple, cost effective, and utilize accessible materials while achieving the desired manufacturing quality.

#### 6.1.1 Additive Manufacturing

Additive manufacturing, also known as 3D printing, is a technique best suited for parts with complex geometries and lower structural requirements. The team has access to Prusa i3 MK3 printers with PLA filament, ideal for printing molds for CF layups. Additionally, the team has two Ender 3 printers, one of which is shown in Figure 47, with lightweight PLA and PETG filament printing capabilities. Lightweight PLA is the preferred material for non-structural components to minimize the weight of the aircraft.



Figure 47: Ender 3 3D printer

#### 6.1.2 Laser Cutting

Laser cutting, as shown in Figure 48, is an efficient and precise method for producing 2D geometry from materials such as balsa, basswood, and plywood. Its advantages include fast production and consistency, making it a reliable method for part fabrication. In addition, wood is generally lighter than 3D-printed alternatives and offers higher strength-to-weight ratios. However, the anisotropic properties of wood require careful attention to grain orientation. Laser-cut parts are primarily employed in ribs and internal structures.



Figure 48: Laser Cutter

#### 6.1.3 Carbon Fiber Manufacturing

Composite materials offer a high strength-to-weight ratio, making them ideal for aircraft applications. CF is available as COTS sheets and tubes, dry weave, and prepreg (dry weave impregnated with epoxy). COTS spars are available in limited sizes and cross sections but are preferable to manual layups for their higher quality and tighter tolerances. Layups are used for parts with more complex geometries and require custom molds (see Section 6.1.1 and 6.1.4) to hold the CF in the desired shape while 24-hour epoxy resin cures. Dry weave is used in layups, and the resulting composite is cured inside a vacuum bag with peel ply and breather fabric to absorb excess resin. This method was selected over curing prepreg weave due to the additional cost and limited shelf life of prepreg CF. Dry layups and COTS spars are processed with Dremel tools, which provide a clean and controlled cut. Sandpaper is used when necessary to smooth out bumps for safety concerns.

#### 6.1.4 Manual & CNC Machining

Computer numerical control (CNC) machining, as shown in Figure 49, permits the manufacturing of certain geometries with very high precision due to its automated nature, relying on computer software to control the movement of the cutting tools. However, CNC machining is most commonly used for metals, which are relatively dense, and most tasks that can be completed via CNC machining can also be accomplished with additive manufacturing (Section 6.1.1), which is a quicker, simpler, and cheaper process. When machined parts are needed, they may be outsourced when there is a lack of on-campus resources.

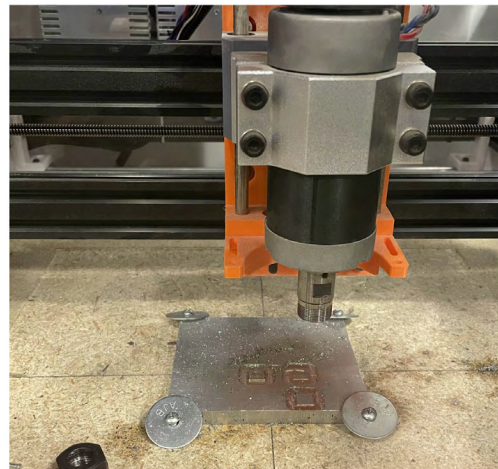


Figure 49: CNC Manufacturing

#### 6.2 Manufacturing Process Selection

Structural requirements, manufacturability, cost, and weight were considered when selecting materials for different components. Each technique and material in Section 6.1 was assessed based on efficiency, accessibility, and cost in order to meet budget and timeline constraints.

##### 6.2.1 Fuselage

The fuselage was manufactured using a wet CF layup process. Female molds were designed in two halves. Each half of the mold was then 3D-printed in sections and linked together. Multiple iterations of spreading spackling paste, applying spray paint, and sanding created a smooth surface finish. CF layers were laid up inside the female molds in alternating 90-45-90 degree orientations. After curing in a vacuum, as shown in Figure 50, holes were drilled along the fuselage length to help align the two halves. The processed fuselage half is shown in Figure 51. The two fuselage halves were mated by applying epoxy and putting screws through the pre-drilled holes in both halves. After curing, the motor mount was reinforced by applying a single-ply CF layup over a piece of balsa attached to the nose.



Figure 50: Fuselage Layup under Vacuum



Figure 51: Fully Processed Fuselage Half

## 6.2.2 Aerodynamic Surfaces

The wing, vertical stabilizer, and horizontal stabilizer consist of a wood buildup around COTS CF spars. The wing spar chosen was too short due to the limited availability of large COTS CF spars, so small spar extenders were 3D printed and attached to the ends. The ribs were laser-cut from 1/8 inch basswood stock. Pocketing was implemented in each rib, with servo mount cutouts near control surfaces. The ribs were positioned evenly along the wingspan and attached to the spar with cyanoacrylate (CA) glue. Laser-cut balsa stringers spanned the ribs, and leading edges featured a small dowel to ensure a satisfactory airfoil shape after the MonoKote was applied. Figure 52 shows the MonoKote covered vertical stabilizer, and uncovered wing ribs.

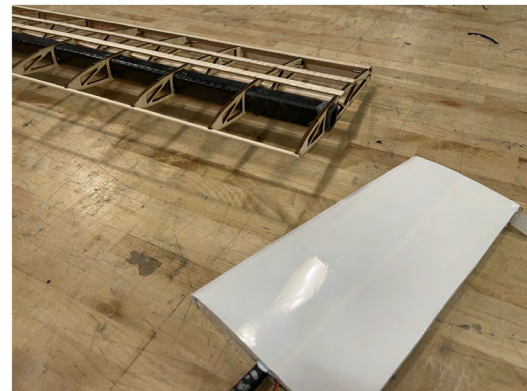


Figure 52: Aerodynamic Surfaces

## 6.2.3 Control Surfaces

The ailerons, flaps, elevator, and rudder were constructed from laser-cut 1/16 inch balsa sheets with a 3D-printed interface between the control surfaces and the hinges. The balsa plates were attached to the interface using CA glue, and small balsa ribs were spaced evenly throughout the inside of each control surface to provide extra support. Each surface was wrapped in MonoKote to smoothly transition from the 3D-printed interface to the wood and protect the soft balsa, an example of which is shown in Figure 53. The control surfaces were later attached to the wing and stabilizers using evenly-spaced nylon hinges.



Figure 53: Control Surfaces

## 6.2.4 Landing Gear

Competition rules [1] required the X-1 to be loaded at the center of the plane, so the landing gear was mounted to the wing instead of the fuselage. To meet this requirement, a custom CNC-machined landing gear assembly that mounts directly to the wing spar was designed. The tailwheel was COTS and bolted to the end of the tailcone.

The main landing gear, shown in Figure 54, was manufactured from a 1/4 inch 7075-T6 aluminum sheet. The parts were outsourced from an external CNC manufacturer due to a lack of on-campus

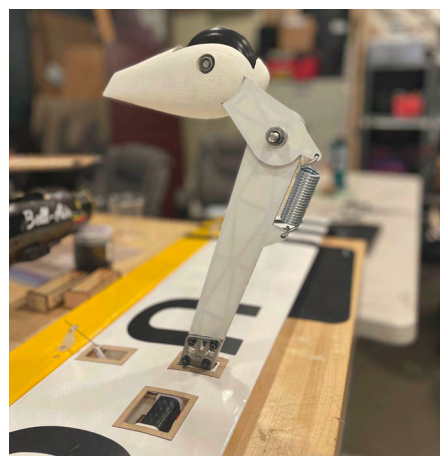


Figure 54: Landing Gear

resources. A key feature of the design was the integration of a shock-absorbing spring system to better manage impact loads.

With modularity in mind, small aluminum mounts enabled reusability of the main landing gear struts. The mounts were installed during the wing buildup, and the main landing gear struts were attached to the mounts using M5 bolts. Lastly, COTS wheels and axles were bolted to the struts, thus completing the main landing gear system.

### 6.2.5 Payloads and Mission Components

The pylons holding the fuel tanks were 3D printed using PETG filament in multiple parts, oriented to avoid shear stress parallel to layer lines. The parts were glued together with CA for a final weight of 0.072 lb. The fuel tanks were incrementally filled with pennies and UV resin, and cured at different stages to ensure the target weight of 4.63 lb per fuel tank was precisely met.

The X-1 test vehicle's fuselage was manufactured from thin COTS CF rods and plates that were hand-cut using Dremel tools. The wing was hand-carved from a sheet of polystyrene foam attached and reinforced by a CF rod. To protect the surface, the foam was laminated with packing tape. The release fin, tail, and control surfaces were also hand-cut from COTS CF plates using Dremel tools. All parts were glued together using CA glue. Since later testing revealed electromagnetic interference between the LiDAR and GPS modules, a thin layer of copper tape was applied across the bottom surface of the right wing.

### 6.3 Manufacturing Schedule

The planned and actual schedules for the construction of both prototypes and the competition aircraft are shown in Figure 55. Unforeseen events, like the wildfires that broke out across Los Angeles in January, restricted access to team working areas and the timeline was shifted to adapt.

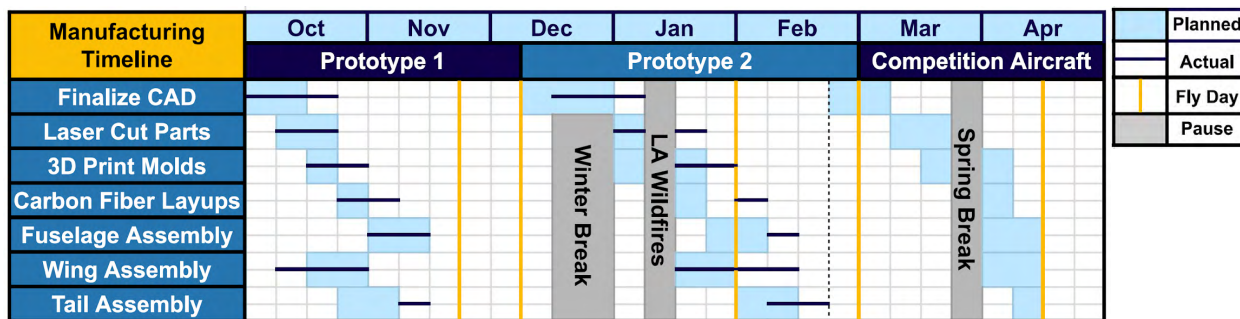


Figure 55: Manufacturing Timeline

## 7. Testing Plan

### 7.1 Test Objectives and Schedule

To ensure that the aircraft satisfied the target design objectives, many ground and flight tests of the aircraft and its subsystems were performed. These tests are outlined in Table 24 and Figure 56.

**Table 24: Test Objectives**

Subsystem	Test Goals
<b>GROUND TESTS</b>	
Aerodynamics	X-1 aerodynamic forces are measured at various AOAs through wind tunnel tests to verify CFD predictions Wheel pant drag with and without fairing is measured at various AOAs through wind tunnel tests to verify efficacy
Propulsion & Electronics	X-1 autopilot functions by manually toggling the limit switch Current continuity is checked throughout all propulsion and avionics systems on both the X-1 and main aircraft Full radio TX functionality with the aircraft's avionics system such as telemetry and stabilized control is achieved
Structures	Wings and fuselage can withstand maximum predicted bending loads from flight from FEA Pylon securement mechanism withstands full payload weight and increased load from high-g flight maneuvers X-1 release mechanism tolerances and release angle is verified
<b>FLIGHT TESTS</b>	
Aerodynamics	Stick-free straight-and-level trimmed flight as well as sufficient control authority is achieved Lift, drag, speeds, and AOAs are measured to corroborate CFD predictions Mission times & laps are measured to corroborate sizing predictions
Propulsion & Electronics	Takeoff and cruise power consumptions as well as maximum achievable speed are measured to confirm propulsion-system sizing predictions Multiple X-1 testbed flights are performed to validate GNC system and autonomous landing capabilities X-1 is released in flight to confirm that mechanism works as designed and sets the X-1 on an appropriate trajectory to achieve landing in the bonus-box
Structures	Wings as well as pylon attachment and X-1 release mechanisms withstand loads from flight and touchdown

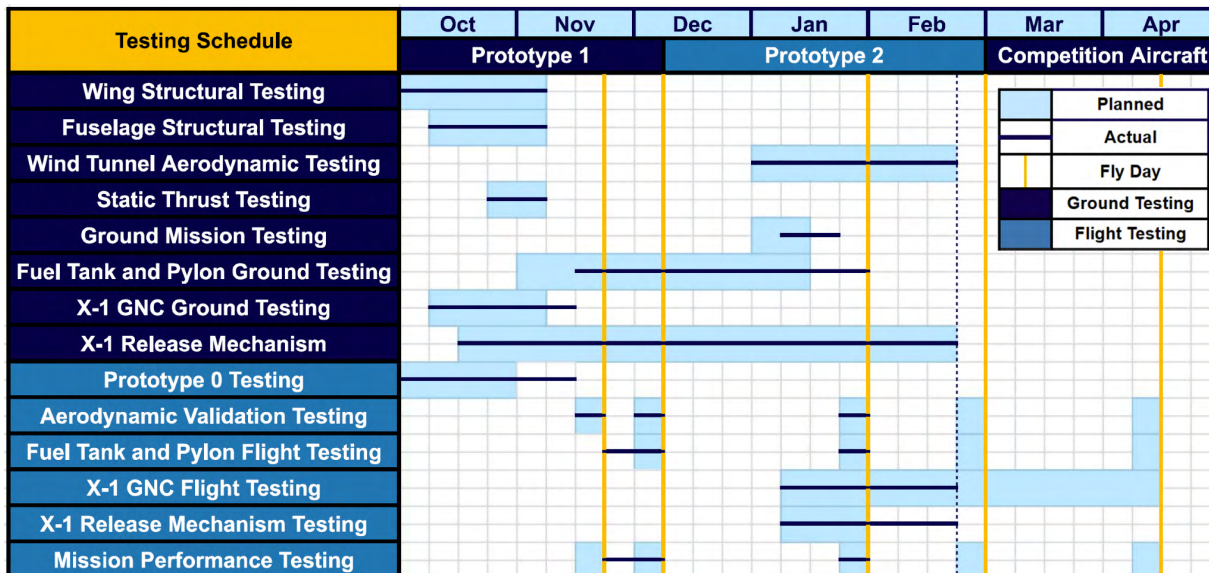


**Figure 56: Testing Schedule**

## 7.2 Ground Testing

### 7.2.1 Wing Structural Testing

To verify the structural integrity of the wing, an identical copy of the wing was built for stress testing until failure. The wing was placed upside down and clamped between two custom-cut foam pieces spanning the center of the wing. This served to stabilize the wing and distribute clamping loads. Weights were hung from the main spar, simulating an upward load akin to lift. The load was applied by gradually adding sand to four 5-gallon buckets. Along the wingspan, 4 load points were placed: two at the wingtips, and two 15 inches inward from the wingtips. Hexagonal 3D-printed pieces were glued with CA flush against the spar on either side of each load point to prevent the buckets from sliding as weight was added in increments of 10 lbf. This setup is shown in Figure 57.



Figure 57: Fuselage Structural Test Setup

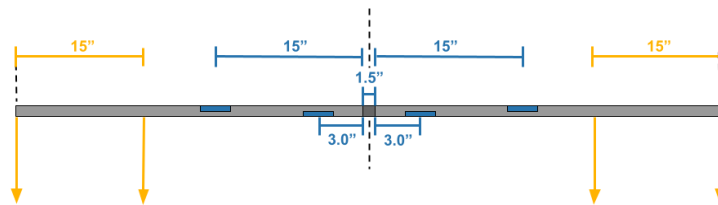


Figure 58: Diagram of Strain Gauge and Load Point Placements

Four strain gauges were added to the wing spar. They were placed 3 in and 15 in outwards from the wingbox on each side. The strain gauges were placed at the top and bottom of the wing spar in order to get both tension and compression data for each strain gauge position. Figure 58 shows a diagram of these placements. The yellow arrows represent the load points and the blue rectangles represent the strain gauge locations.

### 7.2.2 Fuselage Structural Testing

A structural test was performed to confirm the fuselage's ability to withstand large lifting loads. A mock 12-inch section of the fuselage was manufactured via a CF layup as described in Section 6.2.1. The fuselage section was mounted to two wooden beams using C-clamps and each wooden beam was then clamped to a workbench for stability. For a 3g turn, this section was predicted to undergo a tensile load of 60 lbf. To ensure the fuselage section experienced a uniform load, a square CF spar was secured to the underside and used as a



Figure 59: Wing Structural Test Setup

fixture for two carabiners on either end. The carabiners supported a metal rod carrying a large bucket, which was necessary for augmenting weight throughout the structural test. This setup is shown in Figure 59. Measurements of the fuselage deformation in the vertical direction were recorded for each increase in weight added.

### 7.2.3 Wind Tunnel Aerodynamic Testing

As described in Section 4.2.8, the X-1's aerodynamic sizing was optimized for a 70 ft/s release speed and 10 ft/s vertical descent rate. This was based on empirical approximations of 3D aerodynamic effects on the  $C_L$ - $\alpha$  slope, as well as CFD simulations using a simplified surface model of the X-1. It was hypothesized that the real X-1 would lose some lift because of its central mounting plate and manufacturing discrepancies. Thus, more realistic coefficients were desired, particularly for use in the custom Simulink-based [23] control law. The real X-1 was tested in UCLA's wind tunnel, featuring a 24 in x 24 in test section, deemed large enough to ignore wall effects. A variable- $\alpha$  mount was designed and attached to the X-1, as shown in Figure 60, so that its lift could be measured from -2 to 12 degrees  $\alpha$ , providing an accurate  $C_L$ - $\alpha$  slope. This data was collected at 70 ft/s (the expected drop speed) as well as 40 and 100 ft/s, determined in Simulink [23] to be the lower and upper bounds of the X-1's expected flight envelope.

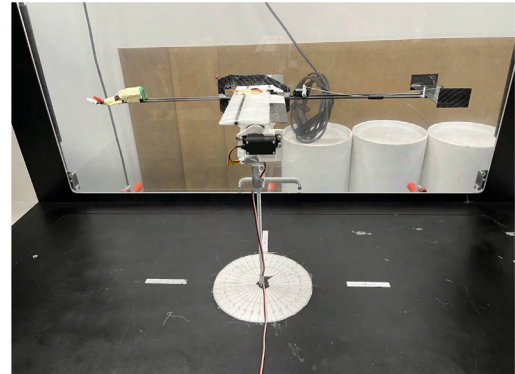


Figure 60: X-1 Wind Tunnel Testing

Additionally, the wheel pant fairing was tested using the same variable- $\alpha$  mount in this tunnel at 106 ft/s to validate CFD predictions outlined in Section 5.3.1.2. The drag values for landing gears with and without a fairing were compared from -4 to 12 degrees  $\alpha$ . This setup is shown in Figure 61. Wind tunnel results are presented in Sections 8.1.2.

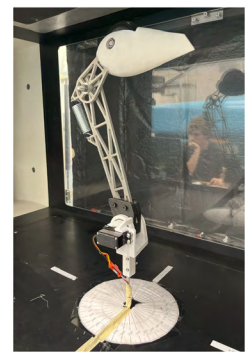


Figure 61: Wheel Pant Wind Tunnel Testing

### 7.2.4 Static Thrust Testing

The selected propulsion system was statically thrust tested to compare experimental vs. theoretical thrust and current. An alternate propulsion battery, the MaxAmps 8s 29.6 V 3250 mAh LiPo, was also tested. Preliminary testing of the MaxAmps and Gaoneng branded batteries demonstrated better performance of the latter. Per cell, the Gaoneng battery had half the MaxAmps battery's nominal internal resistance at only 2.5 mΩ, resulting in less voltage sag when drawing current from the



Figure 62: Static Thrust Testing Apparatus

motor. The motor and propeller were fixed to a custom aluminum stand with a load cell to measure thrust as shown in Figure 62. The load cell was monitored by an Arduino Uno microcontroller and interfaced with a laptop. The internal logging capabilities of the selected ESC were used to record battery current and voltage, which was then used to calculate electrical power draw. Based on the theoretical propeller performance values from the propulsion sizing script, the team selected the APC 17x13x2, 18x12x2, 18x12Ex2, 18x14x2, 19x12Ex2, and 20x14x2 propellers to test with the Scorpion A-5025 310 Kv motor.

### 7.2.5 Ground Mission Testing

To obtain an estimate for GM times, mock GMs were carried out according to the rule set [1]. The two sections of GM, the pylon and fuel tank/X-1 installations, were measured separately ten times to measure variation and identify areas of improvement.

### 7.2.6 Fuel Tank and Pylon Ground Testing

To validate the load capacity and safety factor of the pylons, structural tests were conducted to reproduce the forces experienced during flight. The spar hole in the pylon was secured, either on a CF spar or using paracord. The bottle was mounted onto the pylon, and paracord was wrapped around the bottle and hooked to a fish scale. The full setup is shown in Figure 63. The pylon was subjected to a gradually increasing force up to the target load value, or to failure, by monitoring the fish scale readout. This procedure was repeated with every iteration of the pylon design to ensure consistency throughout testing.

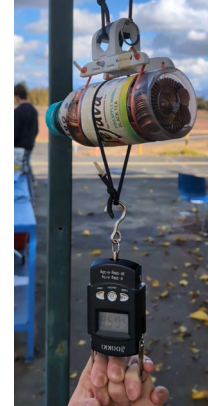


Figure 63: Early Stage Pylon Structural Testing

### 7.2.7 X-1 GNC Ground Testing

Following integration onto the X-1 airframe, wired connections between avionic components were tested for continuity using a multimeter before powering them on with the avionics battery. The FC was then flashed with Ardupilot through STM32CubeProgrammer [24]. All avionics were tested for cross-functionality through the live terminal on Mission Planner [20] after connecting the FC to a computer through USB. Autopilot was manually toggled by holding the limit switch, plugging in the avionics battery, and releasing the limit switch. The X-1 was then rotated in every direction to check



Figure 64: Competition Mission with Waypoints

for elevator and aileron servo response. To verify that data can be uploaded and saved to the FC, the waypoint mission depicted in Figure 64 was uploaded through Mission Planner [20] onto the board. A list of parameters, such as the X-1's expected aerodynamic characteristics, were configured to the FC. After power cycling the avionics, the FC was plugged back into the computer to confirm it had received the mission as expected by reading the saved waypoints. Once ready for flight, the following Mission Planner [20] status messages are checked: stable tracking of barometric and LiDAR altitude, accurate detection of speed, and a GPS satellite count of at least 10.

### 7.2.8 X-1 Release Mechanism Testing

The initial ground test was conducted using a release mechanism with a servo, pushrod, and 3D-printed case. A mock X-1 was attached to the release mechanism and dropped from a stationary test block. Ground testing mainly served to verify clearance between the CF fin and the case, push rod travel distance, and the angle of X-1 release.

## 7.3 Flight Testing

### 7.3.1 Prototype 0 Testing

An initial prototype called Prototype 0 (P0), shown in Figure 65, was constructed to verify aerodynamic sizing characteristics and obtain pilot input regarding aircraft stability and control. It was designed to be easily repairable as a low-budget, easy-to-assemble mockup of the main aircraft. Thus, it was manufactured using foam board for the wings and fuselage with the same dimensions as P1. An avionics system identical to that of P1 was implemented for early testing of the electronics and to collect data for post-flight analysis.



Figure 65: Prototype 0

### 7.3.2 Aerodynamic Validation Testing

As part of the flight plan, an aerodynamic validation test flight was included. Rather than perform competition laps, the purpose of this flight was to fly consistently straight and level in the M1 configuration to extrapolate critical flight parameters and compare them with values determined in initial sizing. The flight consisted of three laps, each with 1000 ft straights at constant speed. From the data collected in these flights, Equations 32 through 34 from Fossen [25] were used to extrapolate the average  $C_L$  and  $C_D$  values for the M1 configuration.

$$\alpha = \arctan\left(\frac{u_b}{w_b}\right) \quad (32)$$

$$F_x = \frac{1}{2} \rho S_w (C_L \sin(\alpha) - C_D \cos(\alpha)) V^2 \quad (33)$$

$$F_z = \frac{1}{2} \rho S_w (-C_L \cos(\alpha) - C_D \sin(\alpha)) V^2 \quad (34)$$

Here  $u_b$  and  $w_b$  are, respectively, the normal (parallel to vertical stabilizer, pointing up) and axial (parallel to centerline of plane, pointing from nose to tail) directional components of the velocity in aircraft-centered coordinates. Likewise,  $F_x$  and  $F_z$  are the axial and normal directional forces on the aircraft (extrapolated from accelerometer data and subtracting off thrust). In addition, power draw data could be derived from transmitter data, and thus average power draw during flight could be verified. Section 8.2 describes the results in detail.

### 7.3.3 Fuel Tank and Pylon Flight Testing

Pylon designs that passed ground testing were flight tested at the next fly day. Overall ease of installation and pylon fit were observed. A Runcam camera was mounted to the nose of the aircraft and pointed towards a mounted pylon and fuel tank, and footage was reviewed to detect any unwanted movement or potential failures.

### 7.3.4 X-1 GNC Flight Testing

GNC system testing was conducted in various stages with multiple small test aircraft. First, a 3 ft wingspan testbed was created as shown in Figure 66. Since GNC system testing coincided with main aircraft development, test beds were equipped with a motor and RX to manually simulate a drop from the main aircraft. Autonomous flight was triggered with a switch on the pilot's TX, after which the motor of the test bed turned off and autonomous flight commenced. In the event of malfunctions, the autopilot could be immediately aborted and the testbed landed manually. GNC system test flights gauged the reliability of LiDAR-guided landing accuracy and control algorithms against natural conditions such as wind and inclined landing sites. The FC supports flight logging stored onto an on-board SD card. Logs were collected after each flight and analyzed for debugging and control algorithm performance.

Once GNC system testing proved successful on the large testbed, a motor-propelled 1.5-scale model of the X-1 was created to explore the dynamics of controlling a smaller aircraft with a custom autopilot script. The 1.5-scale model was equipped with a RX for manual RC control to fly up to release altitude as shown in Figure 67. Flight plans simulated the X-1 being dropped upwind and landing in the bonus box. Various

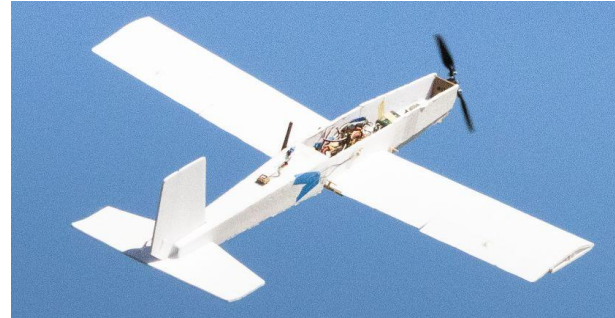
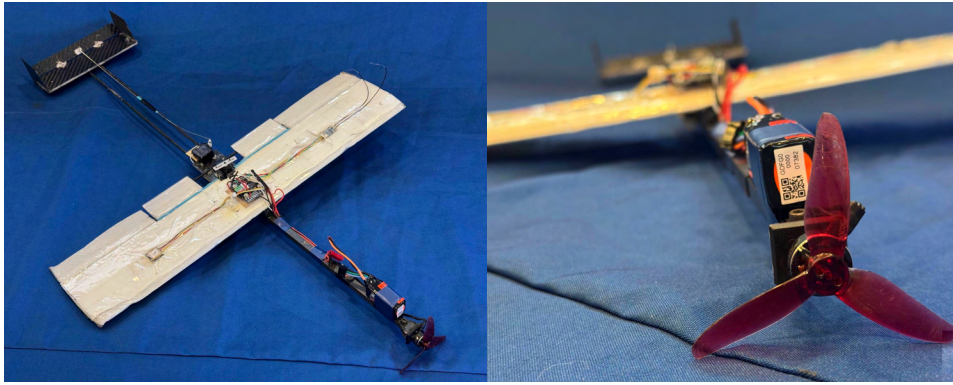


Figure 66: Initial GNC Tests with the Large Testbed



**Figure 67: 1.5-Scale GNC Testbed**

release conditions were tested, including several release positions, altitudes, and velocities. After the custom control algorithm was solidified and the release mechanism was developed, testing transitioned to drop tests using the actual X-1 from the main aircraft.

### 7.3.5 X-1 Release Mechanism Testing

The release mechanism detailed in section 7.2.8 was attached to successive prototypes of the main aircraft starting with P0. Initially, a mock X-1 airframe without electronics was used to test the release mechanism. The CF release fin was added, followed by counterweights to ensure the CG and mass of the mock vehicle were the same as the actual X-1. For flight, a back-facing camera was added to the front of the main aircraft fuselage to see if the X-1 was held securely and released at a favorable angle. Once it was verified that the X-1 mock vehicle released consistently, the actual X-1 was dropped from P0.

### 7.3.6 Mission Performance Testing

Mission performance testing was conducted, where total flight time and total lap count per mission would be measured to predict scores for M1, M2, and M3 flights. Team members with indicator flags were positioned at turning points of the competition lap. Data from the ESC was analyzed to ensure the propulsion system performed adequately during M2, where the aircraft was carrying fully-loaded fuel tanks. For M3, logs from the X-1 test vehicle's FC were collected and analyzed to ensure that the X-1 had a controlled trajectory throughout its entire flight. The X-1 test vehicle's autonomous flight functionality was tested numerous times under varying wind conditions to ensure consistent landing and bonus box navigation.

## 7.4 Pre-Flight Checklist

The checklist shown in Table 25 was devised to ensure safe and repeatable operation of the team's prototypes, properly functioning subsystems, and assist in go/no-go decisions based on aircraft and flying-field conditions.

**Table 25: Pre and Post Flight Checklists**

FLIGHT BRIEFING			
Pilot & FAA Number:	Date:		
Payload Configuration:	Flight Description:		
Total Aircraft Weight (lbf):	Flight Duration:		
CG (in from nose):	Wind Conditions:		
POWER-OFF PREFLIGHT		POWER-ON PREFLIGHT	
Internal Systems		Electrical Systems	
Battery voltages (V):		Receiver on	
Batteries, receiver, & ESC secured	Y/N	Nominal & failsafe control surface check	
Avionics & sensors installed	Y/N	Verify all sensors calibrated & log accurately	
All internal wiring secured	Y/N	Control & telemetry range check	
Propeller removed	Y/N	X-1 avionics functional and control check (M3 only)	
External Walkaround Inspection		Propeller installed	
Wings, Ailerons, & Flaps secured	Y/N	Motor full power run-up, verify performance	
Vertical Stabilizer & Rudder secured	Y/N	Download & reset Pixhawk data logs	
Horizontal Stabilizer & Elevator secured	Y/N	TAXI & BEFORE TAKEOFF	
All control surface linkages secured	Y/N	Flight plan briefed	Y/N
Landing Gear secured	Y/N	Wind direction verified & aircraft lined up	Y/N
Bottle payload weighed & secured (M3 empty)	Y/N	Arm aircraft & final control deflection check	Y/N
X-1 & release mechanism secured (M3 only)	Y/N	Verify all personnel ready, clear for takeoff	Y/N
Wingbox & fairing secured		POST FLIGHT	
Fuselage door closed, secured	Y/N	Aircraft stopped & disarmed	
Motor secured	Y/N	Flight and avionics batteries disconnected	
Verify no visual or feel-damages	Y/N	Pilot & chief engineer written debrief complete	

## 8. Performance Results

### 8.1 Subsystem Performance

#### 8.1.1 Structural Testing

The wing held 160 lbf split evenly between the four load points before the spar failed. Figure 68 shows the recorded strain from each of the four strain gauges relative to the total load applied. Figure 69 shows the deformation at the tip of the wing for each load amount.

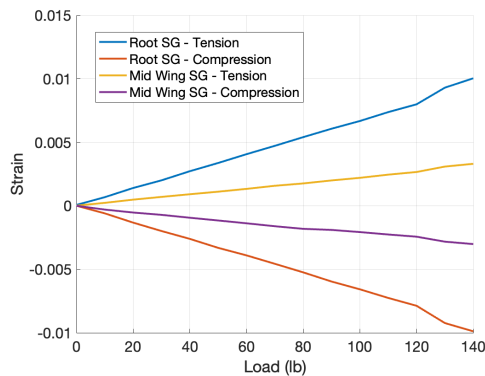


Figure 68: Strain Gauge Readings

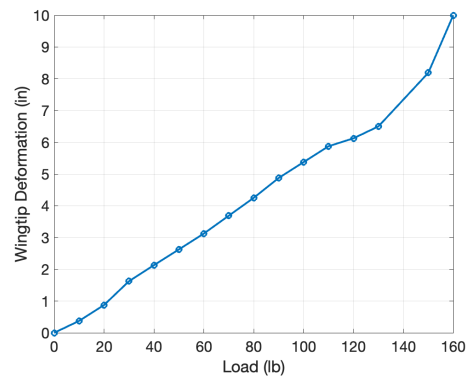


Figure 69: Wingtip Deformation

To extrapolate the actual maximum load of the wing, the four-point load case was converted into an equivalent uniform load case. Based on these conversions, the wing spar experienced a maximum bending moment that corresponds to a uniform load of 257 lbf. The initial spar was sized to withstand a load of 360 lbf (180 lbf maximum lift times a factor of safety of 2). The actual wing's strength undershot this design metric by 103 lbf. This was most likely due to manufacturing defects in the hexagonal spar. Even with this deficiency, however, the spar was deemed satisfactory for flight due to confidence in the 1.42 factor of safety and manufacturing supply constraints.

In regards to the fuselage structural test, the total load applied to the test section amounted to 70.20 lbf and resulted in a vertical deformation of 0.94 in. No cracks or breaks were observed, confirming the structural integrity of the fuselage.

### 8.1.2 Wind Tunnel Aerodynamic Testing

After converting X-1 lift and drag measurements from the wind tunnel to their associated coefficients, the  $C_L$  vs.  $\alpha$  curve plot shown in Figure 70 was generated.

The lift coefficients at the three measured speeds were averaged and linearly fitted for -2 to 8 degrees  $\alpha$  to ignore stall effects. As predicted, the real  $C_L$ - $\alpha$  slope, 0.0561, was lower than the theoretical prediction of 0.0615. This value was updated in the X-1's custom control law, leading to more accurate bonus box targeting.

From the wheel fairing wind tunnel test, the drag curves shown in Figure 71 were produced. At 0 degrees  $\alpha$ , the fairing was found to reduce drag by 0.19 lbf (a 7% reduction), higher than the 0.06 lbf drag reduction predicted by CFD. This discrepancy was likely due to the proximity of the wheel base to the upper test-section wall, making tunnel wall effects influential. Since both CFD and wind tunnel tests showed a drag reduction from the wheel fairings, they were implemented on the main aircraft.

### 8.1.3 Static Thrust Testing

Table 26 shows static thrust testing results with six different propellers, the Gaoneng 8s 3300 mAh propulsion battery, and the Scorpion A-5025 310 Kv motor. As seen in the table, experimental and

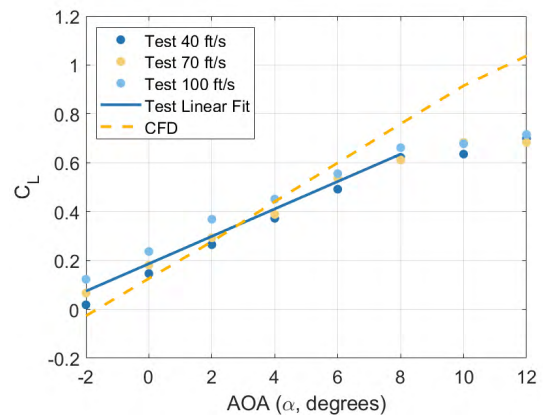


Figure 70: X-1 Glider  $C_L$  vs.  $\alpha$  Curve

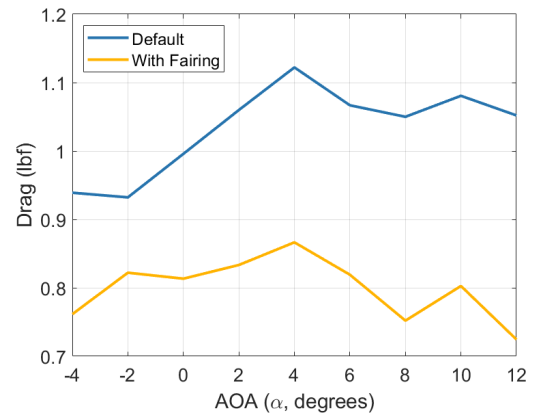


Figure 71: Wheel Fairing Efficacy - Drag vs.  $\alpha$  Curve

theoretical results were close, especially for the selected 18x14x2 propeller. An average internal resistance of  $2.5\text{ m}\Omega$  per cell was measured for these batteries. This is less than the  $5\text{ m}\Omega$  assumption used for the propulsion-sizing script, contributing to the overperformance of most of the combinations tested.

**Table 26: Static Thrust Testing Results**

Propeller	Experimental			Theoretical	
	Minimum Voltage per LiPo cell (V)	Maximum Thrust (lb)	Maximum Current (A)	Maximum Thrust (lb)	Maximum Current (A)
<b>17x13x2</b>	3.50	20.98	92	18.81	103
<b>18x12x2</b>	3.48	19.56	97	18.11	93
<b>18x12Ex2</b>	3.48	20.90	102	20.97	102
<b>18x14x2</b>	3.45	18.50	101	17.47	102
<b>19x12Ex2</b>	3.35	22.31	112	24.23	116
<b>20x14x2</b>	3.11	24.65	126	23.18	136

#### 8.1.4 Ground Mission Testing

Following final construction of the pylons, fuel tanks, X-1 test vehicle, and release mechanism, a mock ground mission was conducted. After multiple run-throughs, the shortest achieved time was 67 seconds: 12 seconds to mount pylons, and 51 seconds to attach the test vehicle and mount fuel tanks with the help of power tools.

#### 8.1.5 Fuel Tank and Pylon Testing

The aerodynamic team cited an absolute maximum load of 20g (factor of safety of 2) during sharp turns. Multiplied by a full fuel tank weight of 4.63 lbf, each pylon could experience a maximum load of 92.6 lbf. During ground testing, the final pylon design was validated to at least 110 lbf, an additional 14% buffer over the prescribed factor of safety. Three flights were then performed using unloaded, half-loaded, and fully-loaded fuel tanks, mimicking a typical mission flight path as shown in Figure 72. All three flights were successful and no issues were captured with the on-board camera.



**Figure 72: Bell-Air Flying M3**

#### 8.1.6 X-1 GNC Testing

The simulated drop tests of the 3 ft testbed validated the autopilot's capability to navigate to a waypoint and land. The flight plan featuring a conventional landing sequence with a glide slope resulted in consistent overshoot of the landing waypoint. The helical landing flight plan with the aircraft loitering to the ground maintained precise accuracy over multiple trials. Additionally, the process of loitering down

reduced speed and resulted in softer landings. Therefore, the helical landing flight plan was chosen for its increased accuracy and safety.

The first autonomous flight of the 1.5-scale X-1 resulted in a safe landing and proper flare. Initial tests used the default ArduPilot [19] waypoints as the control law. On the first flight test day, the 1.5-scale X-1 landed in the bonus box five out of seven times. All flights were completed in under 30 seconds from the time of release, a desirable outcome that maximized the time spent flying laps on the main aircraft prior to release.

After the waypoint-based control law proved to be inconsistent from spontaneous wind conditions, extensive testing with the custom autopilot script was conducted with the 1.5-scale X-1. Once the custom autopilot proved to be versatile after troubleshooting and debugging with the 1.5-scale X-1, testing transitioned to the X-1 itself. The X-1, equipped with the custom autopilot script, was then dropped by the competition aircraft from a height of 200 ft to simulate M3. Tests releasing the X-1 at varying velocities and positions proved successful, landing in the center of the bonus box each time. Logs were monitored later to confirm that the X-1's target trajectory was changed dynamically depending on its altitude and random wind conditions. Figure 73 shows the X-1 after being released. Initial drop testing was promising with the X-1 landing inside the bonus box perfectly.



Figure 73: X-1 GNC Testing

### 8.1.7 X-1 Release Mechanism Testing

The ground tests of the release mechanism were acceptable and demonstrated its reliability in controlled conditions. In flight testing, however, the mechanism was inconsistent when releasing the X-1 due to a tendency to jam. To remedy this, a spring was added to the final mechanism to exert a downwards force on the X-1, helping dislodge it from the main aircraft. The mechanism was also simplified to allow easier 3D printing in such a manner that layer lines would not create additional friction between the fin and release mechanism.

## 8.2 Aircraft Flight Performance

Overall, the aircraft handled well and was easy to fly. Pitch and roll response was quick even with a fully-loaded M2, and thrust response was ascertained to be adequate. These observations qualitatively

validated stability and handling predictions. Results calculated using the methods discussed in section 7.3.2 are summarized and compared in Table 27.

**Table 27: Mission Flight Parameters, Predicted and Calculated**

Parameter	M1 Predicted	M1 Calculated	M2 Predicted	M2 Calculated	M3 Predicted	M3 Calculated
Drag coefficient	0.042	0.049	0.046	0.089	0.047	0.077
Lift coefficient	0.160	0.230	0.164	0.145	0.192	0.103
Power Draw (W)	587	685	1759	2132	788	1114

To verify performance for M2 and M3, average lap times and flight speeds were extrapolated from the mock mission flights. The target cruise speeds of 106 and 131 ft/s for M2 and M3 respectively were consistently achieved and maintained in every lap.

For M2, the full target payload was able to be carried, but the mission took 110 s compared to the predicted 91 s. This loss was attributed to several factors, mainly the takeoff taking longer than anticipated and suboptimal flight paths with individual straights taking 2.0 to 2.5 s longer than expected.

For M3, all targets were achieved and a total of 7 laps were flown before the X-1 test vehicle was released. On average, each lap took 36.0 s, slower than the predicted 31.9 s. However, the X-1 test vehicle successfully landed in the target 2.5-point landing zone faster than the expected 30 s and still settled within the allotted time frame of 5 minutes.

In addition to direct mission performance validation, the max g-loading during flight for mock M2 and M3, respectively, were calculated from onboard IMU data to be 6.5 and 7.5 g, thus verifying the structural sizing. The performance for both flight missions is expected to further improve and approach predicted values with practice as flight paths are further optimized.

The 2024-25 UCLA DBF Team, shown in Figure 74, is excited to partake in the 2025 DBF Fly-Off and is proud to present Bell-Air!



**Figure 74: 2024-25 UCLA Team & Bell-Air**

## 9. Bibliography

- [1] AIAA, "2024-25 DBF Rules," Reston, VA, 2024.
- [2] Dassault Systems, "Solidworks," [Online]. Available: <http://www.solidworks.com/>.
- [3] Anderson, J., Introduction to Flight, McGraw-Hill Education, New York, NY, 8th ed., 2016.
- [4] Raymer, D. P. "Initial Sizing," Aircraft Design: A Conceptual Approach, 2nd ed., Washington, DC, 1992, pp. 112, 280-283.
- [5] S. Boyd and L. Vandenberghe, "Unconstrained Optimization," *Convex Optimization*, 7th ed., Cambridge University Press, Cambridge, 2004, pp. 455-514.
- [6] Python. [Online]. Available: <https://www.python.org/>.
- [7] Drela, Dr. M., "QPROP," QPROP Propeller/Windmill Analysis and Design, Mar. 2007
- [8] APC Propellers Performance Data [Online]. Available: <https://www.apcprop.com/technical-information/file-downloads/>
- [9] "XFLR5," 2019. [Online]. Available: <http://www.xflr5.tech/xflr5.html>.
- [10] "Airfoil Tools," [Online]. Available: <http://airfoiltools.com/>.
- [11] Selig, M., "UIUC Airfoil Data Site," University of Illinois Urbana-Champaign, 1994. [Online]. Available: [https://m-selig.ae.illinois.edu/ads/coord\\_database.html](https://m-selig.ae.illinois.edu/ads/coord_database.html).
- [12] M. Drela, "XFOIL," MIT, 2013. [Online]. Available: <http://web.mit.edu/drela/Public/web/xfoil>.
- [13] Prosser, D., "XOptFoil2," 2024. [Online]. Available: <https://jxjo.github.io/Xoptfoil2/>.
- [14] Jones, R. T., "Correction of the Lifting-Line Theory for the Effect of the Chord," NACA-TN-817, July 1941.
- [15] Air Density Online. [Online]. [https://airdensityonline.com/track-results/Tucson\\_Dragway/](https://airdensityonline.com/track-results/Tucson_Dragway/)
- [16] Ansys® Academic Research Mechanical 2021, ANSYS, Inc., <https://www.ansys.com/>.
- [17] "Matlab," Mathworks. [Online]. Available: <https://www.mathworks.com/products/matlab.html>.
- [18] "Altium," [Online]. Available: <https://www.altium.com/>.
- [19] ArduPilot Firmware, ArduPilot. [Online]. Available: <https://firmware.ardupilot.org/>.
- [20] Oborne, M., "The Mission Planner," ArduPilot Dev Team, 2024 [Online]. Available: <https://ardupilot.org/planner/>.
- [21] "MAVLink". [Online]. Available: <https://mavlink.io/en/>.
- [22] Lua, PUC-Rio. [Online]. Available: <https://www.lua.org/>.
- [23] "Simulink", Mathworks. [Online]. Available: <https://www.mathworks.com/products/simulink.html>.
- [24] "STM32CubeProgrammer", STMicroelectronics. [Online]. Available: <https://www.st.com/en/development-tools/stm32cubeprog.html>.
- [25] Fossen, T. I., Hansen, M. J., Sørensen, K., Cristofaro, A., and Johansen, T. A., "On estimation of wind velocity, angle-of-attack and sideslip angle of small UAVs using standard sensors," *2015 International Conference on Unmanned Aircraft Systems (ICUAS)*, Denver, CO, 2015, pp. 510-519

# VIPER AND VENOM



**AIAA DBF 2024-2025 DESIGN REPORT  
EMBRY-RIDDLE AERONAUTICAL UNIVERSITY  
DAYTONA BEACH, FLORIDA**



## Nomenclature

<b>Symbols</b>		<b>Subscripts</b>	
$\alpha$	Angle of attack	$a$	aileron
$AR$	Aspect ratio	$e$	elevator
$\beta$	Sideslip angle	$r$	rudder
$b$	Span	$f$	flap
$c$	Chord		
$C$	Aerodynamic coefficient	<b>Abbreviations</b>	
$\delta$	Control surface deflection	AIAA	American Institute of Aeronautics and Astronautics
$FS$	Factor of safety	APC	Advanced Precision Composites
$n$	Load factor	CAD	Computer-Aided Design
$\tilde{N}_o$	Neutral point	CFRP	Carbon Fiber Reinforced Polymer
$q_\infty$	Freestream dynamic pressure	CG	Center of Gravity
$Re$	Reynolds number	COTS	Commercial Off-the-Shelf
$S$	Planform area	DBF	Design, Build, Fly
$S.M.$	Static margin	EFT	External Fuel Tank
$t/c$	Thickness-to-chord ratio	ERAU DB	Embry-Riddle Aeronautical University, Daytona Beach
$T/W$	Thrust-to-weight ratio	FEA	Finite Element Analysis
$V_\infty$	Airspeed	FS	Factor of Safety
$\bar{V}$	Volume coefficient	EPP	Expanded Polypropylene
$W$	Weight	GFRP	Glass Fiber Reinforced Polymer
$W/S$	Wing loading	GM	Ground Mission
<b>Units</b>		HT	Horizontal Tail
A	Amps	IFT	Internal Fuel Tank
$^\circ$	degrees	LE	Leading Edge
ft	feet	LiPo	Lithium Polymer
g	Acceleration under gravity	MAC	Mean Aerodynamic Chord
in	inches	MLG	Main Landing Gear
lb	pounds	NLG	Nose Landing Gear
mAh	milliamp-hours	PLA	Polylactic Acid
psi	pounds per square inch	ROC	Rate of Climb
RPM	revolutions per minute	TE	Trailing Edge
s	seconds	VIPER	Versatile Intelligence Platform for Experimental Release
V	Volts	VT	Vertical Tail
W	Watts		
Wh	Watt-hours		



## 1 Executive Summary

### 1.1 Selected Design Summary and Mission Requirements

This document details the design, manufacturing, and testing of the Versatile Intelligence Platform for Experimental Release (VIPER), Embry-Riddle Aeronautical University Daytona Beach's (ERAU DB) aircraft for the 2025 American Institute of Aeronautics and Astronautics (AIAA) Design, Build, Fly (DBF) competition. VIPER was designed to perform missions inspired by the historical X-1 supersonic flight test program. Mission 1 (M1) is a delivery flight that demonstrates the aircraft's flight capability. Mission 2 (M2) is a captive carry flight of fuel tanks and the autonomous X-1 test vehicle, VENOM. Mission 3 (M3) is a launch flight that demonstrates fuel tank transport and the deployment and autonomous navigation capabilities of VENOM. The Ground Mission (GM) demonstrates the aircraft's ability to quickly change from the clean "fleet bomber" configuration to the full payload "test program" configuration. Additionally, VIPER must be flight-ready within five minutes for each mission.

### 1.2 Development Process Summary

VIPER was designed, manufactured, and tested by a team of over 130 undergraduate students. The aircraft was designed in three phases: conceptual, preliminary, and detailed. The conceptual design phase saw requirement definition and scoring sensitivity analyses which informed aircraft and subsystem configuration selections. The preliminary design phase utilized analysis methodology and trade studies to determine aircraft sizing, aerodynamic characteristics, subsystem design, and performance estimates. The detail design phase finalized performance parameters, structure, subsystems, and weight and balance. The manufacturing plan oversaw the selection of critical processes and aircraft fabrication. Finally, an extensive test plan was developed to ensure all system requirements were met and to evaluate VIPER's mission performance. A final performance review was conducted to validate the design and mission capabilities of the aircraft.

### 1.3 System Performance and Capabilities

As shown in Figure 1-1, VIPER features a low-wing, single-tractor engine, tail boom with a conventional empennage, and tricycle landing gear. The propulsion system was optimized for efficiency and dynamic thrust to best fit mission requirements. The circular fuselage cross-section minimized drag while providing internal volume for structures, payload, and avionics. A final analysis of VIPER's performance, as shown in Table 1-1, provided confidence that the system can achieve the goal of winning the 2025 competition as the top-scoring aircraft.

Table 1-1: Predicted performance of VIPER.

Parameter	M1	M2	M3	GM	Total
Gross Weight (lb)	15	39	17	-	-
Lap Time (s)	28	28	30	-	-
Number of Laps	3	3	9	-	-
Mission Time (s)	99	99	300	90	-
Fuel Tank Weight (lb)	-	25	0	0	-
X-1 Weight (lb)	-	0.13	0.16	0.16	-
Predicted Mission Score	<b>1.00</b>	<b>1.84</b>	<b>2.92</b>	<b>0.33</b>	<b>6.09</b>

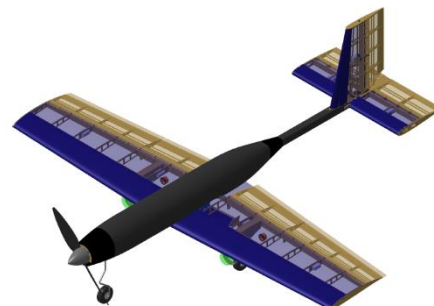


Figure 1-1: VIPER selected configuration.



## 2 Management Summary

### 2.1 Team Composition and Organization

The ERAU DB DBF was led by the Project Lead and Chief Engineer, overseeing administrative and technical aspects, respectively. They also managed communication with faculty and industry advisors. The 130-member team was divided into six functional groups: Design, Supply Chain, Production Design, Manufacturing, Testing, and Research and Development. The Project Lead and Chief Engineer supervised these groups, forming the Executive Board as shown in Figure 2-1.

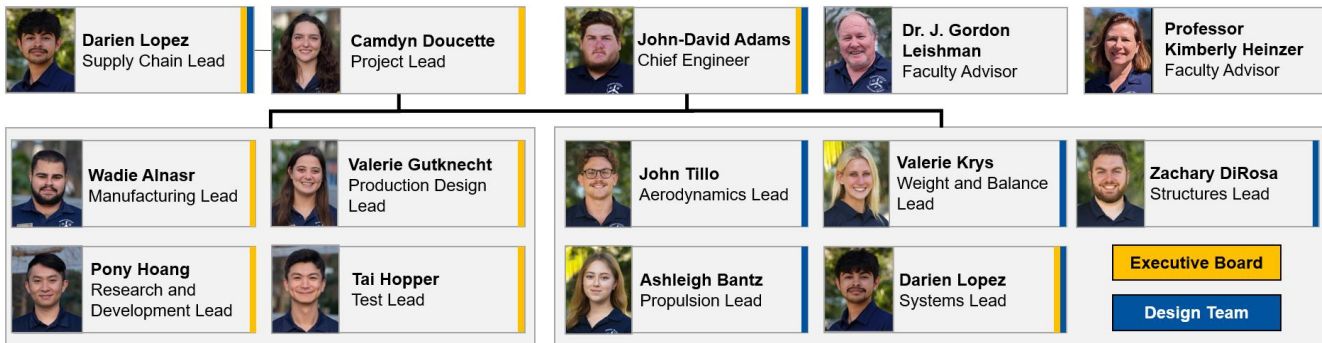


Figure 2-1: ERAU DB DBF leadership structure.

The Project Lead was the primary point of contact and was responsible for the schedule, personnel management, and the non-technical scope of the team. The Chief Engineer led the Design Team, which consisted of the Aerodynamics Lead, Propulsion Lead, Weight and Balance Lead, Systems Lead, and Structures Lead. This team was responsible for the conceptual, preliminary, and detail design of VIPER. The Supply Chain Lead managed the team's budget, ordered materials, and served as a secondary point of contact for external communication. The Production Design Lead managed a team of five design engineers who developed the computer-aided design (CAD) model for the aircraft and subsystems. The Manufacturing Lead managed a team of 60 students who fabricated the aircraft and its subsystems. The Test Lead managed a team of three test engineers and two pilots who developed test plans, executed the flight tests, conducted data analysis, and provided feedback to inform design changes. The Research and Development Lead managed a team of 50 students who investigated advanced aerodynamics concepts, novel fabrication techniques, and potential subsystem designs. The responsibilities and skills of each functional group are shown in Table 2-1.

Table 2-1: Responsibilities and skills required of functional groups.

Functional Group	Responsibilities	Skills Required
Design Team	Preliminary, conceptual, and detail aircraft and subsystem design, data processing, report writing	Programming, 3D modeling, finite element analysis, extensive aircraft design knowledge
Supply Chain	Budget management, material procurement, point of contact	Financial literacy, communication skills, knowledge of ERAU DB procedures
Production Design	Aircraft 3D modeling, model management, laser cut sheet creation, tooling design	CATIA, knowledge of structures, system integration, design for manufacturing



Functional Group	Responsibilities	Skills Required
Manufacturing	Aircraft and subsystem fabrication, develop critical build processes, aircraft upkeep	Wood/composite fabrication, laser cutting, power tool operation, safety knowledge
Testing	Develop and execute test plans, validate aircraft and subsystems, data collection	Avionics knowledge, technical writing, flight dynamics, testing methodology
Research & Development	Subsystem development, research advanced mechanisms, documentation	Engineering design process, CATIA, manufacturing, testing methodology

## 2.2 Project Milestones

Key milestones and deliverable dates were planned over an eight-month window, as shown in Figure 2-2. The schedule was designed to accommodate three aircraft iterations with adequate time for testing and design refinement between each. The parallel workflow enabled tasks to overlap, thereby best utilizing the team's resources. The Executive Board evaluated progress weekly.

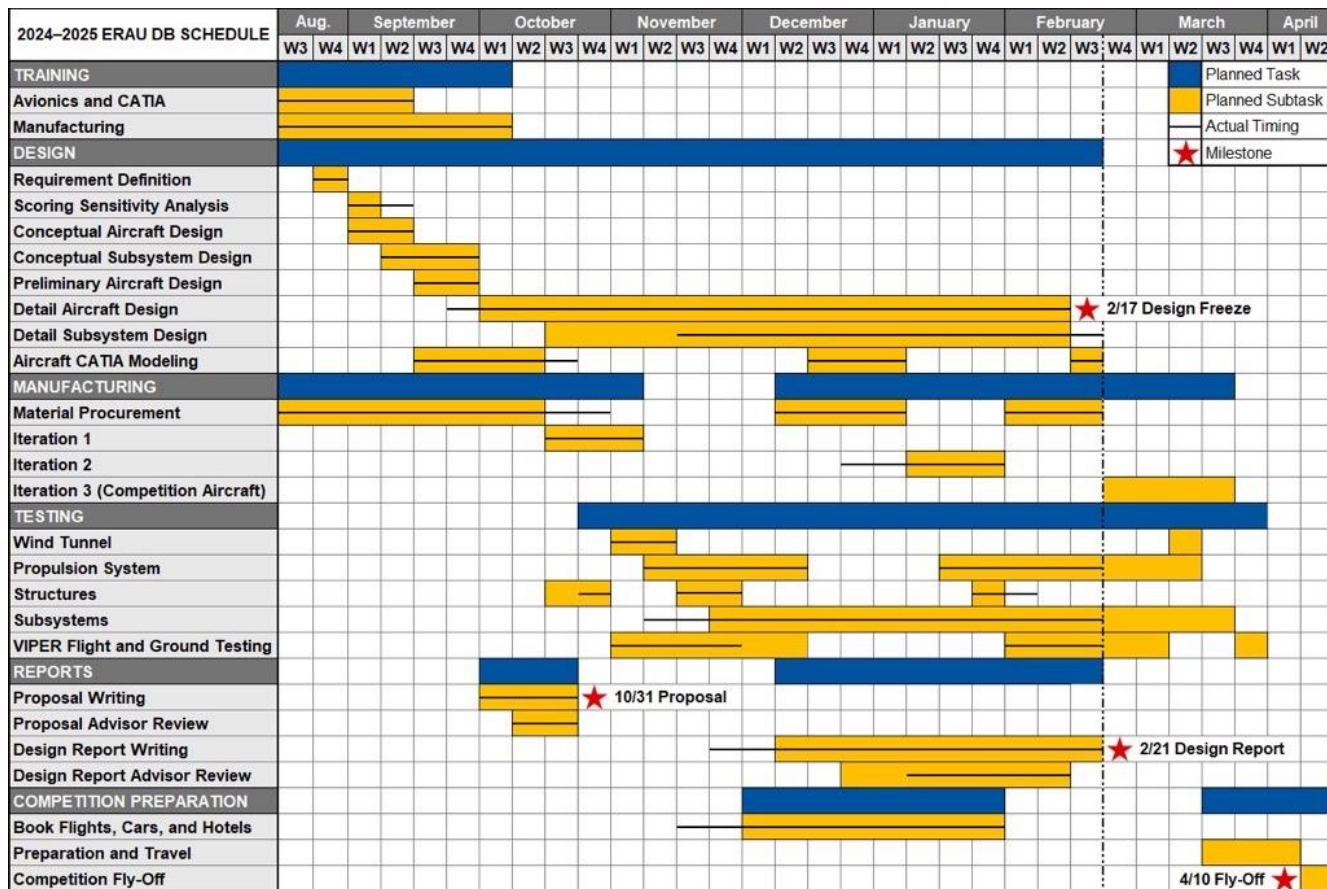


Figure 2-2: ERAU DB milestone Gantt chart.

## 3 Conceptual Design

The conceptual design phase aimed to develop an aircraft configuration that best fulfilled the mission objectives. The team selected VIPER's initial aerodynamic, propulsive, and subsystem configurations through requirement definition, scoring sensitivity analysis, and comparative analysis.



### 3.1 Mission Requirements

#### 3.1.1 Problem Statement

The competition ruleset involves the design of a captive carry aircraft, simulated by integrating pylons, external fuel tanks, and the X-1 test vehicle. M1 is a delivery flight that demonstrates VIPER's flight capabilities. M2 focuses on speed during a captive carry mission, and M3 simulates an endurance flight with the release of the X-1 into a designated landing zone. The GM emphasizes the rapid implementation of the external components. Success depends on integrating subsystems and achieving optimal flight performance for each mission.

#### 3.1.2 Mission and Score Summary

The total report score is determined by combining the proposal and design report scores, as shown in Equation 3-1. The total mission score equals the sum of the flight and GM scores, as given by Equation 3-2. The maximum mission score is seven points. A participation score is awarded with one point given for attendance, two points for passing technical inspection, and three points for attempting a flight mission. The overall competition score is a function of the total report, mission, and participation score, as given by Equation 3-3.

$$\text{Total Report Score} = 0.15 * \text{Proposal Score} + 0.85 * \text{Design Report Score} \quad (3-1)$$

$$\text{Total Mission Score} = M1 + M2 + M3 + GM \quad (3-2)$$

$$\text{Competition Score} = \text{Total Report Score} * \text{Total Mission Score} + \text{Participation} \quad (3-3)$$

All flight missions follow the flight path shown in Figure 3-1. After following the designated flight path, a lap is completed only when the aircraft crosses the start/finish line.

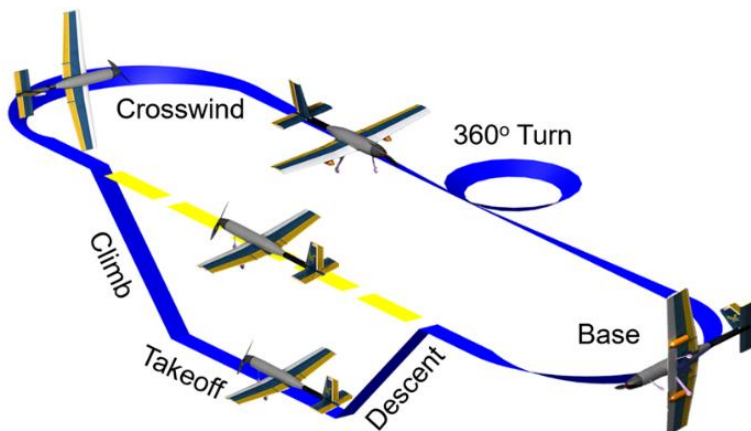


Figure 3-1: Mission flight path.

**Mission 1 – Delivery Flight:** M1 is a proof-of-flight demonstration in which three laps are flown without any payload. One point is awarded for completing the mission within five minutes.

**Mission 2 – Captive Carry Flight:** M2 simulates the captive carry of the X-1 and loaded fuel tanks. One point is awarded for completion, plus an additional fractionalized point based on fuel weight and three-lap time, normalized to the competition's highest score as defined in Equation 3-4.



$$M2 = 1 + \frac{\left[ \frac{Fuel\ Weight}{Total\ Time} \right]_{ERAU\ DB}}{\left[ \frac{Fuel\ Weight}{Total\ Time} \right]_{Max}} \quad (3-4)$$

**Mission 3 – Launch Flight:** M3 simulates the launch of the X-1. The X-1 is released on the final lap, executing a 180° turn, then glides down to a designated landing zone. The drop zone and designated landing zones are shown in Figure 3-2. Two points are awarded for completion, and one additional point is awarded as a function that incorporates the number of laps flown in five minutes before release, the weight of the X-1 test vehicle, and the bonus box score, as given by Equation 3-5. Notice that these scores are normalized using the highest score achieved in the competition.

$$M3 = 2 + \frac{\left[ \frac{N_{Laps} + Bonus\ Box\ Score}{X - 1\ weight} \right]_{ERAU\ DB}}{\left[ \frac{N_{Laps} + Bonus\ Box\ Score}{X - 1\ weight} \right]_{Max}} \quad (3-5)$$

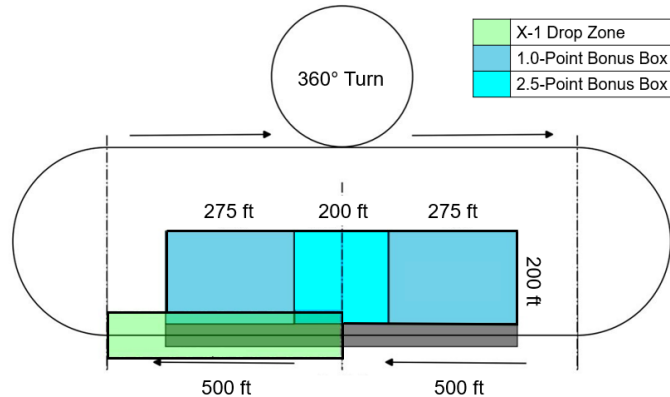


Figure 3-2: Mission flight path with X-1 landing zones.

**Ground Mission – X-1 Flight Test Program Demonstration:** The GM simulates the transformation of the fleet bomber aircraft into the test program configuration. The mission begins with the aircraft in its clean configuration. Next, the pylons, fuel tanks, and X-1 test vehicle are installed, with the judge pausing between each step to verify proper installation. Once configured, the X-1 test vehicle is released during the demonstration. The total time required to complete the procedures is ultimately normalized against the fastest performance in the competition to calculate the mission score out of one point, as given by Equation 3-6.

$$GM = \frac{[Mission\ Time]_{Min}}{[Mission\ Time]_{ERAU\ DB}} \quad (3-6)$$

### 3.2 General, Mission, and Subsystem Requirements

The requirements outlined in Table 3-1 represent the critical design criteria derived from the competition rules [1]. These requirements served as the foundation for the design process, ensuring that the aircraft adhered to regulations and satisfied the competition's necessary performance and compliance standards. To ensure that all



requirements were met, a Means of Compliance (MoC) column was included, where R indicates certification by review and T indicates certification by test. A State of Compliance (SoC) column is provided for each requirement, where C indicates compliance and NC indicates non-compliance.

*Table 3-1: Design requirements and compliance matrix.*

Category	Subcategory	Requirement	Number	MoC	SoC
Aircraft	Configuration	The aircraft wingspan must be less than or equal to 6 ft	AC-01	R	C
		The aircraft must not be rotary wing or lighter-than-air	AC-02	R	C
		Aircraft MTOW must not exceed 55 lb	AC-03	R	C
		All components must remain attached in flight except in M3 where the X-1 deploys	AC-04	T	C
	Structure	Aircraft must pass a wingtip load test with the maximum designed takeoff weight at 2.5g	AC-05	T	C
		All permanent components must be secured using locking devices	AC-06	R	C
	Performance	Aircraft must be propeller-driven and electric powered	AC-07	R	C
	Propulsion	Propulsion system and propeller must be commercial off-the-shelf (COTS) parts	AC-08	R	C
		Aircraft must have an externally accessible switch to turn on the radio control system	AC-09	R	C
		All propulsion batteries must consist of a single type (Lithium based or NiCad/NiMH)	AC-10	R	C
		Aircraft must have a separate receiver/servo battery	AC-11	R	C
		Propulsion battery total stored energy must not exceed 100 Watt hours (Wh)	AC-12	R	C
		Arming fuse maximum continuous discharge current rating must be below 100A	AC-13	R	C
		The aircraft must enter the staging box in the clean configuration with all payloads removed	OP-01	R	C
Operation	General	Aircraft assembly and payload installation must be completed in less than five minutes	OP-02	T	C
		All flight missions must be completed within five minutes	OP-03	T	C
		A minimum of two external fuel tanks must be installed during M2 and M3	OP-04	R	C
		Fuel tanks may be empty during the GM and M3	OP-05	R	C
		The aircraft must land structurally intact and come to a complete stop on the paved runway	OP-06	T	C
		Flight controls must remain operational between all configuration demonstrations	OP-07	T	C
	Ground	The aircraft may be placed on blocks during staging and ground mission	OP-08	R	C
Subsystems	X-1 Test Vehicle	The weight of the X-1 test vehicle must be less than 0.55 lb	SY-01	R	C
		The X-1 must be carried under the fuselage	SY-02	R	C



Category	Subcategory	Requirement	Number	MoC	SoC
Subsystems	X-1 Test Vehicle	The X-1 must be carried between the external fuel tanks	SY-03	R	C
		There must be a 0.25-inch gap between the wings of the X-1 and any part of the aircraft	SY-04	R	C
		The X-1 must release at an altitude of 200 - 400 ft AGL on command via the pilot's transmitter	SY-05	T	C
		The X-1 must be an autonomous glider	SY-06	R	C
		The X-1 must feature flashing lights that are observable by the judges after release and remain on after landing	SY-07	T	C
	Fuel Tanks	The external fuel tanks must be commercially available beverage bottles with a minimum capacity of 16 fl-oz	SY-08	R	C
		The fuel tank outer mold line must not be modified	SY-09	R	C
		All external fuel tanks must be identical in size, shape, and brand	SY-10	R	C
		Fuel tanks must be constructed using materials other than glass.	SY-11	R	C
		Fuel tanks must be filled with inert materials to achieve a desired mission weight	SY-12	R	C
	Pylons	A single internal fuel tank may be used	SY-13	R	C
		All external fuel tanks must be attached using pylons	SY-14	R	C
		Pylons must be removable	SY-15	R	C
		The pylon assembly must be designed so that fuel tanks remain fully visible when viewed from the front and rear of the aircraft	SY-16	R	C

In addition to the non-negotiable requirements, the team established self-imposed requirements and allowances, outlined in Table 3-2, to ensure the aircraft's safety and performance.

Table 3-2: Self-imposed requirements.

Category	Subcategory	Requirement	Number	MoC	SoC
Aircraft	Configuration	The maximum takeoff distance must be 100 ft	ACS-01	T	C
		The conversion from fleet aircraft to program demonstrator should take no more than 90 seconds	ACS-02	T	NC
		The aircraft must be modular for transport	ACS-03	R	C
		The aircraft configuration must not obstruct the storage or deployment of the X-1	ACS-04	R	C
	Structure	Ultimate loads must be 1.5 times greater than limit loads unless otherwise specified	ACS-05	R	C
	Propulsion	Propulsion battery use must not exceed 85%	ACS-06	T	C
Subsystems	X-1	The X-1 must not exceed 0.2 lb	SYS-01	R	C
		The X-1 must have sufficient control authority to land within $\pm 50$ ft of a specified point	SYS-02	T	C
	Pylon	The pylon must be able to support 35 lb	SYS-03	T	C

### 3.3 Scoring Sensitivity Analysis

A scoring sensitivity analysis was used to identify key variables and design parameters that were critical to maximizing the total mission score. M1 and the GM were not subject to the sensitivity analysis because M1 has no performance criteria, and the GM is mechanism dependent. Focusing on M2 and M3, the scoring parameters were decomposed into design parameters such as load factor and airspeed. A parametric study then quantified the change of each parameter relative to scoring potential, as shown in Figure 3-3 and Figure 3-4. These results guided the ranking of the design parameters.

From the M2 sensitivity plot shown in Figure 3-3, the score was found to vary inversely with mission time and linearly with payload weight. A decrease in lap time became possible by an increase in the design load factor or airspeed, but the load factor gave the highest increase.

M3 sensitivity as shown in Figure 3-4 demonstrated the impact of the bonus box score, placing the highest emphasis on achieving the 2.5-point bonus to increase the scoring by 120%. The analysis showed that the weight of the X-1 impacted the M3 score significantly less than the bonus box score. Overall, the scoring analysis indicated that payload weight, lap time, and X-1 landing position had the greatest impact on mission score and guided the configuration selection process.

### 3.4 Aircraft Configuration

The configuration selection was based on an analysis of previous DBF aircraft [2][3] and full-scale captive-carry aircraft. After evaluating several designs for the general configuration, propulsion system, wing, tail, landing gear, fuel tanks, and pylons, decision matrices were created to quantify the design parameters. Table 3-3 describes the decision matrix process, while Table 3-4 explains the multipliers used for the mission-critical parameters.

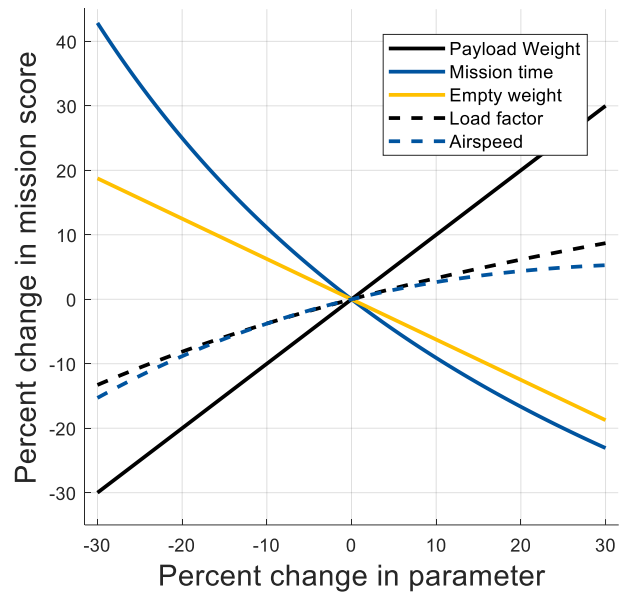


Figure 3-3: M2 scoring sensitivity.

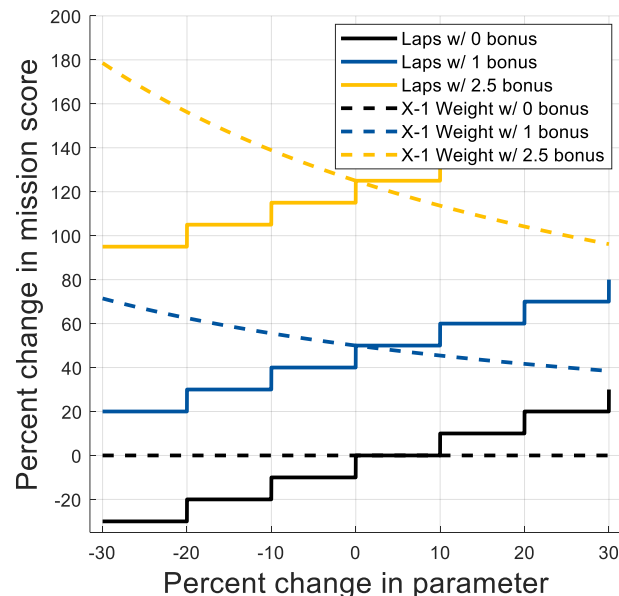


Figure 3-4: M3 scoring sensitivity.



Table 3-3: Decision matrix process.

Step	Process
1	Decide the critical design parameters for each decision matrix.
2	Apply a scoring factor based on requirement from 1 (worst) to 3 (best).
3	Assign each design a score from 1 (worst) to 5 (best).
4	Calculate the weighted average and choose the highest score.

Table 3-4: Factor values and reasoning for parameters.

Parameters	Factor	Reasoning
Structural Design	3	Design must handle expected load cases per AC-05
Drag	3	Minimize to achieve M2 and M3 cruise speed most efficiently
X-1 Release Risk	3	Mitigate component and X-1 interference per ACS-04
Battery Consumption	3	100 Wh battery capacity limit per AC-12
Handling Qualities	3	Balance stability, controllability, and maneuverability for minimum lap times
Weight	2	Airframe and system weight reduces available payload weight
Payload Integration	2	Ease and speed of GM payload integration per ACS-02
Ground Handling	2	Straight tracking and controllability for long takeoff roll
Takeoff Performance	1	100 ft requirement per ACS-01
Manufacturability	1	Manufacturing quality and timeline considerations

### 3.4.1 General Aircraft Configuration

VIPER's configuration selection compared three designs: tail boom, conventional, and blended wing body (BWB), as shown in Table 3-5. Although the BWB offered minimal drag and the highest cruise efficiency, it was not chosen because of structural and payload integration challenges. The conventional configuration was easier to manufacture and integrate subsystems but suffered from increased weight and drag. The tail boom design was chosen for its ample payload space, manufacturing simplicity, and low drag. Additionally, a circular fuselage was chosen to match the payload geometry and minimize wetted area for optimal aerodynamic efficiency.

Table 3-5: General aircraft configuration selection matrix.

Parameter	Factor	Tail Boom	Conventional	BWB
Drag	3	3	2	5
Structural Design	3	5	4	2
Handling Qualities	3	4	4	2
Weight	2	3	2	3
Payload Integration	2	5	5	1
Takeoff Performance	1	3	2	5
Manufacturability	1	4	3	1
Total		59	49	41



### 3.4.2 Propulsion Configuration

Three options were considered for the propulsion system: single tractor, twin tractor, and pusher, as shown in Table 3-6. Although the twin tractor minimized X-1 deployment risk and improved takeoff performance, it was not chosen because of drag and energy inefficiencies that fell short of AC-12. Despite its favorable weight and drag, the pusher configuration imposed significant post-release risk to the X-1, violating ACS-04. Although the single tractor configuration posed a moderate risk to X-1 deployment from propeller slipstream effects, it was chosen for the best propulsion efficiency, adequate thrust for M2, and structural simplicity following ACS-05 and ACS-06.

*Table 3-6: Motor placement and configuration selection matrix.*

Parameter	Factor	Single Tractor	Twin Tractor	Pusher
		4	3	5
Drag	3	5	3	4
X-1 Release Risk	3	3	5	1
Weight	2	5	3	5
Takeoff Performance	1	4	5	1
Total		50	44	41

### 3.4.3 Wing Configuration

Three options were evaluated for wing placement: low, mid, and high, as shown in Table 3-7. The high-wing configuration offered excellent flight stability and ease of structural design but did not comply with ACS-04 because both the landing gear and the X-1 would be mounted to the fuselage. The mid-wing was not chosen because of manufacturing complexity and limited internal volume. The low-wing configuration was chosen for its desirable takeoff performance in ground effect, good controllability, and ease of internal payload integration, which aligned with requirements OP-02 and ACS-02.

*Table 3-7: Wing placement selection matrix.*

Parameter	Factor	Low	High	Mid
		3	4	2
Structural Design	3	3	4	2
Weight	2	3	3	3
Payload Integration	2	4	3	1
Handling Qualities	2	5	2	4
Takeoff Performance	1	5	3	4
Manufacturability	1	4	4	2
Total		42	35	28



### 3.4.4 Tail Configuration

Four distinct geometries were considered for the tail configuration: conventional, V-tail, H-tail, and T-tail, as shown in Table 3-8. The V-tail configuration offered maneuverability and weight savings but was not chosen because of potential controllability issues. While the T-tail and H-tail configurations offered stability and control power, their complex structural design and manufacture were less attractive. The conventional configuration was deemed the most suitable option because it balanced maneuverability, manufacturability, and takeoff performance while meeting the requirements of ACS-01.

*Table 3-8: Tail configuration selection matrix.*

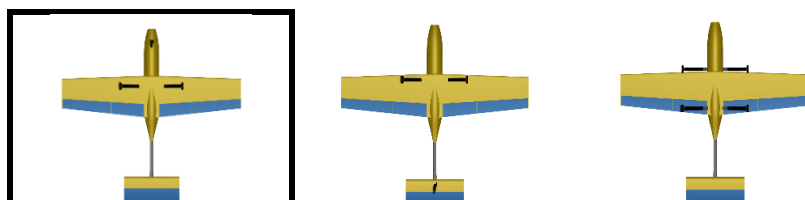


Parameter	Factor	Conventional	V-Tail	H-Tail	T-Tail
Structural Design	3	5	3	2	1
Weight	2	4	5	3	3
Handling Qualities	1	4	2	3	3
Manufacturability	1	5	1	2	2
Takeoff Performance	1	4	4	3	3
Total		36	26	20	17

### 3.4.5 Landing Gear Configuration

Three options were evaluated for the landing gear configuration: tricycle, tail-dragger, and quadricycle, as shown in Table 3-9. The tail-dragger configuration's shorter gear length reduced drag and weight but was not chosen because of poor ground controllability. The quadricycle configuration was not chosen because of low takeoff performance and increased drag and weight. The tricycle configuration was ultimately preferred for its ease of ground handling and payload integration while complying with requirements ACS-01 and ACS-05.

*Table 3-9: Landing gear configuration selection matrix.*



Parameter	Factor	Tricycle Gear	Tail-dragger	Quadricycle
Structural Design	3	3	5	4
Drag	3	3	4	1
Ground Handling	2	5	1	2
Payload Integration	2	5	2	4
Weight	2	3	5	2
Total		44	43	31



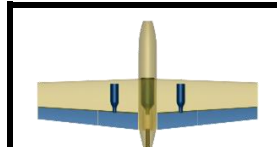
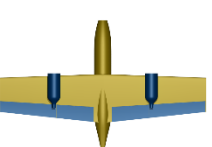
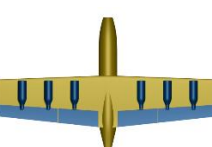
### 3.4.6 Subsystem Configuration

The process in Table 3-3 was used to define the systems that VIPER would use for its missions. Unique subsystem requirements led to individually selecting parameters rather than applying the reasoning as previously described in Table 3-4.

#### 3.4.6.1 General Fuel Tank Configuration

The fuel tank configuration selection sought to minimize the drag, adverse handling characteristics, and installation time of the system while maximizing the payload following OP-04, SY-08, and ACS-02. Three configurations were considered to accommodate the desired payload, as identified by the scoring analysis. Configuration 1 utilized two minimum-size external fuel tanks (EFTs) and one larger internal fuel tank (IFT). Configuration 2 utilized two large EFTs, simplifying installation but increasing drag and roll inertia. Configuration 3 utilized multiple small EFTs to distribute structural loads but introduced installation inefficiencies. The decision matrix shown in Table 3-10 favored Configuration 1, balancing handling qualities and performance with installation simplicity.

*Table 3-10: Fuel tank configuration selection matrix.*

				
Parameter	Factor	Configuration 1	Configuration 2	Configuration 3
Handling	3	5	3	2
Installation Efficiency	2	3	5	1
Drag	2	5	3	2
Weight Distribution	1	4	1	3
Structural Integrity	1	3	1	4
Total		38	27	19

#### 3.4.6.2 Fuel Tank Pylons

As detailed in Table 3-11, handcuff clamp, adapter, and snap-fit fuel tank pylons were considered to comply with requirements SY-14 and SY-15. Additional considerations included assembly time following ACS-02. While the adapter mechanism enabled rapid assembly, it introduced potential failure points. The snap-fit design was eliminated because it failed to meet the AC-06 criteria for a permanent feature. Ultimately, the handcuff clamp configuration was selected for its quick assembly capabilities and secure carriage of the payload.

*Table 3-11: Fuel tank pylon configuration selection matrix.*

Parameter	Factor	Handcuff Clamp	Adapter	Snap-fit
Structural Integrity	3	5	2	1
Installation Efficiency	3	4	3	5
Weight	2	2	4	3
Drag	2	2	4	3
Simplicity	1	3	5	4
Total		38	36	34



### 3.4.6.3 VENOM Release Mechanism

Three release mechanisms were evaluated for compliance with SY-05: spring-assisted, gravity, and articulating, as shown in Table 3-12. Although the gravity mechanism was easier to integrate, it did not mitigate collision risk upon release. The articulating mechanism was not chosen because of its complexity. Ultimately, the spring-assisted mechanism was selected for its reliability in releasing VENOM and its minimal drag.

*Table 3-12: Release mechanism configuration selection matrix.*

Parameter	Factor	Spring-assisted	Gravity	Articulating
<b>Reliable Release</b>	<b>3</b>	5	1	4
<b>Drag</b>	<b>2</b>	5	5	1
<b>Installation Efficiency</b>	<b>2</b>	4	5	2
<b>Structural Integrity</b>	<b>2</b>	3	4	1
<b>Simplicity</b>	<b>1</b>	3	5	1
<b>Total</b>		<b>42</b>	<b>36</b>	<b>21</b>

### 3.4.6.4 VENOM

Initial design considerations for VENOM's configuration were guided by the imposed weight requirement SYS-01, while additional considerations were given to the positional requirements SY-03 and SY-04 and the light visibility requirement SY-07. Three configurations were considered: flying wing, BWB, and conventional, as shown in Table 3-13. The BWB configuration offered an ideal balance of weight and drag but posed release control challenges because of the need for inverted mounting. The conventional configuration was attractive for its controllability but was rejected because of its high weight and clearance issues in violation of SY-04. The flying wing configuration was chosen for its low weight and minimal interference while complying with positional requirements.

*Table 3-13: VENOM configuration selection matrix.*

Parameter	Factor	Flying Wing	BWB	Conventional
<b>Weight</b>	<b>3</b>	5	4	2
<b>VIPER Interference</b>	<b>2</b>	5	2	3
<b>Structural Integrity</b>	<b>2</b>	4	5	3
<b>Avionics Integration</b>	<b>2</b>	4	4	5
<b>Controllability</b>	<b>2</b>	2	3	4
<b>Total</b>		<b>45</b>	<b>40</b>	<b>36</b>



### 3.5 Selected Configuration

To best comply with OP-03, OP-04, and SY-02, VIPER featured a conventional low-wing design with a tail boom, conventional tail, tricycle landing gear, and single tractor propulsion system, as shown in Figure 3-5. The aircraft carried two EFTs, one IFT, and VENOM for its flight missions.

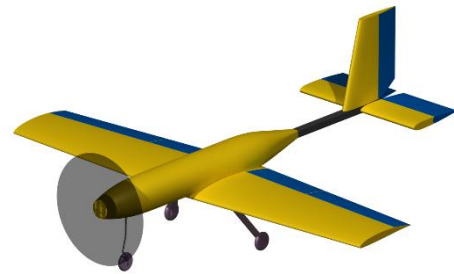


Figure 3-5: Selected configuration.

The objective of the preliminary design phase was to determine the aircraft's sizing, aerodynamic performance, and payload capacity. A combination of trade studies, analysis, and simulations were used to refine the design parameters, providing the foundation for the detailed design phase.

### 4 Preliminary Design

#### 4.1 Design Methodology

The design methodology followed an iterative process based on industry practices and past ERAU DB design cycles. First, the aircraft configuration was selected based on an analysis of mission requirements and competition constraints. The initial weight was estimated based on historical ERAU DB aircraft [2][3], and a numerical optimization was conducted in MATLAB [4] to maximize performance within the battery energy limits and selected weight fractions. Alongside this optimization, a constraint diagram depicting the relationships between thrust-to-weight ratio, ( $T/W$ ), and wing loading, ( $W/S$ ), informed the initial sizing. The aircraft's aerodynamics and handling qualities were calculated using DATCOM [5] and verified in SURFACES, a vortex lattice solver [6]. The propulsion system was sized using the Advanced Precision Composite's (APC) performance database [7] to meet speed requirements. The internal structural elements were modeled in CATIA-V5 [8] for the detail design. FEMAP Nastran [9] was used to verify the structural performance requirements. Manufacturing began upon the design freeze, consisting of composite fabrication, wooden construction, and additive manufacturing. Once completed, the aircraft underwent ground and testing where the collected data was fed back into the design cycle for potential performance improvements. This design methodology is illustrated in Figure 4-1.

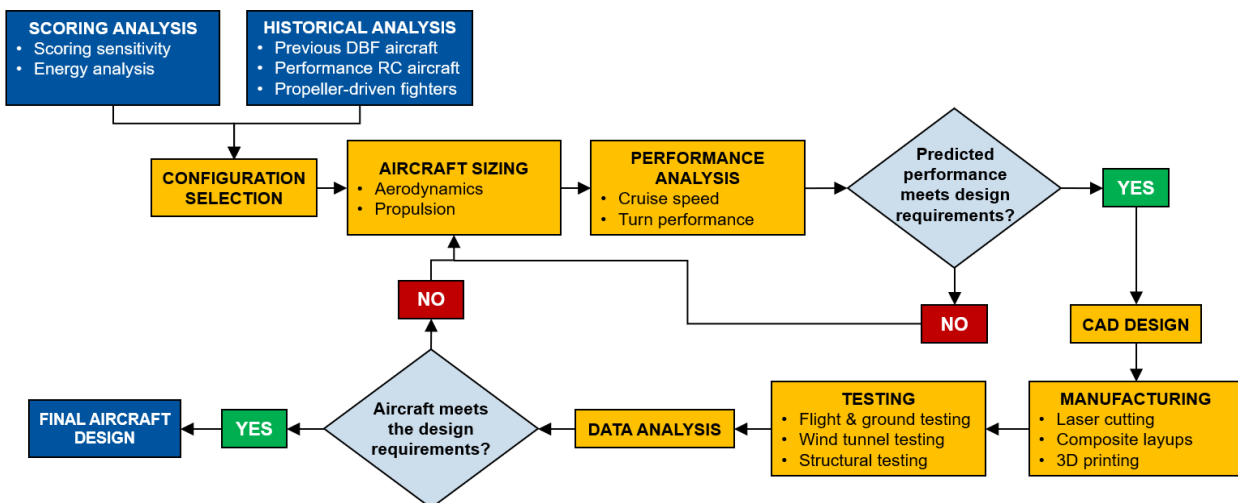


Figure 4-1: Design methodology flowchart.



## 4.2 Trade Studies

### 4.2.1 Initial Performance Optimization

Optimal design points were determined from a performance study focusing on the trade-offs between airspeed and payload weight. M1 and the GM were excluded from this analysis, as M1 is completion-based, and the GM is independent of flight performance. An objective function based on the M2 and M3 scoring equations was subjected to a gradient-based optimization method that identified the highest-scoring variable combinations. A 75% energy efficiency factor was applied to the function. A performance mesh shown in Figure 4-2 was used to evaluate the energy consumption per lap, linking airspeed to target lap times using historical competition data [2][3]. A second-degree polynomial fitted to the energy surface constrained the optimization in accordance with AC-13 and ACS-06, ensuring a balance between lap time, cruise speed, and payload weight while minimizing energy consumption.

Mission 2 optimization arrived at a 39 lb aircraft, 25 lb of which being payload, completing three laps in 99 seconds at a cruise speed of 125 ft/s. To assess the robustness of the results, the optimizer was linearized at the design point, including the assumed aerodynamic characteristics and an initial 15 lb empty weight. Perturbations had a marginal impact on the performance target, confirming the stability of the solution.

M3 required consideration of the X-1 landing zone's impact on mission performance. While all M3 laps must be completed within the 5-minute time window, only the laps before the X-1 is released count toward the mission score. The weight of the X-1 was bounded by subscale RC aircraft, Micro Air Vehicle analysis, and SYS-01, with an additional conservative payload estimate of 1.5 lb applied to the aircraft's M3 weight.

Energy-based performance sizing indicated that at 75% energy efficiency, the aircraft could complete ten laps in the 5-minute window, achieving nine scoring laps at a cruise speed of 90 ft/s with 28-second lap times. The initial analysis identified a 0.1 lb X-1 as optimal, though increasing weight within the lower bound did not significantly affect total lap count. This result suggested flexibility in the weight of X-1 if future considerations necessitate adjustments.

*Table 4-1: Optimizer bounds and results.*

Parameter	Lower Bound	Upper Bound	Result
<b>M2 Payload (lb)</b>	0	40	25
<b>M2 Lap Time (s)</b>	20	60	28
<b>M2 Airspeed (ft/s)</b>	-	-	125
<b>X-1 Weight (lb)</b>	0.10	0.55	0.10
<b>M3 Lap Time (s)</b>	20	60	27
<b>M3 Airspeed (ft/s)</b>	-	-	90

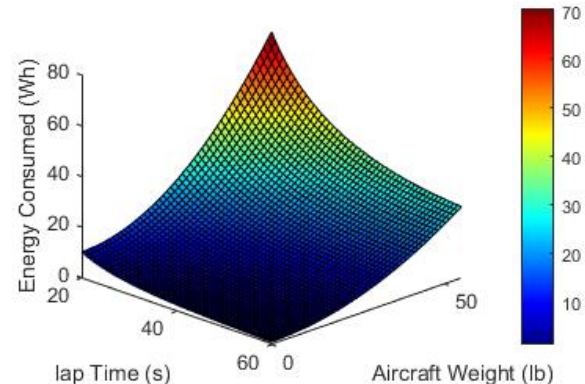


*Figure 4-2: Energy mesh over a single lap.*

### 4.2.2 Fuel Tank Sizing and Placement Analysis

Based on the results of the configuration selection performed in Section 3.4.6.1, the payload weight for M2 had to be distributed between two EFTs and one IFT. A MATLAB [4] program was developed to analyze the trade-offs of payload distribution across the tanks to assess the aerodynamic, structural, and performance implications.



In compliance with SY-08, the EFTs could be any bottle with a volume of at least 16 fl oz, and the IFT could be a bottle of any volume. Empirical measurements and manufacturer specifications for potential IFTs and EFTs, including volume, average width, and average height, are given in Table 4-2. The M2 target payload weight of 25 lb was distributed based on the volume fraction of the fuel tank to the total available volume. The drag coefficients for the EFTs were estimated by approximating the containers as axial cylinders and applying Hoerner's [10] empirical data and Roskam's [11] formulas. Fuel tank sizes under the 16 fl oz competition limit SY-08 were omitted from the drag analysis, as they would be stored inside the aircraft. Equation 4-1 from Roskam [11] was used to estimate the drag coefficients for the EFTs as given in Table 4-2.

$$C_{D_0} = \frac{C_f(S_{\text{wet}}/S_{\text{ref}})}{(1 + k_{\text{shape}})} \quad (4-1)$$

The analysis assessed the EFT impact on the wing structure by approximating it as a cantilever beam and relating its weight and position along the wing to the impact on bending moment distribution. Moving the EFTs outboard decreased the wing's in-flight bending moment and increased the potential load factor in turns. As a consequence of rolling inertia gain that resulted from placing weight outboard, the aircraft's roll performance was affected and quantified by the time required for the aircraft to roll to a bank angle of 85 degrees. These two parameters were balanced to ensure the maximum turning performance.

The best solution was found by creating a cost function with weighted coefficients on each of the parameters normalized to their maximum value, before being added together for an overall score. These weighted coefficients were determined by rating the importance of each performance goal. The ideal EFT configuration was determined to be two 16 fl oz bottles placed at 11.25 inches spanwise, prioritizing aerodynamic and roll performance over bending minimization. The EFTs hold 5 lb on each wing with the remaining 15 lb in a 2-liter (67.6 fl oz) bottle IFT.

Table 4-2: IFT and EFT bottle standard size and estimated drag.

Volume (fl oz)	Diameter (in)	Standard Height (in)	Estimated $C_{D_0}$	Volume (fl oz)	Diameter (in)	Standard Height (in)	Estimated $C_{D_0}$
12.0	2.40	5.55	-	24.0	2.90	8.25	0.031
16.0	2.55	6.25	0.027	32.0	2.60	8.75	0.036
16.9	2.55	7.25	0.031	64.0	4.90	10.25	0.024
20.0	2.85	7.25	0.028	67.6	4.70	12.00	0.031

### 4.3 External Geometry

#### 4.3.1 Wing

Continuing from the performance optimizer discussed in Section 4.2.1, a constraint diagram was constructed using Gudmundsson's method [12]. This diagram shows performance targets as functions of  $W/S$  and  $T/W$ . Because M2 has the highest flight performance demands with its heavy payload, the diagram was created based on its specific design targets. A constant rate and angle of climb, constant velocity turn, constant cruise velocity, and 100-ft takeoff requirement per ACS-01 served as the design constraints for M2 as plotted in Figure 4-3.

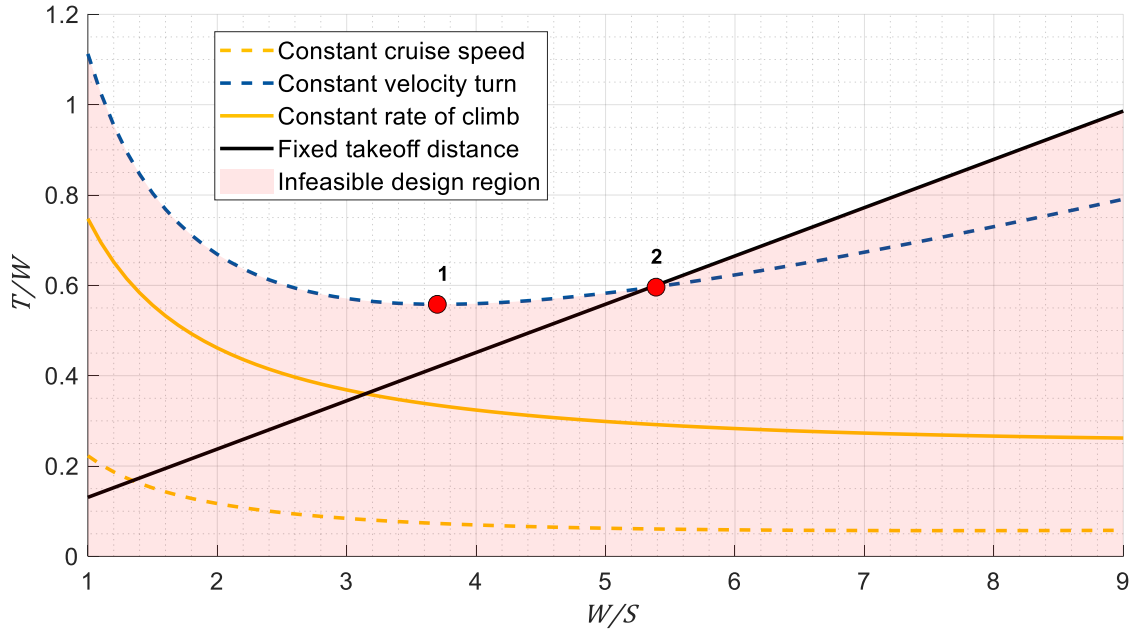


Figure 4-3: Constraint diagram.

$T/W$  and  $W/S$  were optimized at Points 1 and 2. In light of requirement AC-01, the full six ft of allowable wingspan was used to prioritize lift performance. The possible wing loading and thrust loading quantities for VIPER and their respective design implications are tabulated below in Table 4-3.

Table 4-3: Summary of design parameters at optimum points.

Point	$W/S$	$T/W$	Wing Area ( $\text{ft}^2$ )	Aspect Ratio	Thrust Requirement (lb)
1	3.70	0.55	10.54	3.42	21.45
2	5.40	0.60	7.22	4.98	23.40

It was found that lap time impacted the score more than payload, as outlined in Section 3.3, making it imperative that the wing design minimized drag. This observation resulted in the selection of the smaller,  $7.22 \text{ ft}^2$  wing at Point 2. The higher aspect ratio associated with this point was the primary factor in this decision because of lower induced drag. To maintain a continuous wing spar, the quarter-chord sweep was set to  $0^\circ$ . A taper ratio of 0.4 was ideal for most low-sweep wings for its more efficient lift distribution [13]. If such taper was used for this design point, however, integrating structural components in the outboard wing would become challenging without using an airfoil with a greater thickness. A thicker airfoil provided the required structural strength, but it increased sectional drag which negatively impacted overall aerodynamic performance. Ultimately, a taper ratio of 0.7 was chosen for balanced spanwise lift efficiency while also allowing for the integration of internal components and structures. The final wing planform dimensions are listed in Table 4-4. The wing was initially split into a flat inboard and a  $5^\circ$  cranked dihedral outboard section, resulting in high lateral stability. The wing was converted to a flat-top with an equivalent dihedral angle of  $0.69^\circ$ , effectively increasing roll authority while maintaining marginal stability. Additionally, the change eliminated structural complexities associated with the cranked wing planform.



Table 4-4: Final wing geometry.

Parameter	Value
Span (ft)	6.00
Area (ft <sup>2</sup> )	7.22
Aspect Ratio	4.98
Root Chord (in)	17.0
Taper Ratio	0.70
Mean Aerodynamic Chord (MAC) (in)	14.6
Quarter-Chord Sweep (°)	0.00
Dihedral Angle (°)	0.69

The mission weights and speeds resulting from the score optimizer allowed the calculation of the wing lift requirements for major flight conditions. M2 and M3 cruise Reynolds Numbers ( $Re$ ) were calculated to be 913000 and 655000, respectively. Equation 4-2 expresses the lift requirement as a function of load factor and dynamic pressure. Equation 4-3 introduces an airfoil  $C_{l_{max}}$  correction factor for aspect ratio effects [13].

$$C_{L_{Aircraft}} = \frac{2nW}{\rho V^2 S_W} \quad (4-2)$$

$$C_{l_{Airfoil}} = \frac{C_{L_{Aircraft}}}{1 + \frac{2}{\pi A}} \quad (4-3)$$

The associated airfoil section  $C_l$  required of each condition is shown in Table 4-5. The table shows the highest lift requirement, excluding flap assistance.

Table 4-5: Mission segment lift requirements. Clean unless specified otherwise.

Mission Segment		$n_z$ (g)	$W$ (lb)	$V_\infty$ (ft/s)	Required $C_{L_{Aircraft}}$	Required $C_{l_{Airfoil}}$
M1	Takeoff (flaps)	1	15	90	0.23	0.26
	Cruise	1	15	90	0.23	0.26
M2	Takeoff (flaps)	1	39	60	1.36	1.54
	Cruise	1	39	125	0.31	0.35
	Turns	5	39	125	1.41	1.60
M3	Takeoff (flaps)	1	17	40	1.34	1.51
	Cruise	1	17	90	0.26	0.29
	Turns	10	17	90	1.25	1.51

VIPER's wing airfoil section requirements were divided into the following flight conditions: takeoff, landing, cruise, and level constant velocity turn (CVT). The performance of various airfoils was compared using the XFLR5 software [14] with its unique batch airfoil analysis feature. Because of the difficulty in manufacturing smooth wing surfaces, these simulations were performed by assuming an early onset of flow transition. Basic information and performance data of the most capable airfoils that were considered are summarized in Table 4-6.



Table 4-6: Wing airfoil section decision matrix.

		M2 (Re = 910000)			M3 (Re = 655000)	
Airfoil	t/c (%c)	C <sub>l<sub>max</sub></sub>	L/D at cruise	L/D in CVT	C <sub>l<sub>max</sub></sub>	L/D in CVT
Clark Y	11.72	1.54	57.0	72.0	1.48	101.0
SD7034	10.51	1.61	43.5	86.5	1.57	104.0
SD7062	13.98	1.68	48.4	110.0	1.64	90.4
SG6042	10.00	1.67	58.2	84.5	1.63	121.0

A comparison of the promising airfoils led to the selection of the SG6042. This airfoil was chosen for its high  $C_{l_{max}}$  and excellent L/D in M2 cruise and M3 turns. The predictions were compared with wind tunnel measurements [15], which validated the software analysis in these flight conditions. For the CVT configuration, software calculations predicted a lift-to-drag ratio of 121, closely matching the measured value of 111. Additionally, the airfoil's maximum thickness location at the quarter-chord allowed for easy integration of the wing spar. Plain flaps were selected to comply with requirement ACS-01. These flaps were not only effective in providing improvements in maximum lift, but they were also easier to manufacture.

#### 4.3.2 Empennage

The initial empennage sizing was influenced by the takeoff requirement ACS-01 and was determined by analyzing the tail geometries of historical DBF aircraft. Airfoil selection followed, which considered the parasitic drag, manufacturability, and integration of servos. Two symmetrical NACA airfoils were considered for the horizontal and vertical stabilizers, as shown in Table 4-6. The NACA 0012 was selected for both stabilizers for its ease in manufacturing and integration of large servos required to maintain deflection at high airspeeds.

Table 4-6: Empennage airfoil considerations.

Airfoil	t/c (%c)	C <sub>l<sub>max</sub></sub>	C <sub>d<sub>0</sub></sub>	Notes
NACA 0010	10	1.38	0.004	Low drag
NACA 0012	12	1.39	0.006	Ease of manufacturing, servo integration

Tail volume coefficients of historical DBF competition aircraft were calculated using Equations 4-4 and 4-5. Table 4-7 summarizes the empennage geometries and volumes of past competition aircraft with similar mission profiles.

Table 4-7: Historical DBF aircraft tail geometries.

Component	Parameter	USC 2020 [16]	ERAU DB 2023 [2]	ERAU DB 2024 [3]	Average
Horizontal Tail	$\bar{V}_{HT}$	0.60	0.47	0.56	0.54
	Aspect Ratio	4.44	2.60	3.24	3.43
	Taper Ratio	1.00	1.00	1.00	1.00
Vertical Tail	$\bar{V}_{VT}$	0.05	0.08	0.05	0.06
	Aspect Ratio	0.71	1.40	1.35	1.15
	Taper Ratio	0.60	0.70	0.74	0.68



Given VIPER's high payload and resulting longitudinal mass moments of inertia, the team chose to make the tail volume coefficients higher than those of historical aircraft to assist in static stability. The HT was initially sized to a 24-inch span and 10-inch chord with no taper. The initial VT had a span of 16 inches, with a root chord of 12 inches and a taper ratio of 0.7. This tail sizing resulted in high directional stability in addition to a 23% static margin. To allow for more maneuverability, the tail lever arm was reduced by six inches and the VT span was reduced by two inches. After these changes, VIPER still featured higher tail volume coefficients. The final sizing for the horizontal and vertical stabilizers is summarized below in Table 4-8.

*Table 4-8: Final empennage parameters.*

Parameter	Horizontal Stabilizer	Vertical Stabilizer	Parameter	Horizontal Stabilizer	Vertical Stabilizer
<b>Span (in)</b>	24.0	14.0	<b>Aspect Ratio</b>	2.40	1.37
<b>Root Chord (in)</b>	10.0	12.0	<b>MAC (in)</b>	10.0	10.31
<b>Tip Chord (in)</b>	10.0	8.40	<b><math>S(\text{in}^2)</math></b>	240.0	142.80
<b>Taper Ratio</b>	1.00	0.70	<b><math>\bar{V}</math></b>	0.61	0.07

#### 4.3.3 Fuselage

The fuselage sizing process for VIPER was driven by the volumetric and structural requirements of its internal payloads, with the 2-liter (67.6 fl oz) soda bottle serving as the IFT. The performance trade study detailed in Section 4.2.2 determined that increasing the IFT volume enhances aircraft dynamic performance and provides structural benefits by centralizing mass distribution. The IFT diameter of 4.7 inches dictated the primary fuselage cross-section, with additional allowances to accommodate structural reinforcements required for the estimated 39 lb MTOW. As shown in Figure 4-4, the IFT is positioned over the center of gravity (CG) to optimize load distribution. The avionics and central payload bay were sized to 24.8 inches, twice the length of the IFT, to facilitate efficient loading and unloading and ensure adequate volume for avionics integration. The forward and aft sections of the fuselage are tapered to reduce drag while maintaining structural integrity. The tail boom was sized according to the required tail arm length, transitioning into the fuselage near the rear wing section, where the final bulkhead terminated the structure. This configuration ensured rigid continuity while maintaining optimal aerodynamic flow along the longitudinal axis.

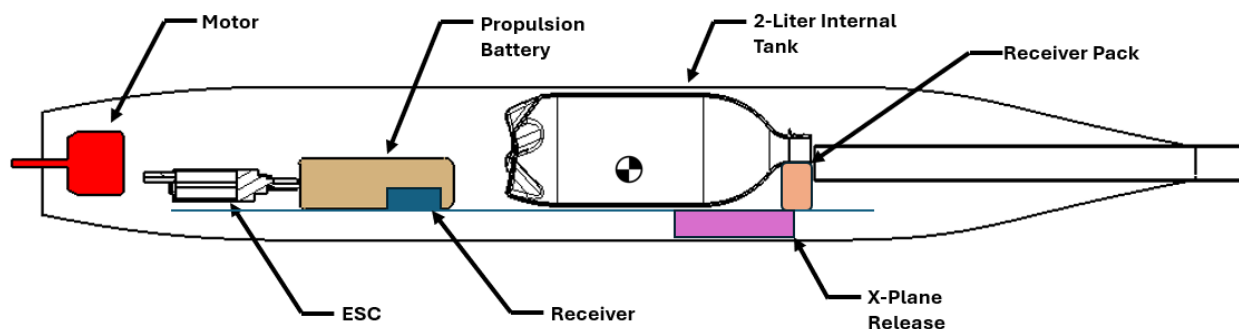


*Figure 4-4: Fuselage internal layout.*

#### 4.3.4 Landing Gear

The tricycle main landing gear (MLG) location was determined using Gudmundson's method [12] based on the most forward and aft CG limit (See Section 4.6.1). The nose landing gear (NLG) supported 9% of the aircraft's weight. The aircraft had a tail strike angle of 15.4° and a tip-back angle of 13.8°, each within an acceptable range of 15° to 20°. The overturn angle is 59.2°, as shown in Figure 4-5, ensuring ground stability during takeoff and landing. In the case of tail strike, this landing gear geometry ensures VENOM's safety.

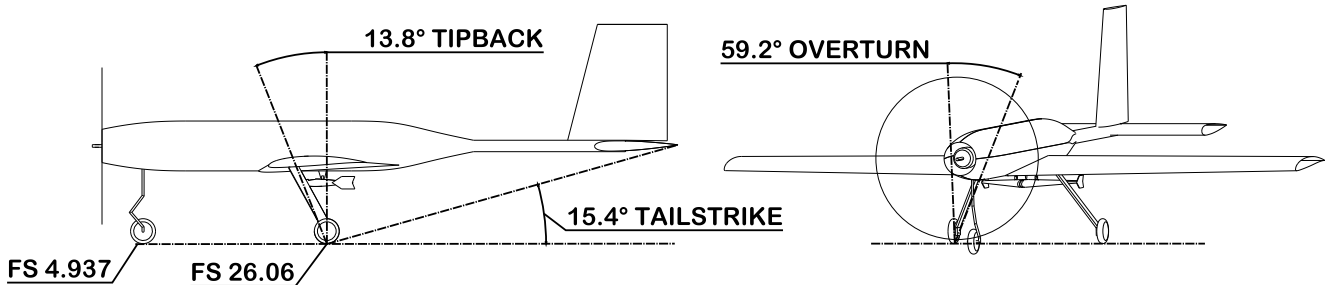


Figure 4-5: Landing gear geometry.

#### 4.3.5 Payload Configuration

Several requirements influenced placement and integration to optimize performance when selecting the payload configuration of VIPER. The internal layout was designed to balance payload weight, ensuring even weight distribution around the CG to minimize roll inertia and maximize stability. The 2-liter IFT was centrally aligned within the fuselage for structural integrity and aerodynamic efficiency. The EFTs were mounted on pylons at 31.25% of the half-span to prevent interference with aileron and flap functionality. Drag reduction strategies included streamlining pylons and optimizing bottle shape and orientation through wind tunnel testing, which is further detailed in Section 7.2.3. VENOM was secured aft of the MLG to improve drop survivability and minimize collision risks upon deployment per SY-03 and ACS-04. This placement also used CG positioning to ensure stable deployment dynamics without compromising the aircraft's flight capabilities. These considerations ensured that VIPER complies with competition requirements while achieving the best level of performance.

#### 4.4 Drag

The drag model for VIPER was developed using Hoerner's [10] and Roskam's [11] and methods that combine numerical and empirical approaches. The drag is categorized into induced drag caused by lift generation and parasitic drag ( $C_{D_0}$ ) caused by boundary layer friction, surface imperfections, and form effects. The total drag coefficient is expressed by Equation 4-6.

$$C_D = C_{D_0} + \frac{C_L^2}{e\pi AR} \quad (4-6)$$

The parasitic drag dominated VIPER's high-speed flight regime, primarily because of the landing gear and external stores. Wind tunnel testing and OpenVSP [17] simulations validated the drag estimates, showing that the landing gear contributed nearly 60% of the total drag, followed by external stores at 15%. The transition from M1 (clean configuration) to M2 and M3 (external stores added) resulted in a 15% drag increase, primarily from interference and form drag. Figure 4-6 shows the parasitic drag breakdown by component.

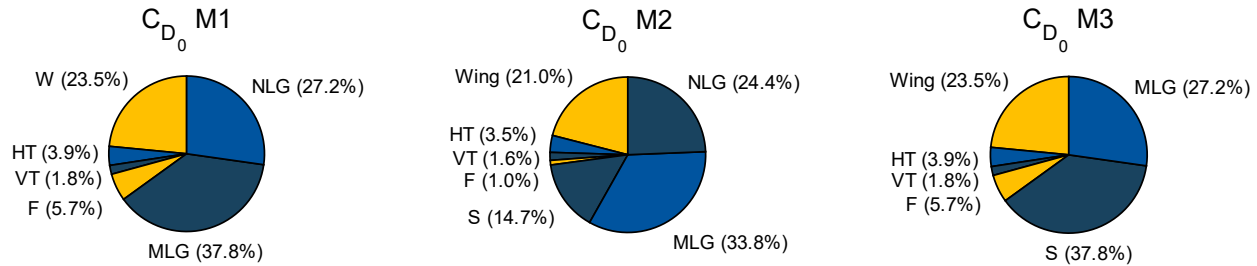


Figure 4-6: Mission drag breakdown.

The mission drag polar indicated that VIPER operated on either side of the peak lift-to-drag ratio. This was necessary to meet lap requirements within the set time constraints. During turns, drag increased significantly because of the higher load factor, with estimated values of 6.95 lb in cruise and 24.1 lb in turns for M2, as well as 3.55 lb in cruise and 23.35 lb in turns for M3. These estimates, based on component drag calculations, likely underpredicted total drag because of the incomplete modeling of parasitic effects. To account for this, a 1.5 safety factor was applied, yielding corrected cruise drag estimates of 10.43 lb (M2) and 5.33 lb (M3). Potential drag reduction strategies, such as wing-to-body fairings and wheel pants, could mitigate interference and form drag, enhancing efficiency across all mission phases. Given mission conditions, M2 experiences the highest drag impact, making optimization crucial for improving performance within DBF competition constraints.

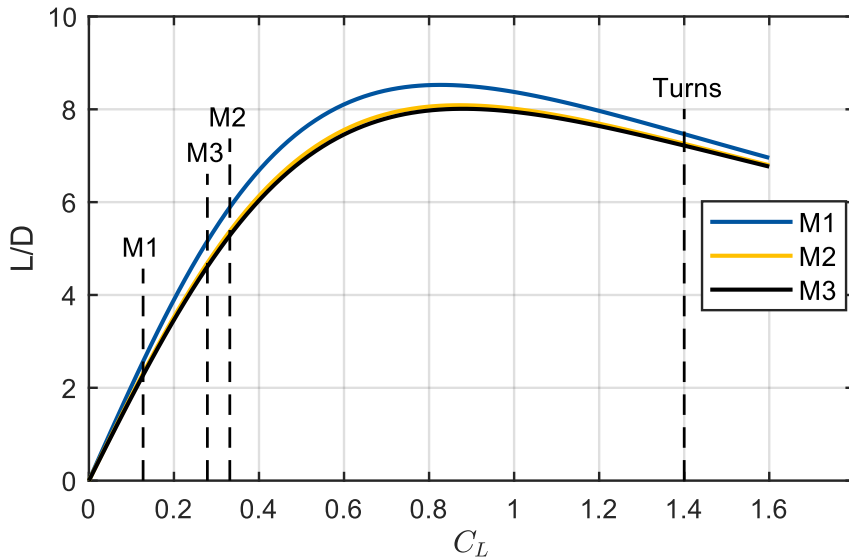


Figure 4-7: Mission drag polars.

## 4.5 Propulsion

### 4.5.1 Constraint Analysis

The constraint diagram from Section 4.3.1 was used to plot the  $T/W$  required of the aircraft as a function of  $W/S$  to meet the desired 100-ft takeoff, rate of climb (ROC), CVT, and max cruise speed of 125 ft/s. Table 4-3 provided an estimated  $T/W$  value of 0.6.



#### 4.5.2 Propulsion Selection

The development of VIPER's propulsion system was driven by the demand for exceptional versatility to meet the competition's diverse mission goals. Requirements AC-07, AC-12, and AC-13 limited the aircraft's performance. In addition, requirements AC-08 to AC-11 limited hardware selections for the system and avionics. These constraints necessitated a focused approach to optimize the propulsion system for maximum performance across all mission profiles. VIPER's propulsion system development began with the propeller, as it was the most limiting component. A motor was then chosen to achieve the necessary RPM and power output, and a battery was selected to provide the required power within the fuse limits per AC-13. Table 4-9 outlines the analysis of previous ERAUDB DBF aircraft propulsion systems, which provided a starting point and ensured that VIPER's propulsion system delivered the power, efficiency, and adaptability needed to surpass this year's mission demands.

*Table 4-9: Historical ERAU DB propulsions systems.*

Component	2024: WRENCH	2023: ROOSTER	2022: MULLET
<b>Motor</b>	Kontronik PYRO 1000-34L Comp	T-Motor 7215 220kV	Mad Components M6 Code 12 IPE 400KV
<b>Propeller</b>	Falcon 20x15C Falcon 18x12C	APC 20x10E APC 18x12E	APC 16x12E APC 16x12E

##### 4.5.2.1 Propeller Selection

The propulsion system was designed to balance the power required for M2 with the endurance needed for M3. To achieve the *T/W* of 0.6, the system needed to produce 24 lb of thrust for M2 and 8.5 lb for M3 during turning maneuvers. For cruise conditions, the required thrust was 10.43 lb for M2 and 5.33 lb for M3. Extensive data from APC on their nylon propellers was closely analyzed to identify the optimal propeller and RPM combination capable of generating these thrust values. Equation 4-7 was used to calculate the ultimate RPM value for a 20-inch diameter carbon fiber racing propeller on an electric motor. This equation is APC's [7] suggested RPM limit with a safety factor of 0.8.

$$\text{Maximum RPM} = \frac{270,000 \times 0.8}{\text{Propeller Diameter}} = \frac{216,000}{20} = 10,800 \text{ RPM} \quad (4-7)$$

This number represents the cutoff RPM at which the system's safety becomes a concern. Much of APC's available test data used propellers made of nylon, which were found to have lower performance in previous years compared to their carbon fiber counterparts [3]. Because of the carbon propeller's rigidity and light weight, the propeller can spin at a higher RPM before the tips deflected under aerodynamic forces. Therefore, APC's nylon propeller data served as a baseline for evaluating propellers of various diameters and pitches, with the understanding that carbon fiber propellers would deliver better performance.

Analysis of APC's data revealed that achieving the target of 24 lb of thrust for M2 was theoretically unachievable because of constraints AC-12 and AC-13. However, previous testing of 100 A-rated fuses by the ERAU DB DBF team showed that they could sustain a continuous current of 135 A for at least 60 seconds and endure up to 200 A for a maximum of two seconds. This insight allowed the team to size the system with greater flexibility, reducing concerns about amperage draw during takeoff. As a result, the propellers were optimized to generate the



maximum thrust possible while maintaining the desired airspeed. An 18x12 carbon propeller was selected for M2, while a 17x12 carbon propeller was selected for M3. Table 4-10 lists APC's nylon propeller performance data, with two data points included to capture the range in which the desired thrust falls.

*Table 4-10: Nylon propeller data at cruise.*

Propeller	RPM Limit ( $FS = 0.8$ )	RPM	Airspeed (ft/s)	Thrust (lb)	Power (Watts)
18x12E	12,000	10,000	126.94	19.189	4,257.05
		11,000	123.88	27.589	6,299.20
17x12E	12,700	7,000	88.45	7.280	1,131.12
		8,000	89.79	11.176	1,840.73

#### 4.5.2.2 Battery Selection

With initial propellers selected, the focus shifted to compatible batteries. Lithium-polymer (LiPo) batteries were chosen for their high-power density and fast discharge rates, which are crucial for optimal system performance for both M2 and M3. The key trade-off in battery selection involved balancing voltage and capacity while ensuring compliance with AC-12. The total energy capacity of a battery was calculated using Equation 4-8.

$$Energy_{Wh} = 1000 * mAh * Voltage_{nominal} \quad (4-8)$$

Two battery configurations were selected: a 3300 mAh 8S LiPo battery prioritizing high voltage output to improve power delivery and takeoff performance for M2, and a 4500 mAh 6S LiPo battery prioritizing endurance for M3. The batteries remained within the 100 Wh limit, with actual values of 97.7 Wh and 99.9 Wh, respectively.

#### 4.5.2.3 Motor Selection

The most prominent aspect of motor selection was the speed constant, RPM per Volt (KV). VIPER required a motor that could operate at a maximum voltage of 31.2 V to account for a voltage sag of 0.3 V per cell. Equation 4-9 was used to calculate the minimum KV needed to achieve the target RPM for M2 and M3.

$$RPM = KV \times V_{battery} \quad (4-9)$$

Based on the maximum RPM limit calculated in Section 4.5.2.1, the minimum KV of 400 was determined. The Xnova Lightning 4535-460KV not only surpassed this requirement but also offered a high continuous power rating. When powered by the 8S battery, the motor reached a maximum of 13,600 RPM, while the 6S battery resulted in a maximum of 10,200 RPM. Although APC's data offered insight into the required motor power, additional calculations were performed to validate the motor's compatibility with the overall propulsion system. The target mission flight times, which were calculated in Section 4.2.1, were used to calculate the discharge rate,  $C_{DR}$ . This value was then multiplied by the Wh of the battery to calculate the maximum continuous power allowed.

$$Flight\ time\ in\ minutes = \frac{60\ minutes}{C_{DR}} \quad (4-10)$$

$$Continuous\ Power = C_{DR} \times Watt\ hours \approx 3,900\ W \quad (4-11)$$



This continuous power was calculated to be 3,900 W for an M2 flight time of one minute and 39 seconds, while a flight time of four minutes and 30 seconds for M3 was used to calculate a continuous power of 1,300 W. The Xnova had a continuous power rating of 6,600 W which allowed VIPER to operate in undesirable flight conditions at its high M2 wing loading. Equation 4-12 from Roskam [11] was used to calculate the power required at cruise for M2 and M3. A graph depicting required power versus velocity for each mission is shown in Figure 4-8.

$$P_{level} = P_{turn} = \frac{1}{2} \rho V^3 S C_{D_0} + \frac{2W^2}{\rho V S_w} \left( \frac{1}{\pi e AR} \right) \quad (4-12)$$

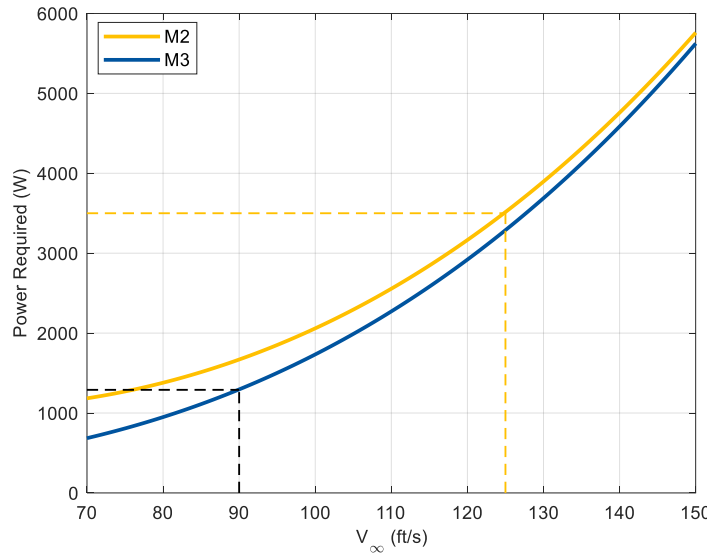


Figure 4-8: Power consumed in M2 and M3

#### 4.5.3 Performance

##### 4.5.3.1 Takeoff

This year's take-off phase is evaluated by time to liftoff and energy consumption, rather than ground roll distance like in previous competitions. A Gudmundsson-based simulation [12] modeled thrust, weight, lift, and drag over the takeoff roll. This model incorporated airspeed during ground roll and Tucson's density altitude effects, which increase energy demand. APC propeller data [7] estimated thrust and power consumption. Takeoff time and energy consumption were recorded for various propeller-battery combinations at mission weights. As shown in Table 4-11, larger diameter propellers reduced the takeoff time because of a higher static thrust.

Table 4-11: Estimated takeoff performance for each mission.

Mission	MTOW (lb)	Propeller	Cell Count	Ground Roll (ft)	Time (s)	Energy (Wh)
M2	39	17x10E	8	36.70	1.45	10.07
	39	17x12E	8	33.62	1.36	9.86
	39	18x10E	6	53.37	1.88	8.27
M3	15	18x12E	6	6.63	0.53	3.34
	15	19x12E	6	5.44	0.46	2.36
	15	20x10E	6	5.40	0.45	2.33



#### 4.5.3.2 Rate of Climb

The rate of climb (ROC) for each mission was calculated using Equation 4-13 [13], which relates the aircraft's excess available power to the weight. The predicted ROC for each mission is shown in Figure 4-9.

$$ROC = 60 \left( \frac{T * V - D * V}{W} \right) \quad (4-13)$$

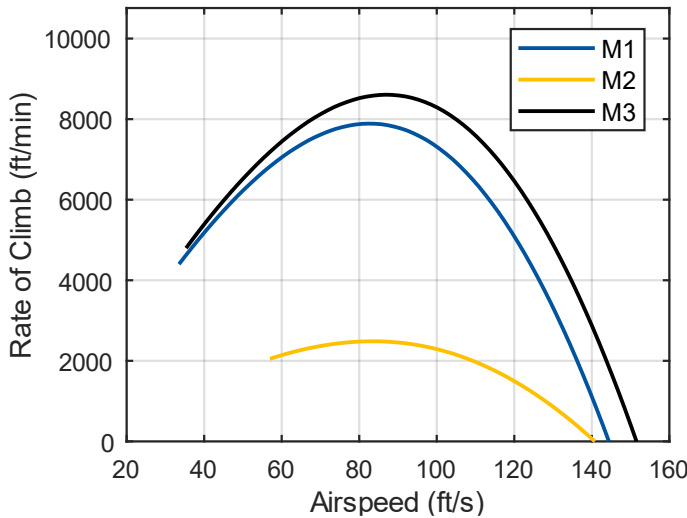


Figure 4-9: Mission rate of climb.

#### 4.5.3.3 Cruise

The cruise airspeeds for VIPER were optimized based on the performance analysis discussed in Section 4.2.1 to balance thrust, efficiency, and power consumption. Propeller and RPM selections were derived from APC data [7] to meet mission-specific cruise targets, as shown in

Table 4-12. For M1 and M2 (125 ft/s), an 18x10E propeller was used at 7,000 RPM and 10,500 RPM, respectively.

For M3 ft/s, a	Mission	Cruise Airspeed (ft/s)	Cruise RPM	Cruise Propeller	(90)
	<b>M1</b>	125	7,000	18x12E	
	<b>M2</b>	125	10,500	18x12E	
	<b>M3</b>	90	9,500	17x12E	

17x12E propeller at 9,500 RPM improved propulsive efficiency at lower airspeeds.

Table 4-12: Mission cruise conditions.

Mission	Cruise Airspeed (ft/s)	Cruise RPM	Cruise Propeller
<b>M1</b>	125	7,000	18x12E
<b>M2</b>	125	10,500	18x12E
<b>M3</b>	90	9,500	17x12E

#### 4.5.3.4 Turns

The turn performance of VIPER was estimated using Raymer's [7] turn radius in Equation 4-14, relating maximum load factor ( $n_z$ ) and airspeed ( $V_\infty$ ) to minimum turn radius ( $R$ ). Load factor is limited by aerodynamic stall at low



speeds and structural limits at high speeds. Figure 4-10 shows the load factors for M2 and M3 as a function of airspeed, while Equation 4-15 accounted thrust effects. Figure 4-11 compares the minimum mission turn radius in the power-on and power-off conditions, aiding maneuverability analysis and mission compliance.

$$R = \frac{(V_\infty/g)^2}{\sqrt{n_z^2 + 1}} \quad (4-14)$$

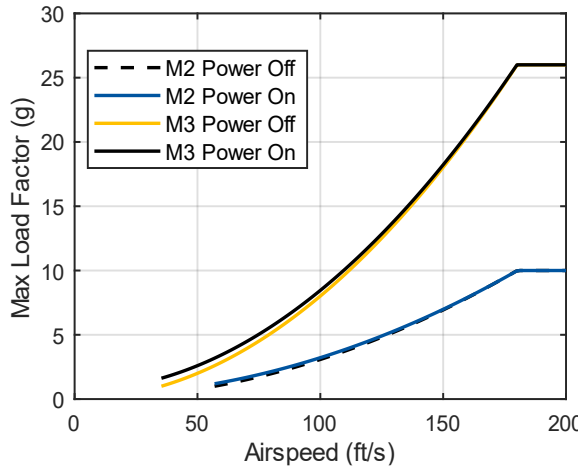


Figure 4-10: Mission max load factor envelope.

$$n_{eff} = n_z + \frac{T \sin \alpha}{W} \quad (4-15)$$

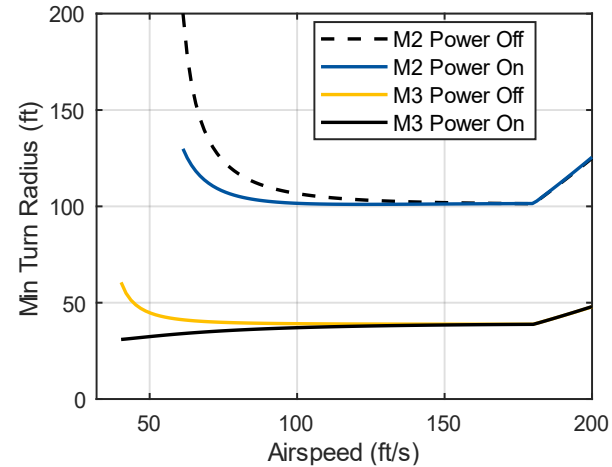


Figure 4-11: Mission turn radius envelope.

## 4.6 Stability and Control

VIPER's initial sizing aimed to ensure positive stability for all missions and flight conditions. The handling qualities of VIPER were evaluated based on static stability, dynamic stability, and controllability. Stability in the wind axis was primarily calculated using the DATCOM [5] method and verified with SURFACES [6], a vortex lattice method.

### 4.6.1 Static Stability

DATCOM [5] and SURFACES [6] were used to determine the static stability derivatives of VIPER. To encompass the gross weights of M2 and M3, the wing and horizontal stabilizer were trimmed at -2° and -1°, respectively. The two methods yielded values, shown in Table 4-11, that generally agreed and achieved the desired stability.

Table 4-11: Summary of static stability (M2).

Parameter	Symbol	DATCOM	SURFACES
Pitch Stability (l°)	$C_{Ma}$	-0.01410	-0.01460
Directional Stability (l°)	$C_{N\beta}$	0.00290	0.00314
Lateral Stability (l°)	$C_{I\beta}$	0.00383	-0.00532
Neutral Point	$\tilde{N}_o$	42.8% MAC	43.4% MAC
Static Margin	$S.M.$	17.8%	18.4%

### 4.6.2 Stability CG Range

The aft CG limit was primarily defined by the aircraft geometry and was restricted by the neutral point with full power. Without power effects, the neutral point was calculated to be at 42.8% MAC. At windmilling power, the



neutral point shifted forward to 41.3% MAC. Full-power propulsive effects brought the neutral point a further 4.5% forward to 36.8% MAC. The forward CG limit, beyond which the aircraft cannot maintain level flight, was defined by elevator power, flap configuration, and ground effect. Using Equation 4-16, limiting case was with full flaps in ground effect, leading to a forward CG limit of 20% MAC. The forward and aft CG limits are shown in Figure 4-12.

$$(\tilde{x}_{CG\_{fwd}\_{IGE}})_{dirty} = \tilde{x}_{CG\_{fwd}\_{OGE}} + \tilde{\Delta x}_{GE} = \tilde{N}_{o_{wp}} + \left( \frac{-(C'_{M_0} + C_{M_{\delta e}} \delta_{e\_max\_{up}} + \Delta C_{M-wf})}{C_{L\_max\_{dirty}}} \right)_{OGE} \pm 0.5 \frac{d\varepsilon}{d\alpha} \frac{C_{M_{\delta e}}}{a_w T_e} \quad (4-16)$$

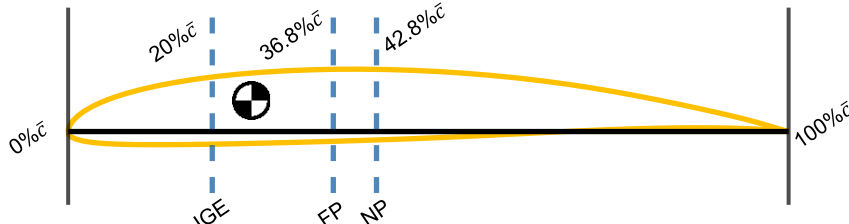


Figure 4-12: Forward and aft CG limits.

#### 4.6.3 Dynamic Stability

The dynamic stability of VIPER was calculated about its longitudinal, directional, and lateral axes for all missions, with the damping coefficients for roll, pitch, and yaw rates obtained from SURFACES [6]. VIPER's pitch, yaw, and roll damping coefficients are summarized in Table 4-12.

Table 4.12: VIPER aerodynamic damping derivatives.

Parameter	Symbol	Value (°)
Pitch Damping	$C_{Mq}$	-0.1823
Yaw Damping	$C_{Nr}$	-0.0039
Roll Damping	$C_{Lp}$	-0.0073

For longitudinal motion, short period and phugoid modes were considered and analyzed. Lateral-directional motion was coupled and consisted of the Dutch Roll, Spiral, and Roll modes. The five dynamic modes for VIPER were evaluated in SURFACES [6] using the aircraft's weight distribution, external geometry, and flight conditions. All oscillatory modes were determined to be stable and damped. Table 4-13 summarizes the time to half amplitude,  $t_{1/2}$ , of the five modes.

Table 4-13: VIPER free response (no control input) to in-flight disturbances.

Parameter	Mission	Longitudinal		Lateral/Directional		
		Short Period	Phugoid	Dutch Roll	Spiral	Roll
$t_{1/2}$	M1	0.3257	6.2	1.8851	24.6523	0.1165
	M2	0.3442	14.0	3.0400	47.9362	0.1177
	M3	0.1175	7.8	0.7709	26.0971	0.1243



#### 4.6.4 Controllability

VIPER's control surfaces comprised of flaps, ailerons, elevators, and rudder. The flaps on the inboard wing deflect  $+45^\circ$  and  $-30^\circ$ , enabling a short takeoff in its 39 lb M2 configuration, as well as doubling as spoilers to arrest the landing roll. All other control surfaces had a  $\pm 30^\circ$  deflection because of mechanical limitations imposed by the servos. To achieve a high level of crosswind controllability, the rudder comprised 45% of the vertical stabilizer area. The elevator was sized at 45% of the aft HT chord and 100% of its span. The elevator-to-chord ratio was increased from the initial 40% to facilitate tighter turns in VIPER's lighter configurations. The ailerons covered the outer 60% wingspan and the aft 30% of the chord. DATCOM [5] and SURFACES [6] were used to evaluate the controllability of VIPER and validate the control surface sizing. A summary of the results at the M2 cruise condition is shown in Table 4-14.

Table 4-14: Control surface powers.

Parameter	Control Variable	DATCOM ( $^\circ$ )	SURFACES ( $^\circ$ )
Lift Variation with Elevator	$C_{L_{\delta e}}$	0.0115	0.01087
Pitch Control Power	$C_{M_{\delta e}}$	0.0332	0.02865
Roll Control Power	$C_{l_{\delta a}}$	0.0127	0.01138
Adverse Yaw	$C_{N_{\delta a}}$	-	-0.00010
Side Force Variation with Rudder	$C_{Y_{dr}}$	0.0050	0.00456
Yaw Control Power	$C_{N_{dr}}$	-0.0029	-0.00259
Lift Variation with Flaps	$C_{L_{\delta f}}$	0.0170	0.01633
Pitch Variation with Flaps	$C_{M_{\delta f}}$	-	0.00399

The associated control surface trims for takeoff, cruise, and landing were calculated for M2 and M3. Airspeed and angle-of-attack were considered for elevator deflections to ensure steady and level flight. Additionally, the required rudder deflection angle to maintain heading in high crosswinds was determined by analysis of historical weather data from the Tucson International Airport [18], with the upper quartile crosswind value of 26.4 ft/s from the past four years selected as the representative scenario. Table 4-15 summarizes the control surface deflections for takeoff, landing, cruise, and crosswind conditions.

Table 4-15: Required elevator deflection  $\delta_e$  at cruise (left), and rudder deflection  $\delta_r$  in a 26.4 ft/s crosswind (right).

Mission	Condition	$\alpha$ ( $^\circ$ )	$\delta_e$ ( $^\circ$ )	Mission	Condition	$\beta$ ( $^\circ$ )	$\delta_r$ ( $^\circ$ )
M2	Cruise	3.6	2.5	M2	Cruise	12.8	15.9
	Takeoff/Landing	14.4	9.5		Takeoff/Landing	21.4	27.7
M3	Cruise	2.3	3.8	M3	Cruise	15.9	19.9
	Takeoff/Landing	7.6	6.2		Takeoff/Landing	27.5	35.9

In the unlikely event of a fuel tank pylon failure leading to an asymmetrical weight distribution across the longitudinal axis during M2, it was essential to calculate the necessary control inputs to maintain level flight. The required aileron and rudder deflection angles are given in Table 4-16.



Table 4-16: Required control surface deflections following unilateral pylon failure.

Mission	Condition	$\delta_a$ (°)	$\delta_r$ (°)
M2	Cruise	2.63	0.50
	Takeoff/Landing	11.40	1.91

#### 4.7 Risk Analysis

Each phase of VIPER's design, construction, and flight testing presents a set of risks, with each being given a severity level, S, and probability of occurrence, P. These factors were assessed on a scale of 1 to 5, with 1 being the lowest and 5 the highest. The values were then multiplied to obtain the risk factor (RF). After the risks were identified, strategies for mitigation were developed and implemented to reduce the probability of occurrence. These mitigation strategies, including testing, quality control (QC), and training, are shown in Table 4-17

Table 4-17: Risk factor analysis.

Risk Category	Risk	S	P	RF	Mitigation Strategy
Structural Risks	Fuselage Structural Failure	5	2	10	Conduct stress analysis, implement material testing, reinforce critical areas
	Carry-Through Structural Failure	5	1	5	Use FEA modeling to predict stress points; Perform static load testing
	Pylon Failure	4	2	8	Fatigue test under simulated flight conditions
Avionics & Control Risks	Control Surface Servo Failure	5	2	10	Redundant servo systems; implement pre-flight function checks
	Battery Capacity Loss in Flight	3	3	9	Install onboard telemetry with real-time alerts; Maintain battery health checks
	X-1 Release Failure	3	3	9	Conduct rigorous flight testing under varying conditions
Operational Risks	Aircraft not Staged in 5 Minutes	5	2	10	Implement timed staging practice sessions; Define clear team roles
	Overlook Manufacturing Defects	3	2	6	Employ a multi-step QC system: Conduct material inspections
Environmental Risks	Loss of Hatch in Flight	3	2	6	Flight test to assess; vibration testing
	Crosswind Take-off/Landing	1	5	5	Train pilots in crosswind procedures

#### 4.8 Predicted Mission Score

The predicted competition scores were based on the scoring analysis conducted in Section 3.3, the cruise performance calculated in Section 4.5.3.3, and the turn performance calculated in Section 4.5.3.4. The estimated fly-off values were derived from the known performance of previous DBF aircraft, as shown in Table 4-18.



*Table 4-18: Simulated mission performance.*

Mission	VIPER	Competition Maximum	Final Score
M1	Pass	Pass	1
M2	15.15 lb/min	18.00 lb/min	1.84
M3	9 laps + 25 bonus	12 laps + 25 bonus	2.92
GM	90 seconds	30 seconds	0.33
<b>Predicted Mission Score</b>			<b>6.09</b>

## 5 Detail Design

The Detailed Design phase finalized VIPER's structural, aerodynamic, and subsystem configurations to ensure the best and most reliable performance. Using the parameters defined in the Preliminary Design phase, the team refined the airframe structural design for weight reduction, increased strength, and ease of assembly.

### 5.1 Final Aircraft Parameters

The final aircraft parameters of VIPER are summarized in Table 5-1.

*Table 5-1: Final aircraft parameters.*

Parameter	Length (in)	Parameter	Wing	HT	VT
Fuselage	45.00	Airfoil	SG 6042	NACA 0012	NACA 0012
Fuselage Diameter	6.00	Span (in)	72.00	24.00	14.00
Tail Boom	15.00	MAC (in)	14.59	10.00	10.31
Total Tail	24.25	LE Sweep (°)	2.04	0.00	14.42
		Area (in <sup>2</sup> )	1039.9	240.0	142.8
		Aspect Ratio	4.98	2.40	1.37
		Control Surface Ratio (%)	30	40	50
		Incidence (°)	-2.00	-1.00	0.00

### 5.2 Structural Characteristics

#### 5.2.1 Layout and Design Methodology

VIPER featured a semi-monocoque design that balanced strength, rigidity, and ease of manufacturing while maintaining a lightweight airframe. As shown in Drawing 3 of 5, all loads were transferred into the fuselage to minimize failure points. To optimize load paths, structural continuity was incorporated, enhancing efficiency while minimizing weight. Aerodynamic loads from the wings and empennage caused reactions in the wing carry-through and tail boom, respectively. Inertial and aerodynamic loads from the EFT acted on the internal pylon structure of the wing, and inertial loads from the motor affected the forward section of the fuselage. Ground loads were transferred through the MLG into the main spar and the fuselage.

The expected operational loads and structural analysis resulted in the load paths shown in Drawing 3 of 5. Chordwise ribs and spanwise spars managed aerodynamic loads within the wing. The main spar was made of carbon-fiber-reinforced polymer (CFRP), taking advantage of its high strength-to-weight ratio, while the trailing edge (TE) spar was constructed from plywood because of its strength and cost efficiency. Aerodynamic and

inertial loads were distributed from the EFT to an internal structure within the wing. A balsa shear web was integrated into the wing's glass-fiber reinforced polymer (GFRP) leading edge (LE), forming a D-box that resisted the expected torsional loads from the EFTs drag, while increasing the wing's stiffness and bending strength. The tail boom was constructed using a CFRP square tube to resist bending and torsional loads from the empennage. The fuselage incorporated a torque box design with longerons and bulkheads to effectively transfer loads from the motor and tail boom, as shown in Drawing 3-5.

### 5.2.2 Operational Limits

The structural design of VIPER was optimized for the maneuvers expected in M2 and M3, including continuous high-g turns. To accommodate these demands, fighter jet loading limits of 6.5 to 9 g were applied [13], along with a safety factor of 1.5 in accordance with ACS-05 and 14 CFR Part §23.303 [19]. Flight envelopes, shown in Figure 5-1, were generated using the methodology outlined in 14 CFR Part §23.331-341 [19].

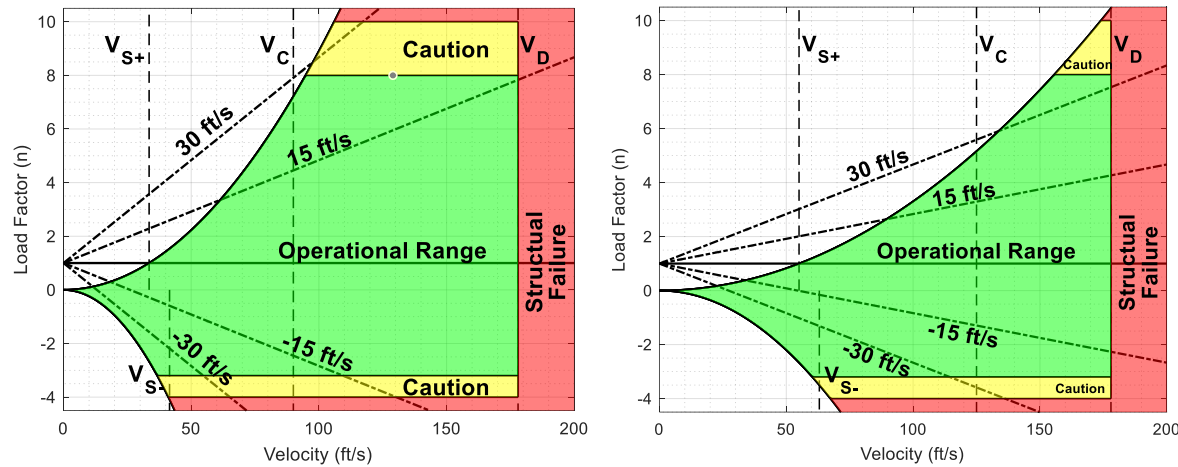


Figure 5-1: Structural flight envelopes for M2 (left) and M3 (right).

### 5.2.3 Fuselage

The internal layout was primarily constructed from plywood, which was chosen for its strength-to-weight ratio and ability to handle expected loads from the IFT. A carbon tow-reinforced 1/8-inch plywood torque box transferred the inertial motor loads throughout the structure. A hatch spans between the top two longerons and the second and third bulkheads, providing access to the avionics and housing of the IFT. To accommodate internal components, a continuous 1/8-inch plywood floor was used. The floor was reinforced with a box beam for added bending and torsional stiffness, which acted as an additional longeron, relieving stress on the skin. The corners of the hatch cutout were rounded for even load transfer and reduced stress concentrations. Aerodynamic loads experienced by VENOM were transferred into the aft section of the box beam, where a 1/8-inch plywood plate securely houses the release mechanism. The tail boom slotted through four aft bulkheads and was secured by two #10-32 2-inch steel bolts. The skin was fabricated using a 2-ply layup of Style 120 E-glass 4H Satin Weave to take advantage of its increased impact resistance and radio transmissivity compared to CFRP. The glass fibers were oriented in a [0/90, ±45] layup to support bending and torsional loads.



### 5.2.4 Wing

The aerodynamic and inertial loads from the EFTs played a significant role in determining the main structural layout of the wing. The drag generated by the EFT created torsional loads on the wing structure. To accommodate these forces, the back of the LE was closed with a balsa shear web, forming a D-box. This design improved the wing's torsional resistance while simultaneously increasing its bending strength. Inertial loads from high-g turns subjected the wing to both positive and negative g loading. To further analyze the structural effects of the EFT on the wingspan, shear and bending moments were calculated and used to examine the impact of the EFT along the wing and determine the optimal structural positioning. Lift distribution was calculated using Schrenk's Approximation, as outlined in Equation 5-1, to ensure accurate load distribution during high-g maneuvers. Shear and bending moment diagrams for the wing, shown in Figure 5-2, demonstrate the load relief provided by the EFTs during a 5-g maneuver with 5-lb bottles.

$$L'_{Schrenk} = \frac{L'_{Elliptical} + L'_{Planform}}{2} \quad (5-1)$$

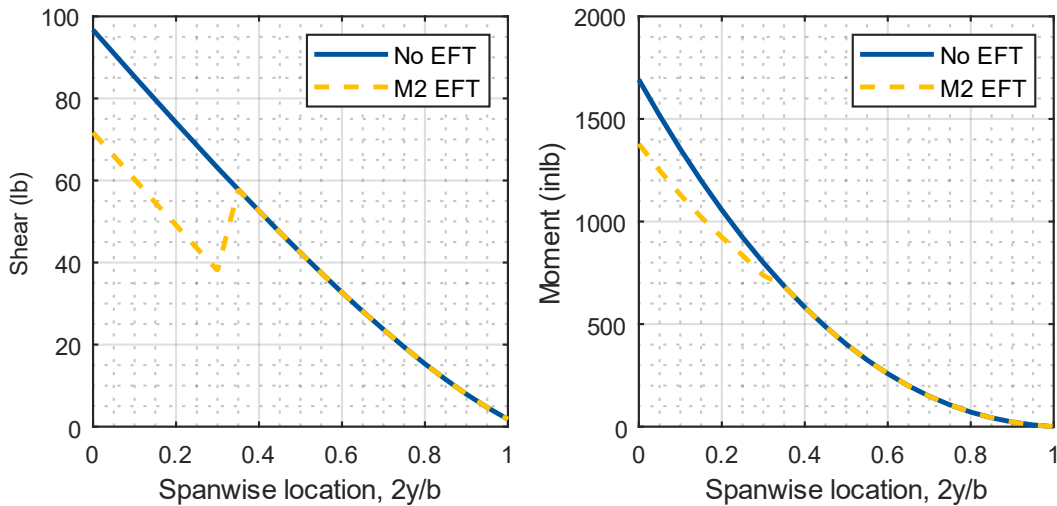


Figure 5-2: Wing shear and bending moment diagrams for M2 turn condition.

The wing structure was primarily made of balsa, bass, and plywood connected by a full-span main spar and D-box. The main spar is a COTS twill weave CFRP square tube [20]. The LE used GFRP for ease of manufacturing with the tight airfoil radius while preventing interference with GPS signals for the X-1. To support the EFT, a box beam made of 1/8-inch plywood was incorporated to distribute bending and torsional loads into the D-box, rear spar, and ribs, as shown in Drawing 3 of 5. The rear spar was attached to a bulkhead within the fuselage to act as an anti-rotation mechanism. To validate the structural integrity of the CFRP spar, historical [2] and current testing data were analyzed and compared to manufacturer specifications [20], as discussed in Sections 7.2.1 and 8.1.4. The braided weave spar surpassed the ultimate allowable bending stress of 58 ksi by 7%, but did not comply with ACS-05, thereby prompting a redesign. A similar test on the twill weave spar confirmed its capability to withstand larger loads with a safety factor of 1.5 in accordance with ACS-05. For a 5 g M2 turn, the bending stress



experienced was calculated to be 50% of the allowable 80 ksi ultimate load, with a margin of safety of 99%. The values were calculated using Equations 5-2 and 5-3.

$$\sigma = \frac{My}{I} \quad (5-2)$$

$$\text{Margin of safety} = \left( \frac{\text{Allowable}}{\text{FoS} * \text{Applied}} - 1 \right) \times 100 \quad (5-3)$$

### 5.2.5 Empennage

The empennage was made primarily of balsa, bass, and plywood, with a COTS CFRP square tube tail boom to withstand the in-flight loads. The HT was constructed with a layout similar to the wing, featuring a COTS CFRP pultruded square tube as the main spar, and ribs constructed with bass and balsawood in each tail. The spar was designed to be removable so that the HT could be detached to comply with ACS-03. The LE was constructed from balsawood sheeting to utilize its high strength-to-weight ratio and low cost. The VT followed a similar layout, using comparable materials. The HT and VT main spars passed through the tail boom, serving as the primary load-bearing structure for the aerodynamic forces. A 3D-printed tail cap secured the assembly for in-flight rigidity but did not bear significant structural loads. The spar was removable, allowing the horizontal tail to be detached for ACS-03 compliance. The HT and VT were bolted to the tail boom using 2.5-inch #10-32 COTS bolts, ensuring a secure connection. Similarly, the tail boom was bolted to the fuselage, providing a rigid and reliable attachment.

### 5.2.6 Landing Gear

The NLG was made from a titanium rod with bends introduced to act as a dampening system. A diameter of 3/16 inches was chosen to prevent buckling when the aircraft was fully loaded. The MLG used a spring leaf design for a dampening method. Each strut was constructed from carbon tow in a 1/4-inch layup. The same carbon tow wrapped the MLG to the main spar, transferring the ground loads into the wing carry-through. Based on historical and analytical data, the highest anticipated landing load was 7.5 g [2]. Per ACS-05, the gear was designed to bear loads up to 11.25 g. An FEA was conducted to evaluate the design's ability to withstand impact loads. The analysis was meshed using TET10 elements and constrained at the spar's attachment point. A vertical 219-lb load was applied to the axle hole to simulate an 11.25-g impact. The maximum principal stress, analyzed for compression because of the CFRP material, resulted in 124 ksi, which is 72% of the ultimate compressive stress [20], as shown in Figure 5-3.

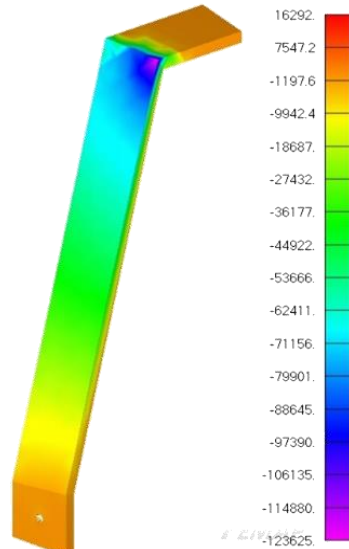


Figure 5-3: MLG Analysis.

### 5.2.7 Pylons

#### 5.2.7.1 External Fuel Tank Pylons

The EFTs were mounted to VIPER's wing by 3D-printed nylon pylons per SY-14 specifications. Each pylon featured a fixed forward ring and a handcuff-style rear clamp, securing the EFT with two #10-32 carbon steel bolts



fastened into nylon locknuts embedded in the wing structure. The 3D-printed design enabled rapid prototyping and complex streamlining, optimizing aerodynamics and manufacturability.

As shown in Drawing 5 of 5, the clamping arrangement constrained all translational movement of the EFT while utilizing a single clevis pin for efficient ground mission loading. In compliance with AC-06, the #10-32 bolts were installed through the pylon base into the wing structure (Drawing 3 of 5). The bolts were pre-set within the pylon and aligned with an internal locating feature for rapid assembly. The clevis pin components were safety-wired to the pylon to prevent hardware loss.

#### **5.2.7.2 X-1 Pylon and Release Mechanism**

The X-1 Pylon was designed to secure the glider to a release mechanism while adhering to both AC-06 and SY-04, shown in Drawing 5 of 5. Permanent fasteners affixed the pylon to the aircraft's undercarriage, positioned aft of the main landing gear. The pylon and its integrated release mechanism, constructed from PET-G filament for its strength and durability, housed two servos that actuated retention pins upon pilot command to ensure a reliable deployment. The X-1 featured two hardpoints on its upper surface which interfaced directly with the retention pins to maintain a secure connection. The mechanism incorporated two biased springs that generated a temporary nose-down pitching moment upon deployment for a controlled release. The pylon was positioned for accessibility in GM, allowing the X-1 to easily attach onto VIPER. During GM, the assembly crew member communicates with the pilot to open or close the mechanism while loading to secure the vehicle for flight.

#### **5.2.8 Fuel Tanks**

The densities of SY-12-compliant materials, including sand, concrete, and steel shot, were analyzed to determine the optimal fuel tank payload. Volume-to-weight comparisons revealed that neither sand nor concrete alone could provide the desired weight. A system of equations was developed in MATLAB [4] to compute the ideal mixture of concrete and steel shot while ensuring full bottle capacity to mitigate slosh effects. The resulting composition was 68.5% concrete and 31.5% steel shot for the 15-lb IFT, and 36.3% concrete and 63.7% steel shot for each 5-lb EFT. A cylindrical 2-liter soda bottle was selected for the IFT because of its ideal mass distribution and simplified loading. During GM the IFT is loaded through the avionics bay hatch and secured with nylon straps and side-release clamps, chosen for their reliability and speed. As shown in Drawing 5 of 5, the wing box bulkheads and rear bulkhead secure the bottle within the fuselage.

#### **5.2.9 VENOM**

##### **5.2.9.1 Design Description**

VENOM is an autonomous flying wing glider optimized for lift-to-drag ratio and a low-profile captive carry state, as shown in Drawing 4 of 5. Its 3D-printed fuselage houses the flight controller, battery, GPS, and servos. Like other flying wing aircraft, it required a forward CG for longitudinal stability. A MATLAB [4] script using DATCOM [5], and XFLR5 [14] guided aerodynamic analysis and stability calculations. Longitudinal stability was achieved through three key design choices: positioning the LiPo battery forward, using a reflexed airfoil, and applying wing sweep to shift the MAC aft. Initial directional instability was corrected with endplate winglets. Full-span elevons provided ample control authority during stabilization and flight. VENOM's general parameters are summarized in Table 5-2.



Table 5-2: VENOM general parameters.

Parameter	Value	Parameter	Value
Span (in)	12	$C_{M_\alpha}$ (/°)	-0.0082
Root Chord (in)	6.6	$C_{N_\beta}$ (/°)	0.0015
Tip Chord (in)	2.6	$C_{I_\beta}$ (/°)	-0.0012
Airfoil	MH60	$\tilde{x}_{CG}$ (%MAC)	23
Area (in <sup>2</sup> )	54.72		

### 5.2.9.2 Mission Compliance and Indicator Lights

VENOM featured multicolored LED strips on the upper and lower surfaces, ensuring visibility during flight and after landing to comply with requirement SY-07. Power management ensured continuous operation post-release. Table 5-3 documents the voltage, estimated current draw, and power for each component of VENOM's avionics. The estimated power-on time was determined using Equation 5-4 that relates the battery's 300 mAh capacity to the current draw. The time exceeded the 5-minute mission window which allows for powering on during assembly.

$$Power\ On\ Time = \frac{300\ mAh}{950\ mA} = 0.316\ hours = 19\ minutes \quad (5-4)$$

Table 5-3: VENOM avionics and power requirements.

Component	Item Name	Qty.	Voltage (V)	Current Draw (mA)	Power (W)
Flight Controller	Matek F405 MINI-TE	1	5	100	1
GPS	NewBeeDrone GPS	1	5	150	0.75
LED Light Strip	GEMFAN LED 08	2	5	100	0.5
Control Servos	Micro-3.7g servos	2	5	300	3
Limit Switch	KW12-3 Lever Arm Micro Limit Switch	1	-	-	-
Battery	GNB 2s 300 mAh	1	7.6	-	-
<b>Total</b>				<b>950</b>	<b>4.75</b>

### 5.2.9.3 Control System

VENOM ran ArduPilot [21], an open-source software for autonomous flight, in compliance with SY-06. The elevon configuration complied with SYS-02 through pitch and roll control. The onboard accelerometer, gyroscope, and GPS were used to determine accurate attitude states. VENOM remained disarmed and its control surfaces did not actuate in the passive captive carry mode. When dropped by the pilot, VENOM'S flight controller awaited detection of a sudden decrease in altitude. After the 15-ft threshold value was satisfied, VENOM's avionics activated and executed the autonomous flight pattern specified in Figure 5-5. To ensure compliance with the altitude requirement SY-05, VIPER ascended to 220 ft before dropping VENOM. The full VENOM post-flight sequence is shown in Figure 5-4. The flight sequence complied with maneuver and flight line safety requirements and met SYS-02, which maximized landing accuracy in the 2.5-point bonus scoring zone.

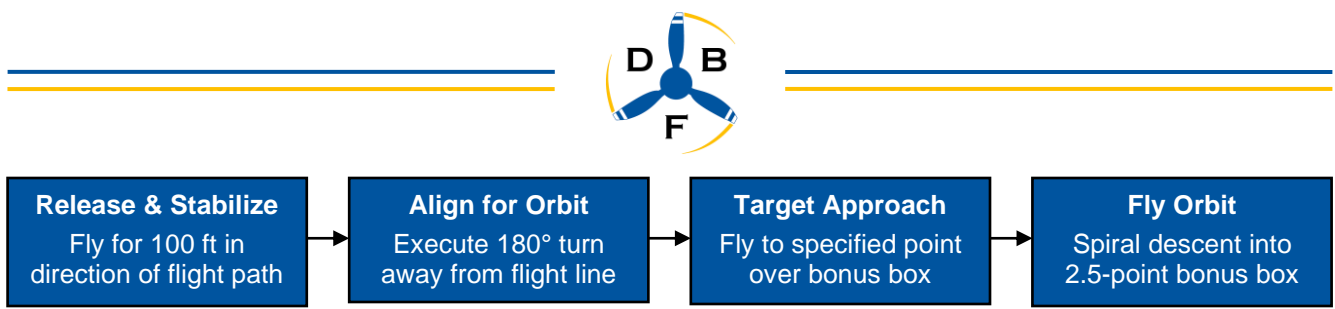


Figure 5-4: VENOM post-release flight sequence.

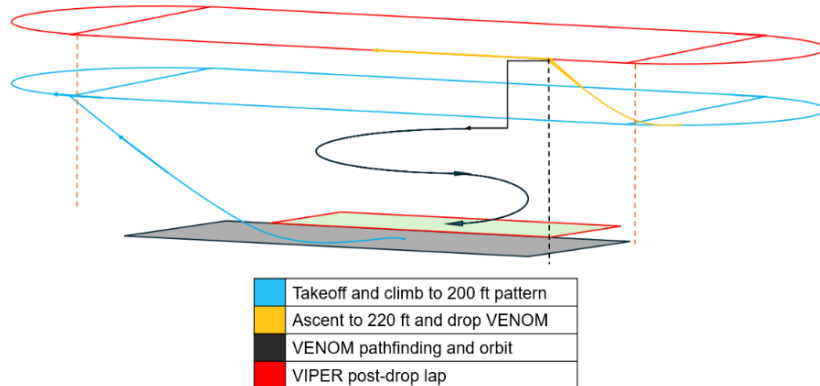


Figure 5-5: VIPER and VENOM flight path.

### 5.2.10 VIPER Avionics

VIPER's avionics were installed as shown in Figure 5-6. The motor was mounted on the front of the aircraft in a tractor configuration. The batteries were strapped immediately behind the motor and ESC with a hook and loop. Lightweight Pilot-RC servos [22] were selected for the control surfaces because of their low weight, high torque, and weight-bearing capability. The control surface servos were connected to the receiver with braided wire routed inside the wings and tail boom. VIPER was equipped with sensors from the FrSky ecosystem for accurate flight test data collection. Airspeed was measured by the PAS100ADV pitot-static sensor, and propulsion data by the FAS300ADV current sensor. Data was viewed live on the transmitter and logged as blackbox data in the receiver. The TDSR18 receiver included an accelerometer, barometer, and altimeter for flight assistance. The ESC logged motor RPM, battery health, and throttle input while the system communicated with the pilot using a dual-band in the 2.4 GHz and 900 MHz frequencies for extended range and redundancy.

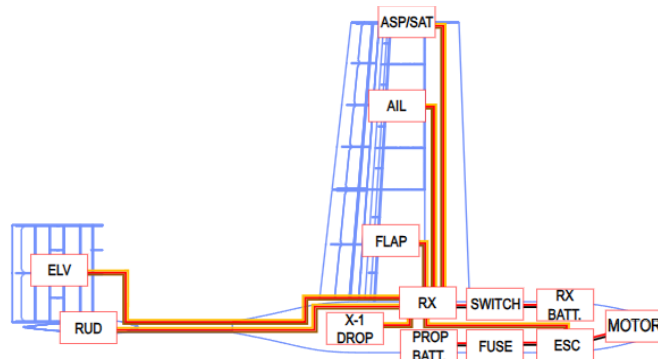


Figure 5-6: VIPER avionics and wiring diagram, top down. Servos are symmetrical.



### 5.3 Weight and Balance

The weight and balance data for each flight configuration, as shown in Table 5-4, were recorded about the datum located at the fuselage nose, butt line, and water line for the x, y, and z axes, respectively. Loading factors that varied with each mission included one IFT of 15 lb, two EFT and pylon sets of 5 lb each, and VENOM of 0.16 lb. By placing these components in neutral locations, negligible CG variance allowed for static stability in each configuration. The propulsion and receiver batteries functioned as ballasts, with slight adjustments along the x-axis fine-tuning the center of gravity as required.

*Table 5-4: Weight and balance for each mission profile.*

Component	Weight (lb)	CG <sub>x</sub> (in)	CG <sub>y</sub> (in)	CG <sub>z</sub> (in)
Wing	4.12	26.03	0.00	-2.80
Horizontal Tail	0.30	62.92	0.00	0.02
Vertical Tail	0.36	61.43	0.00	6.60
Fuselage	2.32	21.99	0.00	-0.26
Main Landing Gear	0.56	26.24	9.50	-9.70
Nose Gear	0.14	4.94	0.00	10.25
Avionics	1.86	7.12	0.00	-0.88
Tail Boom	0.44	46.43	0.00	0.00
Propulsion System	1.92	2.09	0.00	0.00
Battery	1.56	12.97	0.00	-0.79
Empty	<b>13.58</b>	<b>20.30</b>	<b>0.00</b>	<b>-1.23</b>
<b>Mission 1</b>				
Overall	<b>13.58</b>	<b>20.30</b>	<b>0.00</b>	<b>-1.23</b>
<b>Mission 2</b>				
IFT	15.00	23.55	0.00	0.53
Port EFT & Pylon (Loaded)	5.00	26.91	-11.14	-6.31
Starboard EFT & Pylon (Loaded)	5.00	26.91	11.14	-6.31
X-1	0.16	26.57	0.00	-4.24
Overall	<b>38.74</b>	<b>23.30</b>	<b>0.00</b>	<b>-1.87</b>
<b>Mission 3</b>				
X-1	0.16	26.57	0.00	-4.24
Port EFT & Pylon (Empty)	0.34	26.91	-11.14	-6.31
Starboard EFT & Pylon (Empty)	0.34	26.91	11.14	-6.31
Overall	<b>14.42</b>	<b>20.69</b>	<b>0.00</b>	<b>-1.50</b>



## 5.4 Final Design Performance

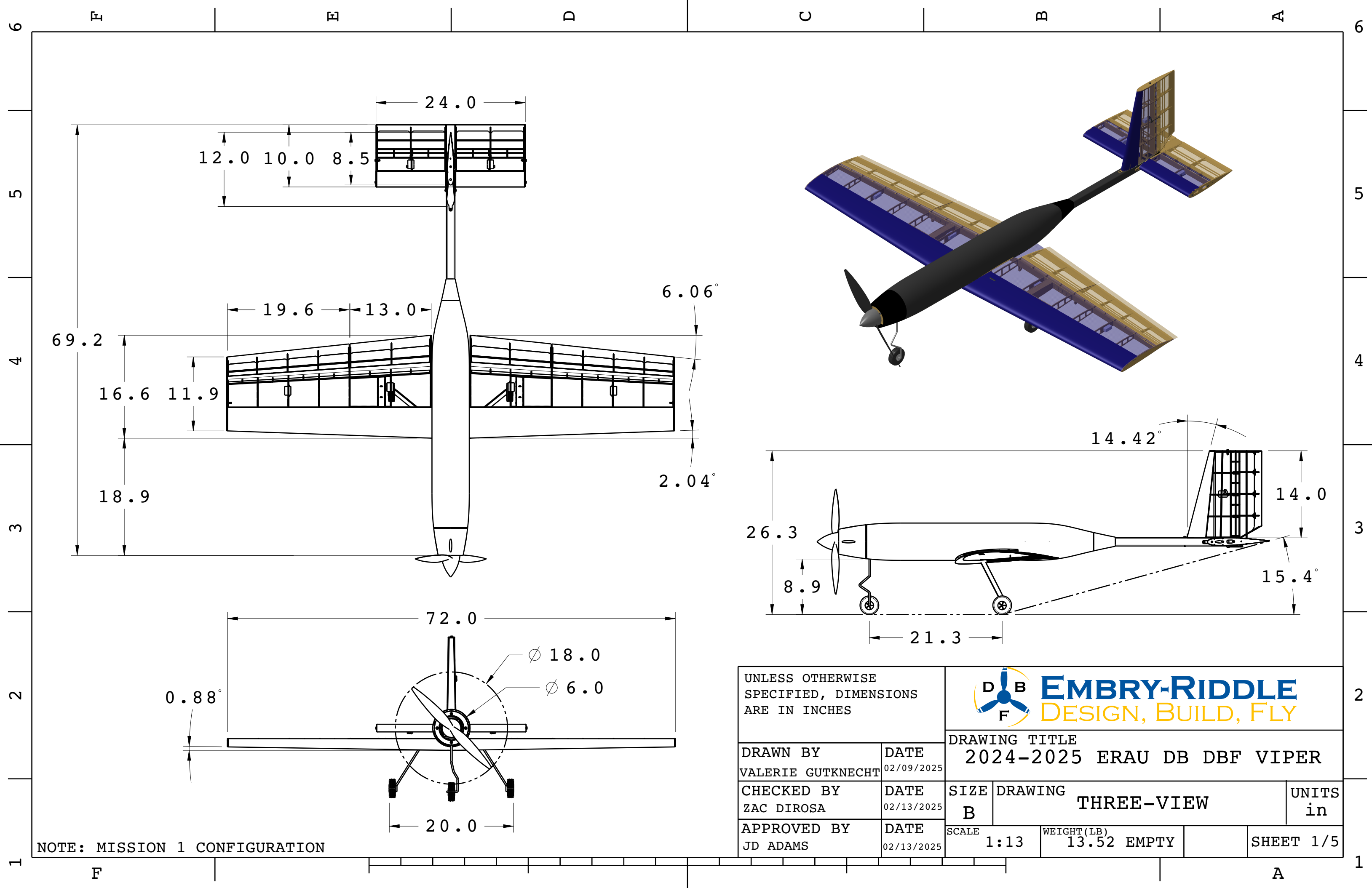
The final flight and mission performance parameters are given in Table 5-5.

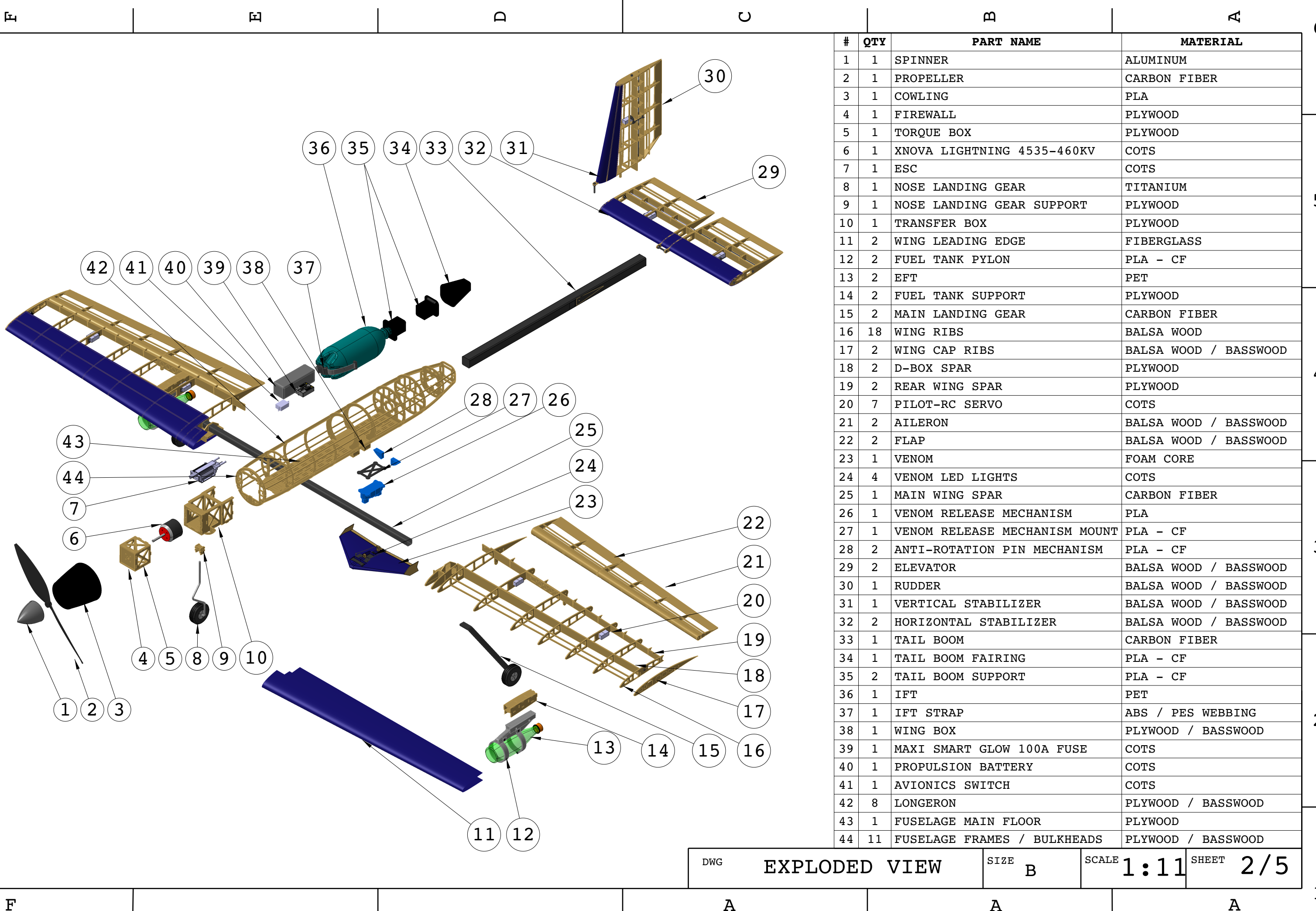
Table 5-5: Final flight and mission performance parameters.

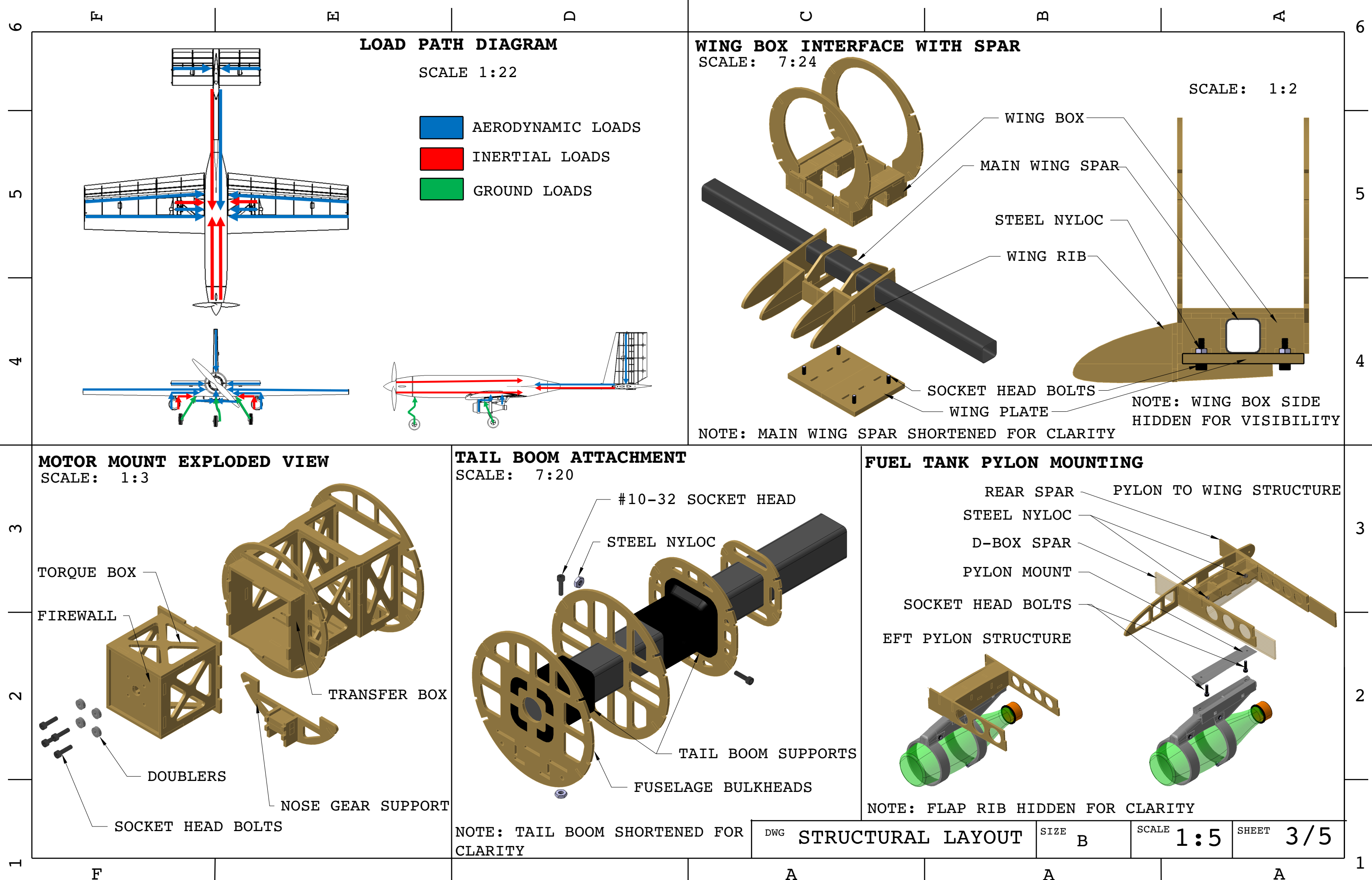
Parameter	M1	M2	M3	GM
Gross Weight (lb)	13.58	38.74	14.42	-
Wing Loading (lb/ft <sup>2</sup> )	1.88	5.37	2.00	-
Cruise Airspeed (ft/s)	125	125	90	-
Thrust to Weight	0.6	0.6	0.6	-
Mission Time (min)	1.65	1.65	300	1.5
Payload Weight (lb)	-	25	-	-
X-1 Weight (lb)	-	0.13	0.16	-

## 5.5 Drawing Package

The following section shows the detailed drawings of VIPER and all subsystems. It includes the 3-view drawing, systems layout, structural layout, and drawings of mission configurations and subsystems. All drawing elements were created in CATIA V5-6R2020 [8].

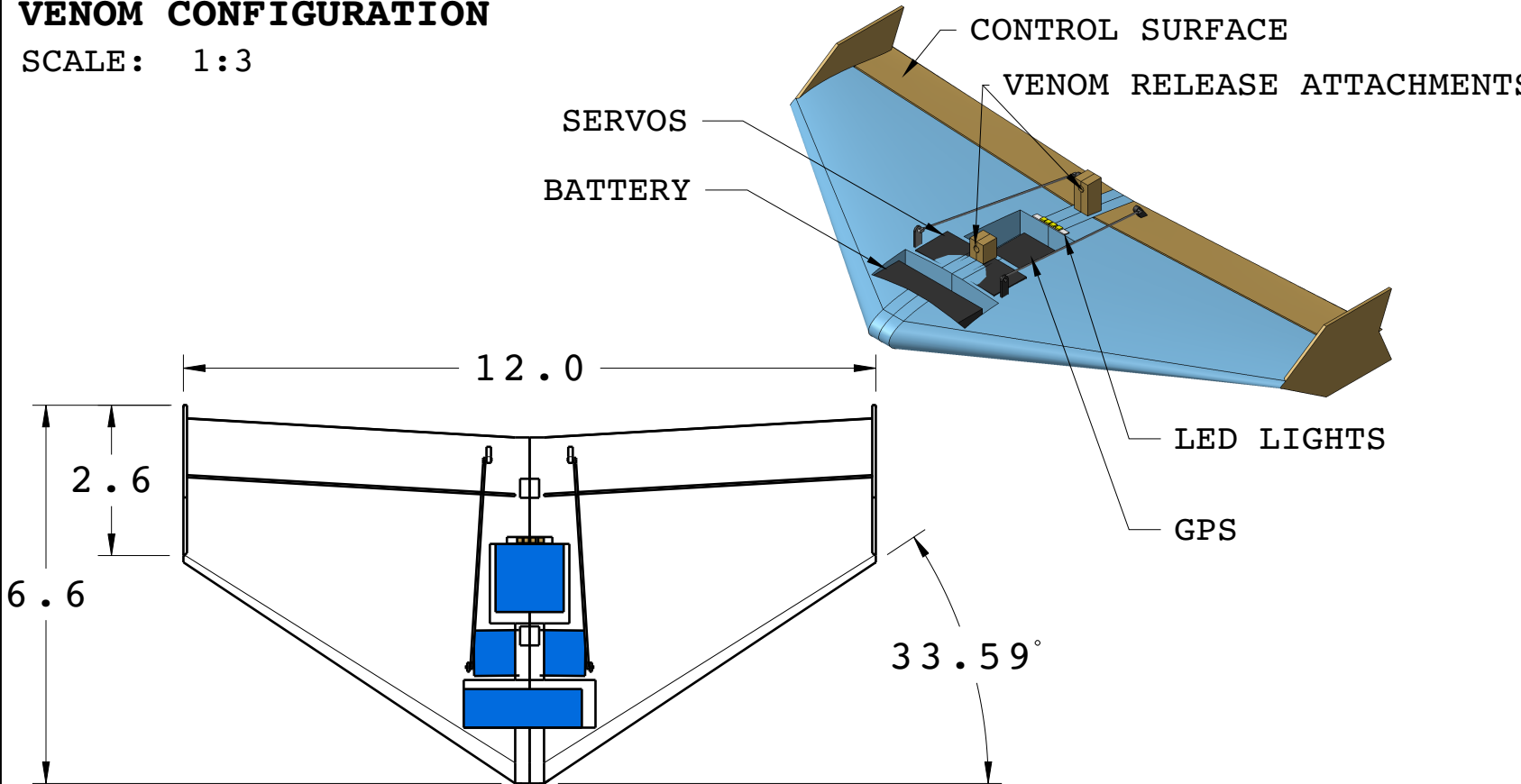






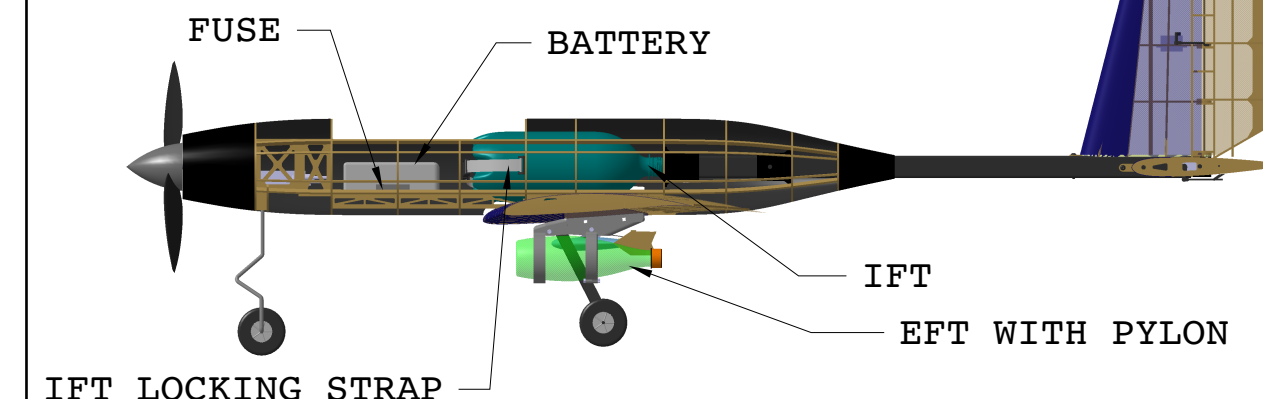
## VENOM CONFIGURATION

SCALE: 1:3

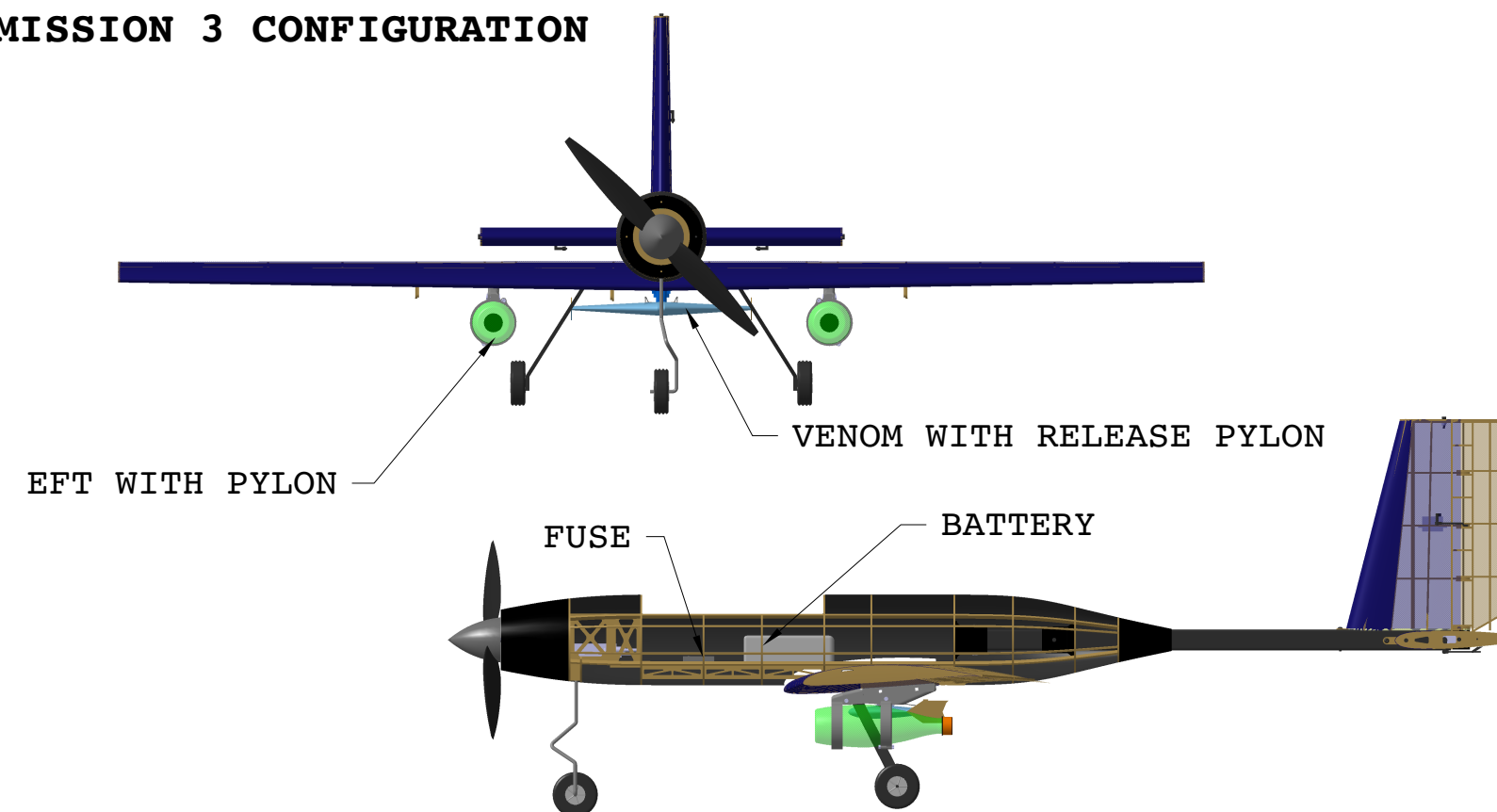


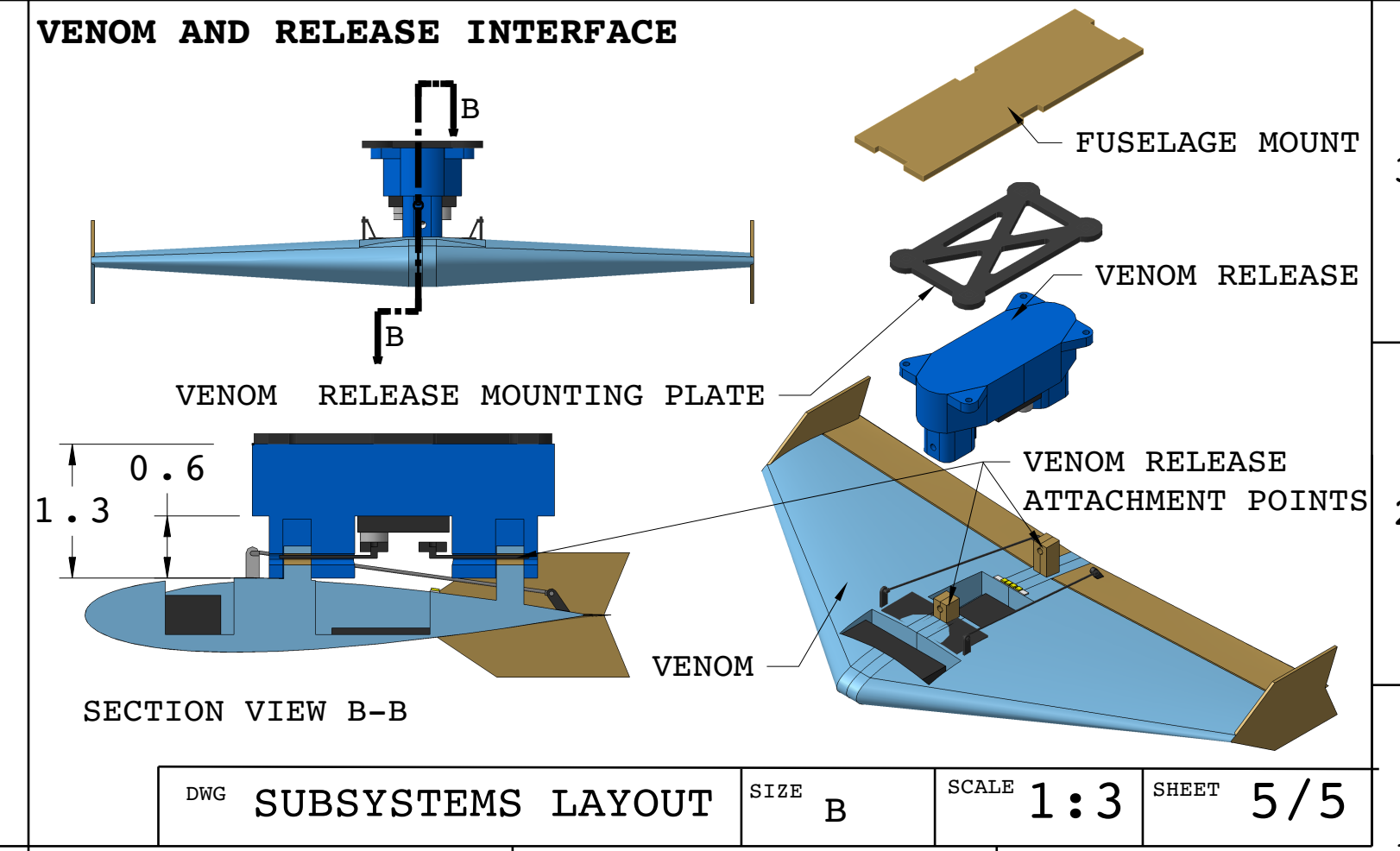
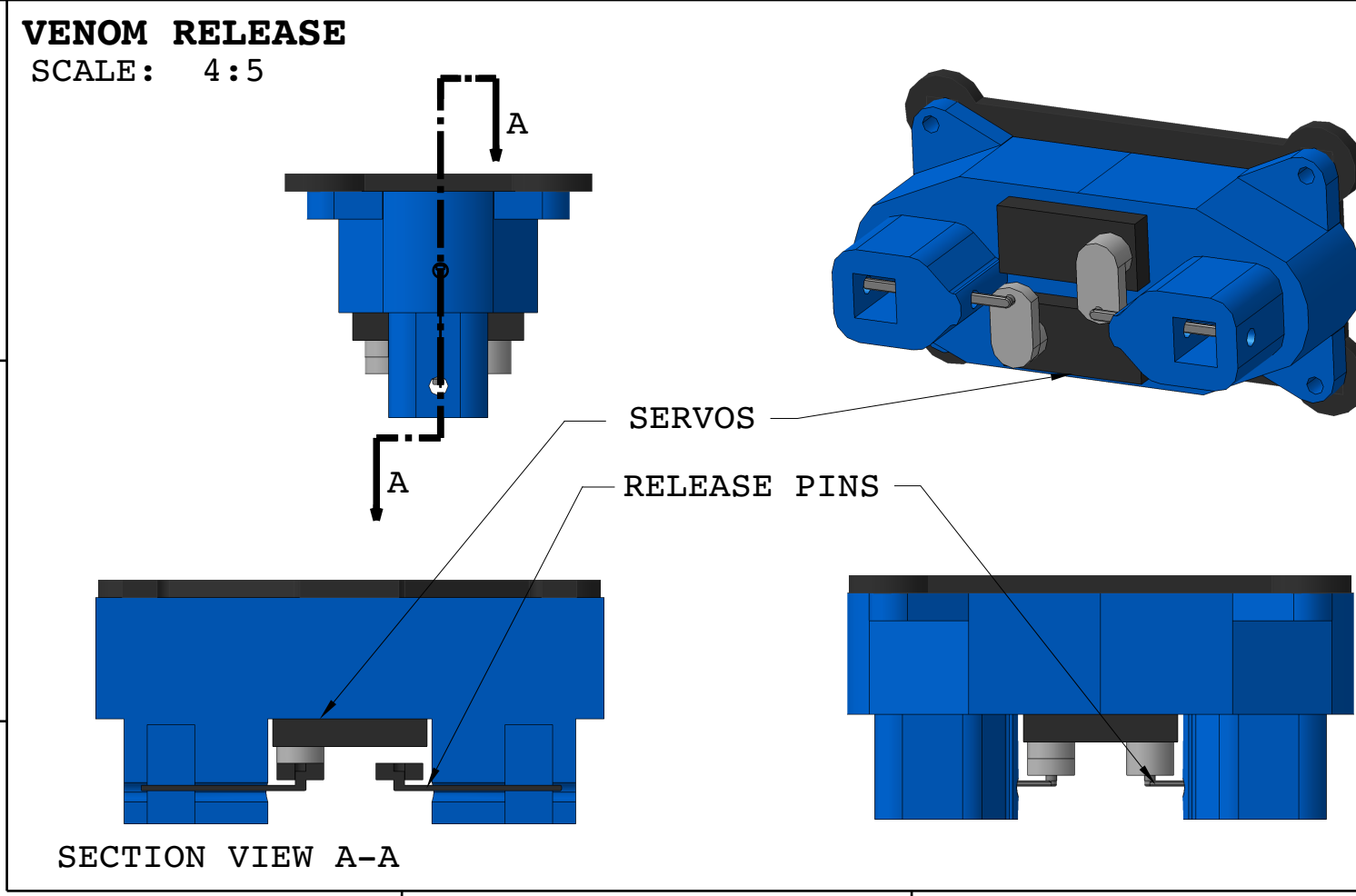
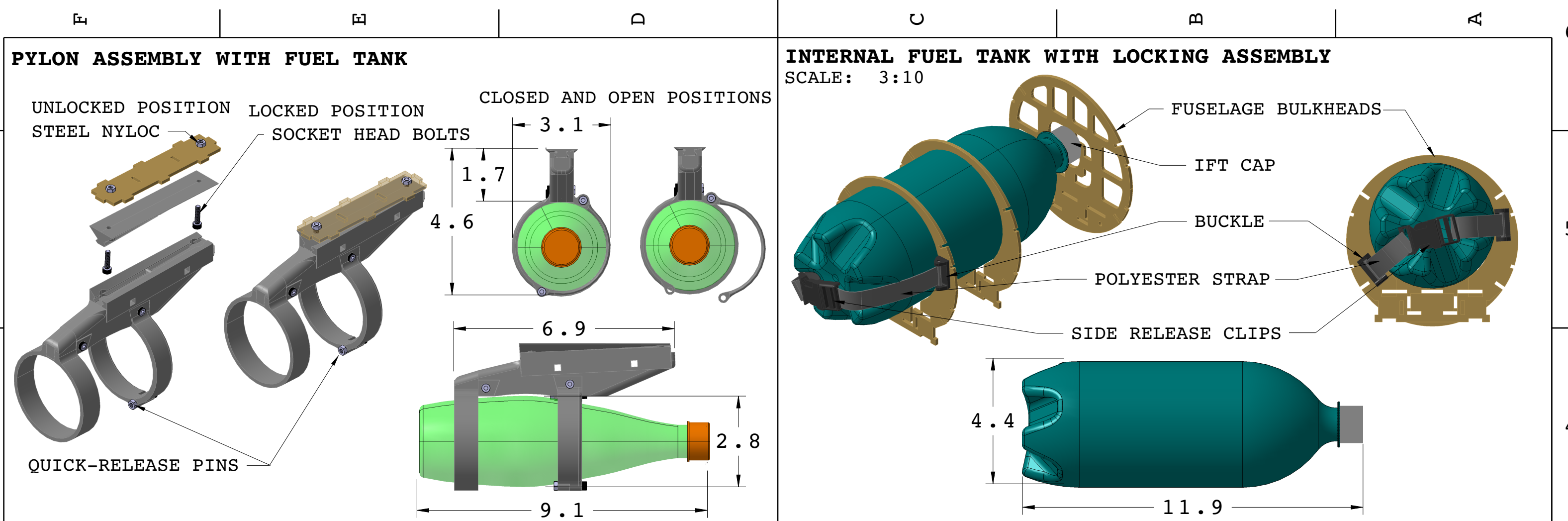
## MISSION 2 CONFIGURATION

## MISSION 2 CONFIGURATION



## MISSION 3 CONFIGURATION







## 6 Manufacturing Plan

### 6.1 Manufacturing Process

Various manufacturing processes were evaluated to determine the best fabrication techniques for each component, ensuring the lowest structural weight and best level of aircraft performance.

#### 6.1.1 Wooden Construction

Wooden construction methods, such as balsa, basswood, and plywood buildups, were considered for their ease of assembly, low density, and affordability. The components can be integrated to take advantage of the properties of each type of wood, reducing weight without compromising strength. Additionally, wooden parts can be produced accurately and rapidly with a laser cutter. The primary drawback of wooden construction was the lack of design flexibility because of the anisotropic nature of the material.

#### 6.1.2 Molded Composite Construction

Molded composite components, which were considered for their high stiffness and strength-to-weight ratio, were ideal for primary structures like the skin, landing gear, and leading edges. Reusable 3D-printed molds enabled the fabrication of precise, high-tolerance parts with complex curves. Unfortunately, the method's cost, complexity, and safety concerns limited its actual use.

#### 6.1.3 3D Printing

Fused deposition modeling (FDM) 3D printing was considered for geometrically complex components. Though FDM printing often yields more brittle parts, engineering-grade filaments such as continuous fiber Onyx and nylon produce components are capable of bearing the required loads. Polylactic acid (PLA) filament proved a cost-effective option for producing composite molds.

#### 6.1.4 CNC Machining

CNC milling techniques allowed for the fabrication of high-strength and high-tolerance metallic parts which are ideal candidates for critical structural components. However, milled parts offered little benefit over other methods because of their higher production cost and component weights.

#### 6.1.5 Foam Core Composites

Foam core composite manufacturing was a desirable option for producing complex curvature parts at a low cost. A hot wire cutter allowed for rapid manufacturing, making it an efficient and cost-effective production method, although parts produced with this method required reinforcement such as with composites. Foam cutting was ideal for small components with moderate strength requirements.

#### 6.1.6 Selection Process and Results

The decision matrix shown in Table 6-1 was used to assist in selecting the materials and processes to be utilized for airframe assembly. In accordance with ACS-05, preference was given to methods that yielded high-strength, low-weight components. The remaining categories were ranked based on their impact on component cost, manufacturability, and design flexibility. Wooden construction was utilized the most, followed by molded composites, 3D printing, foam core, and CNC machining. A combination of the processes was ultimately selected for VIPER's construction.



Table 6-1: Manufacturing process decision matrix.

Criteria	Factor	Wood	Composite	3D Print	Foam	Machining
Strength	3	4	5	2	2	5
Weight	3	5	4	3	4	1
Design Flexibility	2	3	5	5	3	4
Manufacturability	2	5	2	4	3	2
Cost	1	4	2	4	4	1
Total		47	43	37	34	31

## 6.2 Selected Manufacturing Processes

### 6.2.1 Fuselage

The fuselage was composed of a wooden substructure surrounded by GFRP skin. Wooden components were designed to fit together with tabs for mechanical strength and permanently joined with a combination of epoxy and cyanoacrylate (CA) glue. The GFRP skin was secured to the substructure with slow-cure epoxy. Figure 6-1 shows that the skin and substructure were clamped together while curing to ensure a strong bond. 3D-printed tail boom adapters were bonded to the aft bulkheads using epoxy. A summary of the manufacturing methods selected for the fuselage is listed in Table 6-2.

Table 6-2: Fuselage component manufacturing processes.

Assembly	Component	Material	Dimension	Method
Semi-Monocoque Fuselage	Formers, Longerons	3-Ply plywood	1/8-inch thick	Laser-cut
	Stringers	Balsawood	1/8-inch thick	Hand-cut
	Skin	GFRP E-glass	2 Ply	In-house layup
	Tail boom	CFRP	1 3/8-inch x 1 3/8-inch	COTS
	Floor	Basswood	1/8-inch thick	Laser-cut
Wing Carry-Through	Wing plate	5-Ply plywood	1/4-inch thick	Laser-cut
	Formers	3-Ply plywood	1/8-inch thick	Laser-cut
Tail Box	Tail connectors	PLA	N/A	3D-printed
Landing Gear	NLG	Titanium	1/4-inch diameter	COTS



Figure 6-1: From left to right: fiberglass skin layup in 3D printed mold, vacuum bagging and cure, skin-substructure clamp using the same molds, and final product with good adhesion.



### 6.2.2 Wings and Landing Gear

The wings were composed of wood and composite materials. One end of the CFRP main spar served as a reference plane for locating the ribs, mitigating tolerance stack-up. The ribs were temporarily affixed with CA glue to check alignment before being permanently attached with epoxy glue. The main landing gear was molded from carbon fiber tow and attached to the main spar with a tow wrap for better bending performance. The GFRP leading edge (LE) was then epoxied to the substructure and fixed in place for the cure time. A summary of selected methods is given in Table 6-3.

*Table 6-3: Wing component manufacturing processes.*

Assembly	Component	Material	Dimension	Method
Wings	Leading edge	GFRP E-Glass	3-ply	In-house layup
	Main spar	CFRP	7/8-inch x 7/8-inch	COTS
	Rear spar & main ribs	3-Ply plywood	1/8-inch thick	Laser-cut
	Tip ribs	Balsawood	1/8-inch thick	Laser-cut
Flaps/Ailerons	Ribs, spar	Basswood	1/8-inch thick	Laser-cut
	Trailing edge	Balsawood	1/8-inch thick	Laser-cut
Wings/Flaps/Ailerons	Skin	Ultracote	-	COTS
	Stringers	Balsawood	1/8-inch thick	Hand-cut
Landing Gear	MLG	CFRP	1/4-inch thick	In-house layup

### 6.2.3 Empennage

Much like the wings, the empennage stabilizers were manufactured about one end of their CFRP spars to ensure proper rib alignment and placement. The surfaces were constructed with balsawood, basswood, and CA glue to minimize structural weight and manufacturing time. Plywood tabs interfaced with the tail boom through a 3D-printed adapter and were epoxied to the HT and VT. A summary of the processes used is given in Table 6-4.

*Table 6-4: Empennage component manufacturing processes.*

Assembly	Component	Material	Dimension	Method
HT/VT	Main spar	CFRP	1/4-inch x 1/4-inch	COTS
	Aft spar & ribs	Basswood	1/8-inch thick	Laser-cut
	Leading edge	Balsawood	1/16-inch thick	Steam formed
Rudder/Elevator	Spar & ribs	Basswood	1/8-inch thick	Laser-cut
	Trailing edge	Balsawood	1/8-inch thick	Laser-cut
All Components	Skin	Ultracote	-	COTS
	Stringers	Balsawood	1/8-inch thick	Hand-cut

### 6.2.4 Fuel Tank Pylon and X-1 Release Pylon

The fuel tank pylons were primarily composed of 3D-printed components. The rings securing the bottle were printed out of Onyx filament, as was the adapter that interfaced with the wing. The X-1 release pylon was made primarily of nylon filament. The hardware, materials, and processes chosen for the pylons are given in Table 6-5.



*Table 6-5: Pylon component manufacturing processes.*

Assembly	Component	Material	Dimension	Method
Fuel Tank Pylon	Bottle rings	Onyx	-	3D-printed
	Clevis pin	Aluminum	-	COTS
	Seating gasket	UMMAGRIP	-	COTS
X-1 Release Pylon	Release system	Nylon filament	-	3D-printed
	Interface arms	Aluminum rod	1/16-inch	COTS

## 6.2.5 VENOM

The wings of VENOM were made from CFRP reinforced EPP and epoxied to a 3D-printed center pod. EPP was chosen for its light weight and adequate strength at VIPER's M2 cruise speed. They were made using a hot wire foam cutter, which gave precise, complex wing geometry. Table 6-6 summarizes the selected processes.

*Table 6-6: VENOM component manufacturing processes.*

Assembly	Component	Material	Dimension	Method
Wings	Spars	CFRP	-	COTS
	Wing sections	EPP	-	Hot wire cut
	Winglets & elevons	Balsawood	1/16-inch thick	Laser-cut
Center Pod	Wing carry-through	PLA	-	3D-printed

### **6.3 Manufacturing Milestones**

The Gantt chart shown in Figure 6-2 guided the timeline and team coordination across three iterations of VIPER. After each iteration, the schedule was refined by comparing predicted and actual timelines.

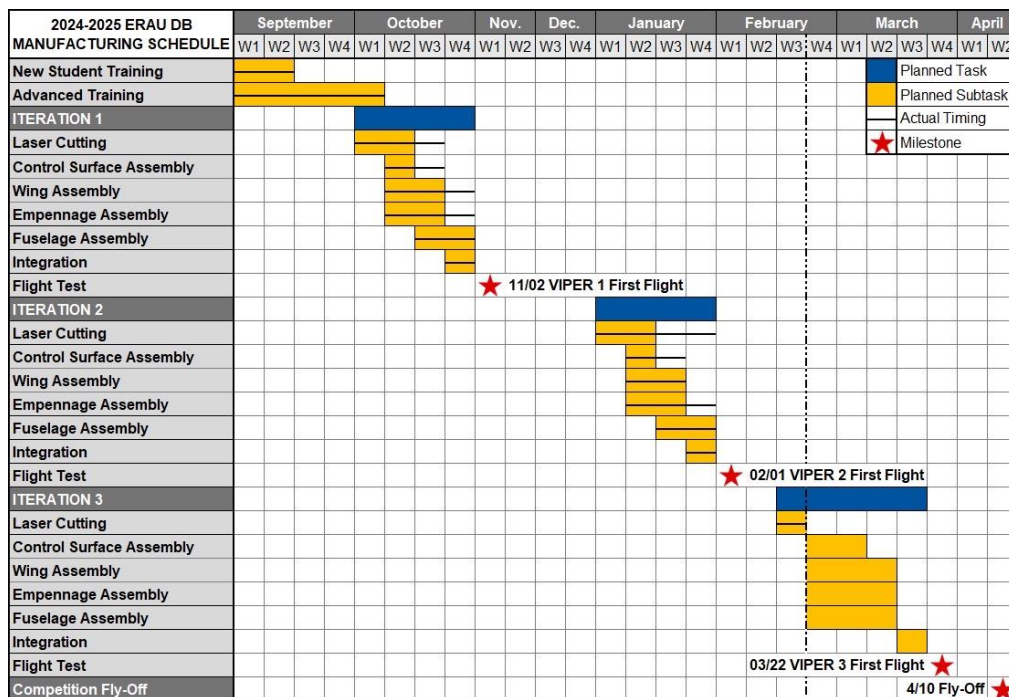


*Figure 6-2: 2024-2025 ERAU DB manufacturing timeline.*



## 7 Testing Plan

VIPER and its subsystems underwent phased testing to validate functionality, reliability, and performance. This structured approach initiated with bench-level tests. It then developed into incremental ground and flight tests, which mirrored the competition aircraft's design methodology as described in Section 4.1.

Three iterations of VIPER were tested. Iteration 1 validated aerodynamics, flight characteristics, and propulsion system. Data from Iteration 1 was used to optimize Iteration 2, which flew all mission profiles including full payload flight profiles at competition speed. Once a maximum flight envelope was established, Iteration 3 was constructed as the final competition aircraft.

### 7.1 Test Objectives

The test objectives in Table 7-1 were established to ensure all design requirements and constraints were met.

*Table 7-1: Test objectives.*

Phase	Category	Objectives
Bench Tests	Static Thrust Tests	Validate propulsion system performance when changing battery, motor, and propeller configuration by collecting throttle, thrust, and power data.
	Structural Tests	Locate and redesign potential points of failure in the structure of the aircraft. Conduct tests to validate calculations and determine flight envelope.
Ground Tests	Dynamic Thrust Tests	Optimize propulsion system configuration. Gather thrust, throttle, and power data from propulsion system. Validate thrust values of the propulsion system in a dynamic environment.
	Wing Tunnel Tests	Gather drag data from external stores on the wing.
	Subsystem Integration Tests	Validate systems prior to flight. Optimize human factors interaction with systems to maximize GM score.
	Flight Tests	Record aerodynamic and propulsion performance data. Simulate conditions to identify and expand the performance envelope.

### 7.2 Bench and Ground-Based Testing

Ground testing was planned to simulate competition conditions in a controlled setting, and to provide data to refine the design, validate predictions, optimize performance, and reduce flight test risks.

#### 7.2.1 Structural Tests

Structural tests confirmed the limit loads in the aircraft's structure. Destructive testing of two potential spars validated calculations and defined the flight envelope. A 3-point bending test was performed on potential wing spars for the aircraft. The spars were supported at both ends, with a load applied at the center. Weight was added in 5-lb increments with 5-second holds to detect structural deformities. The distance from the supported ends to the spar's center was marked to calculate the stress values outlined in Section 5.2.4. Additionally, the loaded aircraft underwent a weighted wingtip test before flight to verify flight safety and performance limits were met.



### 7.2.2 Static Thrust Tests

Static thrust tests were used to tailor the propulsion system for each mission. Thrust, motor power, battery performance, and throttle input were measured. Tests were structured such that a consistent current or RPM would be held. Performance parameters were then recorded and compared to the manufacturer's specifications. Test results were used to refine the design decisions. The modular aluminum static thrust stand housed avionics and allowed rapid reconfiguration of components such as the propeller, motor, and battery, as shown in Figure 7-1. Safety features included an emergency kill switch and a fuse. Static testing was primarily used for propeller selection. Initial tests with APC plastic propellers revealed efficiency losses at high RPMs, likely because of aerodynamic buffeting at higher tip speeds. Testing results revealed that Falcon CFRP propellers of identical blade geometry were far more energy efficient across all operating points. This outcome heavily influenced propeller selection. Falcon propellers with diameters ranging from 17 inches to 19 inches were chosen because they were better optimized with the mission requirements.

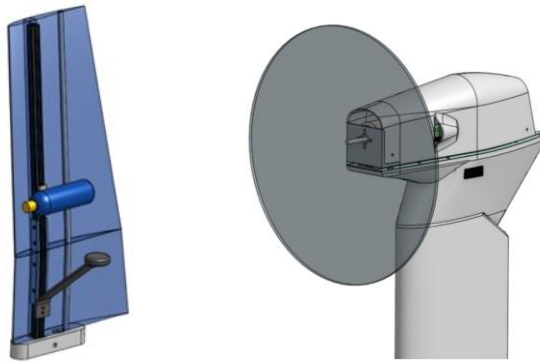


Figure 7-1: CAD (left) and practical assembly of static thrust stand (right).

### 7.2.3 Wind Tunnel Tests

Wind tunnel testing assessed drag buildup from external stores, aiming to optimize EFT orientation and evaluate the benefits of retractable landing gear. A half-span wing accommodated the stores, and tests were conducted at wind speeds of 90 ft/s and 125 ft/s across  $-10^\circ$  to  $+18^\circ$  angle of attack ( $\alpha$ ) sweep in 1-degree increments. This approach provided lift and drag measurements for the various configurations. Aerodynamic forces on the wing and stores were recorded using a 6-DoF external force balance. Tufts provided flow visualization and identified regions of separation, while video recordings helped identify the potential for wing flutter.

A modular thrust test stand housed the propulsion system to gather dynamic propulsion data, which allowed for rapid component swaps. Tests evaluated two motors and three propellers with a propulsion battery, which measured thrust, power consumption, and efficiency. The data collected identified the best configuration for maximizing thrust while minimizing power consumption. Airspeeds of 90 ft/s and 125 ft/s were used to simulate mission speeds. This wind tunnel testing greatly influenced the propeller selection for the competition aircraft. The wing performance model and dynamic thrust model are shown in Figure 7-2.



*Figure 7-2: Wing performance model (left) and dynamic thrust model (right) [23].*

#### 7.2.4 Subsystem Integration and Testing

A standard mounting system was developed for the X-1 and EFT pylons, as shown in Figure 7-3. This mounting approach allowed rapid prototyping on the aircraft. The EFT pylon was comprised of two components. One component constrained the bottle while the other secured the pylon to the wing. These components were subjected to structural testing which involved suspending weights from the bottle to simulate ultimate loads.

The X-1 test program was crucial for maximizing mission scores. The X-1 was deployed from a COTS aircraft for early testing to minimize risk to VIPER. Multiple preliminary X-1 vehicles were created with various design configurations. Each followed a standardized progression from ground tests to avionics integration and flight envelope expansion. Initial flight tests were unpiloted drops that analyzed free-response flight qualities. Top-performing designs progressed to piloted and autonomous flight testing. After evaluating all designs against scoring constraints, the best-performing X-1, VENOM, was selected.

The design and integration of subsystems were critical for achieving a competitive mission score. All pylons must be quickly interchangeable to comply with SY-15 and ACS-02. Subsystem design focused extensively on human factors integration to prioritize actuation time for GM score. Time trials were conducted for GM testing to simulate the procedures, influencing design based on system interactions. Staging blocks were initially used but later removed as they interfered with the X-1 pylon mechanism because of its proximity to the MLG.



*Figure 7-3: Common mounting system (left) and X-1 prototype mounted to COTS airframe (right).*

### 7.3 Flight Testing

The flight test campaign followed a progressive, risk mitigation methodology. Initial evaluations included taxi tests and motor run-ups to verify the overall integrity of the aircraft and its propulsion system. These were followed by proof-of-flight trials, low-g maneuvers, and incremental load testing, culminating in full mission simulations, as shown in Figure 7-4. Three aircraft iterations focused on separate and distinct testing objectives. Iteration 1 validated the initial stability and control characteristics, as defined in Section 4.6. Iteration 2 focused on evaluating endurance, propulsion efficiency, and payload integration. Iteration 3 verified the mission flight envelopes and completed a certification flight ahead of the competition. VIPER used FrSky sensors to monitor airspeed, power metrics, and GPS positioning for all iterations. Data was logged onto the transmitter, while onboard instrumentation notified the flight crew if the flight envelope had been exceeded. To increase the efficiency of flight tests, a modular torque box was added to the nose section of the aircraft. This allowed swapping of propulsion system components, primarily the motor, to minimize downtime during tests.



Figure 7-4: VIPER Iteration 2 proof of flight.

### 7.4 Test Schedule

Table 7-2 summarizes the completed and upcoming tests prior to the competition flyoff.

Table 7-2: Test schedule.

Date	Type	System	Objectives
Oct. 19	Flight	Pilot	Primary pilot selection
Oct. 26	Flight	Subsystem	Determine glide characteristics of prototype X-1 designs
Nov. 2	Flight	Iteration 1	Maiden flight; validate preliminary aircraft design
Nov. 9	Flight	Iteration 1	Test M2 endurance and propulsion system configurations
Nov. 11	Wind Tunnel	Subsystem	Gather drag data of external stores on the wing and
Nov. 16	Flight	Subsystem	Refine flight vehicle characteristics when manually piloted
Nov. 25	Wind Tunnel	Propulsion	Gather thrust data for various propulsion systems
Nov. 30	Ground	Structure	Test the ultimate strength of wing spars
Jan. 25	Flight	Subsystem	Gather quantitative flight characteristics of prototype X-1 designs
Feb. 1	Flight	Iteration 2	Maiden flight; gather aerodynamic and basic performance data
Feb. 8	Flight	Iteration 2	Incrementally load aircraft up to 39 lb
Feb. 15	Flight	Iteration 2	Load aircraft to 39 lb, gather performance data
Feb. 22	Flight	Iteration 2	Validate flight performance with various propulsion configurations
Mar. 8	Flight	Iteration 2	Gather quantitative flight performance data, perform all missions
Mar. 22	Flight	Iteration 3	Maiden flight
Mar. 29	Flight	Iteration 3	Pre-tech and first-flight certification



## **7.5 Test Checklists and Procedures**

Preflight procedures began 48 hours before a flight test with a briefing to review test cards containing the objectives, schedules, and operations. Preflight checks were conducted by the Flight Test Engineer and pilot upon arrival at the test field. The test followed the predefined test card, shown in Figure 7-5, on which postflight notes and data were recorded. During the debrief, team members reviewed the results to make decisions on potential design modifications to the aircraft. A test card as well as Ground, Preflight, and Postflight checklists are shown below in Table 7-3, Table 7-4, and Table 7-5.

*Table 7-3: Ground inspection checklist.*

Category	Item	Status
Fuselage	Aircraft skin tear-free	<input type="checkbox"/> Check
	Servos, linkages, and horns	<input type="checkbox"/> Secure
	All surfaces	<input type="checkbox"/> Secure
	Landing gear	<input type="checkbox"/> Secure
Motors	Motor & firewall	<input type="checkbox"/> Secure
	Propeller balanced and damage-free	<input type="checkbox"/> Check
	Prop direction	<input type="checkbox"/> Correct
Electrical & Controls	Propulsion battery	<input type="checkbox"/> Check
	Servo, receiver plugs	<input type="checkbox"/> Check
X-1 Vehicle	X-1 vehicle battery	<input type="checkbox"/> Secure
	X-1 battery	<input type="checkbox"/> Check
	X-1 ground station	<input type="checkbox"/> Check

*Table 7-4: Preflight checklist.*

Category	Item	Status
Power & Setup	Propulsion battery	<input type="checkbox"/> Installed
	Receiver battery	<input type="checkbox"/> Installed
	CG	<input type="checkbox"/> Correct
	Wingtip test	<input type="checkbox"/> Pass
	Receiver switch	<input type="checkbox"/> On
Control	Surface directions	<input type="checkbox"/> Correct
	Range check	<input type="checkbox"/> Pass
	Radio failsafe	<input type="checkbox"/> Pass
Final Checks	Throttle down/safe	<input type="checkbox"/> Pass
	Arming plug	<input type="checkbox"/> Disarm
	Propulsion run-up	<input type="checkbox"/> Pass
	Wind/takeoff direction	<input type="checkbox"/> Chosen
	Pilot ready to fly	<input type="checkbox"/> Go/No-Go

*Figure 7-5: Test card.*

*Table 7-5: Postflight checklist.*

Category	Item	Status
Power Down	Throttle down and safe	<input type="checkbox"/> Check
	Arming plug	<input type="checkbox"/> Installed
	Batteries	<input type="checkbox"/> Removed
Inspection & Data	Airframe health	<input type="checkbox"/> Check
	Propulsion system health	<input type="checkbox"/> Check
	Data	<input type="checkbox"/> Logged
	Debrief	<input type="checkbox"/> Complete

## 8 Performance Results

### 8.1 System Performance

#### 8.1.1 VENOM

VENOM's deployment system was designed to ensure successful separation and mission execution. Biased springs were used to induce an initial nose-down pitching moment, preventing in-flight collisions with VIPER.

Multiple descent strategies were evaluated, including waypoint-based altitude reductions and autonomous landing commands. A single loiter-unlimited function proved to be the most reliable flight profile. These tests were conducted with prewritten missions on the Ground Control Station platform Mission Planner. Additionally, it was observed that heavier models exhibited improved gust resistance, consistently landing within the designated 200 ft  $\times$  200 ft bonus box. A combination of EPP with green and yellow LEDs was found to provide the best visibility during daytime operations.

Testing examined the effects of mounting orientation. The results showed that maintaining a zero-lift angle of attack while stowed significantly improved efficiency while alternative orientations increased drag. Flight data comparisons between mounting styles revealed that the cross-mounted configuration drew considerably more power during flight than the in-line setup, particularly during sustained 125 ft/s flight segments. The power consumption for each orientation is shown in Figure 8-1, where the red boxes represent the mounting hardpoints as seen in Drawing 5 of 5.

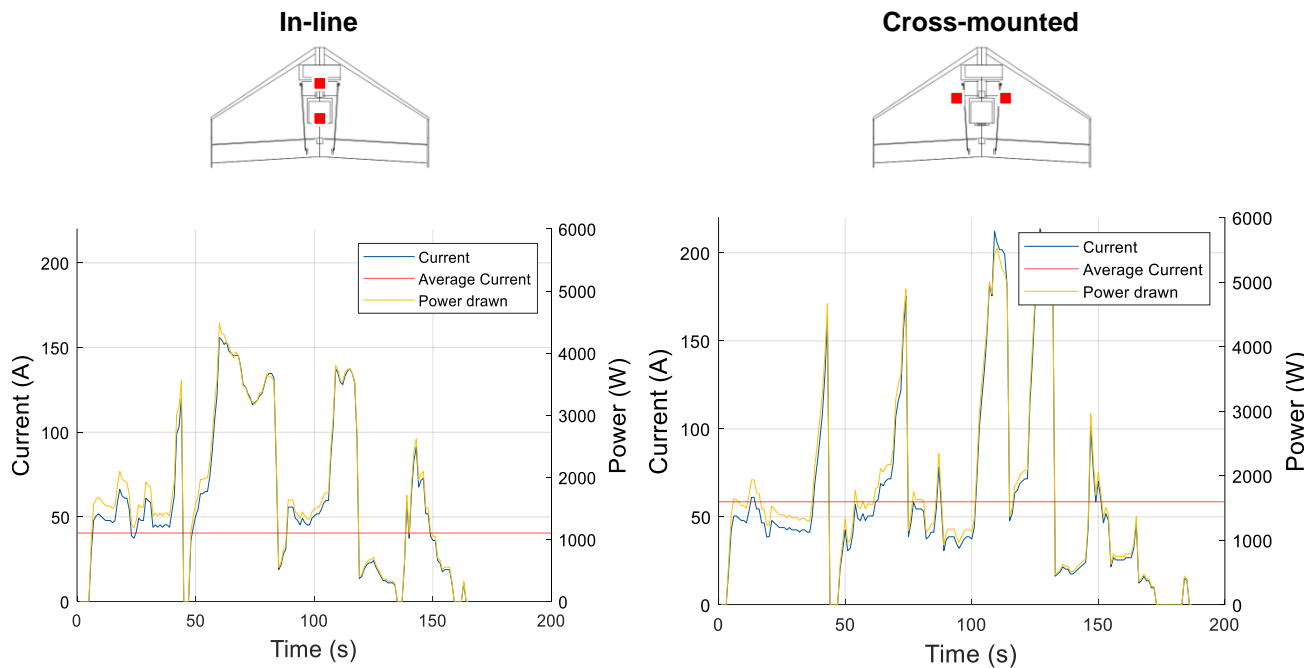


*Figure 8-1: VENOM mounting patterns versus propulsion system power consumption.*

#### 8.1.2 Fuel Tank Pylons

Wind tunnel and flight tests evaluated the drag and control effects of the EFTs and pylons, as outlined in Section 7.2.3. Flight testing was primarily qualitative, with the pilot noting reduced directional stability and roll response, though the aircraft remained controllable. Wind tunnel testing quantified the drag impact, revealing that adding the



EFTs and pylons reduced the wing's L/D by 16.5%, as shown in Figure 8-2. To minimize drag, additional tests examined the optimal bottle geometry and orientation. Two 16.9 fl oz bottles were tested for drag at different orientations: one with the cap facing into the wind and the other facing away. The test results are detailed in Table 8-1. The Perrier bottle had the lowest drag because of its streamlined shape, performing best with the cap oriented aft and exhibiting 8.9% less drag than a cylindrical shape, like that of a Bubly bottle.

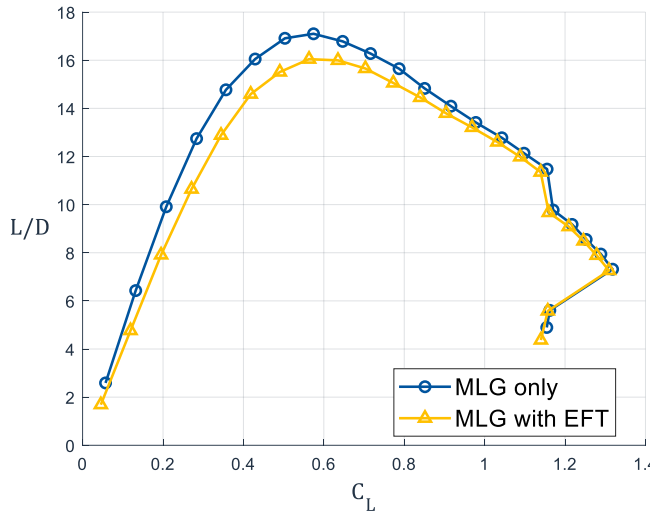


Table 8-1: Bottle orientation and drag values.

Bottle	Frontal Diameter	Orientation	$\Delta C_{D_0}$
Perrier	2.80 in	Cap forward	0.0060
		Cap aft	0.0041
Bubly	2.65 in	Cap forward	0.0060
		Cap aft	0.0045

Figure 8-2: Lift performance for EFT, pylons, and MLG.

### 8.1.3 Propulsion

Flight testing revealed that the propulsion system described in Section 4.5 was less efficient than expected and required a higher continuous power output. Figure 8-3 presents the RPM, airspeed, and power consumption of the 18x12C Falcon propeller, powered by a 4500 mAh 6S battery, during a 21-lb flight test. The results indicated that this propulsion configuration failed to achieve the desired lap times because of insufficient dynamic thrust. The propellor flight test data is shown in Figure 8-3, where airspeed in ft/s has been scaled to align with the range of power consumption in Watts, with the corresponding scale factor provided by Equation 8-1.

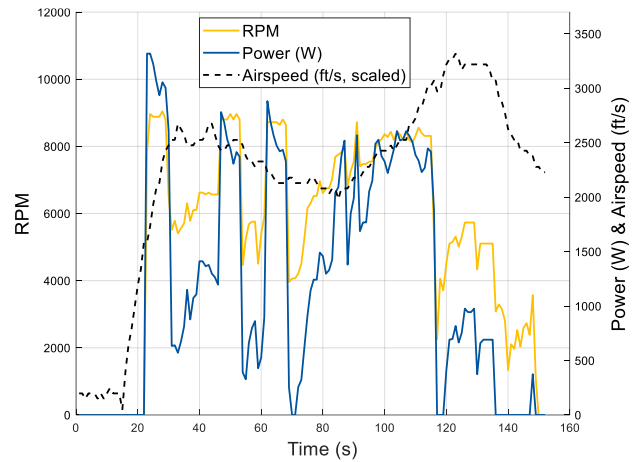


Figure 8-3: 18x12C propeller flight test data.

$$\text{Normalized Airspeed} = \text{Airspeed} \times \frac{\text{Power}_{max}}{\text{Airspeed}_{max}} \quad (8-1)$$

To maximize propulsion power while still in compliance with AC-13, the battery voltage was increased. Consequently, the maximum RPM increased but torque remained constant. To match to the new battery-motor



configuration, a propeller with a smaller diameter and higher pitch was preferred. The decrease in propeller diameter allowed it to produce more thrust at a higher RPM before reaching the torque of the previous system. The propellers considered in this assessment are listed in Table 8-2 with their corresponding specifications.

*Table 8-2: Propellers considered.*

Mission	Propeller	Battery	Target RPM	Power (Watts)	Dynamic Thrust (lb)
M2	17x12C	8S 3300 mAh	~10,000	~3,400	Goal ~ 15
M3	18x12C	6S 4500 mAh	~7,500	~1,300	Goal ~ 8.5

### 8.1.4 Structure

As detailed in Section 7.2.1, a three-point bending bench test was conducted to determine the ultimate strength of the braided weave CFRP main spar. The test results indicated that the spar could not withstand a load equivalent to a 4-g turn, as expected in M2. This finding confirmed that the initial spar was insufficient for the anticipated loads. A high-modulus twill weave spar was selected due to its superior layup process, cross-sectional geometry, and failure properties, as provided by the manufacturer [20]. This option resulted in a stiffer wing structure. Subsequent testing confirmed that the upgraded spar could withstand all expected loads while taking advantage of the high specific-strength composites. To improve the factor of safety, an additional structure was implemented to support a continuous layup for the aircraft's leading edge. This design leveraged the tension properties of GFRP to help reduce bending stress on the spar.

### 8.1.5 Subsystem Integration

Payload loading trials were conducted following requirements OP-02 and ACS-02, following the procedure outlined in Section 7.2.4. Through practice and multiple design iterations, the fuel tank pylons and insertion methods were refined. Fastening the bolts that secured the EFTs took the most amount of time during the GM runs. The minimum GM loading time demonstrated was one minute and 53 seconds, exceeding the time requirement set by ACS-02. To meet the required time constraint, improvements were made to the EFT installation method, IFT insertion method, and pylon attachment methods.

## 8.2 Complete Aircraft Performance

Table provides a comparative analysis of the aircraft's design performance versus its actual performance across all missions, normalized to the final mission score. Key differences included an increased M2 mission time, an increased weight of VENOM, and a reduced M3 lap count, which negatively impacted overall scoring. These differences to the initial performance estimates did not fully account for additional drag components, such as interference drag, or the propulsion system's energy consumption. Consequently, the airframe proved somewhat less efficient than predicted. However, improvements in structural efficiency, achieved through advanced manufacturing techniques, reduced the empty weight and increased the load factor. While airspeed reductions were necessary to enhance efficiency, they had minimal impact on



*Figure 8-4: VIPER Iteration 2 flight testing.*



demonstrated lap times. Increasing the X-1 weight ensured consistent placement within the 2.5-point bonus box, which was identified as a key factor in scoring potential by the sensitivity analysis. Despite the potential performance variations, shown in Table 8-3, the final predicted mission score of 5.52 remained highly competitive, confirming that VIPER met all design requirements and delivered a strong performance within the mission constraints. Table 8-4 details the composition of the predicted mission score.

*Table 8-3: Complete aircraft design versus actual performance.*

Mission	Parameter	Design	Actual	Difference
<b>All</b>	Empty Weight (lb)	15	13.58	- 9%
	Load Factor (g)	6	10	+ 67%
<b>GM</b>	Mission Time (s)	90	113	+ 26%
<b>M1</b>	Gross Takeoff Weight (lb)	15	13.58	- 9%
	Cruise Airspeed (ft/s)	125	125	0%
	Lap Time (s)	30	24	- 20%
	Mission Time (s)	100	85	- 15%
<b>M2</b>	Gross Takeoff Weight (lb)	39	38.74	- 1%
	Cruise Airspeed (ft/s)	125	115	- 8%
	Lap Time (s)	27	32	+ 19%
	Mission Time (s)	99	124	+ 25%
	Payload Weight (lb)	25	25	0%
	X-1 Weight (lb)	0.1	0.16	+ 60%
<b>M3</b>	Gross Takeoff Weight (lb)	17	14.42	- 15%
	Cruise Airspeed (ft/s)	90	90	0%
	Lap Time (s)	30	32	+ 7%
	Mission Time (s)	300	217	- 28%
	X-1 Weight (lb)	0.1	0.16	+ 60%
	Laps Completed	10	6	- 40%

*Table 8-4: Final mission scores.*

Mission	Design	Actual	Difference	Est. Fly-Off Maximum	Final Score
<b>M1</b>	Pass	Pass	N/A	-	1
<b>M2</b>	15.15 lb/min	12.10 lb/min	- 20%	18 lb/min	1.67
<b>M3</b>	9 laps + 25 bonus	21.63	- 36%	12 laps + 25 bonus	2.58
<b>GM</b>	1.5 min	1.88 min	+ 26%	0.5 min	0.27
<b>Total</b>					<b>5.52</b>



## Bibliography

- [1] “2024-25 Design, Build, Fly Rules,” Competition Information, AIAA, retrieved 19 February 2025.  
<https://www.aiaa.org/dbf/competition-information/rules-resources>
- [2] Embry-Riddle Aeronautical University Daytona Beach Design, Build Fly Team, “AIAA Design, Build, Fly Team – ROOSTER Competition Aircraft 2022-2023,” Embry-Riddle Aeronautical University, 2023
- [3] Embry-Riddle Aeronautical University Daytona Beach Design, Build Fly Team, “AIAA Design, Build, Fly Team – WRENCH Competition Aircraft 2023-2024,” Embry-Riddle Aeronautical University, 2024
- [4] “MATLAB,” Numeric Computing Platform, 2024a, MathWorks
- [5] “United States Air Force Stability and Control DATCOM,” AFWAL-TR-83-3048, 1978.
- [6] “Surfaces Pro,” Vortex Lattice Method Solver, Flight Level Engineering, 2021.
- [7] “Performance Data,” Advanced Precision Composites, 2023.
- [8] “CATIA, “Computer-Aided Design, V5-6R2020, Dassault Systems.
- [9] “Finite Element Modeling and Postprocessing,” Advanced Simulation Application, Siemens, 2022.
- [10] Hoerner, S. F., *Fluid-Dynamic Drag*, Hoerner Fluid Dynamics, Midland Park, NJ, 1965.
- [11] Roskam, J., “Airplane Design,” 2nd ed., DAR Corporation, 2003.
- [12] Gudmundsson, S., *General Aviation Aircraft Design: Applied Methods and Procedures*, 2nd ed., Butterworth-Heinemann, Oxford, U.K., 2021.
- [13] Raymer, D. P., “Aircraft Design: A Conceptual Approach,” 6th ed., AIAA, 2018
- [14] XFLR5, Airfoil Analysis Tool, Drela, M, 2019.
- [15] Selig, M. S., Giguère, P., Lyon, C. A., and Ninham, C. P., *Summary of Low-Speed Airfoil Data*, Vol. 1, SoarTech Publications, Virginia Beach, VA, 1995.
- [16] “AIAA Design Build Fly Competition Summary 2019–20,” Previous Competitions, AIAA, retrieved 20 February 2025. [www.aiaa.org/dbf/previous-competitions](http://www.aiaa.org/dbf/previous-competitions)
- [17] “VSPAERO,” Vortex Lattice Method Solver, OpenVSP, 2012VENMON
- [18] Weather Underground, “Monthly Weather History for Tucson, AZ (KTUS), April 2024,” The Weather Company, April 2024. Available at:  
[www.wunderground.com/history/monthly/us/az/tucson/KTUS/date/2024-4](http://www.wunderground.com/history/monthly/us/az/tucson/KTUS/date/2024-4) [Accessed 20 Feb. 2025].
- [19] U.S. Government Publishing Office, *Title 14 Code of Federal Regulations, Part 23 – Airworthiness Standards: Airplanes*, 2017. Available at: <https://www.govinfo.gov/content/pkg/CFR-2017-title14-vol1/pdf/CFR-2017-title14-vol1-part23.pdf> [Accessed 20 Feb. 2025].
- [20] DragonPlate, *Carbon Fiber Roll-Wrapped Twill Square Tube (0.75" ID x 0.75" ID x 24")*, DragonPlate – Allred & Associates, 2025. Available at: <https://dragonplate.com> [Accessed 20 Feb. 2025].
- [21] ArduPilot, *ArduPilot: Open Source Autopilot*, ArduPilot, 2025. Available at: <https://ardupilot.org/> [Accessed 20 Feb. 2025].
- [22] Pilot RC, *PW-21AH 21kg (1/2 Alu Arm) Servo*, Pilot RC, 2025. Available at: <https://pilot-rc.com/pw-21ah-21kg-1-2-alu-arm/> [Accessed 20 Feb. 2025].
- [23] “Onshape,” Computer-Aided Design, Parametric Technology Corp., 2023. [www.onshape.com/en](http://www.onshape.com/en)